Applications of multinuclear magnetic resonance to the characterisation of zeolites

Challoner, Robin

APPLICATIONS OF MULTINUCLEAR MAGNETIC RESONANCE TO THE CHARACTERISATION OF ZEOLITES

by

ROBIN CHALLONER

B.Sc., University of Durham (1986)

A thesis submitted for the degree of Doctor of Philosophy of the University of Durham.

Grey College

September 1989

All men dream: but not equally. Those who dream by night in the dusty recesses of their minds wake in the day to find that it was vanity: but the dreamers of the day are dangerous men, for they may act out their dream with open eyes, to make it possible.

T. E. LAWRENCE

Seven Pillars of Wisdom.

MEMORANDUM

The research presented in this thesis has been carried out at the Department of Chemistry of the University of Durham between October 1986 and September 1989. It is the original work of the author unless stated otherwise. None of this work has been submitted for any other degree.

Applications of Multinuclear Magnetic Resonance to the Characterisation of Zeolites

by

ROBIN CHALLONER

Abstract

The following research is primarily concerned with the characterisation of the novel, unidimensional, zeolite theta-1 by solid-state multinuclear magnetic resonance spectroscopy. Some study has also been made of the zeolites ZSM-5 and NaY.

The high-silica form of as-synthesised theta-1 is studied by high-resolution ^{13}C and ^{29}Si MASNMR. The ^{13}C spectra are interpreted as showing the presence of both neutral and protonated diethylamine template molecules. These observations are discussed in terms of the possible presence of acid sites and their spatial distribution. The ^{29}Si NMR results are consistent with the template molecules occupying the 10-T channels only. The ^{29}Si spin-lattice relaxation mechanism is investigated under a variety of conditions. Changes in the ^{29}Si NMR spectra on calcination indicate the possibility of a minor framework rearrangement.

Theta-1 synthesised using a diethanolamine template is also investigated. The template distribution is examined, and evidence for structural modification by the presence of the template is presented. The nature of the non-framework aluminium species produced on hydrothermal dealumination and the broad linewidths observed for such species in ^{27}Al NMR are also investigated.

The signal response to the application of a single pulse of finite duration to a system of $I=^{3}/2$ nuclei is used to illustrate the differences between selective and non-selective excitation of the central transition, and the requirements for quantitivity. A series of model compounds is investigated by quadrupole nutation NMR, and more complex zeolite systems containing quadrupolar nuclei are investigated by a variety of techniques.

ACKNOWLEDGEMENTS

I thank my supervisors Robin Harris, Ken Packer and Mike Taylor for their help and guidance throughout the period of research. I am grateful to the B.P. Research Centre at Sunbury (RCS) for making available a considerable amount of spectrometer time in addition to many other facilities. I am particularly grateful to Dave Roberts for the acquisition of much of the ^{27}Al NMR data obtained at 104.22 MHz, and for providing details on the quantitation procedure. I thank Mike and Dave for numerous discussions concerning quantitation and linebroadening mechanisms in ^{27}Al NMR, and also for allowing the collaboration of data. I am also grateful to Sammi Barri and Dave Walker for helping me with the synthetic work. I acknowledge all the members of the NMR group at RCS who have helped me.

I thank all of the past and present members of the group at Durham who have made a positive contribution to the research presented in this thesis. I am particularly indebted to Angelika Sebald and Pete Jackson for spending a considerable amount of their time introducing me to NMR.

On a more personal note, I thank my tennis-playing friends - Dave, Al, Pete, Jane, Penny and Alan for contributing to a thoroughly memorable time at Durham.

I am grateful to Marion Wilson for typing this manuscript, and also to Elizabeth Wood for preparing some of the diagrams.

I am indebted to B.P. and the S.E.R.C. for an award under the CASE scheme.

ABBREVIATIONS

The following have been used:

MAS	Magic-Angle Spinning
NMR	Nuclear Magnetic Resonance
r.f.	radio frequency
SP	Single-Pulse Experiment
CP	Cross-Polarization
CRAMPS	Combined Rotation and Multiple-Pulse Spectroscopy
HPPD	High-Power Proton Decoupling
t_1, t_2	Time domains in 2-D NMR
F_1, F_2	Frequency domains in 2-D NMR
SF	Spectrometer Frequency
PA	Pulse Angle
RD	Recycle Delay
NT	Number of Transients
SR	Spin Rate
LB	Exponential linebroadening factor
CT	Contact Time
TPD	Temperature-Programmed Desorption
TGA	Thermal Gravimetric Analysis
ESCA	Electron Spectroscopy for Chemical Analysis
XRD	X-Ray Diffraction
XRF	X-Ray Fluorescence
AA	Atomic Absorption
ppm	parts per million
SBU	Secondary Building Unit
FID	Free Induction Decay
EFG	Electric Field Gradient
PAS	Principal Axis System
S/N	Signal to Noise ratio
TMS	Tetramethylsilane

CONTENTS

Page No.

CHAPTER ONE

INTRODUCTION

1.1 Introduction

Zeolites were first recognised as a new class of material in 1756. The word zeolite was derived from two Greek words meaning to boil and a stone. Subsequent study has since revealed the remarkable ability of zeolites to function as molecular sieves. As microporous solids with a range of uniform pore sizes, zeolites may selectively adsorb or reject molecules depending on their molecular size. Thus, Ca-exchanged zeolite Linde A can separate n-paraffins from a mixture of hydrocarbons. Highly polar zeolite crystals have the added ability to selectively absorb polar molecules in the presence of non-polar molecules. The industrial uses of molecular sieving include thorough drying of organics, separation of hydrocarbons, and the removal of NH_3 and CS_2 from industrial gases.

Zeolites often possess high ion-exchange selectivities for certain cations, and cations neutralizing the electrical charge of the zeolite framework may be exchanged for other cations in solution. Important applications include the collection of harmful products of nuclear fission, water softening and the recovery of precious elements.

The catalytic activity of zeolites was discovered in the late 1950s and has become the most important commercial application of zeolites. A whole range of zeolite catalysts have been developed for reactions such as cracking, hydrocracking, oxidation and isomerization of hydrocarbons. The high-silica zeolite ZSM-5 is a powerful catalyst for the isomerization of C_8 aromatics to isometrically pure xylenes,

for ethylene synthesis and catalytic dewaxing,and for the conversion of methanol to gasoline in a single step.

During the last 10 years, high-resolution solid-state NMR spectroscopy has contributed greatly to our knowledge and understanding of zeolites. Information concerning the formation, structure, and structural modification has been obtained. In spite of the vast number of research publications concerning the application of solid-state NMR to zeolites, the ever increasing number of publications bears witness to the many areas in the zeolite field that have been left unexplored.

1.2 Organisation of the thesis

A brief summary of the contents of the chapters is given below:

Chapter Two contains a review of basic solid-state NMR theory. The important nuclear spin interactions in the solid-state, and methods of reducing the linebroadening influences of dipolar, chemical shift and quadrupolar interactions arising from their anisotropic nature are discussed. An introduction to density matrix theory and a discussion of relaxation phenomena are also given.

Chapter Three is concerned with the experimental considerations. The pulse sequences used and a description of the experimental procedures used are discussed. A brief review of the nuclei studied (with relevance to zeolites) is given, as is a description of the non-NMR techniques used to characterise the zeolites.

Chapter Four contains a detailed description of each of the zeolites investigated. The structural characterisation of the zeolites both by ^{29}Si NMR and XRD is discussed.

Chapter Five starts by considering the effect of a finite pulse duration on a system of half-integer spin quadrupolar nuclei by a density matrix calculation. The results are used to illustrate the conditions required for quantitative analysis of such nuclei and the natural extension of the results to the 2D nutation experiment is considered. A series of model compounds is investigated by nutation experiments under a variety of conditions. The results of the first part of the chapter are then used to investigate unusual behaviour observed in both the aluminium spectrum of NH_4^+-ZSM-5 on dehydration and in the sodium spectrum of fully hydrated NaY zeolite.

Chapter Six discusses the results of a multinuclear magnetic resonance study of high-silica theta-1. ^{13}C NMR indicates the presence of two types of organic diethylamine template and this is interpreted in terms of the possible presence of acid sites. Information on the spatial distribution of the acid site is also provided. Corroborating evidence for a further removed crystallographic site from the main channel of theta-1 is provided by ^{29}Si NMR, and changes in the ^{29}Si NMR spectrum on calcination provide evidence for a minor framework rearrangement. An investigation is also made of the ^{29}Si spin-lattice relaxation mechanisms in theta-1 under a variety of conditions.

Chapter Seven is mainly concerned with the results of a multinuclear magnetic resonance study of theta-1 synthesised with a diethanolamine template, but with some reference to ZSM-5 and its gallium-containing analogue. In the case of theta-1, the results are interpreted in terms of the modifications arising in the ^{29}Si NMR spectrum as a result of the presence of the diethanolamine template, the use of the template as a probe for both bulk and surface acid sites, and the nature of the template interaction with the surface. The bulk acid sites are also observed directly by ^{1}H NMR and are further characterised by temperature programmed desorption of ammonia. The hydrothermal dealumination of both theta-1 and ZSM-5 is performed under strong conditions and the resulting samples are analysed by both quantitative ^{27}Al NMR and temperature programmed desorption of ammonia (in the case of theta-1). The linebroadening mechanism of the non-framework aluminium species is considered, and finally the application of multiple-pulse type sequences to quadrupolar nuclei is investigated.

CHAPTER TWO

BASIC SOLID-STATE NMR THEORY

2.1 Introduction

Nuclear magnetic resonance spectroscopy studies the behaviour of certain atomic nuclei, namely those which have magnetic moments arising from their possessing "spin", in the presence of an applied magnetic field B_0. For a nucleus with a spin quantum number I, the Zeeman interaction results in 2I+1 separate energy levels between which transitions may be caused by absorption of suitable electromagnetic radiation. The splitting of the energy levels, and the frequency of the required radiation, is determined by the spin Hamiltonian:

$$\hbar^{-1}\hat{H}_z = -\sum_i \gamma_i \underset{\sim}{B}_0 \cdot \hat{\underset{\sim}{I}}_i \qquad (2.1)$$

where $\hat{\underset{\sim}{I}}_i$ is the spin vector operator and γ_I the gyromagnetic ratio of the nucleus i. The Zeeman interaction is usually the largest to which a nuclear spin is subjected, although the nuclear spin is typically subject to a number of physically different interactions[1]. Some of these are related to the apparatus and some to the physical properties of the sample. Some cause shifts, while others cause broadening of the NMR lines. The nuclear spin Hamiltonian may be represented by the sum:

$$\hat{H} = \hat{H}_z + \hat{H}_{rf} + \hat{H}_D + \hat{H}_{CS} + \hat{H}_Q + \hat{H}_J + \hat{H}_{SR} \qquad (2.2)$$

where in addition to the Zeeman term which accounts for the interaction of the nuclear magnetic moment with the applied B_0 field, there are terms corresponding to the coupling of the nuclear spins with; the time-dependent radiofrequency field B_1 ($\hat{H}_{rf}$), each other through their magnetic dipole moments ($\hat{H}_D$), electric field gradients ($\hat{H}_Q$), one another *via* electron

spins ($\hat{H}_J$), induced magnetic fields originating from orbital motions of electrons ($\hat{H}_{CS}$), and the magnetic moment associated with the molecular angular momentum ($\hat{H}_{SR}$).

$\hat{H}_Z$ and $\hat{H}_{rf}$ are the so-called external Hamiltonians and are under the control of the experimentalist, while of the remaining internal terms, $\hat{H}_Q$, $\hat{H}_D$ and $\hat{H}_{CS}$ are the most important for the solids studied in this thesis. $\hat{H}_J$ and $\hat{H}_{SR}$ are unimportant in the context of this thesis and are consequently disregarded from further discussion.

All of the intrinsic spin interactions are anisotropic and in a solid, the spin interactions yield NMR frequencies which depend on the orientation of the magnetic field with respect to the molecular or crystal axes. In the case of powders such as zeolite samples, all possible orientations of the crystallites are present and many frequencies are simultaneously observed, which leads to broad, featureless spectra in the absence of the high-resolution techniques outlined below. The situation is in contrast to the solution state where the anisotropy of these interactions is averaged by the tumbling of the molecules.

If no account is taken of the sum over the nuclear magnetic moments (or over the pairs i, k of them), the spin interactions described quantum mechanically in terms of the appropriate Hamiltonians may be expressed as[1,2]:

$$\hbar^{-1}\hat{H}_\lambda = C^\lambda \sum_{\substack{\alpha,\beta \\ =x,y,z}} \hat{I}_\alpha R^\lambda_{\alpha\beta} A^\lambda_\beta \qquad (2.3)$$

The coefficients C^λ are typical constants for each interaction mechanism. $\hat{\underset{\sim}{I}}$ is the nuclear spin vector operator, $\underset{\approx}{R}^\lambda$ a second rank tensor and $\underset{\sim}{A}^\lambda$ a vector which may be the same

spin vector in the case of the quadrupole interaction or another spin vector in the case of the dipolar interaction. The quantities C^{λ}, R^{λ}, and A^{λ} are shown in Table 2.1

TABLE 2.1 The interaction Hamiltonians[2]

λ	Name	C^{λ}	$R^{\lambda}_{\alpha\beta}$	$T_{\alpha\beta} = \hat{I}^{i}_{\alpha} A^{\lambda}_{\beta}$
Z	Zeeman[a]	γ	$\delta_{\alpha\beta}$[b]	$\hat{I}_{\alpha} B_{\beta}$ $B_{\beta}=\{0,0,B_{o}\}$
CS	Chemical shift[a]	γ	$\sigma_{\alpha\beta}$	$\hat{I}_{\alpha} B_{\beta}$
D	Dipole-dipole	$-2\gamma_{i}\gamma_{k}\hbar\frac{\mu_{o}}{4\pi}$	$\frac{1}{2}(3e_{\alpha}e_{\beta}-\delta_{\alpha\beta})r_{ik}^{-3}$ $\underset{\sim}{r} = \sum_{\alpha} \underset{\sim}{e}_{\alpha} x_{\beta}$	$\hat{I}^{i}_{\alpha}\hat{I}^{k}_{\beta}$
Q	Quadrupole[a]	$\frac{eQ}{2I(2I-1)h}$	$V_{\alpha\beta}$ $\sum_{\alpha} V_{\alpha\alpha} = 0$	$\hat{I}_{\alpha}\hat{I}_{\beta}$

[a] Subscript i on γ, $\hat{I}$, σ and Q omitted.

[b] Kronecker symbol.

The tensor $\underset{\simeq}{R}$ may be divided into the sum of isotropic, $\underset{\simeq}{R}_{iso}$, antisymmetric, $\underset{\simeq}{R}_{asym}$, and symmetric, $\underset{\simeq}{R}_{sym}$ parts. These parts are given by[2]:

$$\underset{\simeq}{R}_{iso} = R\delta_{\alpha\beta} \qquad R = {}^{1}/_{3}\mathrm{Tr}\ \underset{\simeq}{R} \tag{2.4}$$

$$\underset{\simeq}{R}_{asym} = \tfrac{1}{2}(R_{\alpha\beta} - R_{\beta\alpha}) \tag{2.5}$$

$$\underset{\simeq}{R}_{sym} = \tfrac{1}{2}(R_{\alpha\beta} + R_{\beta\alpha}) - R\delta_{\alpha\beta} \tag{2.6}$$

The tensors $\underset{\simeq}{R}^{D}$ and $\underset{\simeq}{R}^{Q}$ are traceless (R=0) and symmetric ($R_{\alpha\beta} = R_{\beta\alpha}$). The tensor $\underset{\simeq}{R}^{CS} = \underset{\simeq}{\sigma}$ may contain all three parts. However, since the antisymmetric part of $\underset{\simeq}{\sigma}$ is difficult to

measure because of its small magnitude, $\underset{\sim}{R}^{CS}$ is considered to be a symmetric tensor. For each tensor, a frame of principal axes X, Y, Z exists with tensor components R_{XX}, R_{YY}, R_{ZZ}, and the axes are chosen so that

$$|R_{ZZ} - R| \geq |R_{YY} - R| \geq |R_{XX} - R| \tag{2.7}$$

In this frame the traceless symmetric part of $\underset{\sim}{R}$ can be written as

$$\underset{\sim}{R}_{sym} = \delta \begin{vmatrix} \frac{1}{2}(\eta-1) & 0 & 0 \\ 0 & -\frac{1}{2}(\eta+1) & 0 \\ 0 & 0 & 1 \end{vmatrix} \tag{2.8}$$

where $\delta = R_{ZZ} - R$ (2.9)

and $\eta = (R_{XX} - R_{YY})/\delta \quad ; \; 0 \leq \eta \leq 1$ (2.10)

δ is the anisotropy and η the asymmetry parameter of the interaction. These parameters are indicated in Table 2.2.

TABLE 2.2 Elements of interaction tensors in the principal axis frame X, Y, Z[2]

λ	$R = 1/3 \text{ tr } \underset{\sim}{R}$	δ	η	Orientation of X,Y,Z
CS	$\sigma = 1/3(\sigma_{XX} + \sigma_{YY} + \sigma_{ZZ})$	$\sigma_{ZZ}-\sigma$	$\frac{\sigma_{XX} - \sigma_{YY}}{\sigma_{ZZ} - \sigma}$	Z, axis of greatest screening
D	0	$1/r^3$	0	$Z \parallel \underset{\sim}{r}_{ik}$
		$\lvert\underset{\sim}{r}_{ik}\rvert = r$		
Q	0	$V_{ZZ} = eq$	$\frac{V_{XX} - V_{YY}}{V_{ZZ}}$	Z, axis of greatest EFG

The interaction Hamiltonian may be expressed in spherical tensor components[1,2]:

$$\hbar^{-1}\hat{H}_\lambda = C^\lambda \sum_{\ell=0,2} \sum_{m=-\ell}^{+\ell} (-1)^m A_{\ell m} T_{\ell -m} \tag{2.11}$$

TABLE 2.3 Irreducible tensor operators $T_{\ell m}$ (ℓ=0,2) for the interaction Hamiltonians $\hat{H}_\lambda$ (λ = CS,Q,D) and tensor components $A_{\ell m}$ in spherical coordinates. The components $A_{\ell m}$ are given for the principal axes systems of the different tensors $\underset{\sim}{R}^\lambda$. $\hat{I}_\pm = \hat{I}_x \pm i\hat{I}_y, \hat{S}_\pm = \hat{S}_x \pm i\hat{S}_y$

	Hamiltonians		
Tensors $T_{\ell m}$, $A_{\ell m}$	Chemical shift (CS)	Quadrupole (Q)	Dipolar I - S (D)
T_{00}	$-\frac{1}{\sqrt{3}}\hat{I}_z B_0$	$-\frac{1}{\sqrt{3}}(\underset{\sim}{\hat{I}}^2)$	$-\frac{1}{\sqrt{3}}(\underset{\sim}{\hat{I}}\underset{\sim}{\hat{S}})$
T_{20}	$\frac{2}{\sqrt{6}}\hat{I}_z B_0$	$\frac{1}{\sqrt{6}}[3\hat{I}_z^2 - \underset{\sim}{\hat{I}}^2]$	$\frac{1}{\sqrt{6}}[3\hat{I}_z\hat{S}_z - \underset{\sim}{\hat{I}}\underset{\sim}{\hat{S}}]$
$T_{2\pm1}$	$\mp\frac{1}{2}\hat{I}_\pm B_0$	$\mp\frac{1}{2}[\hat{I}_\pm\hat{I}_z + \hat{I}_z\hat{I}_\pm]$	$\mp\frac{1}{2}[\hat{I}_\pm\hat{S}_z + \hat{I}_z\hat{S}_\pm]$
$T_{2\pm2}$	0	$\frac{1}{2}\hat{I}_\pm^2$	$\frac{1}{2}\hat{I}_\pm\hat{S}_\pm$
$A_{00} = R$	σ	0	0
$A_{20} = \sqrt{\frac{3}{2}}\delta$	$\sqrt{\frac{3}{2}}\delta_{CS}$	$\sqrt{\frac{3}{2}}\delta_Q$	$\sqrt{\frac{3}{2}}\delta_D$
$A_{2\pm1}$	0	0	0
$A_{2\pm2} = \frac{1}{2}\eta\delta$	$\frac{1}{2}\eta_{CS}\delta_{CS}$	$\frac{1}{2}\eta_Q\delta_Q$	0

The elements of the tensors $A_{\ell m}$ and $T_{\ell -m}$ in spherical coordinates can be expressed through the components of the tensors $R_{\alpha\beta}$ and $T_{\alpha\beta}$ in cartesian coordinates (Table 2.3). The components of $A_{\ell m}$ are only given for the principal axis system (PAS) of the different tensors $\underline{\underline{R}}^{\lambda}$, because the spherical tensors $A'_{\ell m}$ in a new frame (x', y', z') are related to the components $A_{\ell m}$ by Wigner rotation matrices $D^{\ell}_{m'm}(\alpha,\beta,\gamma)$ in the form[1,2]:

$$A'_{\ell m} = \sum_{m=-\ell}^{\ell} D^{\ell}_{m'm}(\alpha,\beta,\gamma) A_{\ell m'} \qquad (2.12)$$

The coordinates α,β,γ are the Eulerian angles for the rotation of the PAS in the new frame. For the following cases, only the rotation matrices with $\ell=2$ are required (Table 2.4).

TABLE 2.4 The Wigner rotation matrices[2]: $D_{m'm}(\alpha,\beta,\gamma) = d^{2}_{m'm}(\beta)\exp[i(m'\gamma+m\alpha)]$ [a]

	$d^{2}_{m'm}(\beta)$ [b]		
	m		
m'	2	1	0
$^{+}_{(-)}2$	$\frac{1}{4}(1^{+}_{(-)}\cos\beta)^{2}$	$^{+}_{(-)}\frac{1}{2}(1^{+}_{(-)}\cos\beta)\sin\beta$	$\sqrt{3/8}\sin^{2}\beta$
$^{+}_{(-)}1$	$-\frac{1}{2}(1^{+}_{(-)}\cos\beta)\sin\beta$	$^{+}_{(-)}\left[\cos^{2}\beta-\frac{1^{-}_{(+)}\cos\beta}{2}\right]$	$^{+}_{(-)}\sqrt{3/8}\sin 2\beta$
0	$\sqrt{3/8}\sin^{2}\beta$	$-\sqrt{3/8}\sin 2\beta$	$\frac{3\cos^{2}\beta-1}{2}$

[a] $D^{2}_{Om}(\alpha,\beta,\gamma) = \sqrt{\frac{4\pi}{5}}Y_{2m}(\beta,\alpha)\,.\,D^{2}_{m'O}(\alpha,\beta,\gamma) = (-)^{m'}\sqrt{\frac{4\pi}{5}}Y_{2m'}(\beta,\gamma)$.

[b] For m = -1, -2 use the equation $d^{2}_{-m'-m} = (-1)^{m'+m}d^{2}_{m'm}$.

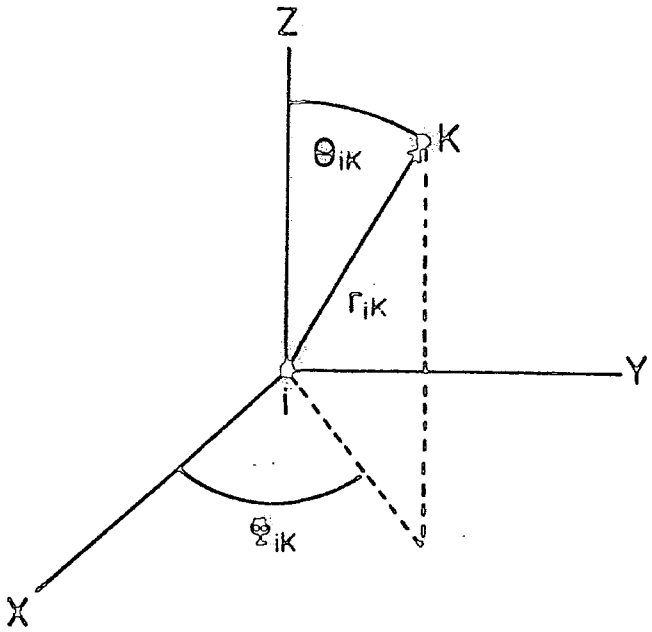

Figure 2.1: Definition of angles used in the desciption of the internal Hamiltonians.

2.2 The internal Hamiltonians

2.2.1 Dipolar interaction

In the principal axis system, the interaction Hamiltonian may be expressed as[2]:

$$\hbar^{-1}\hat{H}_D = C^D A^D_{20} T^D_{20} \qquad (2.13)$$

Use of equation (2.12) and Table 2.4 leads to an expression for the Hamiltonian in the laboratory frame[2];

$$\hbar^{-1}\hat{H}_D = C^D \sqrt{\frac{6\pi}{5}}\, r_{ik}^{-3} \sum_{m=-2}^{+2} (-1)^m Y_{2m}(\Theta_{ik}, \Phi_{ik}) T^D_{2-m} \qquad (2.14)$$

with the spherical harmonics Y_{2m}, and Θ_{ik} and Φ_{ik} the polar and azimuthal angles of the vector $\underset{\sim}{r}_{ik}$ (Figure 2.1).

The secular term of the homodipolar Hamiltonian expressing the interaction between an ensemble of similar spins is given by:

$$\hbar^{-1}\hat{H}^{sec}_{D,II} = \frac{\gamma_I^2 \hbar \mu_o}{4\pi} \tfrac{1}{2} \sum_{i<k} r_{ik}^{-3} (\hat{\underset{\sim}{I}}^i . \hat{\underset{\sim}{I}}^k - 3\hat{I}^i_z \hat{I}^k_z)(3\cos^2\Theta_{ik} - 1) \qquad (2.15)$$

For an isolated pair (i,k) the NMR spectrum shows a doublet with resonance frequencies[2]:

$$\nu = \nu_o \pm \Delta\nu\,(1 - 3\cos^2\Theta_{ik}) \qquad (2.16)$$

where $$\Delta\nu = \frac{1}{2\pi} \cdot \frac{3\gamma_I^2 \hbar}{4 r_{ik}^3} \cdot \frac{\mu_o}{4\pi} \qquad (2.17)$$

In the heterodipolar case, the secular part of the Hamiltonian for two isolated spins is given by:

$$\hbar^{-1}\hat{H}^{sec}_{D,IS} = \frac{\gamma_I \gamma_S \hbar \mu_o}{4\pi r_{IS}^3} (1 - 3\cos^2\Theta)\hat{I}_Z \hat{S}_Z \qquad (2.18)$$

and the splitting frequency is now given by[2]:

$$\Delta\nu = \frac{1}{2\pi} \cdot \frac{\gamma_I \gamma_S \hbar}{4 r_{IS}^3} \cdot \frac{\mu_o}{4\pi} \qquad (2.19)$$

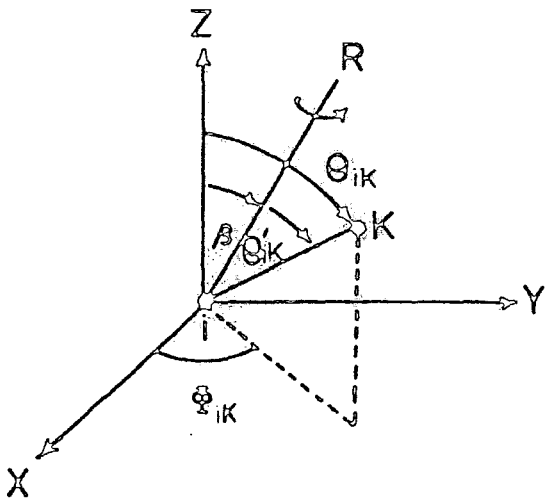

Figure 2.2: Definition of the angles used in the description of magic angle spinning.

Consideration of the above equations reveals that the dipolar coupling is strongly dependent on the internuclear distance and is only important for nuclei that are close to one another. In the case of zeolites, isotopic dilution of such spins as ^{29}Si or ^{13}C ensures that the homodipolar interaction between these spins is small due to large average r_{ik} distances[3]. A similar situation occurs for the ^{27}Al-^{27}Al interaction. In spite of being isotopically abundant, the aluminium nuclei are never neighbours in the framework. For the heterodipolar case, large r_{ik} distances between the nuclei referred to above ensure only a small heterodipolar interaction.

The dipolar interaction may be averaged to zero by either motional effects (i) or magic angle spinning (ii):

(i) Random motion of molecules such as water[3] in the zeolite pores averages the dipolar interaction to zero because the isotopic average $\cos^2\theta_{ik} = 1/3$.

(ii) Rapid sample spinning at a frequency ω_r about an axis inclined to B_0 by an angle β renders the angles θ_{ik} time-dependent. The time-dependence may be expressed by[4,5]:

$$\cos\theta_{ik}=\cos\beta.\cos\theta'_{ik}+\sin\beta.\sin\theta'_{ik}.\cos(\omega_r t+\phi^o_{ik}) \qquad (2.20)$$

where θ'_{ik} is the angle between the internuclear vector r_{ik} and the spinning axis and ϕ^o_{ik} is the azimuthal angle of vector r_{ik} at t=0 (Figure 2.2). Substitution of this expression into equation (2.15) results in a Hamiltonian consisting of two parts, a mean value $\bar{H}_d$ independent of time t and a time dependent part $\hat{H}_d(t)$ periodic with ω_r and zero mean value[4]:

$$\hat{H}_d = \bar{H}_d + \hat{H}_d(t) \tag{2.21}$$

$$\bar{H}_d = \tfrac{1}{2}(3\cos^2\beta - 1) \sum_{i<k} \tfrac{1}{2} \cdot \frac{\gamma_I^2 \hbar^2 \mu_o}{4\pi r_{ik}^3} \cdot (\hat{I}^i \cdot \hat{I}^k - 3\hat{I}_z^i \hat{I}_z^k)(3\cos^2\theta'_{ik} - 1) \tag{2.22}$$

$$\hat{H}_d(t) = \sum_{i<k} \tfrac{1}{2} \cdot \frac{\gamma_I^2 \hbar^2 \mu_o}{4\pi r_{ik}^3} \cdot \{ (\hat{I}^i \cdot \hat{I}^k - 3\hat{I}_z^i \hat{I}_z^k)$$

$$3/2 \sin 2\beta . \sin 2\theta'_{ik} . \cos(\omega_r t + \phi^o_{ik}) \tag{2.23}$$

$$+ 3/2 \sin^2\beta . \sin^2\theta'_{ik} . \cos(2\omega_r t + 2\phi^o_{ik}) \}$$

Similar expressions are obtained in the heteronuclear case. It may be shown that[6]:

$$\langle 3\cos^2\theta_{ik} - 1 \rangle = \tfrac{1}{2}(3\cos^2\beta - 1)(3\cos^2\theta'_{ik} - 1) \tag{2.24}$$

The parameter θ'_{ik} is fixed for a rigid solid, though like θ_{ik}, it takes all possible values if the material is a powder. The term $\frac{1}{2}(3\cos^2\beta - 1)$ therefore acts as a scaling factor on the dipolar powder pattern and the angle is experimentally accessible unlike θ'_{ik}. Thus the time-averaged homonuclear dipolar Hamiltonian $\bar{H}_d$ is zero when β is equal to $54^o44'$. Dipolar broadening (homo- and heteronuclear) can in principle be eliminated by spinning at the "magic-angle" ($54^o44'$). The time-dependent part $\hat{H}_d(t)$ gives rise to spinning sidebands separated from the centreband by multiples of ω_r when the spinning frequency is high enough.

The heterodipolar interaction gives rise to an inhomogeneous linebroadening which may be eliminated even if the spinning frequency is much less than the linewidth of the static spectrum. The homodipolar interaction is, however, homogeneously broadened and in order to average to zero by magic angle spinning, the spinning frequency must exceed the linewidth of the static interaction.

For most of the dipolar interactions in zeolites, spinning frequencies of several kilohertz are sufficient to eliminate the small broadenings that would otherwise result. One exception is the ^{1}H-^{1}H homodipolar interaction of template molecules in the channels where anisotropic molecular motion is unlikely to reduce the magnitude of the interaction to less than 24 kHz. This is in excess of the achievable spinning frequencies and recourse has to be made to multiple-pulse methods. This involves the application of a series of phase alternated pulses that make the time-average of the operator term $(\hat{I}_{\sim}^{i}\hat{I}_{\sim}^{k}-3\hat{I}^{i}{}_{z}\hat{I}^{k}{}_{z})$ zero and thus eliminate homonuclear dipolar broadening.

High-power proton decoupling is used for the removal of ^{1}H-^{13}C heterodipolar interactions. This consists of irradiating the ^{1}H spins at their resonance frequency while observing the resonance of the carbon nucleus. This results in a time averaging of $\hat{I}_{z}$ to zero which causes the elimination of the heteronuclear and part of the homonuclear interaction.

2.2.2 Chemical shift anisotropy

The Hamiltonian expressing the shielding of nuclear spins by surrounding electrons is given by[1,5]:

$$h^{-1}\hat{H}_{CS} = \sum_{i}\gamma_{i}B_{\sim o}\cdot\sigma_{\simeq i}\cdot\hat{I}_{\sim i} \qquad (2.25)$$

where $\sigma_{\simeq i}$ is the chemical shift tensor of nucleus i in the laboratory frame ($B_{\sim o}$ is parallel to the z-direction). Since the contribution of the chemical shift Hamiltonian to the Zeeman energy levels is very small, its influence may be calculated by first-order perturbation theory. Consequently,

only the tensor component σ_{izz} is retained and equation (2.25) may be written as[5] (dropping the indices i):

$$\hbar^{-1}\hat{H}_{CS} = \gamma\sigma_{zz}B_0\hat{I}_z \qquad (2.26)$$

with the z-axis along $\underset{\sim}{B}_0$ (laboratory frame).

The tensor component σ_{zz} may be expressed in terms of the principal values σ_{pp} (p = X,Y,Z) of the chemical shift tensor by:

$$\sigma_{zz} = \sin^2\Theta\cos^2\Phi\sigma_{xx} + \sin^2\Theta\sin^2\Phi\sigma_{yy} + \cos^2\Theta\sigma_{zz} \qquad (2.27)$$

where the angles Θ and Φ have their usual meanings.

σ_{zz} may be expressed in short-hand notation:

$$\sigma_{zz} = \sum_p \lambda_p^2 \cdot \sigma_{pp} \qquad (2.28)$$

where the λ_p's are the direction cosines of the principal axes of the chemical shift tensor with respect to $\underset{\sim}{B}_0$.

In solution, with molecules tumbling rapidly and isotropically, substantial averaging of $\underset{\simeq}{\sigma}$ occurs, so that only one-third of the trace is observed (the average of $\lambda_p^2 = 1/3$). The average value of σ_{zz} is then given by:

$$\sigma_{zz} = 1/3\sum_p \sigma_{pp} = 1/3\,Tr(\underset{\simeq}{\sigma}) = \sigma_{iso} \qquad (2.29)$$

where σ_{iso} is the scalar isotropic chemical shift.

In the general case, the observed shielding constant is given by:

$$\sigma_{zz} = \{\sigma_{iso} + \delta/2\ [(3\cos^2\Theta - 1) + \eta\sin^2\Theta\cos 2\Phi]\} \qquad (2.30)$$

For a microcrystalline powder, all possible orientations are present and a powder spectrum results. The overlap of several NMR resonances broadened by shielding

anisotropy would serve to complicate the spectrum. In such cases, MAS may be used to eliminate the shielding anisotropy. Spinning with a frequency ω_r around an axis which makes an angle β with B_o and at angles χ_p to the principal axes of the chemical shift tensor results in time-dependent modulation of λ_p[4,5].

$$\lambda_p = \cos\beta\cos\chi_p + \sin\beta\sin\chi_p\cos(\omega_r t + \Phi_p^o) \qquad (2.31)$$

where Φ_p^o is the azimuthal angle of the principal axis p at t=0.

Substitution of this expression into equation (2.28) leads to both a time-averaged term $\bar{\sigma}$ and a time-dependent term $\sigma(t)$ in the expression for the chemical shift:

$$\sigma = \bar{\sigma} + \sigma(t) \qquad (2.32)$$

$$\bar{\sigma} = {}^3/_2\sin^2\beta\cdot\sigma_{iso} + \tfrac{1}{2}(3\cos^2\beta-1)\sum_p \sigma_{pp}\cos^2\chi_p \qquad (2.33)$$

$$\sigma(t) = A\cos\omega_r t + \sin\omega_r t + C\cos 2\omega_r t + D\sin 2\omega_r t \qquad (2.34)$$

where A,B,C and D are factors depending on χ_p, Φ^o_p and σ_{pp}.

Spinning at frequencies lower than the shielding anisotropy thus results in the formation of spinning sidebands at multiples ω_r centred around the narrowed resonance at $\bar{\sigma}$. The time averaged shift $\bar{\sigma}$ reduces to σ_{iso} in the case of magic angle spinning. The interaction is inhomogeneous in the sense used in describing the heterodipolar interaction but differs in that it is magnetic field dependent. For the nuclei usually encountered in zeolites, spinning frequencies of several kilohertz will suppress the chemical shift anisotropy although the field dependence of the interaction

is important to bear in mind when comparing linewidths at different magnetic field strengths.

2.2.3 Quadrupolar interactions

Nuclei with $I>\frac{1}{2}$ possess an electric quadrupole moment in addition to a nuclear magnetic moment. The electric quadrupole moment is only important when the nucleus is not in a spherically symmetrical environment which will result in a finite electric field gradient at the nucleus.

In the principal axis system, the Hamiltonian may be written as[2]:

$$\hbar^{-1}\hat{H}_Q = C^Q[V_{XX}\hat{I}_X^2 + V_{YY}\hat{I}_Y^2 + V_{ZZ}\hat{I}_Z^2]$$
$$= \frac{C^Q}{2}[V_{ZZ}(3\hat{I}_Z^2-\hat{I}^2) + \eta_Q(\hat{I}_+^2 + \hat{I}_-^2)] \qquad (2.35)$$

with the principal values V_{XX}, V_{YY}, V_{ZZ} of the E.F.G. tensor and with

$$C_Q = \frac{eQ}{2I(2I-1)}$$

In the presence of a sufficiently strong magnetic field, the nuclear spin angular moment is quantised along the direction of the field and it is more appropriate to consider the Hamiltonian in the laboratory frame. In the laboratory frame, the expression for the interaction Hamiltonian becomes[2]:

$$\hbar^{-1}\hat{H}_Q = C^Q \sum_{m=-2}^{2} (-1)^m . T^Q_{2-m}\delta_Q[\sqrt{3}/2\mathcal{D}^2_{om} + \tfrac{1}{2}\eta_Q(\mathcal{D}^2_{2m} + \mathcal{D}^2_{-2m})] \qquad (2.36)$$

with T^Q_{2-m} and $\mathcal{D}^2_{m',m}$ described in Tables 2.3 and 2.4.

In the high-field case, the effects of the quadrupole interaction on the energy levels m created by the Zeeman interaction can be treated by perturbation theory.

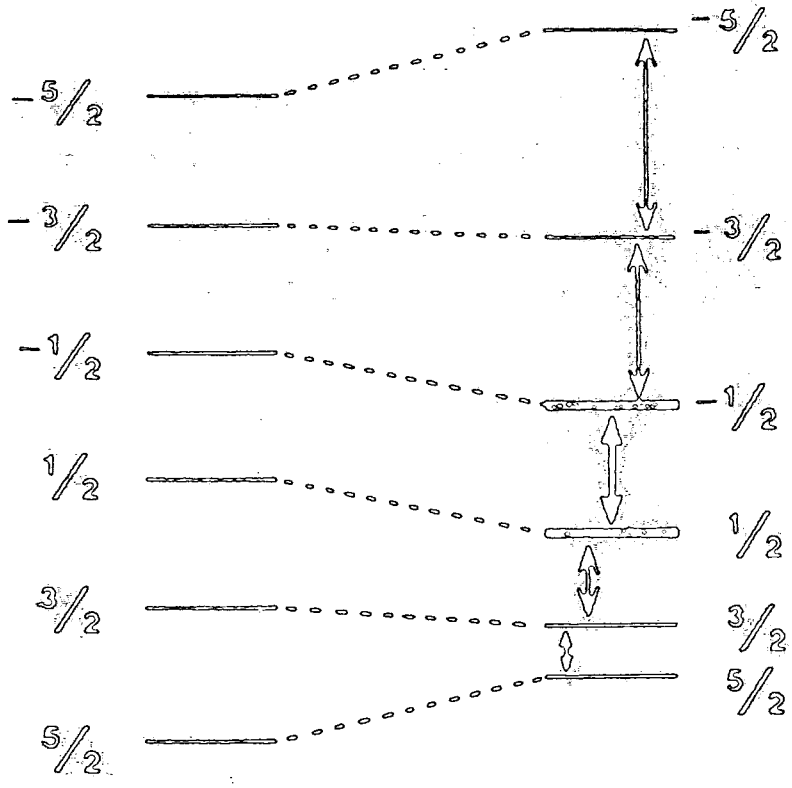

Figure 2.3: Energy levels of an isolated $I = {}^{5}/_{2}$ spin subject to both Zeeman and first-order quadrupolar interactions.

The energy of level m is then given to first order by[5]:

$$E_m = E_m^o + E_m^1 = \langle m|\hat{H}_z|m\rangle + \langle m|\hat{H}_Q'|m\rangle \qquad (2.37)$$

where $\hat{H}_Q'$ is the secular part of the quadrupolar interaction.

$$\hbar^{-1}\hat{H}_Q' = \frac{e^2qQ}{4I(2I-1)}\left[\tfrac{1}{2}(3\cos^2\theta-1)(3\hat{I}_z^2-\hat{I}^2)\right] \qquad (2.38)$$

where θ has its usual meaning and the assumption of axial symmetry is made ($\eta_Q=0$).

The frequency of the transition $m\leftrightarrow m-1$ appears in first order perturbation theory at:

$$\nu_{m\leftrightarrow m-1} = \nu_L - \left[\frac{3e^2qQ}{2I(2I-1)h}\right]\{\tfrac{1}{2}(3\cos^2\theta-1)(m-\tfrac{1}{2})\} \qquad (2.39)$$

Figure 2.3 shows the energy levels of an $I=5/2$ nuclear spin subjected to both the Zeeman interaction $\hat{H}_z$ and the first-order contribution of the quadrupole interaction ($\eta_Q=0$). There is no first-order frequency shift of the central transition ($m=\frac{1}{2}$). The shifts of the other transitions are of the order of $\frac{3e^2qQ}{2I(2I-1)h}$ which is often in the kilohertz region for the quadrupolar nuclei found in zeolites (^{27}Al and ^{23}Na). For microcrystalline zeolite samples, all orientations of the crystallites are present and consequently, the intensity of the non-central transitions is spread over a wide range of possible frequencies. The first-order interaction is inhomogeneous in nature and is scaled by the factor $\frac{1}{2}(3\cos^2\theta-1)$ in the axial symmetry case. In analogy with the discussion of the dipolar and chemical shift interactions, magic angle spinning should eliminate the first-order interaction.

The quadrupole interaction does, however, contribute to the central transition in second-order perturbation

theory. The second-order frequency shift is given[2] by (η_Q=0).

$$\nu_{\frac{1}{2}\leftrightarrow-\frac{1}{2}} = \nu_L - \left[\frac{(3e^2qQ}{2I(2I-1)h})^2 / 16\nu_L\right]\left[(I(I+1)-3/4).(1-\cos^2\theta)(9\cos^2\theta-1)\right] \quad (2.40)$$

Note that elimination of the quadrupolar broadening of the $\frac{1}{2}\leftrightarrow-\frac{1}{2}$ transition may not be achieved by MAS because the orientational dependence is not of the form $(3\cos^2\theta-1)$. The second-order interaction is, however, attenuated by MAS but the narrowing is theoretically limited[7] to a factor of 3.6. Sample spinning at angles other than the magic angle have been used in an attempt to reduce the interaction further, although at such angles any chemical shift anisotropy or dipolar interactions present will not be averaged to zero. In addition, for the second-order quadrupolar interaction, the angle producing the most narrowing depends on η_Q which may vary between crystrallographically distinct sites (if present) leading to narrowing of only part of the NMR signal. Recently, it has been shown that rotation of the sample around two axes inclined at magic angles of the ℓ=2 and ℓ=4 Legendre polynomials leads to the removal of both first- and second-order quadrupolar broadening[8]. Experiments with a double-rotor on the central ($\frac{1}{2}\leftrightarrow-\frac{1}{2}$) transition of sodium-23 in polycrystalline sodium oxalate illustrated the elimination of broadening due to second-order quadrupolar effects - a thirty-fold increase in the resolution was observed compared to magic-angle spinning. However, the technique is far from routine and is unavailable in most laboratories.

Consideration of equation (2.40) also reveals that the second-order quadrupole interaction is inversely proportional to the strength of the magnetic field. It is thus clearly advantageous to work at the highest magnetic fields available, although the contribution of shielding anisotropy to the linewidth of the central transition must be taken into account due to its increased influence at higher magnetic field strengths. However, even at the highest commercially available field strengths, the second-order quadrupolar broadening may be quite significant. At present, there are no known multiple pulse sequences that selectively average the second-order quadrupolar interaction.

The centre of gravity (δ_{CG}) of the central transition lineshape is shifted from the true isotropic chemical shielding (δ_{CS}) by the second-order quadrupolar shift (δ_{QS}). The relative quadrupolar shift of the centre of gravity $\delta_{QS}(m)$ of a single quantum (m,m-1) transition powder pattern lineshape follows from the expression for the MASNMR centreband frequencies $\omega_{m,m-1}$ by integrating it over all possible crystallite orientations in a powder sample, as shown by Lippmaa[9]:

$$\delta_{QS}(m) = -3/40\left[\left(\frac{e^2qQ}{h}\right)^2/\nu_L^2\right]\left[\frac{I(I+1)-9m(m-1)-3}{I^2(2I-1)^2}\left(1+\eta_Q^2/3\right)\right] \quad (2.41)$$

Thus, for a determination of the true isotropic chemical shift, a knowledge of the quadrupole coupling parameters is required. Methods of obtaining the relevant parameters include:

(i) Measurement of the centre of gravity of the lineshape at different magnetic field strengths[9].

(ii) From the arithmetic mean of the spinning sidebands of the first or second spinning sidebands of the least shifted first satellite transition ($\pm^{3}/_{2} \leftrightarrow \pm^{1}/_{2}$)[10].

(iii) Fitting the excitation projection in the 2D mutation experiment to the numerically simulated projection (see Chapter Five)[11].

(iv) The two pulse method of Haase *et al*[12].

(v) Comparison of the central transition lineshape with the calculated MASNMR lineshape[13,14].

The relative merits of these various techniques vary dramatically in the case of zeolites and a comparison of some of these techniques is made in Chapter Five using NH_4^+ -ZSM-5.

2.3 The density matrix and its dynamic behaviour[15,16]

The density matrix is used to describe the state of a spin ensemble as well as its time evolution. The treatment below follows the passage from the probabalistic treatment of a system of a few spins to the statistical treatment of a large ensemble of such systems.

The state Ψ of an isolated spin may be described as a linear combination of eigenstates:

$$\Psi = \sum_{n=1}^{n} C_n |n\rangle \qquad (2.42)$$

It is desirable to describe the magnetisation in terms of the state Ψ of the system.

$$\langle \mu_x \rangle = \langle \Psi | \hat{\mu}_x | \Psi \rangle = \gamma\hbar \langle \Psi | \hat{I}_x | \Psi \rangle = \gamma\hbar \sum_{n=1}^{n} \sum_{m=1}^{m} C_n C_m^{*} \langle m | \hat{I}_x | n \rangle \qquad (2.43)$$

where $\langle \mu_x \rangle$ is the expectation value of the x-component of the magnetic moment, $\hat{I}_x$ is the x-component of the angular momentum operator of the system, and $\langle m|\hat{I}_x|n\rangle$ is a constant A_{mn} which is independent of the state of the system. In the case of the macroscopic magnetization, the ensemble average must be taken:

$$M_x = N_o \overline{\langle \mu_x \rangle} = \gamma \hbar \sum_{n=1}^{n} \sum_{m=1}^{m} \overline{C_m^* C_n} A_{mn} \tag{2.44}$$

where N_o = the number of spins per unit volume.

The eigenfunctions are the same over the whole sample, but the coefficients C_m, C_n may vary. Thus the expectation value is the ensemble average of the expectation values of the operator $\hat{\mu}_x$ for all individual spin systems. The quantities $\overline{C_m^* C_n}$ may be considered as matrix elements $\hat{\rho}_{nm}$ of a matrix which is called the density matrix. The coefficients C_n are complex and may be written as:

$$C_n = C_n(0) \exp(i\alpha_n) \tag{2.45}$$

The density matrix element $\hat{\rho}_{nm}$ may be written as:

$$\hat{\rho}_{nm} = \overline{C_m^* C_n} = \overline{|C_n||C_m|} \; \overline{\exp\{(i\alpha_n - \alpha_m)\}} \tag{2.46}$$

Note that at equilibrium, the nondiagonal elements are null due to the random phase distribution of the complex coefficients, whereas the diagonal elements represent populations. If there is a coherence between the states $|n\rangle$ and $|m\rangle$, the element $\hat{\rho}_{nm}$ will not have a value equal to zero because the product $\overline{|C_n||C_m|}$ is not equal to zero and the average value of $\exp\{i(\alpha_n - \alpha_m)\}$ is not zero. If in the states $|m\rangle$ and $|n\rangle$ only one spin differs in polarization

by one unit, the coherence corresponds to observable transverse magnetisation. If more than one spin differs in polarization, or one spin differs by more than one unit, the coherence is called a multiple quantum coherence.

The time dependence of a state Ψ described by a time-independent Hamiltonian $\hat{H}$ follows from the Schrödinger wave equation:

$$-\frac{\hbar}{i}\frac{d\Psi}{dt} = \hat{H}\Psi \tag{2.47}$$

Substitution of equation 2.42 leads to

$$-\frac{\hbar}{i}\sum_{n=1}^{n}\frac{dC_n}{dt}|n\rangle = \sum_{n=1}^{n}C_nE_n|n\rangle \tag{2.48}$$

where E_n is the eigenvalue corresponding to the state $|n\rangle$ in the time-independent equation:

$$\hat{H}|n\rangle = E_n|n\rangle \tag{2.49}$$

Rearrangement of equation 2.48 leads to:

$$\sum_{n=1}^{n}\left(C_nE_n + \frac{\hbar}{i}\frac{dC_n}{dt}\right)|n\rangle = 0 \tag{2.50}$$

The orthogonality of the eigenfunctions ensures that the above equation is satisfied only if each term of the sum is null:

$$C_nE_n + \frac{\hbar}{i}\frac{dC_n}{dt} = 0 \tag{2.51}$$

The solution of such an equation is straightforward and is given by:

$$C_n = C_n(0)\exp(-iE_nt/\hbar)$$

$$\text{Thus } \Psi(t) = \sum_{n=1}^{n}C_n(0)\exp(-iE_nt/\hbar)|n\rangle \tag{2.52}$$

Assuming that $\hat{H}$ is constant over the whole sample, the time-dependence of $\hat{\rho}_{nm}$ may be obtained from equations (2.45), (2.46), and (2.52):

$$\hat{\rho}_{nm}(t) = \exp\{i(E_m - E_n)t/\hbar\}\hat{\rho}_{nm}(0) \qquad (2.53)$$

where $\hat{\rho}_{nm}(0)$ is the density matrix element at time zero. More generally, the evolution equation may be written as the so-called Liouville-von Neumann equation:

$$\frac{d\hat{\rho}}{dt} = \frac{-i}{\hbar}[\hat{H},\hat{\rho}] \qquad (2.54)$$

which, in the case of a time-independent Hamiltonian has the solution:

$$\hat{\rho}(t) = \exp(-i\hat{H}t/\hbar)\hat{\rho}(0)\exp(i\hat{H}t/\hbar) \qquad (2.55)$$

The Liouville-von Neumann equation is of crucial importance in the quantum-mechanical description of the dynamics in spectroscopic experiments, since the calculation of an observable requires knowledge of $\hat{\rho}$ at the time of interest.

Since magnetisation is detected in the rotating frame, it is useful to transform all the equations to a frame which is the quantum mechanical equivalent of the rotating reference frame (the so-called interaction representation). Exponential operators are used to define this representation where the effects of $\hat{H}_o$ vanish. In the Schrödinger representation this may be done by replacing an operator $\hat{H}$ by an operator $\hat{H}_R$:

$$\hat{H} = \exp(-i\hat{H}_o t/\hbar)\hat{H}_R\exp(i\hat{H}_o t/\hbar) \qquad (2.56)$$

and the density matrix in the rotating frame is given by:

$$\hat{\rho}(t) = \exp(-i\hat{H}_o t/\hbar)\hat{\rho}_R(t)\exp(i\hat{H}_o t/\hbar) \qquad (2.57)$$

In the interaction representation the Zeeman term is removed from the Hamiltonian, $\hat{H} = \hat{H}_z + \hat{H}_{int}$ so that the equation of motion is modified to:

$$\frac{d\hat{\rho}_R}{dt} = \frac{i}{\hbar}[\hat{\rho}_R, \hat{H}_{intR}] \qquad (2.58)$$

The factors of $\hat{H}_{int}$ on which the unitary operators $\exp(-i\hat{H}_o t/\hbar)$ and $\exp(i\hat{H}_o t/\hbar)$ act are the spin functions contained in $\hat{H}_{int}$. For any operator sandwiched between the unitary transformation operators, some of the components in the expansion will acquire a periodic time dependence. Truncation of the Hamiltonian rejects all the terms whose operators depend on time in such a way that their time average vanishes. This is tantamount to retaining only first-order perturbations.

The expectation value of an observable in the rotating frame is given by:

$$\langle O \rangle_R = Tr(\hat{\rho}_R \hat{O}) \qquad (2.59)$$

and it is relevant to note that this employs the spin operator $\hat{O}$ and not $\hat{O}_R$. The expectation value of an observable in the laboratory frame will be of the form:

$$\begin{aligned} & Tr(\hat{\rho}_R \hat{O}_R) \\ = \; & Tr\{\exp(+i\hat{H}_o t/\hbar)\hat{\rho}\exp(-i\hat{H}_o t/\hbar)\exp(+\hat{H}_o t/\hbar)\hat{O}\exp(-i\hat{H}_o t/\hbar)\} \qquad (2.60) \\ = \; & Tr(\hat{\rho}\hat{O}) \end{aligned}$$

which emphasises the fact that the trace of a matrix is independent of the representation used.

The effect of pulses may also be described by rotational operators, and the assumption is usually made that $\hat{H}_{rf}$ is the dominant interaction for the duration of the pulse. This assumption is not always correct even for high power pulsed NMR techniques in the presence of quadrupolar interaction.

For example, the Hamiltonian for a system of isolated quadrupolar nuclei with spin I subjected to a pulse of duration t at the resonance frequency ω_o and transformed to a frame rotating at the excitation frequency is given by[17]:

$$\hat{H}_R/\hbar = \omega_Q(3\hat{I}_z^2-\hat{I}^2) + \omega_{rf}\hat{I}_x \qquad (2.61)$$

where $\omega_Q = (\frac{e^2qQ}{8I(2I-1)\hbar})$ $(3\cos^2\theta-1 + \eta\sin^2\theta\cos2\Phi)$ and θ and Φ have their usual meanings. Thus, the evolution of the spin density matrix in this frame during the r.f. pulse is given by:

$$\hat{\rho}_R(t) = \exp(-it\hat{H}_R/\hbar)\hat{\rho}(0)\exp(it\hat{H}_R/\hbar) \qquad (2.62)$$

In the limiting case of $\omega_Q >> \omega_{rf}$, $\hat{H}_R/\hbar = (I+\frac{1}{2})\omega_{rf}\hat{I}_x$ (2.63)

and $\hat{\rho}_{R(t)} = \exp\{-it(I+\frac{1}{2})\omega_{rf}\hat{I}_x\}\hat{\rho}(0)\exp\{it(I+\frac{1}{2})\omega_{rf}\hat{I}_x\}$ (2.64)

$$= \exp\{-i\theta(I+\tfrac{1}{2})\hat{I}_x\}\hat{\rho}(0)\exp\{i\theta(I+\tfrac{1}{2})\hat{I}_x\} \qquad (2.65)$$

where θ corresponds to the flip angle about the x-axis.

In the other limiting case, $\omega_{rf} >> \omega_Q$ and $\hat{H}_R/\hbar = \omega_{rf}\hat{I}_x$ (2.66)

and $\hat{\rho}_R(t) = \exp\{-i\theta\hat{I}_x\}\hat{\rho}(0)\exp\{i\theta\hat{I}_x\}$ (2.67)

The significance of these results is discussed at a later stage.

2.4 Relaxation

2.4.1 Spin-lattice relaxation

At the start of the Chapter, it was stated that for a nucleus with a spin quantum number I, the Zeeman interaction results in 2I+1 separate energy levels. A group of spin I nuclei placed in a magnetic field would tend to distribute themselves between the energy levels according to a Boltzmann relation, so that for spin-½ nuclei, the ratio of the number of spins in the upper energy state to that in the lower energy state is $\exp(^{-\Delta E}/_{kT})$ at equilibrium. The

resulting Boltzmann equilibrium nuclear magnetisation is usually represented by M_o. After the application of a r.f. pulse as described above, the longitudinal magnetisation M_z is altered with respect to its equilibrium value M_o, and M_z recovers (usually exponentially) according to the equation:

$$(M_z - M_o)_t = (M_z - M_o)_o \exp(^{-t}/T_1) \qquad (2.68)$$

where T_1 is the time constant for spin lattice (or longitudinal relaxation). A π pulse is followed by purely spin-lattice relaxation.

2.4.2 Mechanisms for spin-lattice relaxation

Spin-lattice relaxation occurs as the nuclear magnetic moments lose energy to their surroundings and this occurs by magnetic dipole or electric quadrupole interactions. The transfer of energy from the spins to the lattice requires that local magnetic fields at the nucleus fluctuate at the Larmor frequency in order to induce NMR transitions. The fluctuating local magnetic fields arise as a consequence of the time dependence which molecular motion imparts to the internal Hamiltonian describing the system. Thus the interactions responsible for spin-lattice relaxation in zeolites are:

(1) Dipole-dipole

(2) Chemical shift anisotropy

(3) Quadrupolar.

The effects of spin-rotation and indirect spin-spin coupling are ignored.

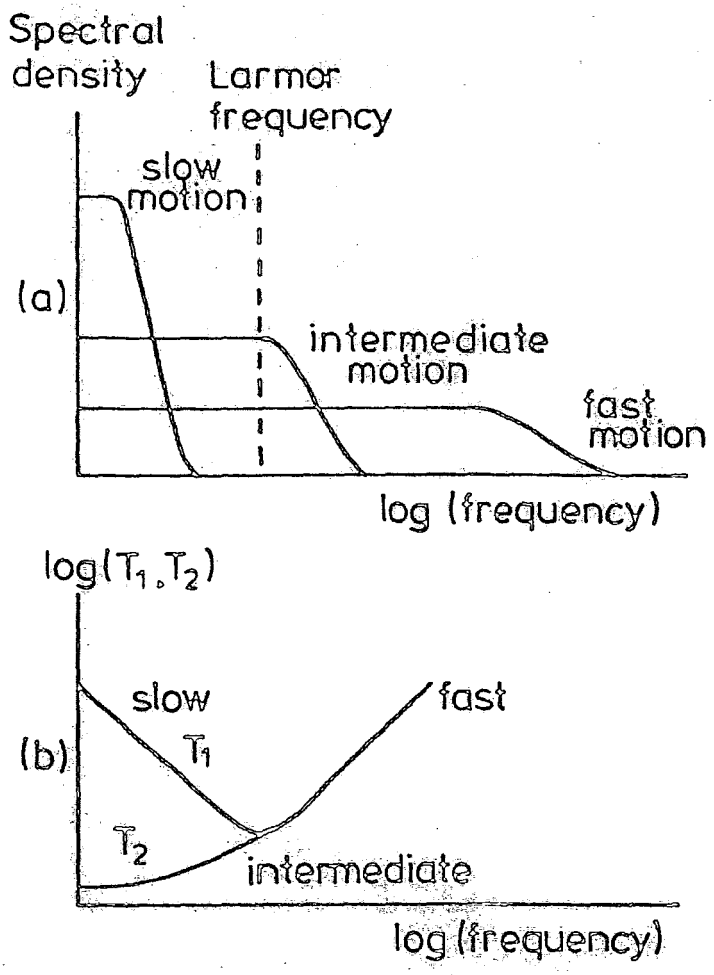

Figure 2.4: Spectral density functions for fast, intermediate, and slow molecular motion with the corresponding plot of $\log(T_1, T_2)$ on the same frequency scale.

(adapted from reference 18)

The above requirement that the local magnetic fields at the nucleus fluctuate at the Larmor frequency makes the spin-lattice relaxation time sensitive to motion in the megahertz region. Of the possible types of molecular motion, only rotational molecular motions are even approximately matched to the Larmor frequency. The distribution function or spectral density function for rotational motion is not known in detail due to the complex nature of the molecular motions but is usually taken to be a Lorentzian function of frequency.

Figure 2.4(a) shows the typical spectral density function for fast, intermediate and slow molecular tumbling[18]- the area under the curves remaining constant. For fast motion, the Fourier component of the motion at the Larmor frequency is small but it is increased as the molecular reorientation rate is slowed down. Slowing the molecular reorientation rate thus allows an increase in the efficiency of T_1 relaxation processes. The maximum efficiency is reached when the condition $\omega_o\tau_c = 1$ holds (where τ_c is the correlation time for the motion and corresponds to the average time taken for a molecule to tumble through one radian). Any further slowing of the molecular motion reduces the component at the Larmor frequency and increases the relaxation time T_1.

For the spin-½ nuclei present in zeolites, the dipole-dipole spin-lattice relaxation mechanism is more important than the shielding anisotropy mechanism whereas for I>½ nuclei, the quadrupolar relaxation mechanism dominates.

In the case where the zeolite pores are occupied by organic template molecules, the ^{29}Si spin-lattice relaxation time would be expected to be dominated by ^{29}Si-^{1}H

dipolar interactions. The irrelevance of the shielding anistropy contribution is justified by the fact that in rigid systems, the silicon T_1 values are much greater than in the case under consideration[19]†. The ^{13}C spin-lattice relaxation times would also be dominated by dipolar interactions with the ^{1}H spins. On removal of the organic template species by calcination and replacement by oxygen molecules, the relaxation times of the silicon spins are dominated by dipolar interactions between the ^{29}Si spins and the unpaired electrons of the paramagnetic oxygen species[20,21].

For quadrupolar spins, modulation of the electric field gradients by the motion of the polar sorbate molecules and/or charge compensating cations is believed to be the most significant spin-lattice relaxation mechanism[22]. In the solid state, relaxation is very complex due to the presence of 2I+1 energy levels and a range of possible relaxation paths. The situation may, however, be simplified by selective excitation as is discussed later.

Further details of the motion could be provided by varying the Larmor frequency and subsequent measurement of the T_1 values. However, it is more feasible to probe other frequency ranges by the measurement of other relaxation times.

2.4.3 Spin-lattice relaxation in the rotating frame

After the application of a $\pi/2$ pulse and a phase shift of $\pi/2$ of the radiofrequency field in the laboratory frame so that the r.f. field lies along the magnetisation in the rotating frame, the magnetisation is subject only to

† ^{29}Si T_1 value of nacrite is ca. 5000s compared to a ^{29}Si T_1 value of ~140s for as-synthesised (TPA$^+$) ZSM-5

the r.f. field and not the B_o field when the r.f. field is applied exactly on resonance. The magnetisation is now in a non-equilibrium situation and it will therefore relax to a much smaller equilibrium value usually with an exponential time constant $T_{1\rho}$. The relaxation rate in the rotating frame will consequently be sensitive to motion at the Larmor frequency in the rotating frame (in the kHz region).

Further information on longitudinal relaxation may be obtained by measurement of the dipolar relaxation time constant T_{1D}, which describes relaxation in the local magnetic field which is typically of the order of the linewidth for dipolar interactions in a rigid lattice, and may correspond to a lower motional frequency regime than the $T_{1\rho}$ measurement.

2.4.4 Spin-spin relaxation

Spin-spin relaxation or transverse relaxation is the process by which magnetisation in the x-y plane decays. This loss of phase coherence in the x-y plane is characterised by a time constant T_2. As in the case of the spin-lattice relaxation time, spin-spin relaxation is sensitive to Fourier components of the motion at the Larmor frequency but differs in that it is also sensitive to fluctuations near zero frequency. Thus, on reducing the molecular reorientation time so that T_1 has passed through its minimum, T_2 will continue to fall while T_1 starts to rise (Figure 2.4(b)). If the molecular reorientation is fast compared to the Larmor frequency, then both relaxation times are affected in the same fashion and $T_1=T_2$.

All T_1 relaxation processes may be considered as T_2 relaxation processes, although other T_2 mechanisms[18], which result from fluctuations at a low enough frequency so that T_1 is unaffected also exist. The most important of these T_2 relaxation mechanisms is chemical exchange.

REFERENCES - CHAPTER TWO

1. U. Haeberlen, "High-Resolution NMR in Solids, Selective Averaging", Academic Press, 1976.

2. G. Engelhardt and D. Michel, "High-Resolution Solid-State NMR of Silicates and Zeolites", J. Wiley and Sons, 1987.

3. J. Klinowski and J.M. Thomas, Adv.Catal., 33, 199 (1985).

4. E.R. Andrew, Phil.Trans.R.Soc.Lond., A299, 505, (1981).

5. K.F.M.G.J. Scholle, Ph.D. Thesis, University of Nijmegen (1985).

6. E.R. Andrew, Prog.NMR Spectrosc., 8, 1 (1971).

7. D. Freude and H.J. Behrens, Cryst.Res.Techn., 16, 36 (1981).

8. A. Samoson, E. Lippmaa and A. Pines, Mol.Phys., 65, 1013 (1989).

9. E. Lippmaa, A. Samoson and M. Mägi, J.Am.Chem.Soc., 108, 1730 (1986).

10. A. Samoson, Chem.Phys.Lett., 119, 29 (1985).

11. A. Samoson and E. Lippmaa, Chem.Phys.Lett., 100, 205 (1983).

12. J. Haase, D. Freude, H. Pfeifer, E. Lippmaa and P. Sarv, Chem.Phys.Lett., 152, 254 (1988).

13. E. Kundla, A. Samoson and E. Lippmaa, Chem.Phys.Lett., 83, 229 (1981).

14. A. Samoson, E. Kundla and E. Lippmaa, J.Magn.Reson., 49, 350 (1982).

15. G.D. Matescu and A. Valeriu, "Teaching the New NMR: A Computer Aided Introduction to the Density Matrix Treatment of Double-Quantum Spectrometry", in Magnetic Resonance, L. Petrakis and J.P. Fraissard (eds.), 1984, D. Reidel Publishing Company, Dordrecht, Holland.

16. A.D. Bax, Ph.D. Thesis, University of Oxford,(1982).

17. R. Jansen, G.A.H. Tijink and W.S. Veeman. J.Chem.Phys., 88, 518 (1988).

18. R. Freeman, "A Handbook of Nuclear Magnetic Resonance", Longman Scientific and Technical (1987).

19. P.F. Barron, R.L. Frost and J.O. Skjemsted, J.Chem.Soc., Chem.Commun., 581 (1983).

20. D.J. Cookson and B.E. Smith, J.Magn.Reson, 63, 217, (1985).

21. J. Klinowski, T.A. Carpenter and J.M. Thomas, J.Chem.Soc., Chem.Commun., 956 (1986).

22. J. Haase, H. Pfeifer, W. Oehme and J. Klinowski, Chem.Phys.Lett., 150, 189 (1988).

CHAPTER THREE

EXPERIMENTAL

3.1 Instrumentation

3.1.1 The Spectrometer Systems

The majority of the work outlined in this thesis was performed on a Bruker CXP-200 spectrometer equipped with a 4.7 Tesla wide-bore (89.5 mm) magnet. The dual-channel spectrometer covers a wide range of operating frequencies. The lower frequency channel is tuneable between 4 and 95 MHz, whereas the higher frequency channel may be switched between 200.13 MHz (^{1}H) and 188 MHz (^{19}F), although for the research outlined in the following chapters, the high frequency channel was not used for fluorine work. The relevant properties of the nuclei used in this thesis are summarised in Table 3.1. The details of the spectrometer construction are well known and further details are given in reference 1.

Some of the work was performed on a Bruker MSL-300 spectrometer which was equipped with a 7.1 Tesla wide-bore magnet, the operation of which is similar to that of the CXP-200 spectrometer. Other systems used include a Varian VXR-300 spectrometer equipped with a 7.1 Tesla narrow-bore magnet, and a solution-state Jeol GX-400 spectrometer which was used for quantitative ^{27}Al work.

All solution-state data were recorded on a Bruker AC-250 spectrometer equipped with a 5.9 Tesla narrow-bore magnet. The samples were run locked to an internal deuterated solvent.

3.1.2 The probes

Two wide-bore (84.5 mm) broad-band, dual-channel high-resolution commercial double-bearing probes covering a

TABLE 3.1 NMR properties of the nuclei studied

Isotope	Spin	% Natural Abundance	Magnetogyric Ratio of $\gamma/10^7 radT^{-1}s^{-1}$	NMR[a] frequency Ξ/MHz	Sensitivity[b]
^{1}H	1/2	99.99	26.75	200.13	1.000
^{13}C	1/2	1.11	6.73	50.32	$1.76x10^{-4}$
^{29}Si	1/2	4.70	5.32	39.76	$3.69x10^{-4}$
^{23}Na	3/2	100	7.08	52.94	$9.27x10^{-2}$
^{27}Al	5/2	100	6.98	52.15	0.207

(a) At a magnetic field strength of 4.7 Tesla.

(b) Relative to protons.

combined frequency range of 20-90 MHz were usually used on the CXP-200 spectrometer. The double-bearing systems allowed samples to be rotated at frequencies between 100 Hz and 5 kHz, although for stable sample spinning, the sample rotor must be both full and homogeneously packed. The sample capacity of the aluminium-free zirconia rotors is approximately 0.7 cm^3. For ^{27}Al studies, the lower frequency range probe could not be used due to a significant aluminium background. Similar double-bearing probes and rotor types were used for experiments performed on the MSL-300 spectrometer. In the case of the VXR-300 spectrometer, both a Varian PLE probe and a narrow-bore double-bearing probe designed by Doty were used for the NMR measurements. Sapphire rotors were usually used for ^{29}Si experiments, whereas aluminium-free zirconia rotors were used in the case of ^{27}Al experiments.

Some of the work performed on the CXP-200 spectrometer required the use of an Andrew-Beams probe. This probe was less sensitive and could not handle the same r.f. power levels as the double-bearing probes, although it had the advantage that it was possible to modify the probe circuitry. The spinning system was, however, inferior to that offered by the double-bearing probe system. KEL-F rotors were used in all cases.

Most of the ^{1}H experiments were performed on a high-power wideline probe. The probe was used for the measurement of T_1 and $T_{1\rho}$, and the acquisition of wideline spectra. The sample was contained in a glass tube between glass stops (volume approximately 200 mm^3). The probe circuitry was modified to ensure short pulse recovery times.

Figure 3.1(a)

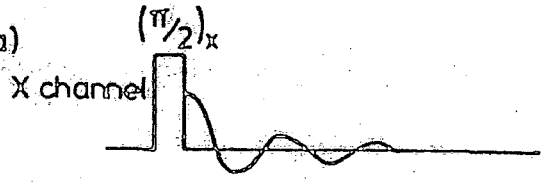

Single-pulse experiment.

Figure 3.1(b)

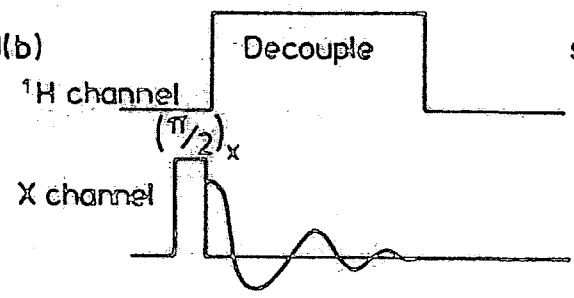

Single-pulse experiment with proton decoupling.

Figure 3.1(c)

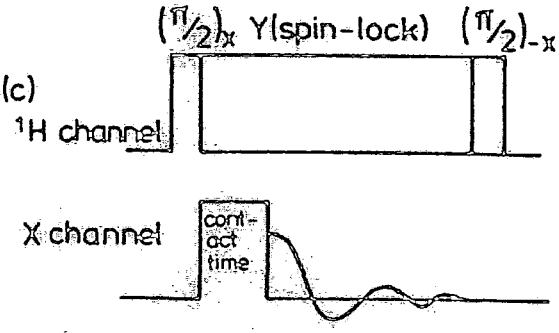

Cross-polarization experiment with proton flipback.

Figure 3.1(d)

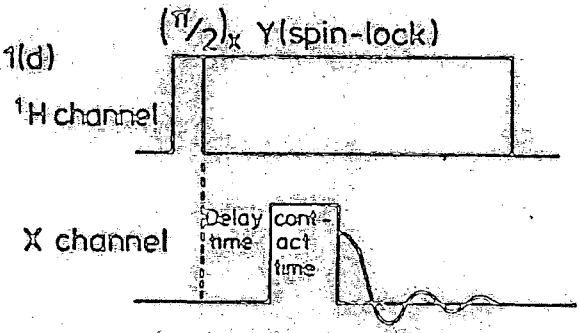

Delay spin-lock cross-polarization experiment.

Figure 3.1(e)

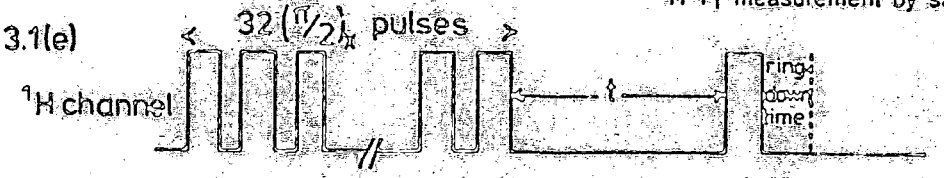

^{1}H T_1 measurement by saturation recovery.

The proton CRAMPS work was performed on a modified Andrew-Beams probe. For a detailed description of the probe design, the interested reader is referred to reference 2. Typical spinning frequencies of the KEL-F rotors were about 3 kHz.

An aluminium-free narrow-bore probe was used for the quantitative aluminium work on the GX-400 spectrometer. The converted solution-state probe was modified to ensure a short ringdown time. Sample spinning frequencies were in the range 4-5 kHz.

The ^{13}C NMR solution-state data were recorded using a broad-band 10 mm VSP probe.

3.2 Pulse sequences

A whole range of pulse sequences have been used for the investigations outlined in this thesis. Some of the less esoteric sequences are reviewed below, and the bulk of the discussion for the less common or novel pulse sequences is reserved for later.

3.2.3 Single-pulse sequences

The single-pulse and proton-decoupled sequences shown in Figures 3.1(a) and (b) were both used in the acquisition of spectra. High-power proton decoupling was used in the case where the nucleus of interest interacted with proton spins. Maximum signal is observed for a $\pi/2$ pulse, and inaccuracies in the pulse duration simply lead to a lower signal intensity than the theoretical maximum. The $\pi/2$ pulse duration was set by adjustment of the transmitter power output until a null signal was observed (which corresponds to a π pulse) when the pulse duration was halved to

yield a $\pi/2$ pulse. The experiment yields quantitative results so long as the recycle delay is of sufficient duration for the nuclei to fully relax. These pulse sequences are ideal when the spins under investigation are abundant and do not have long relaxation times. In the case of very long spin-lattice relaxation times, it is not convenient to wait for the nuclei to fully relax and shorter flip angles are used. Provided that there is no transverse magnetisation just before the pulse, the optimum flip angle (the so-called Ernst Angle) is given by[3] $\cos_{opt}=\exp(^{-t}/T_1)$ where t is the interval between the pulses. If T_1 varies for different peaks in the spectrum, then difficult choices must be made.

3.2.2 Cross-polarization

In many cases, the spins are isotopically or spatially dilute and may be characterised by long T_1 values. On the other hand, proton spins are isotopically abundant and give rise to a stronger signal by comparison. In addition, the spin-lattice relaxation times of the protons will typically be shorter than the corresponding values for the dilute spins. Both of these factors make it desirable to generate the dilute-spin signal from the abundant proton spins. So long as there is a dipolar interaction between the dilute spins and the proton spins, then use may be made of the pulse sequence shown in Figure 3.1(c)[4].

Maximum transverse proton magnetisation is generated by a $\pi/2$ pulse applied to the proton (I) spins which is immediately followed by a $\pi/2$ phase shift of the r.f. so as to spin-lock the proton magnetisation. Immediately

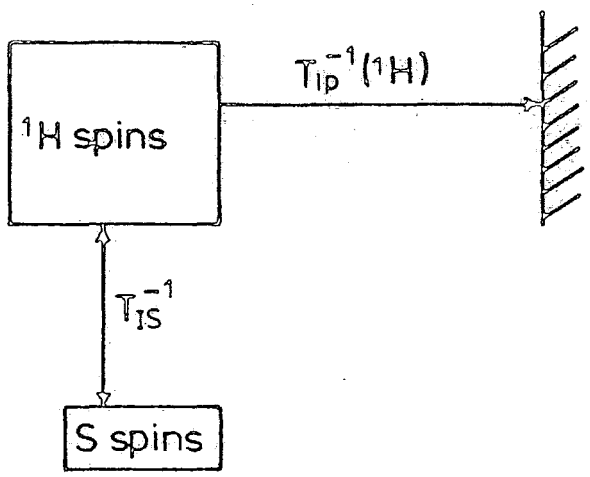

Figure 3.2(a): Magnetisation transfer processes occurring during the contact time.

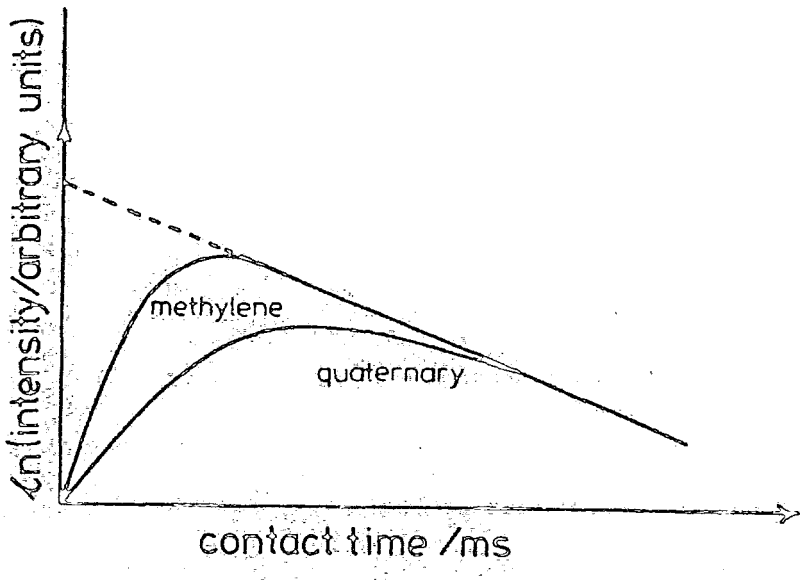

Figure 3.2(b): Variable contact time experiment for a sample containing an equal number of methylene and quaternary carbons.

following the phase shift, the r.f. in the dilute spin channel is switched on, and if the Hartmann-Hahn matching condition holds[5], then maximum polarization transfer efficiency occurs from the abundant proton spins to the dilute spins. The Hartmann-Hahn match is usually set on a reference compound using the same pulse sequence.

The dynamics of the cross-polarization experiment are shown in the idealised diagram in Figure 3.2(a). During the contact time, proton magnetisation relaxes to the lattice at the rate $T_{1\rho}^{-1}(^1H)$ at the same time as it is partially transferred to the dilute spins (S) at the rate T_{IS}^{-1} (T_{IS} is the cross-relaxation time).

For the experiment to succeed, $T_{IS}^{-1} >> T_{1\rho}^{-1}(^1H)$ so that the spins reach a common spin temperature, and then relax to the lattice *via* $T_{1\rho}^{-1}(^1H)$. The rate $T_{1\rho}^{-1}$ of the dilute spin is ignored in this discussion. The rate of cross-polarization depends critically on the dipolar interactions between the proton spins and the dilute spins as expressed by their second-moment M_2^{IS} in the equation[4]:

$$T_{IS}^{-1} = C_{IS} M_2^{IS} / (M_2^{HH})\, 0.5 \qquad (3.1)$$

where C_{IS} is a geometry-dependent term and M_2^{HH} is the second moment of the proton-proton dipolar interactions. Thus, high rates of polarization transfer occur when the, say, (^{13}C-^1H) lineshape is broad and the (^1H-^1H) lineshape narrow.

In order to describe the variation of the dilute spin intensity with contact time, it is necessary to use a mathematical treatment.

Invoking energy conservation in the rotating frame leads to[6]:

$$\frac{d\beta_I}{dt} + \varepsilon\alpha^2 \frac{d\beta_S}{dt} = 0 \qquad (3.2)$$

where β_I and β_S are the inverse spin temperatures of the I and S spins respectively (proportional to the magnetisation $M_I(t)$ and $M_S(t)$ in the rotating frame), α is the mismatch parameter $(\frac{\gamma_S B_{IS}}{\gamma_I B_{II}})$, and $\varepsilon = \frac{N_S\ S(S+1)}{N_I\ I(I+1)}$

The variation of the inverse spin temperature of the I and S spins is given by the following coupled differential equations (for the most general case)[6]:

$$\frac{d\beta_S}{dt} = -\frac{1}{T_{IS}}(\beta_S-\beta_I) - \frac{1}{T_{1\rho}^{(S)}}\beta_S \qquad (3.3)$$

$$\frac{d\beta_I}{dt} = -\frac{\varepsilon\alpha^2}{T_{IS}}(\beta_I-\beta_S) - \frac{1}{T_{1\rho}^{(I)}}\beta_I \qquad (3.4)$$

The coupled differential equations may be solved using the initial conditions:

$$\beta_S(0) = 0 \text{ and } \beta_I(0) = \beta_{IO},$$

$$\beta_S(t) = \beta_{IO}\frac{1}{a_+ - a_-}\{\exp(-a_-t/T_{IS}) - \exp(-a_+t/T_{IS})\} \qquad (3.5)$$

$$\beta_I(t) = \beta_{IO}\frac{1}{a_+ - a_-}\{(1-a_-)\exp(-a_-t/T_{IS}) - (1-a_+)\exp(-a_+t/T_{IS})\} \qquad (3.6)$$

where $a_\pm = a_o[1\pm(1-b/a_o^2)^{\frac{1}{2}}]$

and

$$a_o = \tfrac{1}{2}(1+\varepsilon\alpha^2+T_{IS}/T_{1\rho}^{(I)}+T_{IS}/T_{1\rho}^{(S)}),\quad b = \frac{T_{IS}}{T_{1\rho}^{(I)}}(1+T_{IS}/T_{1\rho}^{(S)}) + \varepsilon\alpha^2 T_{IS}/T_{1\rho}^{(S)}$$

The variation of the magnetisation $M_S(t)$ of the S spins during the contact time is given by[6]:

$$\frac{M_S(t)}{M_{SO}} = \alpha \frac{\gamma_I}{\gamma_S} \frac{\beta_S(t)}{\beta_{IO}} \qquad (3.7)$$

where $\beta_S(t)/\beta_{IO}$ should be inserted according to the above equations and M_{SO} = quantitative S spin intensity.
For the systems studied in this thesis, several simplifying assumptions are made:

(1) The S spins were extremely dilute ($\varepsilon=0$).

(2) The experiment was performed with matched Hartmann-Hahn conditions ($\alpha=1$).

(3) Short $T_{1\rho}$ relaxation of the I spins only.

whereupon:

$$\beta_S(t) = \frac{1}{T_{IS}} \cdot [\exp(-t/T_{1\rho}) - \exp(-t/T_{IS})] \Big/ \left(\frac{1}{T_{IS}} - \frac{1}{T_{1\rho}}\right) \cdot \beta_{IO} \qquad (3.8)$$

$$\beta_I(t) = \exp(-t/T_{1\rho}) \cdot \beta_{IO} \qquad (3.9)$$

Therefore,

$$M_S(t) = \frac{\gamma_I}{\gamma_S} \cdot M_{SO} \cdot \frac{1}{T_{IS}} [\exp(-t/T_{1\rho}) - \exp(-t/T_{IS})] \Big/ (1/T_{IS} - 1/T_{1\rho}) \qquad (3.10)$$

Note that γ_I/γ_S acts as an enhancement factor (the ratio is equal to 3.98 and 5.03 in the cases of carbon and silicon respectively).

A typical plot of the natural logarithm of the function defined by equation (3.10) as a function of contact time is shown in Figure 3.2(b). The diagram shown is typical of a homogeneous system with a single-exponential value of $T_{1\rho}$. The example chosen is for the ^{13}C cross-

polarization signal of a sample containing an equal number of methylene and quaternary carbons[7]. Note that the quaternary carbons cross-polarize more slowly than the methylene carbons but then lose polarization at an identical rate due to a common $T_{1\rho}$ value. Also, for a given contact time, cross-polarization may not be quantitatively reliable, although the quantitative intensities may be obtained by a variable contact time experiment, and subsequent extrapolation to zero contact time.

Thus, in addition to the variable contact time experiment acting as a discriminatory device, information concerning quantitivity is also obtained. Furthermore, the proton $T_{1\rho}$ values and hence the slopes of the plots may not be equal, suggesting either incomplete spin diffusion or more than one proton reservoir as often occurs in inhomogeneous systems.

The cross-polarization pulse sequence used incorporated spin-temperature inversion[8] and flip-back[9] (of the proton spins) in order to reduce artefacts and to reduce the recycle time respectively.

A variation of the cross-polarization experiment is shown in Figure 3.1(d). A delay spin-lock time is inserted between spin-locking the proton magnetisation and switching on the r.f. in the dilute spin channel. Varying the delay time may result in a simplification of a complex spectrum of a heterogeneous system.

It is straightforward to calculate the intensity variation of the dilute spin as a function of delay spin-lock time for a given contact time.

Figure 3.1(f) T_1 measurement by inversion recovery.

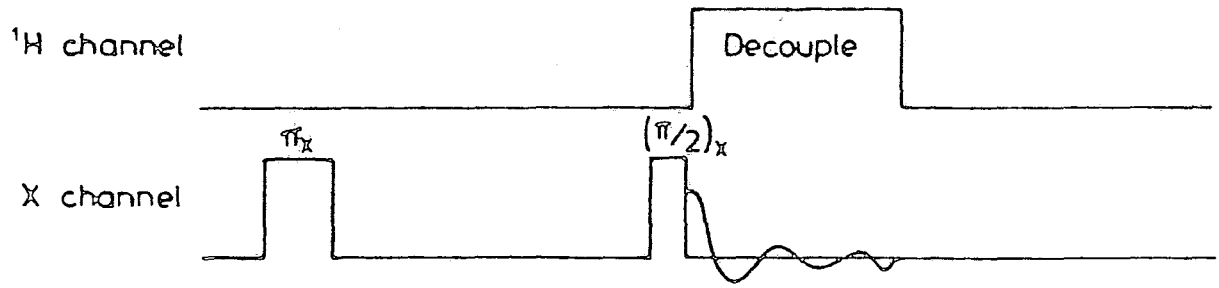

T_1 measurement by cross-polarization (Torchia method).

Figure 3.1(g)

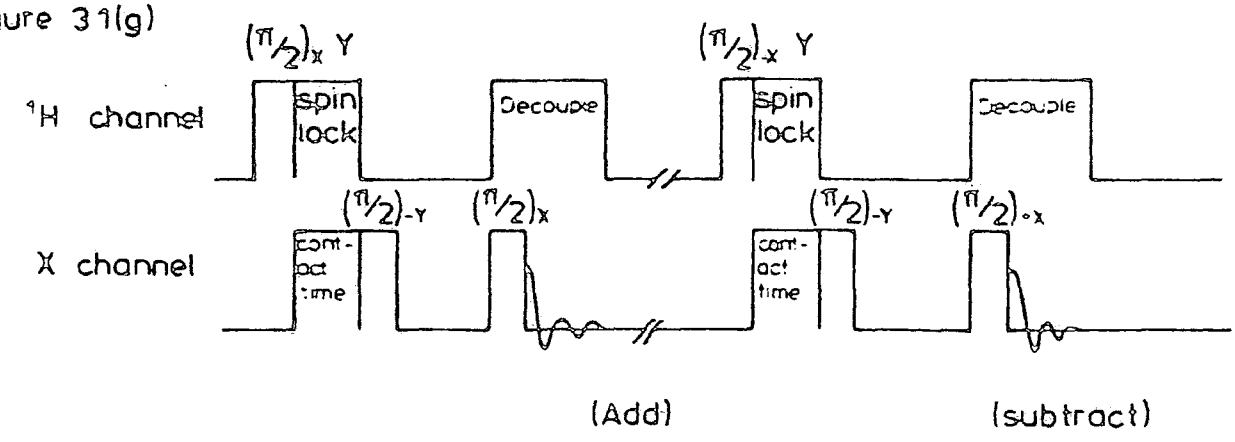

Figure 3.1(h) ^{27}Al T_1 measurement by selective saturation.

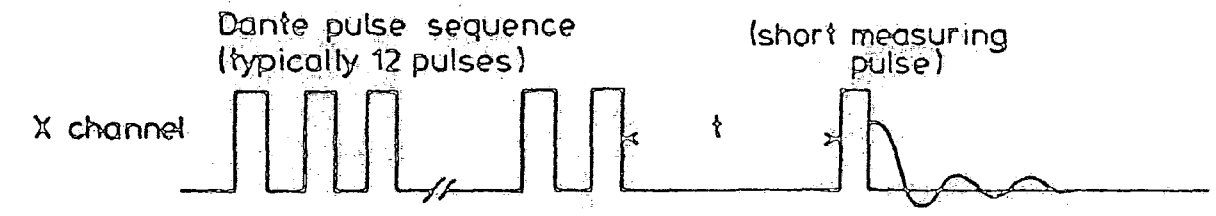

Figure 3.1(i)

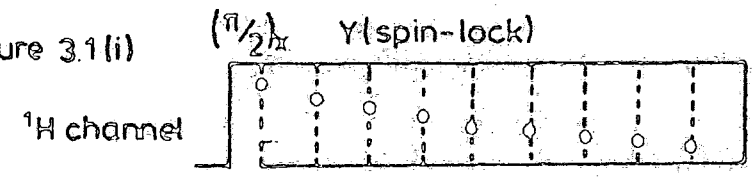

^{1}H $T_{1\rho}$ measurement.

After a delay spin-lock time of O s, the dilute spin magnetisation is given by equation (3.8). However, after a delay spin-lock time τ, and contact time t:

$$\beta_S(\tau,t) = \frac{1}{T_{IS}} \left[\exp(-t/T_{1\rho}) - \exp(-t/T_{IS})\right] \Big/ \left(\frac{1}{T_{IS}} - \frac{1}{T_{1\rho}}\right) \cdot \{\beta_{IO} \exp(-\tau/T_{1\rho})\} \quad (3.11)$$

and therefore $$\frac{M_S(\tau,t)}{M_S(o,t)} = \exp(-\tau/T_{1\rho}) \quad (3.12)$$

and $$M_S(\tau,t) = \left\{\frac{\gamma_I}{\gamma_S} \cdot M_{SO} \cdot \frac{1}{T_{IS}} \left[\exp(-t/T_{1\rho}) - \exp(-t/T_{IS})\right] \Big/ \left(\frac{1}{T_{IS}} - \frac{1}{T_{1\rho}}\right)\right\} \exp(-\tau/T_{1\rho}) \quad (3.13)$$

For a given contact time, the expression in outer brackets in equation (3.13) is a constant, and thus quantitative information may be obtained by extrapolation of the relevant data set to zero delay time for a heterogeneous system, so long as the proton $T_{1\rho}$ and cross-relaxation time associated with a particular peak in the dilute-spin spectrum are known.

3.2.3 T_1 measurement

Spin-lattice relaxation times were obtained using the pulse sequences outlined in Figures 3.1(e) to 3.1(g). The saturation-recovery sequence illustrated in Figure 3.1(e) was only used in the case of protons and consists of applying 32 $\pi/2$ pulses in rapid succession in order to saturate the proton signal. Single-point acquisition of the data for a range of recovery delays leads to the calculation of the spin-lattice relaxation time.

For the inversion-recovery sequence illustrated in Figure 3.1(f), the magnetisation is inverted using a π pulse and a delay time is allowed before the application of

a $\pi/2$ monitoring pulse, followed by acquisition of the whole spectrum. The spin-lattice relaxation time may be obtained from analysis of the recovery data. Such a pulse sequence was typically used to investigate the spin-lattice relaxation characteristics of the silicon spins of the calcined samples.

When dipolar interactions exist between the spins of interest and proton spins, then use may be made of the Torchia method of proton enhancement[10]. The experiment (Figure 3.1(g)) consists of two similar but not identical pulse sequences. In the first sequence, transverse magnetisation corresponding to the dilute spin is generated by the usual cross-polarization experiment. The proton-enhanced dilute-spin magnetisation is then transferred to the z-axis. The instant that the r.f. is switched off is defined as t=0. In the absence of a B_1 field, the proton-enhanced longitudinal magnetisation, $M_{CP}(t)$, changes exponentially from its initial value $M_{CP}(0)$ to its equilibrium value M_0 with time constant T_1. Magnetisation ($M_A(t)$) which does not arise from cross-polarization processes may also be present, and the longitudinal magnetisation $M_{Z1}(t)$ is given by[10]:

$$M_{Z1}(t) = [M_{CP}(0) - M_0] \exp(-t/T_1) + M_0 + [M_A(t)]_Z \quad (3.14)$$

After time t, a $\pi/2$ monitoring pulse is applied and signal detection is made in the presence of high-power proton decoupling. The second sequence is identical to the first except that the proton spin temperature in the second sequence is inverted by a phase shift of π and the sign of the proton-enhanced dilute-spin signal is opposite to that obtained in the first sequence. In contrast, the unwanted magnetisation, $M_A(t)$, is identical to that obtained in the first

sequence. Thus, the longitudinal magnetisation $M_{Z2}(t)$ is given by[10]:

$$M_{Z2}(t) = [-M_{CP}(0) - M_O] \exp(^{-t}/_{T_1}) + M_O + [M_A(t)]_Z \quad (3.15)$$

If the signal derived from the second sequence is subtracted from that derived from the first, the signal after N scans is given by $NM_{CP}(0)\exp(^{-t}/_{T_1})$ where N is an even number. The experiment thus incorporates the usual advantages of cross-polarization into a spin-lattice determination experiment.

Note that during both the inversion-recovery experiment and the proton-enhanced method of Torchia, high-power proton decoupling only takes place during the signal acquisition due to instrumental constraints. During the delay time, heteronuclear dipolar interactions may give rise to transient Overhauser effects due to relaxation of the dilute-spin magnetisation in a proton dipolar field. However, in solids, ^1H-^1H dipolar interactions determine the longitudinal proton polarization and the transient Overhauser effect on the expression for the net signal is cancelled by the spin-temperature inversion nature of the pulse sequence[10].

In the case of non-integral spin quadrupolar nuclei, measurement of the central transition spin-lattice relaxation time is complicated by the effect of the time-evolution of the non-central transitions on the time-evolution of the central transition after perturbation by a r.f. pulse. The problem may be circumvented by selective excitation of the central transition by either a soft pulse[11] or a Dante pulse train. Due to instrumental features, the latter method was used to selectively equalise the populations of the

$m = \pm\frac{1}{2}$ energy levels in the case of relaxation measurements made on aluminium nuclei. After a delay time, the population difference of the two energy levels was measured by means of a short monitoring pulse (Figure 3.1(h). Measurement of the population difference for a range of delay times leads to a spin-lattice relaxation time characterising the central transition relaxation under conditions of selective excitation. For the instance where spin-lattice relaxation measurements were made on sodium nuclei, both the central and non-central transitions were clearly observable and an inversion-recovery type sequence was used. A small angle monitoring pulse was again used to measure the signal for central and non-central transitions after a suitable delay time[12]. The small angle measuring pulse avoids mixing the central and non-central relaxation processes and further details are given in Chapter Five.

3.2.4 $T_{1\rho}$ Measurement[13]

Spin-lattice relaxation measurements in the rotating frame were made on proton spins using the pulse sequence shown in Figure 3.1(i). The pulse sequence is applied on resonance, and following a $\pi/2$ pulse in the proton channel and subsequent spin-locking, the magnetisation is in a non-equilibrium situation and decays to an equilibrium value at a rate governed by an exponential time constant, $T_{1\rho}$, in the case of anhomogeneous sytem. Single-point acquisition of the data leads to calculation of the spin-lattice relaxation time(s) in the rotating frame by fitting of the data set to an exponential decay. In the case of an

Figure 3.1(j)

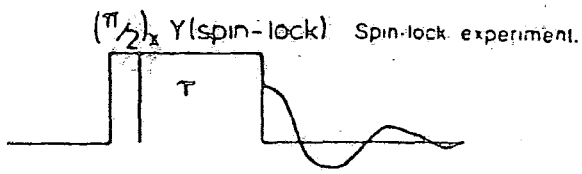

Spin-lock experiment.

Rotation-synchronised CPMG pulse sequence (with proton decoupling)

Figure 3.1(k)

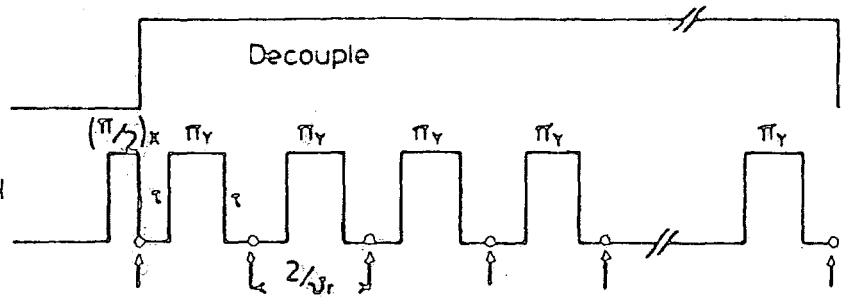

MREV-8 pulse sequence.

Figure 3.1(l)

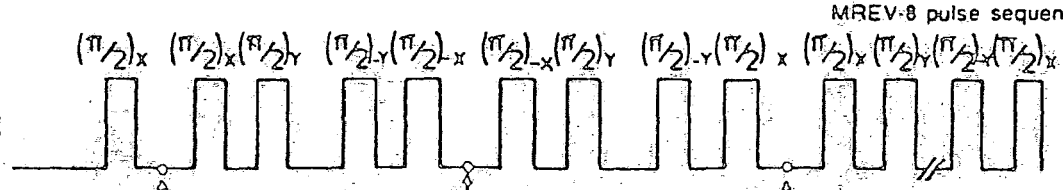

Figure 3.1(m)

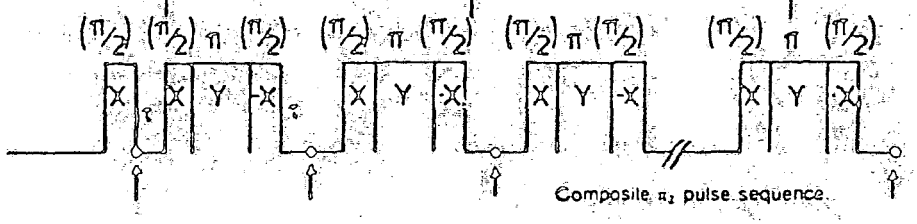

Composite π_2 pulse sequence.

Figure 3.1(n)

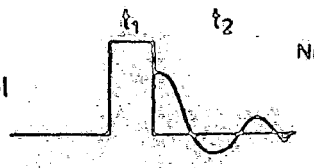

Nutation experiment.

heterogeneous system, the pulse sequence shown in Figure 3.1(j) may be used to simplify the proton spectrum provided that the difference in the proton $T_{1\rho}$s is significant.

3.2.5 T_2 Measurement

Spin-spin relaxation times (T_2) may be measured using the CPMG pulse sequence shown in Figure 3.1(k)[14]. The initial $\pi/2$ pulse generates maximum transverse magnetisation, and the spin isochromats then dephase during the time interval τ. Following the application of a π pulse, the isochromats refocus after a time 2τ to produce an echo. Subsequent dephasing and rephasing of the isochromats in a similar fashion with single-point stroboscopic acquisition leads to a data set which decays with an exponential time constant T_2 in the case of an homogeneous system, and in the absence of modulation. Modulation effects arise due to the failure of the pulse sequence to refocus interactions such as homodipolar coupling or J-coupling. In the solid-state, it is necessary to synchronise the rotor period as indicated in Figure 3.1(k). The pulse sequence was applied to non-integral quadrupolar nuclei and a more complete discussion is given in Chapter Seven.

3.2.6 Multiple-pulse linenarrowing experiments

The linebroadening influences of homodipolar coupling may be removed from a spectrum by application of the MREV-8 pulse sequence[15] shown in Figure 3.1(l). Single-point stroboscopic acquisition of the data in the windows indicated in Figure 3.1(l) corresponds to an averaging of the

homodipolar Hamiltonian in spin-space. Fourier Transformation of the data obtained by the forced precession leads a spectrum free of homodipolar broadening. Further line-narrowing is obtained by combining the multiple-pulse experiment with magic angle spinning (the so-called CRAMPS experiment)[16,17,18]. The frequency domain of the spectrum is scaled by the theoretical factor of $\sqrt{2/3}$. The scaling factor was determined experimentally by the co-addition of signals from the reference sample at a number of offsets differing by 1 kHz, and subsequent Fourier Transformation. In order to obtain the best resolution, the pulse amplitudes and phases must be calibrated accurately and the phase glitches must be minimized using a series of tune-up pulse sequences. Further details concerning these pulse sequences are given in reference 2. In addition, small sample sizes should be used to minimize r.f. inhomogeneity effects. In a MREV-8 (or CRAMPS) experiment, the resolution is optimised by setting the irradiation frequency as close as possible to the signal(s) of interest. The data are obtained in non-quadrature form and it may be necessary to reverse the whole spectrum depending on the position of the irradiation frequency. The symmetric nature of the pulse sequence should cancel errors from r.f. inhomogeneity and inaccurate pulse widths and phases.

The MREV-8 pulse sequence was also applied to aluminium spins in an attempt to see whether the pulse sequence was capable of averaging the quadrupolar interaction, either in whole or in part. The experimental procedure and results are given in Chapter Seven. Other linenarrowing sequences,

Figure 3.1(o)

X channel

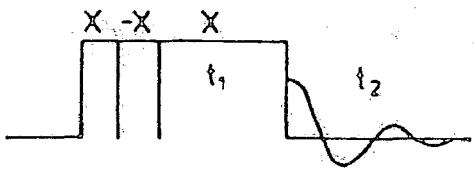

Rotary-echo nutation experiment.

Figure 3.1(p)

^{1}H channel

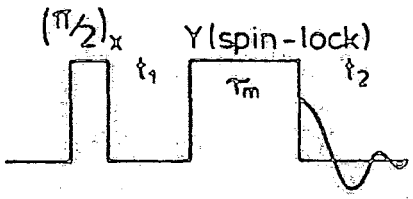

2D exchange NMR experiment.

such as one consisting of π_z pulses[19] (Figure 3.1(m)) are also considered in Chapter Seven.

3.2.7 2D Experiments

A number of 2D techniques were implemented during the course of the work. The nutation experiment shown in Figure 3.1(n) was used to provide information on the quadrupolar parameters and/or relaxation processes[20,21]. The value of t_1 was usually incremented by 2μs and subsequent 2D Fourier Transformation leads to a 2D data array, the projection of which in the F_2 direction yields the normal 1D single-pulse spectrum subject to second-order quadrupolar interactions and chemical shift anisotropy. The projection in the F_1 direction yields the excitation projection from which the quadrupolar parameters may be deduced. Further experimental details are given in Chapter Five. Linebroadening may result in the F_1 projection as a consequence of $T_{2\rho}$ relaxation process and/or a distribution of quadrupolar parameters. Under certain conditions, these two linebroadening mechanisms may be distinguished by use of the rotary-echo nutation experiment[22] (Figure 3.1(o)).

2D chemical exchange experiments[23] were implemented to investigate the possibility of chemical exchange/spin diffusion between the proton spins present on the external surface of a zeolite (Figure 3.1(p)). Due to the mobility of the proton-containing surface species, no multiple-pulse techniques were required to remove homodipolar proton interactions. Given that the system was heterogeneous, a judicious choice of the spin-locking/mixing time allowed the simplification of the spectrum.

The pulse sequence shown in Figure 3.1(p) was also used to investigate the possibility of molecular motion in systems containing quadrupolar nuclei that exhibit a non-central transition spinning sideband pattern in the single-pulse ^{27}Al MASNMR experiment. The experiment is similar to an experiment proposed by De Jong *et al*[24], in which very slow molecular reorientations were studied by analysis of the cross-peaks associated with the spinning sidebands arising from shielding anisotropy. The experiment is described in more detail at a later stage.

3.3 Zeolite synthesis[25,26,27,28]

Zeolites are generally metastable species that are prepared by hydrothermal synthesis from strongly basic reaction mixtures containing silicon (as soluble silicate or colloidal silica), aluminium (as aluminate) and various types of cations. Most of the research in this thesis concerns high-silica zeolites that are generally prepared using organic molecules such as amines and quaternary ammonium salts in addition to the reactants above, although some high-silica zeolites may be prepared without the use of organic molecules of any kind. The role of the organic template is imperfectly understood, but it is believed to exert both a shape directing effect in addition to solubilising and stabilising the silicate species in the starting solution.

In general, the type and crystal properties of the zeolite obtained are highly sensitive to the physical and chemical nature of the reactants used in preparing the reaction mixture, the overall chemical composition of the latter,

the types of cation present, and the conditions (temperature, pressure and time) of the hydrothermal treatment. Zeolite synthesis usually proceeds *via* the formation of an intermediate aluminosilicate gel and, after an induction period, the zeolite crystallises with or without participation of the solution phase. The synthesis mixture therefore consists of a very complex heterogeneous system made up of the amorphous gel, the emergent zeolite crystals and the supernatant solution. These three phases and the starting silicate and aluminate solutions have been studied by a wide range of methods. However, the mechanism by which zeolites form from the gels and the nature of the dissolved species in the reactant solutions are poorly understood.

^{29}Si and ^{27}Al studies (both solid and solution state), in combination with XRD and elemental analysis have provided detailed information on the mechanisms of zeolite formation. The suggested mechanisms apparently differ considerably for different zeolites which suggests that the crystallisation process depends critically on the preparation conditions.

The preparations of some of the high-silica samples are discussed below. In the case of the gallium analogue of ZSM-5, the aluminate source is simply replaced by a gallate source, the synthesis conditions being otherwise similar to those outlined above.

3.3.1 Sample Preparation[29]

3.3.1.1 Synthesis of high-silica theta-1

In order to prepare high-silica zeolite theta-1, 0.4 g of NaOH were dissolved in 50 g of water and the

addition of the NaOH was followed by 9 g of diethylamine which acts as a template in the synthesis. After stirring, 50 g of Ludox AS40 silica solution (containing 40% by weight silica in water) were added. The resultant hydrogel was stirred for a further 30 minutes - the dilute system eventually being transferred to a stainless steel, 150 cm^3 pressure vessel. This was half filled with gel and rotated in the oven to ensure thorough mixing during crystallisation at 448 K. At the end of the crystallisation period, the pressure vessel was cooled and the zeolite filtered, washed and then dried at 373 K. It is important to remove the pressure vessel from the oven soon after crystallisation has occurred because theta-1 is quickly converted to α-cristobalite. The removal of the organic template (calcination) was achieved by heating in a horizontal tubular furnace in a flow of air at 823 K for 12 hours.

3.3.1.2 Preparation of NH_4^+-theta-1

In this case, the starting point was the Na,H-form of theta-1 (sample provided by Dr. S.A.I.Barri). The sample was ion exchanged with ammonium nitrate solution. Approximately 10 ml of a 1 M solution of ammonium nitrate was used for every gram of zeolite (50 g of zeolite were ion-exchanged in total), the ion exchange process was repeated twice with filtering and washing of the sample with distilled water, both in between, and after the ion exchange processes. The sample was then dried in an oven at 373 K and used in the hydrothermal dealumination study outlined in Chapter Seven.

3.3.1.3 Preparation of NH_4^+-ZSM-5

In order to prepare approximately 100 g of the tetrapropylammonium hydroxide form of ZSM-5, initially 4 g of sodium hydroxide and 10.6 g of sodium aluminate were completely dissolved in water, and this was followed by the addition of 70 g of tetrapropylammonium hydroxide solution (containing 20% by weight tetrapropylammonium hydroxide in water). 250 g of Ludox AS40 silica solution were then added with constant stirring until a homogeneous gel resulted. The gel was split between eight stainless steel pressure vessels and heated for 3 days at 448 K. After filtering and washing with distilled water, the sample was dried in an oven at 373 K overnight. The sample was then calcined at 823 K for 12 hours in air to produce the Na,H-form of the zeolite. The sample was then ion exchanged with ammonium nitrate solution in an identical fashion to that described for the Na,H form of theta-1. The resulting NH_4^+-form of ZSM-5 was used in the hydrothermal dealumination studies, the results of which are discussed in Chapter Seven.

3.3.1.4 Synthesis of the gallium analogue of ZSM-5

10 g of gallium metal were dissolved in fuming nitric acid to produce a solution of gallium nitrate. 88 g of the solution were taken and ammonia was added dropwise until the mixture was thick with a gallium hydroxide precipitate (pH 7). The fresh precipitate was filtered out and washed with 200 ml of water and left to stand on the filter paper for half an hour. The gallium hydroxide was dissolved in a solution of 3.2 g of sodium hydroxide in 50 g of water to produce a solution of sodium gallate. Another

50 g of water was added followed by 54 g of diethanolamine and 100 g of Ludox AS40 silica solution. The resultant hydrogel was stirred for a further 30 minutes - the system then being transferred to a stainless steel pressure vessel. As in the case of the synthesis of high-silica theta-1, the pressure vessel was half-filled with gel and rotated in an oven to ensure thorough mixing during crystallisation at 443 K. A sample of Ga-ZSM-5 was also prepared using tetrapropylammonium hydroxide as the template. The synthesis conditions were identical to those given above for the diethanolamine template, apart from the use of 40 g of tetrapropylammonium hydroxide solution (in water) instead of 54 g of diethanolamine, and a total of 70 g of added water instead of the 100 g added in the diethanolamine synthesis. After synthesis, the crystalline product was filtered and washed with distilled water, and then dried in an oven at 373 K prior to calcination.

The as-synthesised forms were initially calcined under nitrogen (773 K for 12 hours) and then heated at 773 K for 12 hours in air. This calcination procedure minimises the possibility of the gallium falling out of the framework when the template is removed. Such a synthesis should result in a Si/Ga atomic ratio of approximately 15 in both cases, which was observed upon characterisation of the samples. The Na,H forms of Ga-ZSM-5 that result on calcination were used without further treatment for ion exchange.

Other synthetic zeolites studied (provided by Drs. S.A.I. Barri and D.W. Walker) include an as-synthesised form of theta-1 (diethanolamine template), a

calcined and ion-exchanged sample of theta-1 prepared with a diethanolamine template, a calcined form of theta-1 prepared with an ammonia template and an as-synthesised form of ZSM-5 (diethanolamine template). A sample of NaY zeolite was provided by Dr. Nock (Nottingham University), and a sample of albite was obtained from Dr. R. Hardy (Geology Department, Durham University).

The samples purchased are listed below together with their sources:

Sample	Source
Aluminium bromide hexahydrate	Aldrich Chemical Co. Inc.
Aluminium chloride hexahydrate	Aldrich Chemical Co. Inc.
Potassium aluminium sulphate	Alfa Products
Sodium aluminium sulphate	Alfa Products
Sodium chloride	Aldrich Chemical Co. Inc.
Borax	BDH
Sodium perborate	BDH
Diethanolamine	Aldrich Chemical Co. Ltd.

3.4 Review of the nuclei studied and the experimental procedures used.

The application of NMR to zeolites has recently been reviewed by Nagy and Derouane[30], and a summary of their review is given below.

3.4.1 Silicon

In the first application of high-resolution solid-state MAS NMR to the investigation of silicates and aluminosilicates, Lippmaa *et al*[31] showed that distinct peaks could be observed in the ^{29}Si MASNMR spectra of solid silicates and aluminosilicates which corresponded to different chemical environments, depending essentially on the number of tetrahedral aluminium atoms in the second coordination sphere of silicon[32,33]. The chemical shifts of the lines belonging to specific Si (nAl) configurations are also influenced by

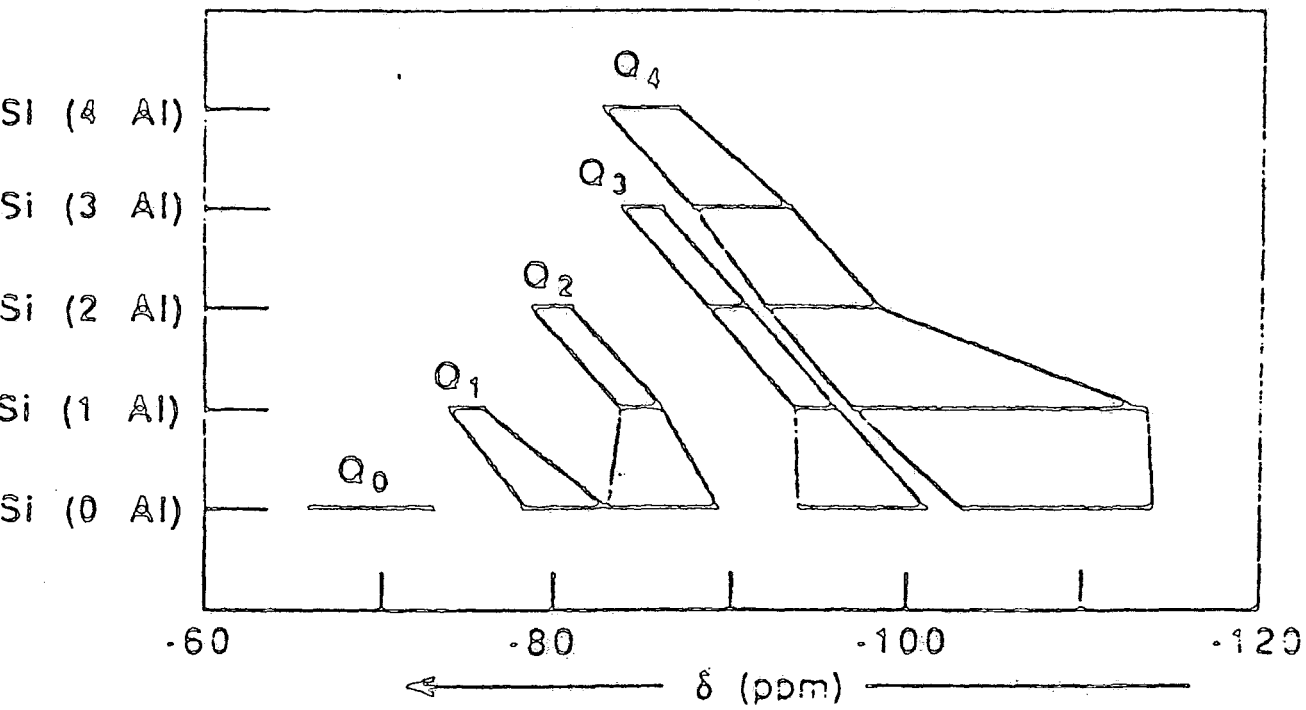

Figure 3.3: ^{29}Si-NMR chemical shifts of aluminosilicates.

(after reference 30)

the different interatomic distances and angles of the Si-O-T linkages (T=Si,Al)[33,34].

In silicates, the ^{29}Si NMR chemical shift range extends from -60 to -120 ppm and may be subdivided into characteristic ranges for monosilicates (Q_0), disilicates and chain end groups (Q_1), middle groups in chains and rings (Q_2), chain branching sites (Q_3) and the three-dimensional cross-linked framework (Q_4)[30]. Substitution of silicon by aluminium leads to a paramagnetic shift (Figure 3.3). The degree of crystallinity and the regularity of the Si,Al distribution is reflected in the sharpness of the resonance lines[30].

The SiOR (R=H, metal or organic cation) defect sites are also readily detected by ^{29}Si NMR. For zeolites of quite different structures, the relevant resonance occurs at about -103 ppm[33,35,36] which is probably due to the similar average Si-O-T angles[30]. Cross-polarization enhances the intensity of the line characterised by SiOH groups for short contact times relative to the lines in the ordinary single-pulse spectrum[36,37]. The concentration of SiOR defect sites increases with decreasing aluminium content[38] in the case of ZSM-5, and as many as 32SiOR per unit cell have been detected in highly siliceous samples. Given that four SiOR correspond to each missing tetrahedral site, eight T-sites must be non-occupied in the structure. These results are in agreement with the model previously proposed for the formation of ZSM-5 zeolite, where double five-membered rings are believed to condense to a structure containing a high number of defect sites[38].

The probability of the $Si(AlO_4)_n(SiO_4)_{4-n}$ units as a function of n may be calculated assuming a binominal distribution and no Al-O-Al linkages[39]. The calculation is independent of the topology of the structure and may be performed on any zeolite[40]. Thus, for a given quantitative single-pulse silicon spectrum, the framework Si/Al ratio of the zeolite may be calculated, although the accuracy of the method becomes questionable for Si/Al ratios greater than 20. Information on the Si,Al ordering on the T- sites of the zeolite framework may be derived by comparison of the relative Si(nAl) populations obtained from NMR peak intensities with model generated Si(nAl) populations[30].

3.4.1.1 ^{29}Si Experimental procedure

The ^{29}Si chemical shifts reported in this thesis are referenced with respect to TMS using the solid sodium salt of trimethylsilyl-1-propanesulphonic acid as a secondary reference material. Typically, the proton r.f. field strength was set using silica gum (r.f. field strength ≈62.5 kHz) and the field was then adjusted to bring the ^1H signal on-resonance. The Hartmann-Hahn match was then set on the reference compound by variation of the silicon r.f. field strength until maximum signal enhancement was observed. Slow spinning, a 1 ms contact time and a recycle delay of 30 s were used. The shift of the single resonance observed in the silicon reference compound is 1.18 ppm with respect to TMS. This procedure was always used for referencing and, afterwards the spectrometer was ready for both cross-polarization and single-pulse ^{29}Si experiments. In

some instances, the Hartmann-Hahn match was set directly on the sample.

3.4.2 Carbon

High-resolution ^{13}C MASNMR may be used to investigate the nature of carbon-containing molecules occluded into the zeolite channels or cavities. The isotropic ^{13}C chemical shift is highly sensitive to the environment of the carbon nucleus, and the ^{13}C NMR spectra usually display narrow and well resolved lines for each kind of distinct carbon atom of the organic species in the zeolite.

^{13}C NMR data have shown that the tetrapropylammonium ions are occluded intact in the ZSM-5 channels[41]. Moreover, two types of methyl groups are observed but at temperatures higher than 523 K, the intensity of the doublet peaks decreases and a sharp peak characterising the methyl groups appears. It has been concluded that heating results in symmetrisation of the tetrapropylammonium ion by rotation, yielding only a single resonance in the ^{13}C NMR spectrum[42].

The ^{13}C MASNMR technique has been applied to a wide variety of organic templates present in as-synthesised ZSM-5 zeolites. The spectra reveal that most of the templates such as butylamine, ethanol and butan-1-ol partly decompose or diffuse out of the framework during the synthesis or drying of the zeolite[28]. ^{13}C MASNMR has also been used to detect the presence of small ZSM-5 particles which contain less than 3 or 4 unit cells in thickness, corresponding to a size that is beyond the XRD limit[43].

Tetrabutylammonium cations are the preferred template for ZSM-11 but, tetrabutylphosphonium ions may also be used in the synthesis of ZSM-11 zeolite. The ^{13}C MASNMR data suggest that the template remains intact during the synthesis, and again there is a doublet splitting of the methyl peak in both cases[44]. The doublet splitting of the methyl peak in both ZSM-5 and ZSM-11 is interpreted in terms of the influence of the different channels on the methyl groups of the template which is located at the channel intersections. It should, however, be noted that spectra reported by Boxhoorn and co-workers do not show splitting of the methyl peaks in the case of ZSM-11[41,42].

It has recently been shown that in the synthesis of zeolite ZSM-48 in the presence of an alkylamine and tetramethylammonium ions, only the n-alkylamine plays a structure-directing role, while the tetramethylammonium ions are the main species incorporated during the growth process, until complete filling of the channels is achieved[45]. In contrast to zeolite ZSM-48, the formation of zeolite ZSM-39 seems to be directed exclusively by tetramethylammonium ions[30]. The crystallisation of zeolite ZSM-39 is accompanied by the de-quaternation of tetramethylammonium ions to produce trimethylammonium ions in equilibrium with trimethylamine. These two organic compounds are essentially occluded in the large cavities of ZSM-39[30].

The ^{13}C NMR chemical shift of the methyl carbons in the tetramethylammonium ion are particularly sensitive to the cage environment of the zeolite[46,47]. A study of a wide range of zeolites has shown that there is a clear correl-

ation between chemical shifts and the size of the cage[47]. The resonance shifts to lower frequency as the size of the cage increases. It seems that the chemical shift is determined almost entirely by the size of the cage, while the structure outside the cage, the framework Si/Al ratio and the density of the tetramethylammonium ions in the cage have a negligible effect on the chemical shifts. Thus, tetramethylammonium ions are excellent probe molecules for estimating the size of the cage trapping the ions, even if the framework structure is unknown.

Organic probes such as pyridine[48] and carbon monoxide[49] have been used as probe molecules to investigate the nature of acid sites in zeolites. The nature of the adsorbed species and by implication the nature of the acid sites may be inferred from the chemical shifts, linewidths and relaxation times.

As an analytical tool, ^{13}C NMR may be used to follow the concentration of reactants and products as a function of time, and hence kinetic constants may be determined. Mechanistic information on catalytic transformations may also be provided[49,50].

3.4.2.1 ^{13}C Experimental procedure

The ^{13}C NMR chemical shifts reported in this thesis are referenced with respect to TMS using solid adamantane as a secondary reference material. The carbon r.f. field strength was adjusted to allow for maximum transverse magnetisation (r.f. field strength ≈ 62.5 kHz) and the Hartmann-Hahn match was then set by variation of the proton

r.f. field strength until a maximum signal was observed. Slow spinning, a 1.5 ms contact time and recycle delay of 5 s were used. The shifts were converted to the TMS scale by using a shift of 38.4 ppm for the higher frequency adamantane shift. After this procedure, the spectrometer was ready for cross-polarization and single-pulse ^{13}C experiments. The experimental procedure outlined above was used in the case of the CXP-200, and was essentially the same for the MSL-300, although different r.f. field strengths were used, and allowance was made for a power droop in the proton channel.

3.4.3 Aluminium

^{27}Al NMR has been used to characterise framework four-coordinate and extra-framework six-coordinate aluminium species[51]. Usually, only the central transition resonance is observed and although this is broadened by a second-order quadrupolar interaction, the difference in chemical shift of the two species is usually sufficient to ensure that the two species are well resolved.

For quantitative measurements, care has to be taken to ensure that a short flip angle is used in order to render the central transition signal intensity independent of the quadrupolar interaction[20]. The procedure for aluminium quantitation is described fully in Chapter Five and no further mention will be made of it here. Recently, Lippmaa *et al*[52] have shown that there is a linear correlation between the chemical shift of the central transition (corrected for the second-order diamagnetic quadrupolar shift) and the mean Al-O-Si bond in framework silicoaluminates. This method can be used to position the aluminium atoms in the different

crystallographic sites if the relevant bond angles have been accurately determined. The method may also be used to complement ^{29}Si NMR data.

^{27}Al NMR has also been used in both dealumination and realumination studies of zeolites[53,54,55,56,57]. Dealumination is performed to increase the thermal stability and acidity of zeolites, whereas realumination is used to effect a different Si,Al ordering in the framework with respect to the ordering that existed before dealumination. Dealumination typically results in broad underlying resonances in the ^{27}Al MASNMR spectra. Nutation experiments performed on dealuminated zeolite Y samples suggest that the non-framework aluminium resulting on dealumination is characterised by a stronger quadrupole interaction than that characterising the framework aluminium[55]. However, results presented in this thesis suggest that the broad linewidth of the non-framework species does not simply result from second-order quadrupolar effects. Incorporation of aluminium into the zeolite framework by treatment of zeolites with $AlCl_3$ has been convincingly demonstrated by ^{27}Al NMR[58,59]. The proposed mechanism for the alumination of ZSM-5 involves both the reactive hydroxyl nests on the external surface and in the internal channels[59].

The existence of penta-coordinate aluminium species has been suggested on the basis of chemical shift measurements in steamed crystalline or amorphous aluminasilicates[60]. It has been suggested that the presence of penta-ccordinated aluminium may reduce the extent of coke formation during hydrocarbon cracking reactions. Recently,

however, this interpretation has been questioned and it has been suggested that the resonance results from non-framework four-coordinate aluminium[55].

3.4.3.1 ^{27}Al Experimental procedure

The ^{27}Al NMR shifts quoted in this thesis are referenced with respect to $Al(H_2O)_6^{3+}$. The sharp resonance of the hexa-aqua cation is visible in all aqueous solutions of aluminium salts, and is therefore easily accessible. A dilute solution of aluminium chloride was used in the vast majority of cases. Ideally, the shift should have been extrapolated to infinite dilution, although in the case of aluminium chloride solution, the observed shift was negligibly dependent on the concentration of aluminium chloride, and no attempt was made to extrapolate the chemical shift to infinite dilution.

When more than one aluminium resonance was present and quantitative peak intensities were required on the CXP-200 spectrometer, the aluminium r.f. field strength was typically set at $\sim 41^2/3$ kHz using a sample of solid aluminium bromide. The pulse duration was then reduced in agreement with the quantitative requirements of Figure 5.2. A similar procedure was used on the VXR-300 spectrometer. For the Jeol GE-400 spectrometer, the complete description is given in Chapter Five. The full experimental descriptions of the more complex nutation and 2D exchange experiments are also given in Chapter Five, as is the description of the Dante T_1 experiment. The full experimental procedure for the multiple-pulse experiments are given in Chapter Seven.

3.4.4 Sodium

The chemical shift range of the sodium nucleus is smaller than that of the aluminium nucleus. In addition, because the nuclear spin quantum number of sodium is smaller than that of aluminium, sodium has a greater second-order quadrupolar width and hence broader central transition lines[28]. Consequently, the spectral resolution is poor when more than one sodium resonance contributes to the spectrum in the solid state.

^{23}Na NMR has been used to provide information of the Si,Al ordering in zeolites. A well resolved second-order powder pattern for the central transition,instead of a broad featureless hump,is observed in the case of an ordered system[61]. ^{23}Na NMR has also been used to study dehydration and rehydration of ZSM-5[62]. ^{23}Na NMR techniques have proved particularly useful in studying the hydration state of sodium cations as well as their interactions with the negative centres of the framework. Apparently, both the linewidth and the chemical shift of sodium depend on the relative amount of aluminium in the samples in the case of ZSM-5[63]. A chemical shift close to zero has been reported for the highly siliceous samples, while the samples containing a higher proportion of aluminium exhibit a spectrum characterised by a chemical shift in the -15 - -20 ppm region. It should be noted that these shift ranges must be very sensitive to the zeolite structure because the ^{23}Na resonances observed for the non-ZSM-5 type zeolites do not fall in the -15 - -20 ppm range for the samples investigated in this thesis. The value of attempting to define such shift ranges seems dubious given

the existence of second-order quadrupolar shifts, and the possible presence of mobility and exchange effects.

^{23}Na NMR has been applied to NaY zeolites containing ionic and metallic sodium clusters in the zeolite pores as demonstrated by Grobet *et al* [64]. The ^{23}Na spectra of the sodium-metal loaded compounds show three different lines: an intense line at 0 ppm, and lines at 673 and 1132 ppm, which are assigned to Na^+ ions in the zeolite, and to sodium metal particles in the supercages of NaY, and metal particles at the crystallite surface. The large shifts in the case of the metallic sodium clusters results from a Knight Shift.

^{23}Na nutation NMR has been applied to dehydration studies of NaA zeolite, and the results have been interpreted in terms of a distribution of quadrupolar parameters and relaxation effects, which lead to a broadening in the excitation projection of the nutation experiment[65]. The presence of relaxation broadening was elegantly demonstrated by the use of rotary echo nutation experiments[22].

3.4.4.1 ^{23}Na Experimental procedure

The ^{23}Na chemical shifts reported in this thesis are referenced relative to Na^+ ions at infinite aqueous dilution. On such a chemical shift scale, solid sodium chloride has a shift of 7.1 ppm. The sodium r.f. field strength was typically set at $\sim 41^2/3$ kHz using solid sodium chloride, and when quantitative results were required, the pulse duration was reduced in accordance with Figure 5.1.

A similar procedure was followed for both the CXP-200 and VXR-300 spectrometers. As in the case of aluminium, the more complex nutation and multiple-pulse experiments are described in Chapters Five and Seven respectively.

3.4.5 Hydrogen

Hydrogen atoms may be present in zeolites in several structurally distinct forms[28]. The catalytic properties of zeolites depend on acidic protons of hydroxyl groups associated with framework aluminium (Si(OH)Al). Hydrogen atoms may also be present in Si-OH groups ("terminal" or "silanolic" hydroxyl groups) at the surface of the zeolite crystallites, in defect sites of the framework or in amorphous material occluded in the zeolite. Al-OH groups of non-framework hydroxoaluminium species, NH_4^+ and other proton-bearing cations, hydroxyl groups associated with metal cations, and chemically or physically adsorbed water molecules are all other potential sources of hydrogen atoms in zeolites[28].

The considerable attention paid to the NMR behaviour of water adsorbed in zeolites has been summarised by Buckingham and McLauchlan[66]. Analcime, natrolite and thomsonite yield ^1H NMR static spectra with linewidths of the order of several tens of kHz, while faujasite yields a sharp resonance due to the absence of orientation effects on the supercages. Relaxation times T_1 and T_2 have been determined as a function of temperature and surface coverage for a wide range of zeolites and information concerning the water mobility and its distribution has been obtained[67,68,69].

In the case of dehydrated zeolites, broad and featureless lines result in the ^{1}H NMR static spectra due to homo- and heterodipolar interactions, and with a lesser contribution from shielding anisotropy[28]. Although the ^{1}H chemical shifts may not be measured with sufficient accuracy, and signals resulting from structurally distinct hydrogen atoms may not be resolved, it is possible to determine the total concentration of protons, and certain types of proton may be differentiated by their T_2 relaxation times[70]. A considerable improvement in resolution is observed on using MAS and a review summarising the information that may be obtained is given in Section 7.10. Multiple-pulse techniques to remove the homodipolar proton interaction in zeolites are only relevant for samples containing the organic template. For dehydrated zeolite samples in the hydrogen form, the proton-proton distances are usually large enough to prevent homodipolar broadening in ^{1}H MASNMR experiments[71], whereas spin exchange averages out the homodipolar interaction in hydrated zeolites.

3.4.5.1 ^{1}H Experimental procedure

The ^{1}H chemical shifts are referenced with respect to TMS. For ^{1}H MAS experiments, TMS was used as the reference material whereas for CRAMPS experiments, adamantane (1.74 ppm with respect to TMS) was used as the secondary reference material. It should be noted that the two proton resonances in adamantane are not resolved by the CRAMPS technique.

3.5 Characterisation by non-NMR techniques

3.5.1 Temperature-programmed desorption (TPD)

Ammonia-TPD measurements were used to measure acid site concentration and strength. The experiment involves adsorbing ammonia onto the sample and then following the desorption of ammonia as a function of temperature. Two considerations must, however, apply before such measurements may be considered as quantitative. The measurements are only quantitative if the nature of the NH_3 desorption peaks is identified unambiguously. The other point is that peak areas measure the number of sites, whereas their position on the temperature scale (maximum desorption rate) is usually believed to be a measurement of their strength. However, the latter may not always be the case. Desorption peak maxima (T_M) are related to the heating rate, β, by the equation[72]:

$$2\log_{10}T_M - \log\beta = \frac{E_d}{2.3RT_M} + \log\left(\frac{E_d \cdot a_m}{RK_o}\right) \qquad (3.16)$$

where a_m is the amount adsorbed at saturation, K_o is the exponential factor in the desorption rate, and E_d is the activation energy for desorption. Clearly, the position of T_M is defined in non-equilibrium (kinetic conditions), in contrast to acid strength which must be defined in terms of an acid-base equilibrium. Hence, the direct use of T_M as an acid strength correlation parameter, without further determination of the other parameters characterising the description process, may sometimes be misleading.

The sample was heated up to the pretreatment temperature (673 K) at 10 K min^{-1} in 50 ml min^{-1} of dry N_2

and then held at 673 K for 3 hours. The system was cooled to 373 K and the gas flow was switched to 50 ml min^{-1} of 1% NH_3 in N_2 for 30 minutes. The flow was switched back to N_2 and the system was flushed out at 373 K for 16 hours. The sample was then heated from 373 K to about 973 K at 5 K/min. The desorbed ammonia was swept by flowing nitrogen into a solution ($2.5 g l^{-1}$) of boric acid. The pH of the boric acid was kept constant by the addition of 0.01 M hydrochloric acid.

Thus, the primary information obtained was the volume of hydrochloric acid added as a function of temperature. This is converted to mass of ammonia desorbed. The curve is presented as a derivative plot to give the more usual presentation of rate of desorption as a function of temperature. The NH_3-TPD experiments were performed by Dr. P. Aukitt (Sunbury-on-Thames).

3.5.2 Thermal gravimetric analysis (TGA)

The TGA studies were performed using a Perkin-Elmer 7 series thermal analysis system. 10 mg of the sample were purged for 5 minutes in 60 ml min^{-1} of dry N_2 at 303 K. The sample weight was then recorded in the 303-1173 K region under dry N_2 flow at a heating rate of 10 K min^{-1}. The technique allows the analysis of the various types of template molecules present in a zeolite sample. In the event that the template is an amine, then the technique may be used to provide information of the types of acid sites present as in the case of the TPD studies - the strongest acid sites desorbing the base at the highest temperature. TGA may also be used to provide an estimate of the water and organic content although the assignments are often limited because the loss of occluded water may

occur simultaneously with the removal of the organic species. The TGA analysis was performed by Mr. S. Prince (Sunbury-on-Thames).

3.5.3 Electron spectroscopy for chemical analysis (ESCA)

Samples were run on a Kratos ES300 XPS spectrometer in fixed retardation mode, using MgKα X-rays (96W) of 1253.6 eV energy. The powder samples were mounted on a 3-sided probe tip using double-sided Scotch adhesive tape. Peak positions were referenced to hydrocarbon at 285 eV (arising from a small amount of surface contamination and possibly from the adhesive tape). Since the tape contains a significant proportion of carbon and oxygen, the elemental ratios for these elements in the sample cannot be accurately measured. The ESCA analysis is surface sensitive to a depth of approximately 30 Å and the elemental ratios calculated (accurate to approximately ±5%) may be compared with elemental ratios calculated from bulk techniques to provide information on elemental distribution. The technique may also be used to probe template distribution. The ESCA experiments were performed by Mr. R. Ward (Durham University).

3.5.4 Powder X-ray diffraction (XRD)

The XRD studies were performed using a Philips PW 1820 automatic diffractometer. The finely ground samples were mounted in the sample holder with care being taken to avoid orientation effects. 2θ values in the 4-32° range were scanned using CuKα radiation and a scintillation counter. The data were transferred to a computer to yield both the d-spacings and the diffraction trace. The XRD experiments were performed by Mrs. E.A. Thomas (Sunbury-on-Thames).

3.5.5 X-ray fluorescence (XRF)

XRF analysis was used to obtain the %wt. of silicon and aluminium present in the zeolite samples for use in quantitative ^{27}Al NMR work. In some instances, XRF was also used to obtain the %wt. of sodium and potassium. The analysis was performed using a Philips PW 1404 wavelength dispersive X-ray fluorescence spectrophotometer fitted with a scandium X-ray tube in the case of silicon and aluminium. The instrument was calibrated *versus* multiple standards and corrects for inter-element interferences. 0.2g of sample is mixed with 7.8g of lithium tetraborate and fused at 1473 K in a platinum crucible to form a bead. The XRF experiments were performed by Dr. D.C. Johnson (Sunbury-on-Thames).

3.5.6 Atomic absorption (AA)

AA was sometimes used to determine the %wt. of sodium and potassium in the zeolite samples. The analysis was performed using a Perkin Elmer 5000 atomic absorption spectrophotometer. The zeolite sample was dissolved in hydrofluoric acid, and the solution was introduced to an air-acetylene burner to yield an atomic vapour in the path of the light beam from the hollow cathode source. The instrument was calibrated using a series of standard water samples varying in sodium and potassium ion concentration. Sodium analysis is made very difficult by contamination problems, and care has to be taken with sample handling in addition to the subtraction of the background signal. The AA experiments were performed by Dr. R. Coult (Durham University).

3.5.7 Microanalysis

Microanalysis was used for the determination of the %wt. of carbon and nitrogen present in the as-synthesised samples containing an organic template. A Carlo Erba 1105 Elemental Analyser was used. The sample is contained in a lightweight tin container and dropped into a vertical quartz tube maintained at 1303 K, through which a constant flow of helium is run. When the samples are introduced, the helium stream is temporarily enriched with pure oxygen. Flash combustion takes place, primed by the oxidation of the container. Quantitative combustion is then achieved by passing the mixture of gases over Cr_2O_3. The gases are then passed over copper at 923 K to remove the excess of oxygen and to reduce oxides of nitrogen to nitrogen. The mixture then passes through a chromatographic column of Parapak QS heated to approximately 373 K and the individual components are then separated and eluted as N_2 and CO_2. A thermal conductivity detector feeds a signal to a potentiometric recorder in parallel with an integrator with a digital printout. The instrument is calibrated by combustion of standard compounds. The experiments were performed by Mrs. M. Cox (Durham University).

REFERENCES - CHAPTER THREE

1. Bruker Spectrospin Ltd., "Pulse NMR Spectrometer CXP Users Manual".

2. P. Jackson, Ph.D. Thesis, University of Durham (1987).

3. R.R. Ernst and W.A. Anderson, Rev.Sci.Instr., 37, 93 (1966).

4. A. Pines, M.G. Gibby and J.S. Waugh, J.Chem.Phys., 59, 569 (1973).

5. S.R. Hartmann and E.L. Hahn, Phys.Rev., 128, 2042 (1962).

6. M. Mehring, "Principles of High Resolution NMR in Solids", Springer-Verlag, 1983.

7. R. K. Harris, Analyst,110, 649 (1985).

8. E.O. Stejskal and J. Schaefer, J.Magn.Reson., 18, 560 (1975).

9. J. Tegenfeldt and U. Haeberlen, J.Magn.Reson., 36, 453 (1979).

10. D.A. Torchia, J.Magn.Reson., 30, 613 (1978).

11. J. Haase, H. Pfeifer, W. Oehme and J. Klinowski, Chem. Phys.Lett., 150, 189 (1988).

12. L.G. Werbelow and A.G. Marshall, J.Magn.Reson., 43, 443(1981).

13. D.C. Ailion, "NMR and Ultraslow motions" in Advances in Magnetic Resonance, Vol.5, Academic Press, New York, 1971.

14. S. Meiboorn and D. Gill, Rev.Sci.Instrum., 29, 688 (1958).

15. P. Mansfield, J.Phys., C4, 1444 (1971); W.K. Rhim, D.D. Elleman and R.W. Vaughan, J.Chem.Phys., 58, 1772 (1978).

16. L.M. Ryan, R.E. Taylor, A.J. Paff and B.C. Gerstein, Chem.Phys.Lett., 72, 508 (1980).

17. L.M. Ryan, R.C. Wilson and B.C. Gerstein, Chem.Phys.Lett., 52, 341 (1977).

18. G. Scheler, U. Haubenreisser and H. Rosenberger, J.Magn. Reson., 44, 134 (1981).

19. R.D. Walker and B.C. Gerstein, Phys.Rev.B, 31, 3167 (1985).

20. A. Samoson and E. Lippmaa, Phys.Rev.B, 28, 6567 (1983).

21. A.P.M. Kentgens, J.J.M. Lemmens, F.M.M. Geurts and W.S. Veeman, J.Magn.Reson., 71, 63 (1987).

22. R. Jansen, G.A.H. Tijink and W.S. Veeman, J.Chem.Phys., 88, 518 (1988).

23. A.J. Vega, J.Am.Chem.Soc., 110, 1049 (1988).

24. A.F. De Jong, A.P.M. Kentgens and W.S. Veeman, Chem. Phys.Lett., 150, 179 (1988).

25. R.M. Barrer, Hydrothermal Chemistry of Zeolites, Academic Press, London (1982).

26. E.M. Flanigan, Adv.Chem.Ser., No.121,119 (1973).

27. L.B. Sand, in Proceedings of the 5th International Zeolite Conference (Naples, 1980), p.1, Heyden, London (1980).

28. G. Engelhardt and D. Michel, "High Resolution Solid-State NMR of Silicates and Zeolites", J. Wiley and Sons (1987).

29. S.A.I. Barri and D. Walker, Private Communication.

30. J.B. Nagy and E.G. Derouane, ACS Symp.Ser., 368, 1 (1988).

31. E.T. Lippmaa, M.A. Alla, T.J. Pekk and G. Engelhardt, J.Am.Chem.Soc., 100, 1929 (1978).

32. E. Lippmaa, M. Mägi, A. Samoson, G. Engelhardt and A.R. Grimmer, J.Am.Chem.Soc., 102, 4889 (1980).

33. E. Lippmaa, M. Mägi, A. Samoson, M. Tarmak and G. Engelhardt, J.Am.Chem.Soc., 103, 4992 (1981).

34. C.A. Fyfe, G.C. Gobby, J. Klinowski, J.M. Thomas and S. Ramdas, Nature, 296, 530 (1982).

35. P. Bodart, J.B. Nagy, G. Debras, Z. Gabelica and P.A.Jacobs, J.Phys.Chem., 90, 5183 (1986).

36. J.B.Nagy, Z. Gabelica, E.G. Derouane and P.A. Jacobs, Chem.Lett., 1105 (1982).

37. J.B. Nagy, G. Engelhardt and D. Michel, Adv.Colloid. Interf.Sci., 23, 67 (1985).

38. R.A. van Santen, J. Keijsper, G. Ooms and A.G.T.G.Kortbeek, Stud.Surf.Sci.Catal., 28, 169 (1986).

39. G. Engelhardt, U. Lohse, E. Lippmaa, M. Tarmak and M.Mägi, Z.Anorg.Allg.Chemie., 482, 49 (1981).

40. J. Klinowski, S. Ramdas, J.M. Thomas, C.A. Fyfe and J.S. Hartman, J.Chem.Soc., Faraday Trans.2, 78, 1025 (1982).

41. G. Boxhoorn, R.A. van Santen, W.A. van Erp, G.R. Hays, R. Huis and D. Clague, J.Chem.Soc.,Chem.Commun., p.264, (1982).

42. G. Boxhoorn, R.A. van Santen, W.A. van Erp., G.R. Hays, N.C.M.Alma, R. Huis and A.D.H. Clague, Proceedings 6th Intern.Zeolite Conf. (Reno, 1983), p.694, Butterworth, Guildford (1985).

43. Z. Gabelica, J.B. Nagy and G. Debras, J.Catal., 84, 256 (1983).

44. J.B. Nagy, Z. Gabelica and E.G. Derouane, Zeolites, 3, 43 (1983).

45. N. Dewade, Z. Gabelica, P. Bodart, J.B. Nagy, G.Giordano and E.G. Derouane, in Proc.Int.Symp. "Innovation in Zeolite Materials Science", Nieuwpoort, Belgium, Sept. 13-17, (1987).

46. R.H. Jarman and M.T. Melchoir, J.Chem.Soc., Chem.Commun., p.414 (1984).

47. S. Hayashi, K. Suzuki, S. Shin, K. Hayamizu and O.Yamamoto, Chem.Phys.Lett., 113, 368 (1985).

48. H.J. Rauscher, D. Michel, D. Deininger and D. Geshke, J.Mol.Catal., 9, 369 (1980).

49. J.B. Nagy, M. Guetton, and E.G. Derouane, J.Catal., 55, 43 (1978).

50. M.W. Anderson and J. Klinowski, Nature, 339, 200 (1989).

51. J.M. Thomas and J. Klinowski, J.Adv.Catal., 33, 199 (1985).

52. E. Lippmaa, A. Samoson and M. Mägi, J.Am.Chem.Soc., 108, 1730 (1986).

53. V. Bosacek, D. Freude, T. Fröhlich, H. Pfeifer and H. Schmiedel, J.Colloid Interface Sci., 85, 502 (1982).

54. D. Freude, T. Fröhlich, H. Pfeifer and G. Scheler, Zeolites, 3, 171 (1983).

55. A. Samoson, E. Lippmaa, G. Engelhardt, G. Lohse and H.G. Jerschkewitz, Chem.Phys.Lett., 134, 589 (1987).

56. E. Brunner, H. Ernst, D. Freude, M. Hunger, C.B. Krause, D. Prager, W. Reschetilowski, W. Schwieger and K.-H.Bergt, Zeolites, 9, 282 (1989).

57. M.W. Anderson, J. Klinowski and K. Liu, J.Chem.Soc., Chem.Commun., 1596 (1984).

58. R.M. Dessau and G.T. Kerr, Zeolites, 4, 315 (1984).

59. C.D. Chang, C.T.-W Chu, J.N. Miale, R.F. Bridger and R.B. Calvert, J.Am.Chem.Soc., 106, 8143 (1984).

60. J.-P.Gilson, G.C. Edwards, A.W. Peters, K. Rajagopalan, R.F. Wormskecher, T.G. Roberie and M.P. Shattock, J.Chem.Soc., Chem.Commun., 91 (1987).

61. R.J. Kirkpatrick, R.A. Kinsey, K.A. Smith, D.M. Henderson and E. Oldfield, Am.Mineral., 70, 106 (1985).

62. K.F.M.G.J. Scholle, Ph.D. Thesis, University of Nijmegen (1985).

63. G. Debras, A. Gourge, B. Nagy and G. De Clippeleir, Zeolites, 6, 161 (1986).

64. P.J. Grobet, G. van Gorp, L.R.M. Martens and P.A. Jacobs, Proc. 23rd Congress Ampere, (Rome, 1986), p.356.

65. G.A.H. Tijink, R. Jansen and W.S. Veeman, J.Am.Chem.Soc., 109, 7301 (1987).

66. A.D. Buckingham and K.A. McLaughlan, Prog.NMR Spectrosc., 2, 63 (1967).

67. H.A. Resing and J.K. Thompson, Adv.Chem.Ser., 101, 473 (1971).

68. H. Pfeifer, Sur.Sci., 52, 434 (1975).

69. H. Pfeifer, A. Gutsze and S.P.Zholanov, Z.Phys.Chem. (Leipzig), 257, 721 (1976).

70. H. Pfeifer, D. Freude and M. Hunger, Chem.Phys.Lett., 91, 307 (1982).

71. J.M. Thomas and J. Klinowski, Adv.Catal., 33, 199 (1985).

72. R.E. Richards and L.V.C. Rees, Zeolites, 6, 17 (1986).

CHAPTER FOUR

STRUCTURES OF THE ZEOLITES STUDIED

4.1 Introduction

Zeolites are microporous, crystalline aluminosilicates consisting of a complex framework of SiO_4 and AlO_4 tetrahedra forming a regular system of inter-connected cavities and channels. The net negative charge of the aluminosilicate framework, equal to the number of constituent aluminium atoms, is balanced by charge-compensating cations located in the voids, which may also contain water or neutral molecules, and in some cases non-silicate anions (*e.g.* Cl^- in sodalite, CO_3^{2-} in cancirinite)[1]. The void space may be up to 50% of the total crystal volume. The various types of zeolite are characterised by the distinct topology of their three dimensional network, the relative proportions (Si/Al ratio) and arrangement (Si,Al order) of the Si and Al atoms in the tetrahedral sites of the framework, and the type and distribution of the cations. Zeolites may be represented by the general oxide formula[1]:

$$M^{n+}_{x/n}\ (AlO_2)_x(SiO_2)_y.qH_2O$$

where M^{n+} represents exchangeable cations - mostly metal cations, but also NH_4^+, H^+, organic cations or transition metal complexes. In all zeolite structures studied to date, it has been found that $y \geq x$. Given that each silicate and aluminate tetrahedron is linked *via* oxygen bridges to four other tetrahedra, the conclusion is that Al-O-Al linkages are forbidden (Loewenstein's rule)[1]. Thus, the minimum Si/Al ratio (y/x) in zeolites is unity, but the ratio may increase to ∞ in aluminium-free frameworks. Other elements such as Ga, Fe, B and P can be substituted for Si and Al in the zeolite framework but, in general, the framework topology is not altered by such substitutions. Taking into account

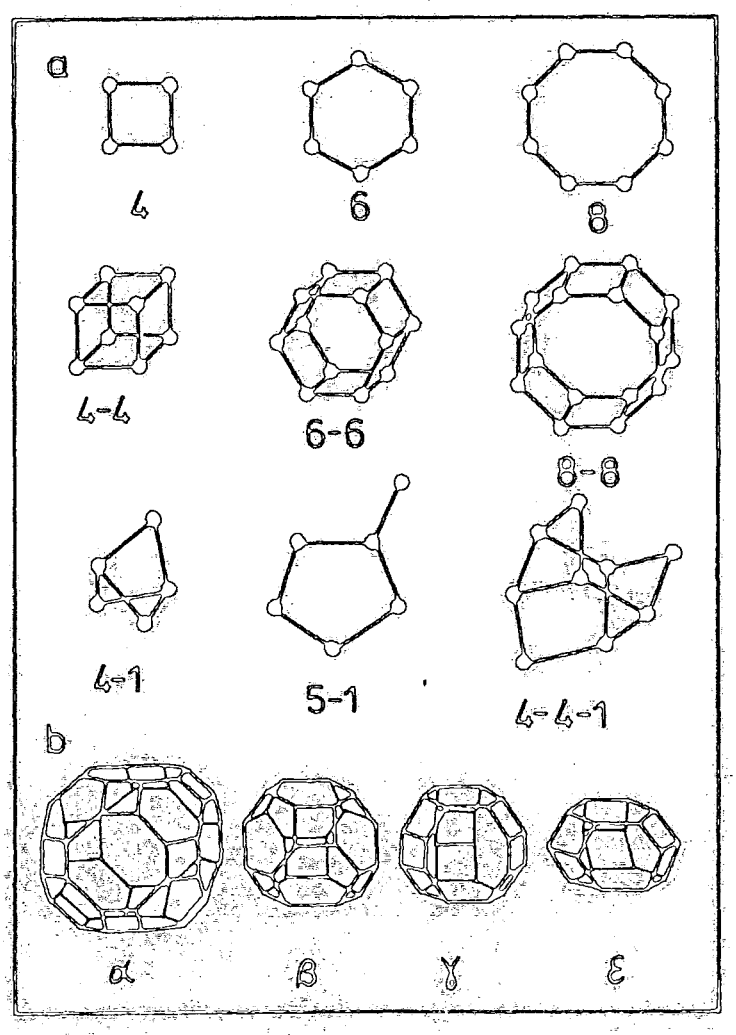

Figure 4.1: a) Secondary Building units.

b) Some examples of larger polyhedral building blocks.

(after reference 3)

isomorphous substitution, interrupted frameworks, hydroxo bridges and aqua and other ligands of framework atoms, the following more general oxide formula for zeolite-type materials based on four-connected frameworks has been proposed by Meier[2]:

$$M_xM'_yN_z[T_mT_n^1\ldots O_{2(m+n+\ldots)-k}(OH)_{2k}](OH)_{br}(aq)_p.qQ$$

where M and M′ are exchangeable and non-exchangeable metal cations, N are non-metallic cations (generally removed on heating), (aq) is chemically bonded water (or other strongly held ligands of T atoms) and Q are sorbate molecules which need not be water. The part in square brackets denotes the four-connected framework, which is usually anionic.

4.2 Classification of zeolite types

TO_4 tetrahedra, where T may be Si or Al, are thus the primary building units of all zeolite frameworks. Chains, sheets and three-dimensional networks may be constructed from these TO_4 tetrahedra, which are linked through shared oxygen atoms[1].

In 1967, Meier proposed the Secondary Building Unit (SBU) concept[3]. The SBUs are constructed from the primary building units. The framework topology of all known zeolite framework types can be constructed from such SBUs and classified in this way. Assuming the entire framework is made up of one SBU only, nine SBUs are derived which are shown in Figure 4.1(a)[1]. In the SBU, Al or Si is present at each corner but the oxygens are not shown. They are located near the mid-points of the lines joining each pair of T-atoms. Several zeolite frameworks can be generated by more than one type of secondary building unit making the SBU classification concept ambiguous[4,5,6]. This

TABLE 4.1 Unit cell compositions and secondary building units of selected zeolites[1]

Name	Typical unit cell composition	Secondary building units			
Analcime	$Na_{16}(Al_{16}Si_{32}O_{96})\cdot 16H_2O$	4	6		
Faujasite	$Na_{12}Ca_{12}Mg_{11}(Al_{58}Si_{134}O_{384})260\cdot H_2O$	4	6		6-6
Ferrierite	$Na_{1.5}Mg_2(Al_{5.5}Si_{30.5}O_{72})\cdot 18H_2O$				5-1
Zeolite ZK-5	$Na_{30}(Al_{30}Si_{66}O_{192})\cdot 98H_2O$	4	6	8	6-6
Zeolite A	$Na_{12}(Al_{12}Si_{12}O_{48})\cdot 27H_2O$	4	6	8	4-4
Zeolite L	$K_6Na_3(Al_9Si_{27}O_{72})\cdot 21H_2O$	4	6		6-6
Zeolite ZSM-11	$Na_n(Al_nSi_{96-n}O_{192})\cdot 16H_2O$				5-1
Mordenite	$Na_8(Al_8Si_{40}O_{96})\cdot 24H_2O$				5-1
Natrolite	$Na_{16}(Al_{16}Si_{24}O_{80})\cdot 16H_2O$				4-1
Zeolite RHO	$(Na,Cs)_{12}(Al_{12}Si_{36}O_{96})\cdot 46H_2O$	4	6	8	8-8
Zeolite THETA-1	$Na_n(Al_nSi_{24-n}O_{48})$				5-1
Zeolite ZSM-5	$Na_n(Al_nSi_{96-n}O_{192})\cdot 16H_2O$				5-1

is self-evident from Table 4.1 which lists a selection of zeolite types together with the corresponding SBUs of the framework. In fact only five out of the nine SBUs shown in Figure 4.1 are required to generate all the zeolite framework types - the 4, 6, 4-1, 4-4-1 and 5-1 units[6]. In some cases, the zeolite framework may be considered in terms of larger symmetrical polyhedra (Archimedean solids). Some important examples of these larger polyhedra are illustrated in Figure 4.1(b). More recently a different topological concept for the description and classification of zeolite framework types has been suggested by Meier and Moeck[7]. "Coordination sequences" representing the numbers of T atoms in the various tetrahedral coordination sphere of each topologically non-equivalent T-site are defined. The topology of the framework is then expressed by the sequences of these numbers up to the fifth nearest neighbour. Although the concept of coordination sequences has proved to be very useful in evaluating the degree of similarity among different zeolite structure types, most classification is still performed using the SBU concept.

The research described in the following chapters concerns mainly the zeolites theta-1 and ZSM-5 but some reference is also made to the zeolite Y. Theta-1 and ZSM-5 are both examples of medium-pore high-silica zeolites and are thus expected to have a high thermal stability in the hydrogen-form for many catalytic and separation applications. Zeolite Y does not fit into the same structural group as the above zeolites and was investigated because of its high sodium content.

A detailed description of the relevant zeolite structures is given below, and the depth of the description is dependent

on the relevance to the research. The complementary nature of ^{29}Si NMR and XRD in the characterisation of zeolite structures is examined in the following descriptions.

4.3 Structure of theta-1

The structure of theta-1 has been studied by both electron diffraction and powder X-ray diffraction[8,9,10]. The crystals used for characterisation were rod-like in shape and were approximately 0.1μm in diameter and 2μm in length. The Si/Al ratio of the theta-1 zeolite was 30 (atomic) and characterisation was performed on the hydrogen form.

Selected area electron diffraction patterns indicate orthorhombic symmetry and reveal unit cell parameters with a short c-axis repeat unit of about 5 Å which is significant in zeolites. Systematic absences in the X-ray diffraction data are consistent with the three possible space groups Cmcm, C2cm, and $Cmc2_1$. Indexing the X-ray powder diffraction pattern on the basis of a c-centered orthohombic unit cell leads to the unit cell dimensions a = 13.836±0.003, b = 17.415±0.004, c = 5.042±0.001 Å, while full-matrix least-squares refinement of one trial structure successfully converged for the space group $Cmc2_1$. A framework density of 20.5 tetrahedral (T) atoms per 1,000 $Å^3$ was calculated from the crystal density of 2.05 gcm^{-3} measured by mesitylene displacement. This corresponds to 24.9T-atoms per unit cell in good agreement with a minimum site multiplicity of 24-T atoms per unit cell for each of the above three space groups.

The framework is made up of five-, six-, and ten-membered rings of TO_4 tetrahedra and can be constructed from complex

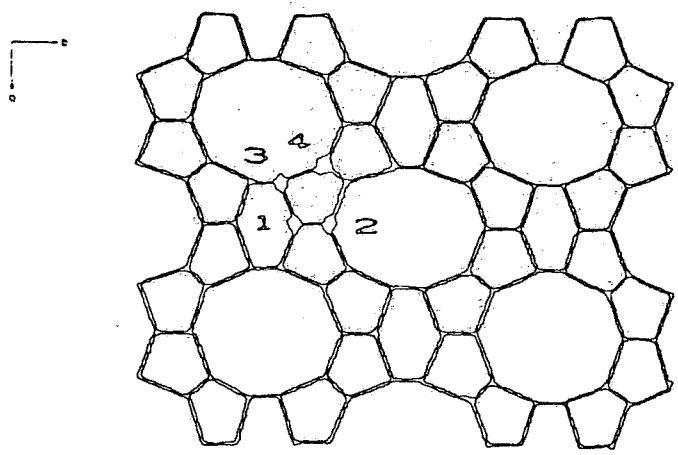

Figure 4.2(a): Projection of theta-1 in the |001| direction.

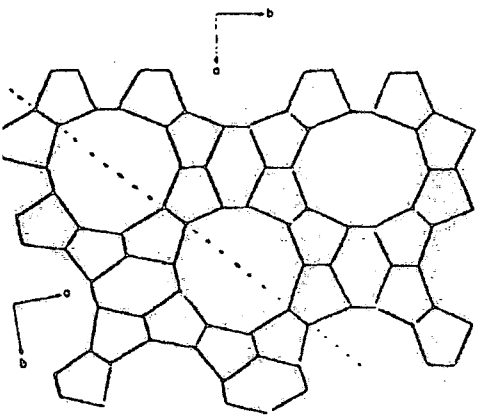

Figure 4.2(b): Twinning of high-silica theta-1 with |110| as the twin plane (projection along |001|).

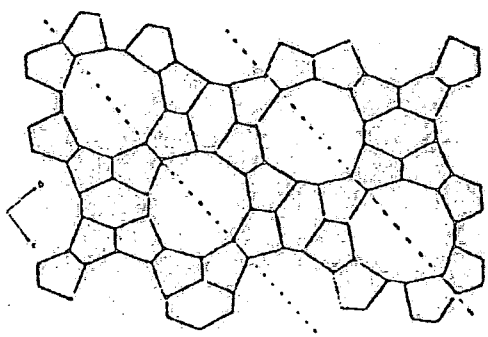

Figure 4.2(c): Projection of ZSM-23 along |001|.

(adapted from reference 14)

5-1T secondary building units. This places the structure of theta-1 in the mordenite group of materials which includes the zeolites mordenite, ferrierite, dachiardite, epistalbite and bikitaite (ZSM-5 and ZSM-11). A projection of the structure along the c-axis (|001|) is shown in Figure 4.2(a). Edge-sharing five-membered rings of TO_4 tetrahedra form zig-zag chains in the a-direction (|100|) giving a repeat distance of 13.8 Å. The zig-zag chains are linked *via* common oxygen atoms in the b-(|010|-) and c-directions by the remaining free corners of the TO_4 tetrahedra. This kind of linkage gives rise to 10-T ring channels along the c-direction, and the same structural feature is found in ferrierite, ZSM-5 and ZSM-11, although with different lattice parameters and specific topologies. The b-c projection of theta-1 is very similar to the a-b projection in bikitaite which consists of interlinking 6-T rings giving an approximate 5 Å repeat distance. Thus, like bikitaite, the topology has a unidimensional channel system. The framework structure of theta-1 is indistinguishable from those of ZSM-22, KZ-2, ISI-1 and NU-10 whose structures have been derived from X-ray powder diffraction data[11]. The framework of theta-1 is also closely related to the frameworks of the high-silica zeolites ZSM-23 and ZSM-48. These zeolites may be constucted from similar chains to form one-dimensional channel systems with 10-T ring channels[12,13].

The crystal morphology and size depends critically on the synthesis conditions[11]. Single-crystals of silica theta-1 may be synthesised using a diethylamine template (∿45 μm in diameter and ∿225 μm in length) under static synthesis conditions. Single crystal X-ray diffraction studies of

silica theta-1 containing the diethylamine template confirm that theta-1 crystallises in the space group $Cmc2_1$, attempts to refine the structure in the space groups Cmcm and C2cm failing[14]. The elliptical 10-T channels were shown to have free diameters of 4.7 and 5.5 Å (calculated assuming an oxygen radius 1.4 Å), which compares with the significantly larger 10-T ring channels of ZSM-5 (5.3 x 5.5 and 5.4 x 5.6 Å).

4.3.1 Twinning

Twinning of silica theta-1 has been observed with |110| as the twin plane[14]. This results in another type of 10-T channel with similar free diameters as the 10-T channel of untwinned silica theta-1 (Figure 4.2(b)). Twinning is believed to cause only slight distortions of the Si-O band lengths and O-Si-O bond angles and consequently, the difference in binding energies between the twinned and untwinned structure is probably very small and as such twinning should occur frequently. Periodical twinning on the |110| plane in distances of (a+b)/2 leads to ZSM-23[12] (Figure 4.2(c)).

4.3.2 Position of the organic template in theta-1

The 10-T channels of as-synthesised silica theta-1 are occupied by the diethylamine template molecules. Free diethylamine molecules may be described as zig-zag chains of carbon and nitrogen atoms with C-C-N and C-N-C bond angles of approximately 109.5°, there being free rotation along the C-C or C-N bond[14]. However, the diethylamine molecule only fits into the channel in a protracted conformation without distortion of the C-C-N or C-N-C bond angles.

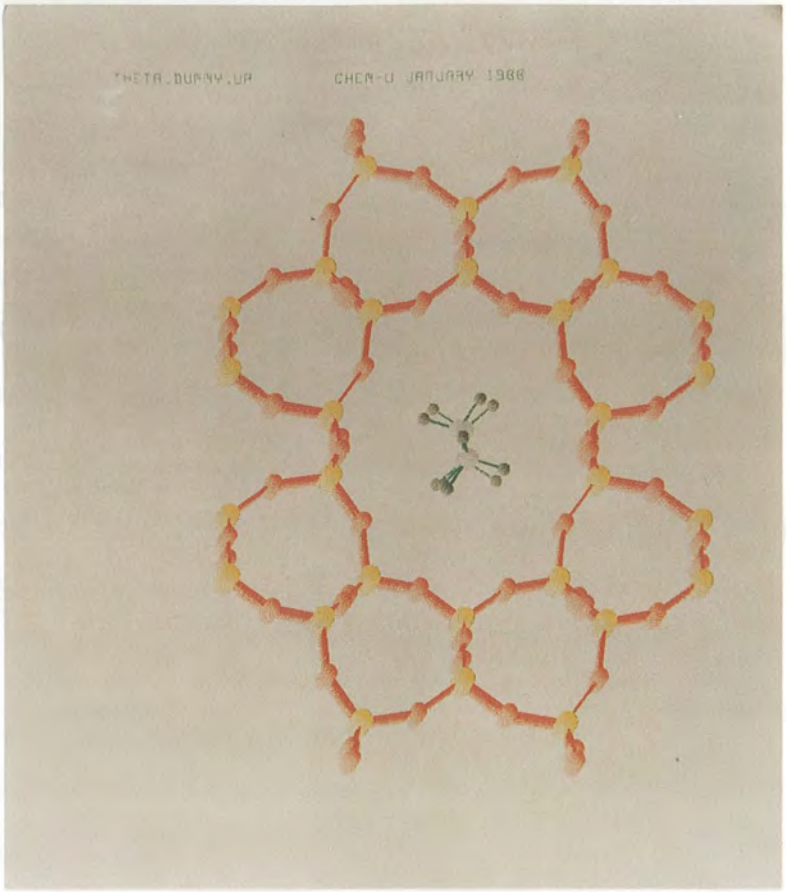

Figure 4.3: Projection of theta-1 in the [001] direction showing the diethylamine template in its lowest energy conformation.

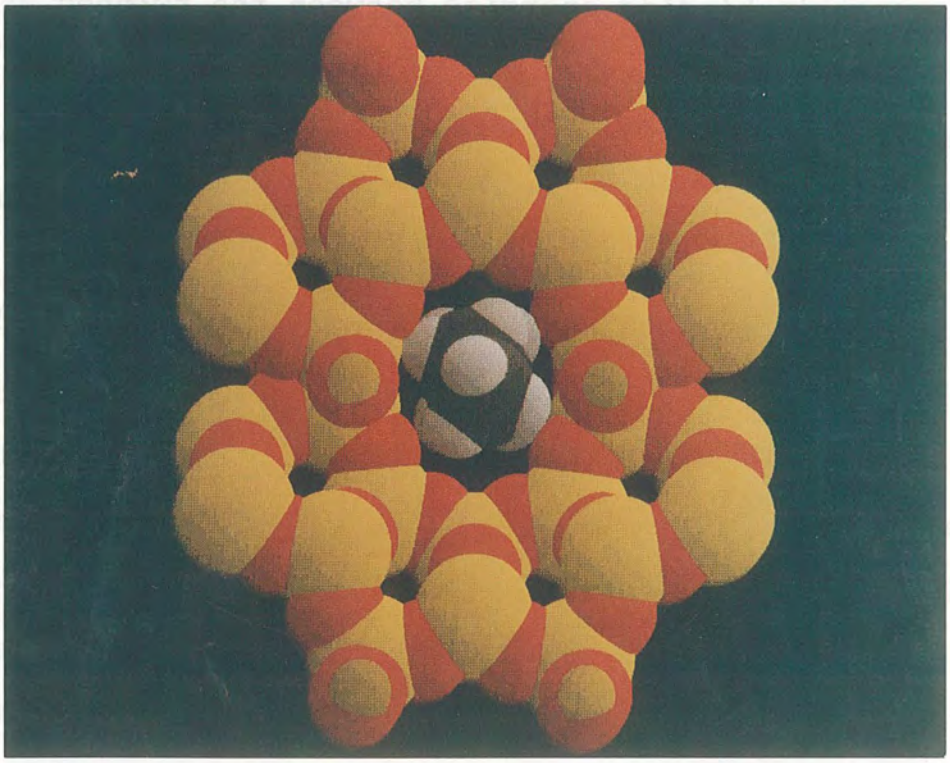

Figure 4.4: Inclusion of the van der Waals radii in Figure 4.3 to reveal significant filling of the channel void by the organic species.

The framework of theta-1 along the c-axis, complete with the diethylamine template in its lowest energy conformation is shown in Figure 4.3. Figure 4.3 is deceptive in the sense that the template would be expected to be very mobile. Inclusion of the van der Waals radii (Figure 4.4) suggests that the channel is filled almost completely by the organic species, and, given the close packing of the template molecules, axial rotation of the molecule about its long axis is the most feasible mode of motion (Table 4.2).

TABLE 4.2 Size of the diethylamine template molecule and the free diameters of the 10-T channel for the high-silica zeolite theta-1[14]

	d_1/Å	d_2/Å	d_3/Å
High-silica theta-1	5.5	4.7	∞
Diethylamine	4.6	4.2	9.1

During structure refinement of as-synthesised silica theta-1, the carbon and nitrogen atoms were located on the mirror planes parallel to |100|, whereas no distinct position in z was expected for these atoms since there was no preferred position of the chain in respect of the |001| channel direction[14]. Slight displacement of atom positions parallel to the |010| axis is possible. However, it was not possible to refine the diethylamine molecule orientation with correct molecular geometries suggesting that the diethylamine molecules in the channel are highly disordered[14]. For structure refinement, the diethylamine molecules were simulated

by C-atoms as scatterers in fixed positions obtained as highest maxima from the difference Fourier map. High temperature factors were used to simulate disorder of the guest molecules. Refinement of occupation factors led to 5.1 carbon atoms per unit cell, in good agreement with density data, which suggests the presence of one template molecule per unit cell. This is in excellent agreement with the short repeat distance in the c-direction.

Given the similarity in diameters of diethylamine and diethanolamine in a protracted conformation, the above results are expected to be applicable to as-synthesised samples of theta-1 prepared with a higher aluminium content and a diethanolamine template. There may, however, be subtle differences in the unit cell parameters given that diethanolamine can interact more strongly with the zeolite framework *via* hydrogen bonding.

It is important to note that the 6-T rings are accessible to small molecules only, such as water and ammonia (but not ammonium ions)[15]. Thus, active sites present in the 6-T channels would be expected to contribute less to the catalytic activity of the zeolite as a consequence of their greater distance from the 10-T channels.

4.3.3 Structural characterisation of theta-1 by ^{29}Si MASNMR

The single-pulse ^{29}Si MASNMR spectrum of a zeolite framework is capable of giving relative populations of chemically distinct species as well as structural information on the immediate neighbourhood of a silicon atom. For

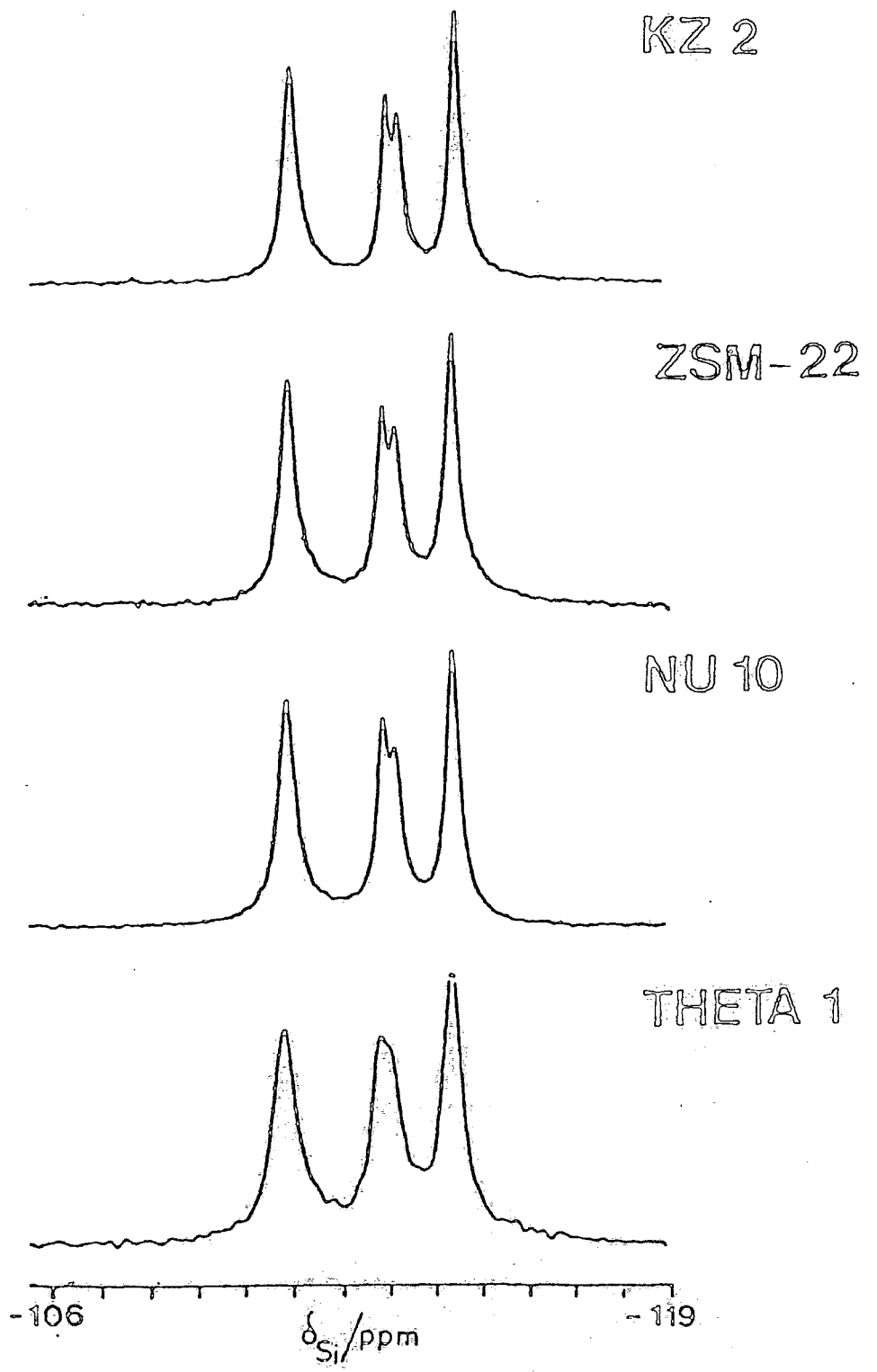

Figure 4.5: Ultra-high resolution ^{29}Si SP MASNMR spectra of theta-1, NU-10, ZSM-22, and KZ-2.

(adapted from reference 23)

high-silica zeolites, although there is only one chemical environment ($Si(OSi)_4$), the spectrum reveals details on the crystallographically distinct tetrahedral species.

Since the NMR shift reflects the local magnetic environment of a nucleus, it can often be related to parameters reflecting the local geometry of the atom in question. The ^{29}Si chemical shift is sensitive to structural features and correlations between <Si-O-Si> bond angles (and Si-O bond lengths) and δSi have been derived based on entirely siliceous systems[16,17,18,19,20,21,22].

The single-pulse ^{29}Si MASNMR spectrum of a highly dealuminated sample of theta-1 is shown in Figure 4.5. The spectra of almost completely siliceous samples of KZ-2, ZSM-22 and NU-10 are also shown[23]. Good samples of theta-1 show three resonances of equal intensity but in the very best samples, the central resonance is clearly resolved into two signals, with the overall intensities being in the ratio 2:1:1:2. These results are in excellent agreement with the X-ray diffraction data that was described above where a space group $Cmc2_1$ containing four sites of relative intensities 8:4:4:8 was found. The four crystallographically distinct sites are indicated in Figure 4.2(a); sites 3, 1, 2, 4 are in the statistical ratio 8:4:4:8. The two four-occupied sites are topologically very similar and are expected to have very similar chemical shifts. The environments of each crystallographically distinct site in terms of bond angles of nearest neighbours are shown in Figure 4.6[14]. The various crystallographic sites were assigned to specific NMR resonances using the correlation between T-O-T bond angle and δSi based on the formula $\delta = -25.44 - 0.579\theta$, where θ is the mean Si-O-Si bond

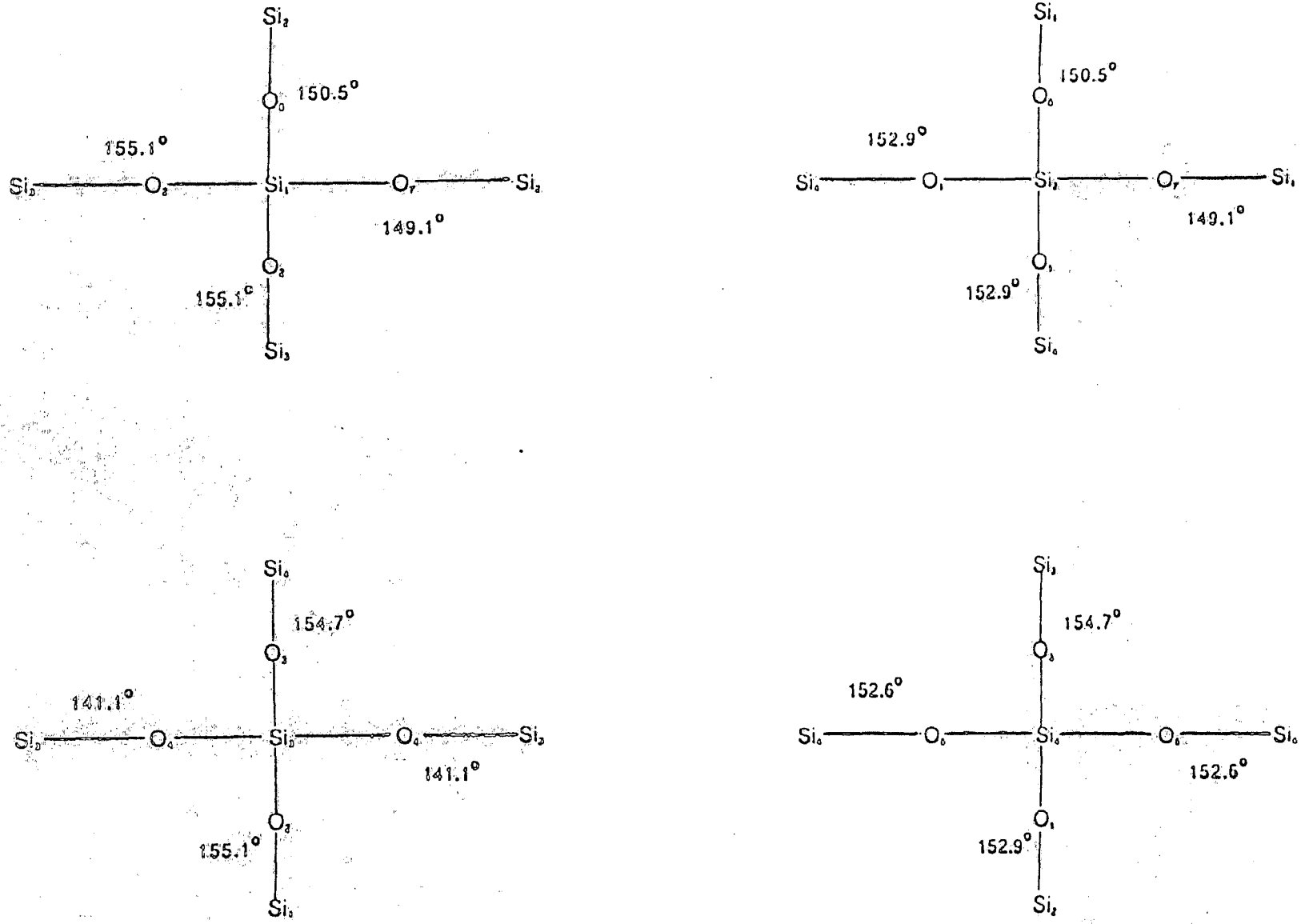

Figure 4.6: Local environments of the crystallographic sites in theta-1 in terms of Si-O-Si bond angles.

angle at a particular crystallographic site[17]. The relevant parameters are compiled in Table 4.3.

TABLE 4.3 Compilation of NMR and X-ray diffraction data for the zeolite theta-1

Site	I	<Si-O-Si>/°	δ/ppm
3	8	148.0	-110.8(7)
2	4	151.4	-112.8(2)
1	4	152.5	-113.0(7)
4	8	153.2	-114.3(3)

The assignment of the crystallographic sites to specific chemical shifts is only tentative. X-ray diffraction analysis for a sample with a higher aluminium content has indicated that sites 2 and 1 are more topologically equivalent than is suggested by the data above[9].

The above formula was obtained by fitting the plot of isotropic $Si(OSi)_4$ ^{29}Si chemical shift against mean T-O-T bond angle to a straight line for a range of zeolites. For the present case of silica theta-1, the data shown in Table 4.3 may be fitted to the formula $\delta = -25.10 - 0.6392\theta$ (correlation coefficient = - 0.97). The bond angle data was obtained from single-crystal studies performed on an as-synthesised sample, whereas the chemical shift performed was obtained for a calcined sample. Discrepancies could conceivably result from slight differences in the unit cell parameters of the calcined and as-synthesised forms.

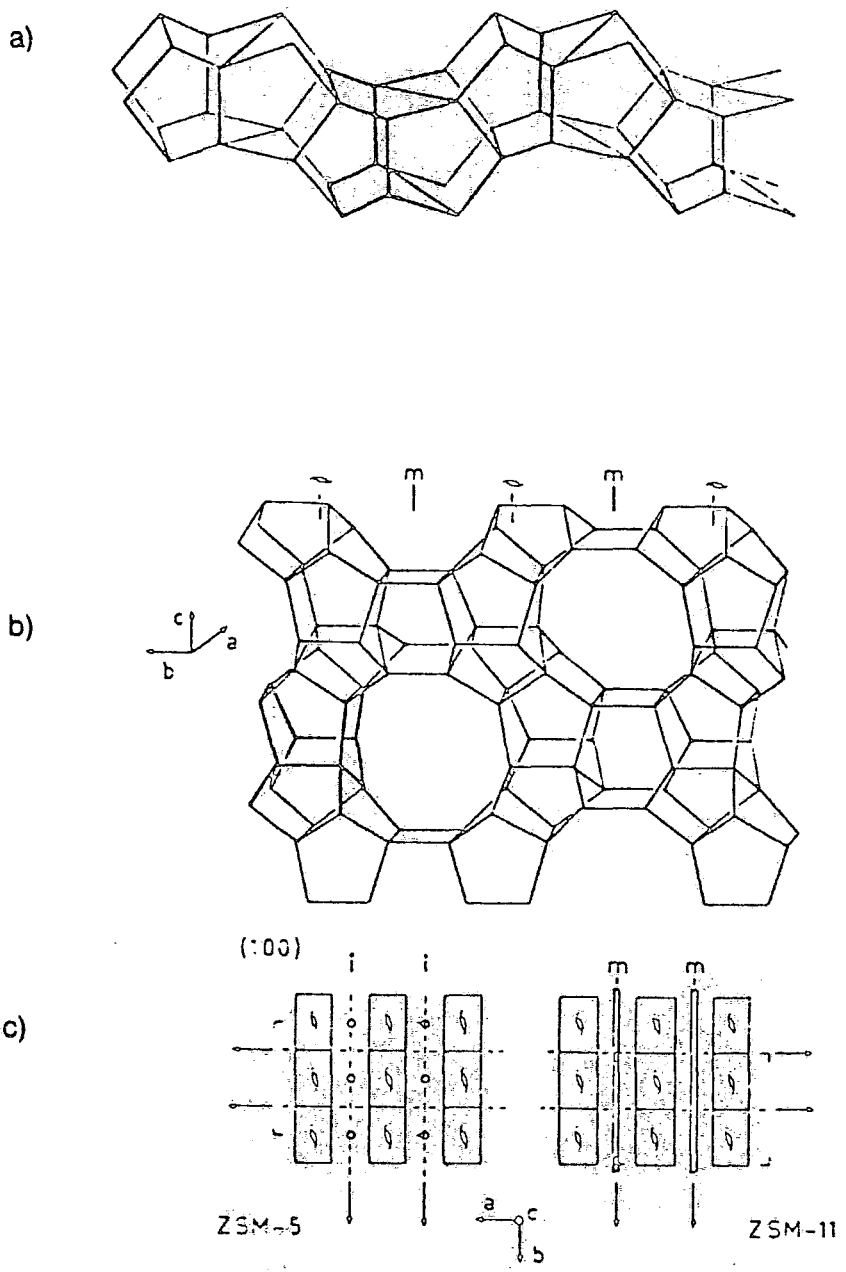

Figure 4.7: a) Position of the SBU (heavily outlined) in a chain of the zeolite framework.
b) |100| slab. The two-fold screw axis and the mirror planes are indicted.
c) Connection of the |100| sheets. ZSM-5 is produced by inversion and ZSM-11 by reflection.

(after reference 24)

4.4 Structure of ZSM-5

The structure of ZSM-5 may be constructed from the same 5-1T SBUs that were used to generate the structure of theta-1 and may be described as follows[24]. In fact, two such units are required to generate the structure of ZSM-5 by simple symmetry operations only. Therefore, it is more correct to consider the double 5-1T unit the real secondary building unit of ZSM-5. This secondary building unit is heavily outlined in Figure 4.7(a). By applying a two-fold screw axis to this SBU, a chain is formed in the direction of the c-axis, see Figure 4.7(b). Other chains are generated by mirror operations in planes parallel to the a-axis and perpendicular to the b-axis. This results in the formation of a |100| slab. The openings in the |100| sheet show the entrances to sinusoidal channels which run parallel to the a-axis, the opening being formed by 10 TO_4 tetrahedra. Finally, the ZSM-5 framework is constructed by interconnection of |100| sheets which are obtained by an inversion symmetry operation of chains into chains of an opposite sheet[25] (Figure 4.7(c)). Two types of channel are present in the ZSM-5 framework: sinusoidal channels which run parallel to the a-axis and straight channels parallel to the b-axis.

A related zeolite, ZSM-11, may be formed by a second mirror operation applied to the |100| sheet (Figure 4.7(c)). In ZSM-11, the two interconnected channels which run parallel to the a- and b-axis are straight. Additional crystallographic information concerning ZSM-5 is compiled in Table 4.4

TABLE 4.4 Crystallographic data for ZSM-5[26]

Channels:	The channel parallel to |010| (aperture 5.4 x 5.6 Å) is interconnected with channels parallel to |100| (aperture 5.1 x 5.5 Å).
Unit cell composition:	$(Na^+, TPA^+)_{25}\ [Si_{71}Al_{25}O_{192}] \cdot xH_2O$
Space group:	Pnma (orthorhombic) a=20.10, b=19.96 and c = 13.41 Å ($P2_{1/n}$ (monoclinic) a = 20.17, b = 19.93 and c = 13.42 Å has been reported for the high-silica form[27]).

The structure described above and the crystallographic information in Table 4.4 were obtained[26] by X-ray diffraction studies of a single crystal of tetrapropylammonium ZSM-5 zeolite (0.05 x 0.07 x 0.20 mm crystal) with an atomic Si/Al ratio of 25. Particularly significant is the observation of an orthorhombic space group Pnma which implies the existence of 12 crystallographically distinct sites. This contrasts with the X-ray diffraction data for calcined silicalite, the pure silica form of ZSM-5[27]. For calcined silicalite, the data are compatible with a space group which requires 24-non equivalent silicon sites in the repeat unit of the structure and signify that the space group $P2_{1/n}$ (monoclinic symmetry) is more appropriate than Pnma. The X-ray diffraction pattern of silicalite shows doublet peaks for 2θ values of 24.4, 29.2 and 48.6°. Wu *et al*[27] simulated peak splitting by the introduction of monoclinic lattice parameters a = 20.17, b = 19.93 and c = 13.42 Å. Thus, it would seem that there are two X-ray crystallographically distinct phases of ZSM-5 zeolites.

The orthorhombic to monoclinic symmetry change has been observed on various treatments of as-synthesised ZSM-5 such as calcination, ion exchange, decationation and dealumination[28,29]. High-silica H-ZSM-5 zeolites and calcined silicalite usually give X-ray diffraction patterns indicative of monoclinic symmetry. X-ray diffraction studies have indicated a monoclinic to orthorhombic symmetry change after either raising the temperature of high-silica ZSM-5 or on loading with various sorbates[27,30,31]. The precise conditions of the symmetry changes depend critically on the aluminium content and the presence of non-framework organic or inorganic material[27,32].

Two different framework topologies of ZSM-5 are not implied by the apparent observation of orthorhombic and monoclinic symmetry forms. The framework topology of samples displaying monoclinic X-ray diffraction patterns is the same as those exhibiting orthorhombic patterns[27]. The transformation between the two symmetries results from minor displacements of atomic positions within the zeolite framework which are usually highly reversible. The orthorhombic to monoclinic symmetry change involves small changes in the unit cell shape and removes symmetry elements such as the mirror planes that are parallel to |010| and bisect the sinusoidal channels, thus resulting in a lowering of the symmetry[27]. The symmetry transition does not essentially alter either the size and shape of the channel openings or the bend angle of the sinusoidal channel of the ZSM-5 framework. The general conclusion from X-ray diffraction studies is that there are only very small structural differences between the topologically equivalent orthorhombic and monoclinic forms of the ZSM-5 framework.

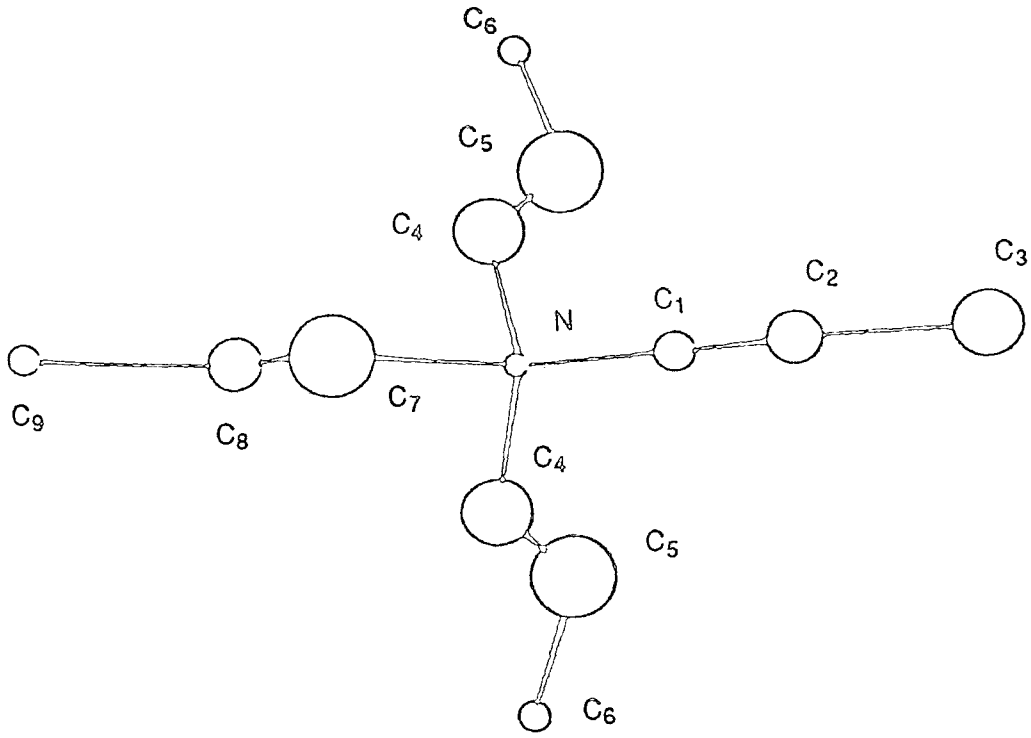

gure 4.8(a): Conformation of TPA$^+$ in ZSM-5, 30% in thermal parameters.

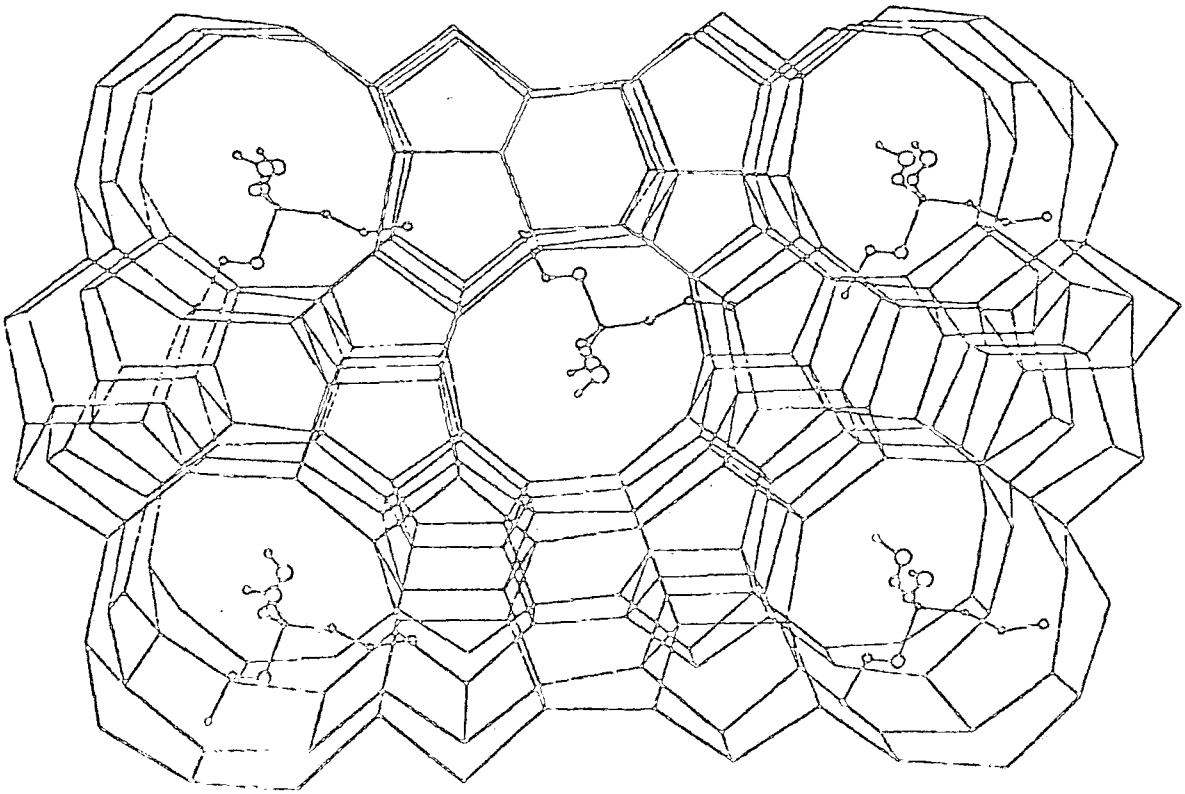

gure 4.8(b): Projection of ZSM-5 in the [100] direction, 10% in thermal parameters.

(after reference 36)

4.4.1 Position of the organic template in ZSM-5

Single crystal structure refinement of ZSM-5 containing the tetrapropylammonium (TPA^+) ion has been performed without any constraint on the atoms[26]. Different levels of refinement and difference Fourier maps revealed that the TPA^+ ion was located in the channel intersections. The thermal parameters of the atoms in the organic cation are much larger than those of the framework atoms suggesting incomplete occupancy of the organic cation in the four channel intersections. The conformation of the organic cation in zeolite ZSM-5 is shown in Figure 4.8(a) and is different from that found in TPA^+Br^- [26,33,34]. The TPA^+ ion contains a mirror plane symmetry with the $N(C_3H_7)_2$ part on the mirror plane at $y=1/4$ and $3/4$ and one C_3H_7 part off the plane. This generates the other propyl group by the mirror plane. The bond angles and bond distances of the TPA^+ ion were not as expected for tetrahedral carbon atoms and the thermal parameters of the atoms in TPA^+ are so large that not much accuracy can be claimed on the individual C-C bond distances and the C-C-C angles. This is similar to the situation observed in as-synthesised silica theta-1 where a similar observation was attributed to disorder of the template molecules[14]. However, including the TPA^+ ion did make a significant improvement in the refinement procedure which at least confirms the presence of the template. The rather large C-C-C angles may be attributed to the "two legs" of the TPA^+ ion stretched into the channels of the framework around the nitrogen atom (Figure 4.8(b)). The symmetry of the TPA^+ ion is roughly C_{2v} (C_s to be exact) rather than C_4 as found in the solid TPA^+Br^- crystal[33].

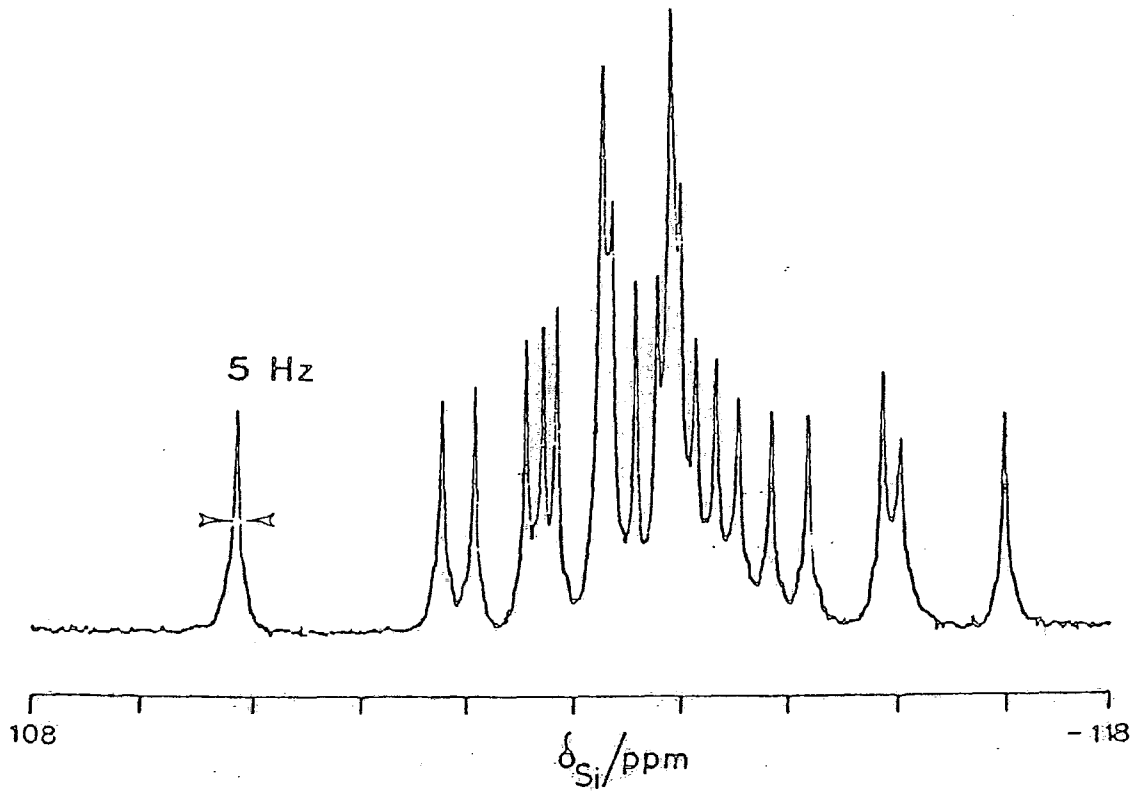

Figure 4.9: Ultra-high resolution ^{29}Si SP MASNMR spectrum of ZSM-5.

(after reference 35)

The situation is expected to be very different when diethanolamine is the template. Consideration of the data in Table 4.4 suggests that diethanolamine is accessible to both the sinusoidal and straight 10-T channels. Given the larger 10-T channel dimensions relative to theta-1, the diethanolamine template is expected to be more mobile in the ZSM-5 framework, particularly in the region of the channel intersections which are absent in theta-1. However, no attempt has yet been made to locate the position of the diethanolamine template molecules in ZSM-5 by X-ray diffraction techniques.

4.4.2 Structural characterisation of ZSM-5 by ^{29}Si MASNMR

The combination of X-ray diffraction data with the ultra-high resolution ^{29}Si MASNMR spectrum of a highly siliceous calcined sample of ZSM-5 allows a more complete description of the zeolite structure than could previously be given. Figure 4.9 shows the ^{29}Si MASNMR spectrum of a highly siliceous sample of ZSM-5 obtained using the spectral resolution improvement methods of Fyfe[35]. In all, 21 signals are observed, which may be unambiguously curve resolved to show 24 resonances confirming that the unit cell contains 24 crystallographically distinct silicon atoms. The result is compatible with the space group $P2_{1/n}$ proposed from X-ray diffraction data, rather than the space group Pnma.

Comparison of the relative intensity of the resonance at -115 to -117 ppm, even in poorly resolved ^{29}Si NMR spectra, may be used to observe the change from orthorhombic to monoclinic symmetry observed in X-ray diffraction studies[28,29].

The ratio of the intensity of the -115 to -117 ppm resonances to those of the -110 to -115 ppm resonances varies from 0.13 to 0.18 for samples with monoclinic symmetry and from 0.30 to 0.45 for those with orthorhombic symmetry. These suggestions by Debras *et al* have led to the conclusion from ^{29}Si NMR spectra that thermal treatment leads to a orthorhombic-monoclinic transformation for ZSM-5 samples with high Si/Al ratios, whereas retention of the orthorhombic form is observed for low Si/Al ratios[29].

Mean Si-O-Si bond angles may be calculated for the crystallographically distinct sites indicated by the resonances in the ultra-high resolution ^{29}Si NMR spectrum of the silica form of ZSM-5 using the quantitative relationship[36] between ^{29}Si chemical shifts and <Si-O-Si> referred to earlier. The relevant data obtained from a spectrum of highly siliceous ZSM-5 are shown in Table 4.5[1].

TABLE 4.5 Calculation of <Si-O-Si> data from NMR data for highly dealuminated ZSM-5 zeolite using the formula $\delta = -25.44-0.57930$

δ/ppm	I	<Si-O-Si>/^{o}	δ/ppm	I	<Si-O-Si>/^{o}
-109.8	1	145.6	-113.7	1	152.4
-111.7	1	148.9	-113.9	5	152.7
-112.0	1	149.4	-114.3	1	153.4
-112.5	1	150.3	-114.5	1	153.7
-112.7	1	150.6	-114.8	1	154.3
-112.8	1	150.8	-115.1	1	154.8
-113.4	3	151.8	-115.9	2	156.2
-113.5	2	152.0	-117.0	1	158.1

The mean Si-O-Si angles calculated cover the range between 146 and 159° which compares with the range 150-164° determined for the 12 crystallographically distinct silicon sites of the orthorhombic space group Pnma by single crystal X-ray refinement of Na_nTPA-ZSM-5[37] (atomic Si/Al ratio = 12), if allowance is made for small changes in the atomic positions in dealuminated H-ZSM-5 with monoclinic symmetry[27]. A reliable assignment of individual ^{29}Si NMR resonances to crystallographically inequivalent sites in high-silica ZSM-5 in the monoclinic space group $P2_{1/n}$ may not be made yet because no detailed crystal structure determination has been carried out so far.

The sorption of organic molecules such as alkanols, decane, benzene, p-xylene, pyridine and acetylacetone results in a significant change in the highly-resolved ^{29}Si NMR spectra of silicalite and highly dealuminated ZSM-5[30,35,38]. Sorbate loading apparently causes displacements of atomic positions within the ZSM-5 framework which is interesting in view of the X-ray diffraction results discussed above. The number, position and intensities of the peaks resolved in the spectra of highly siliceous samples of ZSM-5 loaded with the organic species referred to above are significantly different from those of the sorbate-free samples and are characteristic of the kind of sorbate used. Very low loadings of sorbate molecules are sufficient to induce spectral changes that are fully reversible. The observation of sorbed molecules causing structural modification of the ZSM-5 framework is confirmed by changes in the corresponding X-ray diffraction patterns which indicate a transition from monoclinic to orthorhombic

symmetry and changes in the unit cell dimensions of the sorbate-loaded samples[35].

Similar changes to those outlined above in the ^{29}Si NMR spectrum on sorbate loading have been found when the spectra of calcined high-silica ZSM-5 was measured at different temperatures[35,39,40]. The observed changes are believed to be due to a phase transition from the monoclinic to the orthorhombic form on raising the temperature. Corresponding changes in the powder X-ray diffraction patterns occur over a considerably lower and narrower temperature range[40]. X-ray diffraction studies of the same sample as studied by ^{29}Si NMR revealed orthorhombic symmetry at 333 K and remained essentially unaltered up to 353 K, whereas the ^{29}Si NMR spectra continued to change dramatically in this temperature range[39]. It would seem that ^{29}Si NMR is more sensitive to subtle changes in the framework structure. It is important to realise that there are an infinite number of ways of arranging the framework atoms of ZSM-5 whilst retaining an orthorhombic/monoclinic symmetry and it is probable that the ^{29}Si NMR spectra indicate that the structural changes are not confined to the monoclinic-orthorhombic symmetry transition and proceed over wider ranges of temperature and sorbate loadings than in the XRD patterns. Fyfe *et al* have observed a decrease in the temperature of the monoclinic-orthorhombic phase transition as the concentration of p-xylene is increased[35]. It is possible that adsorbed organics symmetrise the system by increasing the total entropy and thus lowering the temperature at which a lower symmetry isomorph is transformed into a higher symmetry one[41]. Framework aluminium plays the same role as the adsorbed organics -

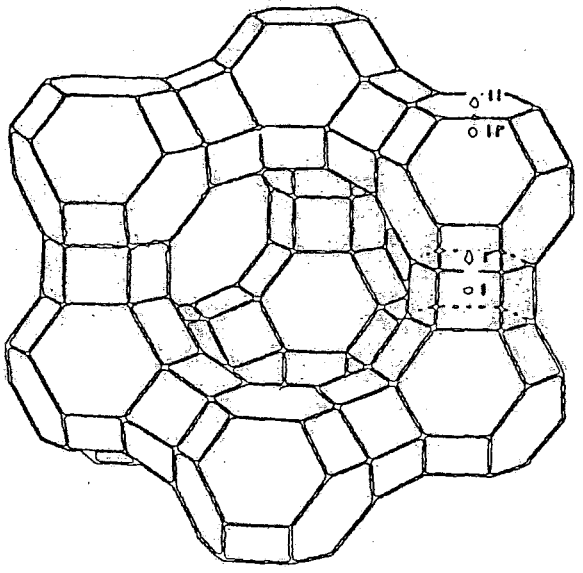

Figure 4.10: Framework structure of zeolite Y. The sites occupied by small guest molecules and the sodium ions are indicated.

(adapted from reference 45)

the temperature at which the monoclinic/orthorhombic transition occurs is primarily controlled by the level of framework aluminium in ZSM-5. Hay and Jaeger found by X-ray diffraction that for samples with Si/Al > 220, the transition occurs at 317-325 K, for Si/Al = 99 at 295 K and for Si/Al<55, below 272 K[39].

4.5 Structure of Zeolite Y

From powder X-ray diffraction studies, zeolite Y has been shown to have the same structure as the naturally occurring mineral faujasite. The unit cell of faujasite contains 192 crystallographically equivalent T-sites, which may be alternatively occupied by Si or Al atoms. Faujasite-type zeolites are available over a wide range of compositions characterised by Si/Al ratios from unity up to very large values approaching infinity. By convention, synthetic faujasite with Si/Al ratios from 1 to 1.5 are termed 'zeolite X' and those with Si/Al ratios above 1.5 'zeolite Y'.

The framework structure of faujasite -type zeolites is shown in Figure 4.10. It may be considered to consist of sodalite cages built up of 24 (Si,Al) atoms interconnected with 36 oxygen atoms[42]. The oxygen atoms form six octahedrally positioned rings containing 4 oxygen atoms and one set of cubically positioned 6-element rings of oxygen atoms. The sodalite unit is found to be distorted from octahedral to tetrahedral symmetry by partial rotations of the tetrahedra.

The sodalite units are placed in tetrahedral co-ordination in the same manner as are the carbon atoms in the diamond

structure and are connected together at their 6-element rings by 6 bridge oxygens. This results in two independent, though interconnecting, 3-D networks of cavities. One network consists of large cavities, sometimes called super-cages, which have a diameter of about 13 Å. They are linked in the tetrahedral, diamond-type lattice by sharing rings of 12 tetrahedra. These rings have a free diameter of about 8 Å. The other network is formed by the linking of the smaller sodalite cages through adjoining rings of 6 tetrahedra, thus forming secondary cavities which are hexagonal prisms, between the sodalite cages. The space group of the resulting structure is Fd3m.

Chemical analysis of the sample used in the X-ray diffraction characterisation suggests that the composition is $Na_2O \cdot Al_2O_3 \cdot 2.8SiO_2 \cdot XH_2O$. For a Si/Al ratio of 1.4, 80 sodium cations are required per unit cell. Fourier analysis located only 48 of these. The most significant problem encountered in using X-ray diffraction for this purpose is that only the stationary cations can be located. Since some of the cations in zeolites are very mobile, especially in the presence of water, often fewer than 50% of the cations can be located for hydrated samples by X-ray diffraction techniques. However, nearly 100% of the cations can be located if the sample is dehydrated to reduce cation mobility, although the dehydration step may itself alter the distribution of cations.

The work of Mortier *et al*[43] and others has shown that there are cations located in the hexagonal prisms, in the sodalite cages and in the supercages of the faujasite structure.

The relevant sites are shown in Figure 4.10. Site 1 is in the centre of the hexagonal prisms, site 1' in the sodalite cage at the double six-ring, site II in the large cage at the single six-ring and site II' opposite II in the sodalite cage; site II' is only occupied by small molecules such as NH_3 and H_2O. Site 1 has a multiplicity of 16 per unit cell; the sites 1', II and II' have a multiplicity of 32. The adjacent sites I and I' are not simultaneously occupied.

I.R. methods have also been used to study cation locations in zeolites. Roessner *et al* have shown[44] by looking at the double-six-ring vibration band, that the cation locations depend on the exchange procedure and thermal treatment of the samples. However, only limited information was obtained for the cations in the supercage and the sodalite cage using I.R.

^{29}Si MASNMR studies of highly dealuminated zeolite Y samples indicate the presence of only one crystallographically distinct site in agreement with the X-ray diffraction data[45]. A <T-O-T> bond angle of 144.8^{o} has been measured[46] for a 53% dealuminated sample of zeolite Y which is reasonable agreement with the calculated value of 141.0^{o} calculated using the ^{29}Si Si(OAl) shift and the formula δ = -25.44-0.57930.

REFERENCES - CHAPTER FOUR

1. G. Engelhardt and D. Michel, "High Resolution Solid-State NMR of Silicates and Zeolites", J.Wiley and Sons, 1987.

2. W.M. Meier, in Proceedings of the 7th International Zeolite Conference (Tokyo, 1986), p.13, Elsevier, Amsterdam (1986).

3. W.M. Meier, in SCI Monograph on Molecular Sieves, p.10, Society of Chemical Industry, London (1968).

4. D.W. Breck, Zeolite Molecular Sieves: Structure, Chemistry and Use, Wiley, New York (1974).

5. R.M. Barrer, Hydrothermal Chemistry of Zeolites, Academic Press, London (1982).

6. R. Gramlich-Meier and W.M. Meier, J.Solid State Chem., 40, 41 (1982).

7. W.M. Meier and H.J. Moeck, J.Solid State Chem., 27, 349 (1979).

8. S.A.I. Barri, G.W. Smith, D. White and D. Young, Nature, 316, 533 (1984).

9. R.M. Highcock, G.W. Smith and D. Wood, Acta Cryst., C41, 1391 (1985).

10. A.G. Ashton, S.A.I. Barri and J. Dwyer, Proceedings of the International Symposium on Zeolite Catalysis, Siofok, Hungary, p.25,(1985).

11. R.A. le Febre, H.W. Kouwenhaven and H. van Bekkum, Zeolites, 8, 60 (1988).

12. A.C. Rohrmann, R.B. la Pierre, J.L. Schlenker, J.W. Wood, E.W. Valyocsik, M.K. Rubin, J.B. Higgins and W.J. Rohrbaugh, Zeolites, 5, 352 (1985).

13. J.L. Schlenker, W.J. Rohrbaugh, P. Chu, E.W. Valyocsik and G.T. Kokotailo, Zeolites, 5, 355 (1985).

14. B. Marler,Zeolites, 7, 393 (1987).

15. Private Communication, S.A.I. Barri.

16. J.V. Smith and C.S. Blackwell, Nature (London), 303, 223 (1983).

17. J.M. Thomas, J. Kennedy, S. Ramdas, B.R. Hunter and D.T.B. Tennakoon, Chem.Phys.Lett., 102, 158 (1983).

18. S. Ramdas and J. Klinowski, Nature (London), 308, 521 (1984).

19. G. Engelhardt and R. Radeglia, Chem.Phys.Lett, 108, 271 (1984).

20. R. Radegalia and G. Engelhardt, Chem.Phys.Lett., 114, 28 (1985).

21. A.-R. Grimmer and R. Radeglia, Chem.Phys.Lett., 106, 263 (1984).

22. A.-R. Grimmer, Chem.Phys.Lett., 119, 416 (1985).

23. C.A. Fyfe, H. Strobl, G.T. Kokotailo, C.T. Pasztor, G.E. Barlow and S. Bradley, unpublished results.

24. D.H. Olson, G.T. Kokotailo, S.L. Lawton and W.H. Meier, J.Phys.Chem., 85, 2238 (1981).

25. G.T. Kokotailo and W.M. Meier, "The Properties and Applications of Zeolites", Special publication, Chemical Society, London, 33, 133 (1980).

26. K-J. Chao, J-C. Lin, Y. Wang and G.H.Lee, Zeolites, 6, 35 (1986).

27. E.L. Wu, S.L. Lawton, D.H. Olson, A.C. Rohrman and G.T. Kokotailo, J.Phys.Chem., 83, 2777 (1979).

28. G. Debras, A. Gourge, J.B. Nagy and G. De Clippeleir, Zeolites, 6, 161 (1986).

29. G. Debras, A. Gourge, J.B. Nagy and G. De Clippeleir, Zeolites, 6, 241 (1986).

30. C.A. Fyfe, G.J. Kennedy, C.T. de Schutter and G.T. Kokotailo, J.Chem.Soc.,Chem.Commun., 541, (1984).

31. L. Liu, W. Zhang, B. Lin, Q. Wer, Q. Yu and W. Zhu, Ranliao Huaxue Xuebao, 13, 106 (1985).

32. H. Nakamoto and H. Takahashi, Chem.Lett., 1013 (1981).

33. A. Zalkin, Acta. Crystallogr., 10, 557 (1957).

34. C. Baerlocher, 6th Int. Zeolite Conference, Reno, Nevada (1983).

35. C.A. Fyfe, H. Strobl, G.T. Kokotailo and G. Barlow, J.Am.Chem.Soc., 110, 3373 (1988).

36. E. Lippmaa, M. Mägi, A. Samoson, M. Tarmak and G. Engelhardt, J.Am.Chem.Soc., 103, 4992 (1981).

37. H. Lerner, M. Draeger, J. Steffen and K.K. Unger, Zeolites, 5, 131 (1985).

38. G.W. West, Aust.J.Chem., 37, 455 (1984).

39. D.G. Hay, H. Jaeger and G.W. West, J.Phys.Chem., 89, 1070 (1985).

40. C.A. Fyfe, G.J. Kennedy, G.T. Kokotailo, J.R. Lyeila, and W.W. Fleming, J.Chem.Soc., Chem.Commun., 740 (1985).

41. J. Klinowski, T. Adrian Carpenter and Lynn F. Gladden, Zeolites, 7, 73 (1987).

42. J. Broussard and D.P. Shoemaker, J.Am.Chem.Soc., 82, 1041 (1960).

43. W.J. Mortier, "Compilation of Extra-Framework Sites in Zeolites", Butterworths, 1982.

44. F. Roessner, K.H. Steinberg and H. Winkler, Zeolites, 7, 47 (1987).

45. J. Klinowski, J.M. Thomas, C.A. Fyfe, G.C. Gobbi and J.S. Hartman, Inorg.Chem., 22, 63 (1983).

46. P. Gallezot, R. Beaumont and D. Bouthomeuf, J.Phys.Chem., 78, 1550 (1974).

CHAPTER FIVE

NMR STUDIES OF HALF-INTEGER SPIN QUADRUPOLAR NUCLEI

5.1 Introduction

Previous results indicate that the r.f. response of a quadrupolar nucleus in a strong magnetic field depends on the transitions that are being excited[1]. The intensity of the spectrum of a quadrupolar nucleus with half-integer spin depends on both the pulse duration and the ratio ω_Q/ω_{rf} (ω_Q defined below and $\omega_{rf} = \gamma B_1$)[2]. For a system of isolated, half-integer spin, quadrupolar nuclei which experience no quadrupole splitting, the duration of the so-called $\pi/2$ pulse which generates maximum transverse magnetisation orthogonal to the rotating component of the magnetic field is $\pi/2\omega_{rf}$[3]. In this case, the whole spectrum is excited (non-selective excitation). If, however, the nuclei are situated in a single crystal and the quadrupole splitting is large, $\pi/2$ pulses can be applied whose amplitude is much smaller than the quadrupole splitting, and which therefore selectively excite individual resonances. In this case, the maximum transverse magnetisation is measured after an r.f. pulse with duration $\pi/2\omega_{eff}$[3], and the effective r.f. field strength is increased by the factor: $\omega_{eff}/\omega_{rf} = \sqrt{(I-m)(I+m+1)}$. Thus, if the central $m = \frac{1}{2} \leftrightarrow \frac{1}{2}$ resonance alone is excited, the duration of the $\pi/2$ pulse is $\pi/[2(I+\frac{1}{2})]$. On comparing the extreme cases of selective and non-selective excitation, it is found that the maximum intensity for selective excitation is lower than that for non-selective excitation by the factor[2]: $\sqrt{(I-m)(I+m+1)}$.

The intermediate region where the amplitude of the r.f. pulse is of the order of the quadrupole splitting is often encountered in practice, especially for polycrystalline samples.

The first part of the chapter describes the results of a density matrix calculation for the case where a single pulse

is applied to a system of $I = {}^{3}/_{2}$ nuclei which experience first-order quadrupole splitting. The analysis is general in the sense that it is valid for all ratios of the quadrupole splitting to the amplitude of the r.f. field, except when the satellites overlap with the central transition in the frequency domain. The differences between selective and non-selective excitation are clearly illustrated and the results are directly applicable to the problems concerning the quantitative investigations of half-integer spin quadrupolar nuclei which are discussed at length.

The realisation that differences between the energy levels may be detected by incrementally increasing the duration t_1 of the resonant r.f. irradiation pulse thus influencing all transitions of the quadrupolar nucleus under investigation, with observation of the following central transition free induction signal decay during t_2 leads to the concept of the 2D nutation experiment[4,5,6,7,8,9,10,11]. The results are presented for a wide range of model compounds and exploratory experiments involving magic angle spinning are also included.

The results of the first part of the chapter are then applied to the investigation of NH_4^+-ZSM-5 and NaY zeolites. Results in the literature have shown that for hydrated ZSM-5, the local symmetry about the aluminium is high and consequently, the quadrupole interaction is small[12]. On dehydration, the linewidth broadens due to a distortion of the AlO_4^- tetrahedra, the distortion depending on the counter ion present in the pores to achieve electric neutrality. The broadening of the aluminium resonance on dehydration of the zeolite is absent when the tetrapropylammonium cation is the counterbalancing

ion, whereas the linewidth doubles at an aluminium frequency of 78.2 MHz for H^+, and for Na^+, the aluminium resonance becomes too broad on dehydration to be detectable[12].

Dehydration studies of NH_4^+-ZSM-5 are presented, and evidence for motional effects in terms of variation in the ^{27}Al MASNMR first-order quadrupolar spinning sideband pattern and central transition shift as a function of temperature are discussed. In order to distinguish between motional effects and a possible phase transition, further evidence is sought by rotary-echo nutation experiments, T_1 values determined by a selective Dante pulse sequence, chemical shift correlation experiments, and variable spinning speed experiments applied to the aluminium nuclei. In addition, theoretical investigations of the effect of motion of the counterbalancing cations and surrounding water molecules on the spectrum of the aluminium nucleus are considered.

Finally, ^{23}Na NMR studies on a NaY zeolite sample are presented. The sample was initially investigated to characterise the sodium environments with a view to indirectly characterising the Brönsted acid sites, but the observation of a very broad resonance in addition to the expected narrow resonance was surprising. The system was further investigated by ^{23}Na variable temperature wideline experiments, nutation experiments and relaxation measurements.

5.2 Calculation of the response of an $I=^3/_2$ spin system to the application of a single r.f. pulse

The equation of motion of the spin density matrix in the interaction representation is given by the Liouville-von Neumann equation:

$$\frac{d\hat{\rho}^*_{ij}}{dt} = \frac{-i}{\hbar} [\hat{H}^*_1, \hat{\rho}^*]_{ij} \qquad (5.1)$$

The Hamiltonian in the interaction representation may be written as:

$$\hat{H}^*_1 = \hat{H}^*_Q + \hat{H}^*_{rf} + \hat{H}^*_D + \hat{H}^*_{CS} + \hat{H}^*_\Delta \qquad (5.2)$$

where $\hat{H}^*_Q, \hat{H}^*_{rf}, \hat{H}^*_D, \hat{H}^*_{CS}$ and $\hat{H}^*_\Delta$ represent the quadrupole interaction, the r.f. interaction, the dipolar interaction, and the chemical shift interaction respectively. If the amplitude of the r.f. field $\omega_{rf} = |\hat{H}^*_{rf}|$ is much larger than the dipolar interaction term $|\hat{H}^*_D|$, then the system under study may be confined to a single spin. A particularly simple Hamiltonian results if also $|\hat{H}^*_{CS}|$, $|\hat{H}^{*(2)}_Q| << |\hat{H}_{rf}|$ and the irradiaton frequency is resonant with the central transition ($\hat{H}_\Delta = 0$)[9]:

$$\hat{H}^*_1 = \omega_Q(3\hat{I}_Z - \hat{I}^2) - \omega_{rf}.\hat{I}_X \qquad (5.3)$$

A consequence of the quadrupole interaction being much smaller than the interaction of the spins with the external static field B_o is that instead of using the full quadrupole Hamiltonian, only the part of the quadrupole interaction which commutes with $\hat{I}_Z$ needs to be taken into account. In first-order, the time-dependent (non-secular terms) may be neglected.

In equation (5.3), $\omega_Q = \frac{e^2qQ}{8\hbar I(2I-1)}\{(3\cos^2\theta - 1) + \eta\sin^2\theta\cos 2\phi)\}$ where the symbols have their usual meanings (Chapter Two).

Thus during t_1, a resonant r.f. field is present and the system evolves in the rotating frame under the combined effect

of the r.f. field and the quadrupole interaction. This means that the eigenfunctions of $\hat{H}_1^*$ depend on the ratio ω_Q/ω_{rf}. During the detection period, t_2, there is no r.f. field present and the FID of the central transition is acquired (assuming that all other transitions are too broad to be detected). The system is now governed by the Hamiltonian $\hat{H}_2$ [9]:

$$\hat{H}_2 = \hat{H}_Z + \hat{H}_{CS} + \hat{H}_Q \qquad (5.4)$$

$\hat{H}_Q$ is the quadrupole interaction which only contributes in second-order to the lineshape of the central transition. With the knowledge of the above Hamiltonians, it is possible to calculate the signal $S(t_1, t_2)$ using density matrix formalism. Using $\hat{\rho}^*(o)$ to represent the equilibrium density matrix in the high temperature approximation at $t_1=0$, then by solution of the Liouville-von Neumann equation at time t_1 ($\hat{H}_1^*$ is time-independent) [7]:

$$\hat{\rho}(t_1) = \exp(-i\hat{H}_1 t_1/\hbar)\hat{\rho}(o)\exp(i\hat{H}_1 t_1/\hbar) \qquad (5.5)$$

(note that the * denoting the interaction representation has been dropped).

Now $\bar{T}^\dagger \exp(\hat{Q})\bar{T} = \bar{T}^\dagger(1 + \hat{Q} + \frac{\hat{Q}^2}{2!}.....)\bar{T}$

$$= \bar{T}^\dagger\bar{T} + \bar{T}^\dagger\hat{Q}\bar{T} + \bar{T}^\dagger\hat{Q}\bar{T}\bar{T}^\dagger\hat{Q}\bar{T} + \ldots$$

$$= \exp(\bar{T}^\dagger\hat{Q}\bar{T})$$

and equation (5.5) may be written as:

$$\hat{\rho}(t_1) = \bar{T}\exp(-i\bar{E}t_1/\hbar)\bar{T}^\dagger\hat{\rho}(o)\bar{T}\exp(i\bar{E}t_1/\hbar)\bar{T}^\dagger \qquad (5.6)$$

where the orthogonal transformation $\bar{T}$ has been used to diagonalise $\hat{H}_1$. The eigenvalues E_j of $\hat{H}_1$ are contained in the diagonal matrix $\bar{E}$:

$$\bar{E} = \bar{T}^\dagger\hat{H}_1\bar{T} \qquad (5.7)$$

$$E_j = \Sigma\Sigma T_{pj} \hat{H}_{1pq} T_{qj} \qquad (5.8)$$

As there is no explicit mixing time $\hat{\rho}(t_1,0) = \hat{\rho}(t_1)$, and if it is assumed that only the coherence between the $m=\frac{1}{2}$ and $m=-\frac{1}{2}$ states is detected then[7]:

$$S(t_1,t_2) = \{\hat{\rho}(t_1)\}_{\frac{1}{2},-\frac{1}{2}} \exp(-i\omega_2 t_2) \qquad (5.9)$$

where ω_2 is the $(\frac{1}{2},-\frac{1}{2})$ transition frequency.

$$\text{Now, } \{\hat{\rho}(t_1)\}_{\frac{1}{2},-\frac{1}{2}} = \Sigma_{ij} (R_{-\frac{1}{2},\frac{1}{2}})_{ij} \exp(-i\omega_{ij} t_1) \qquad (5.10)$$

where $\omega_{ij} = (E_i - E_j)/\hbar$ is the transition frequency in the rotating frame between the eigenstates $|i\rangle$ and $|j\rangle$ of $\hat{H}_1$.

$$(R_{-\frac{1}{2},\frac{1}{2}})_{ij} = T_{\frac{1}{2},i} T_{-\frac{1}{2},j} \sum_k T_{k,i} T_{k,j} \hat{\rho}(o)_{kk} \qquad (5.11)$$

represents the contribution of the coherence between $|i\rangle$ and $|j\rangle$ in the rotating frame during t_1 to the $|\frac{1}{2}\rangle$, $|-\frac{1}{2}\rangle$ coherence detected during t_2. The $(R_{-\frac{1}{2},\frac{1}{2}})_{ij}$ terms may be considered as mixing factors which determine the efficiency of mixing of the original eigenfunctions into eigenfunctions of (5.3). The frequencies ω_{ij} are the nutation frequencies and $(R_{-\frac{1}{2},\frac{1}{2}})_{ij}$ their amplitudes. The nutation frequencies are functions of ω_{rf} and ω_Q, and because ω_Q is orientation-dependent, the nutation frequencies are also orientation-dependent.

For a spin-$^3/_2$ nucleus, an analytical solution for the spectral intensity of the central transition as a function of pulse duration for a given ratio of ω_Q/ω_{rf} may be found. The rotating frame Hamiltonian (5.3) for an $I=^3/_2$ spin may be diagonalised by the orthogonal transformation $\bar{T}$ [13]:

$$\bar{T} = \frac{1}{\sqrt{2}} \begin{pmatrix} \cos\theta_- & -\sin\theta_- & -\sin\theta_+ & \cos\theta_+ \\ \sin\theta_- & \cos\theta_- & \cos\theta_+ & \sin\theta_+ \\ \sin\theta_- & \cos\theta_- & -\cos\theta_+ & -\sin\theta_+ \\ \cos\theta_+ & -\sin\theta_- & \sin\theta_+ & -\cos\theta_+ \end{pmatrix} \qquad (5.12)$$

where $\tan 2\theta\pm = (\sqrt{3}/2)\omega_{rf}/(\omega_Q \pm \omega_{rf}/2)$ (5.12(a))

The corresponding eigenvalues of $\frac{\hat{H}_1}{\hbar}$, the rotating frame energy states are[13]:

$$\begin{aligned} E_1 &= \omega_{rf}/2 + D_- \\ E_2 &= \omega_{rf}/2 - D_- \\ E_3 &= -\omega_{rf}/2 - D_+ \\ E_4 &= -\omega_{rf}/2 + D_+ \end{aligned} \qquad D\pm = (\omega_Q^2 \pm \omega_{rf}\omega_Q + \omega_{rf}^2)^{\frac{1}{2}} \qquad (5.13)$$

The central transition signal following an r.f. pulse of duration t_1 is given by equation (5.10):

$$\hat{\rho}(t_1)_{\frac{1}{2},-\frac{1}{2}} = \sum_{ij} (R_{-\frac{1}{2},\frac{1}{2}})_{ij} \exp(-i\omega_{ij}t_1)$$

where $(R_{-\frac{1}{2},\frac{1}{2}})_{ij}$ is defined in equation (5.11). Given the orthogonal transformation $\bar{T}$, it is possible to evaluate all components of $R_{-\frac{1}{2},\frac{1}{2}}$. It is found that $(R_{-\frac{1}{2},\frac{1}{2}})_{3,1}$ and $(R_{-\frac{1}{2},\frac{1}{2}})_{4,2}$ equal zero and so only four of the six possible nutation frequencies for a spin $I=3/2$ nucleus may be observed[13]. These forbidden frequencies correspond to double quantum transitions, and only single and triple quantum transitions can occur. Thus, for an $I=3/2$ nucleus, the amplitude of the central transition signal following a r.f. pulse is modulated with four different frequencies as a function of t_1 [13]:

$$S(t_1,0) = b(A_{31}\sin\omega_{31}t_1 + A_{41}\sin\omega_{41}t + A_{32}\sin\omega_{32}t + A_{42}\sin\omega_{42}t) \qquad (5.14)$$

where $A_{ij} = (R_{-\frac{1}{2},\frac{1}{2}})_{ij}$ and b is the constant $\frac{N\gamma\hbar^2\omega_o}{16kT}$ (N = total number of spins).

$$
\begin{aligned}
A_{31} &= 3\sin 2\theta_- \sin 2\theta_+ - (1-\cos 2\theta_-)(1+\cos 2\theta_+) \\
A_{41} &= -3\sin 2\theta_- \sin 2\theta_+ - (1-\cos 2\theta_-)(1-\cos 2\theta_+) \\
A_{32} &= -3\sin 2\theta_- \sin 2\theta_+ - (1+\cos 2\theta_-)(1+\cos 2\theta_+) \\
A_{42} &= 3\sin 2\theta_- \sin 2\theta_+ - (1+\cos 2\theta_-)(1-\cos 2\theta_+)
\end{aligned}
\qquad (5.15)
$$

It is clear from equation (5.14) that the application of a pulse of duration t_1 to a spin-$^3/2$ nucleus will influence the transitions of the quadrupolar nucleus according to the ratio ω_Q/ω_{rf}. This results in a coherence between the $|\tfrac{1}{2}\rangle$ and $|-\tfrac{1}{2}\rangle$ states during the detection period, the magnitude of the central transition signal intensity depending on the time evolution of equation (5.14) during t_1. It is possible to calculate the central transition signal intensity as a function of the pulse duration for a crystalline solid from equation (5.15) but before doing that, the equation may be used to illustrate the differences between selective and non-selective excitation:

5.2.1 (a) Selective excitation

In this case $\omega_Q >> \omega_{rf}$ and $\tan 2\theta_\pm = 0$ (equation 5.12(a)). Using $\theta_+ \simeq 0$ and $\theta_- \simeq 0$ for selective irradiation, the central transition signal following the r.f. pulse may be written as $S(t_1,0) = A_{32}\sin\omega_{32}t_1$ because $A_{31} = A_{42} = A_{41} = 0$. The square roots of $D_\pm$ may be expanded using the binominal theorem to obtain a simple expression for ω_{32}:

$$
D_\pm = (\omega_Q^2 \pm \omega_{rf}\omega_Q + \omega_{rf}^2)^{\frac{1}{2}} = \omega_Q\left(1 \pm \frac{\omega_{rf}}{\omega_Q} + \frac{\omega_{rf}^2}{\omega_Q^2}\right)^{\frac{1}{2}} \simeq \omega_Q\left(1 \pm \frac{\omega_{rf}}{2\omega_Q}\right) \qquad (5.16)
$$

Therefore, from equation (5.13),

$$
\omega_{32} = \left(\frac{-\omega_{rf}}{2} - D_+\right) - \left(\frac{\omega_{rf}}{2} - D_-\right) = -2\omega_{rf}. \qquad (5.17)
$$

Also, $A_{32} = -4$, and thus $S(t_1,0) = 4b\sin 2\omega_{rf}t_1$. The important point is that the effective r.f. field along the x axis is $2\omega_{rf}$ (correct to second-order in ω_{rf}/ω_Q).

5.2.2 (b) Non-selective excitation

In this case, ω_Q is taken to be zero. Note that for $\omega_Q = 0$:

$$2\theta_+ = \tan^{-1}\{(\sqrt{3}/2)\omega_{rf}/\omega_Q + \omega_{rf}/2\} = \tan^{-1}\sqrt{3} \qquad (5.18)$$

and that for numerical calculations,

$$2\theta_- = \tan^{-1}\{(\sqrt{3}/2)\omega_{rf}/\omega_Q - \omega_{rf}/2\} + \pi = \tan^{-1}\sqrt{3} + \pi \qquad (5.19)$$

Therefore,

$$A_{31} = 0 \qquad \omega_{31} = -3\omega_{rf}$$
$$A_{41} = -3 \qquad \omega_{41} = -\omega_{rf}$$
$$A_{32} = -3 \qquad \omega_{32} = -\omega_{rf}$$
$$A_{42} = 2 \qquad \omega_{42} = \omega_{rf}$$

and thus, $S(t_1,0) = 8b\sin\omega_{rf}t_1$.

In summary, the results suggest that if only the central transition is excited, the duration of the $\pi/2$ pulse is half that required to generate maximum transverse magnetisation for the central transition in the absence of a quadrupolar interaction. In addition, the maximum intensity for selective excitation of the central transition is half of that for non-selective excitation of the central transition. For the intermediate case, where $\omega_Q \simeq \omega_{rf}$, equation (5.14) becomes an aperiodic function of t_1, and the maximum signal intensity lies between the two extreme cases derived above - the precise value depending on the ratio ω_Q/ω_{rf}. The implication of the

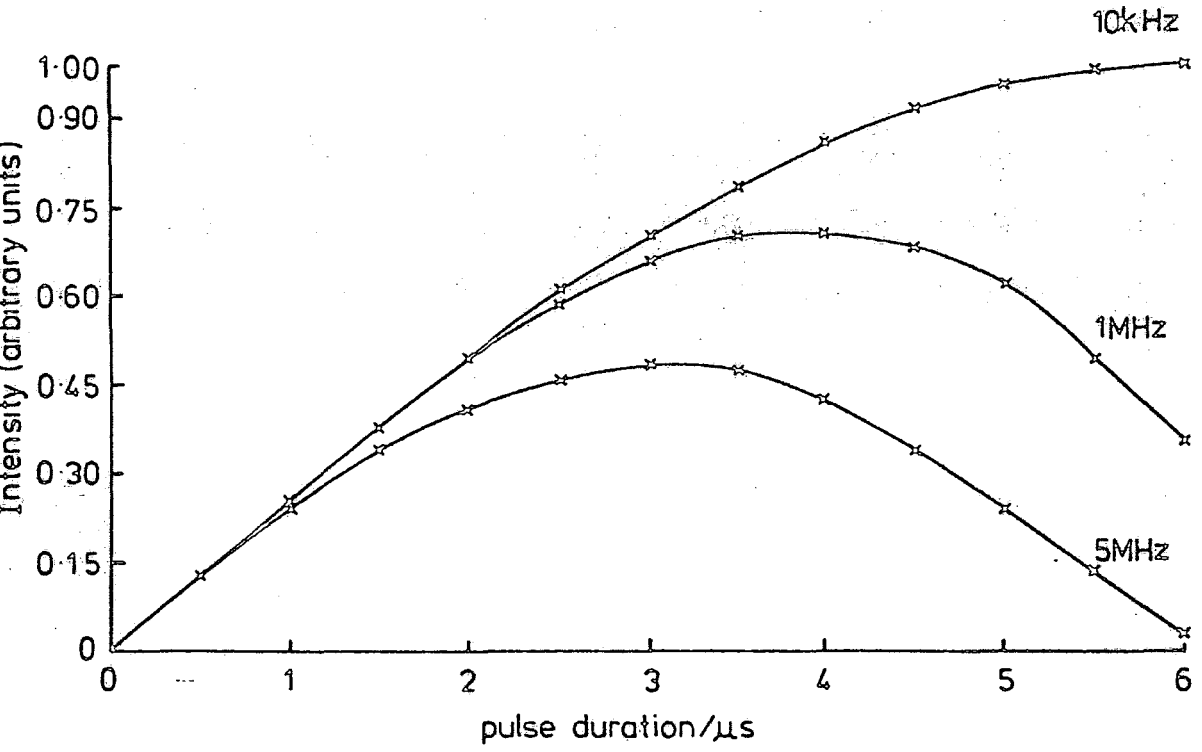

Figure 5.1: Intensity of central transition resonance as a function of quadrupole coupling constant and pulse duration for $\omega_{rf} = 41^2/_3$ kHz and $I = {}^3/_2$.

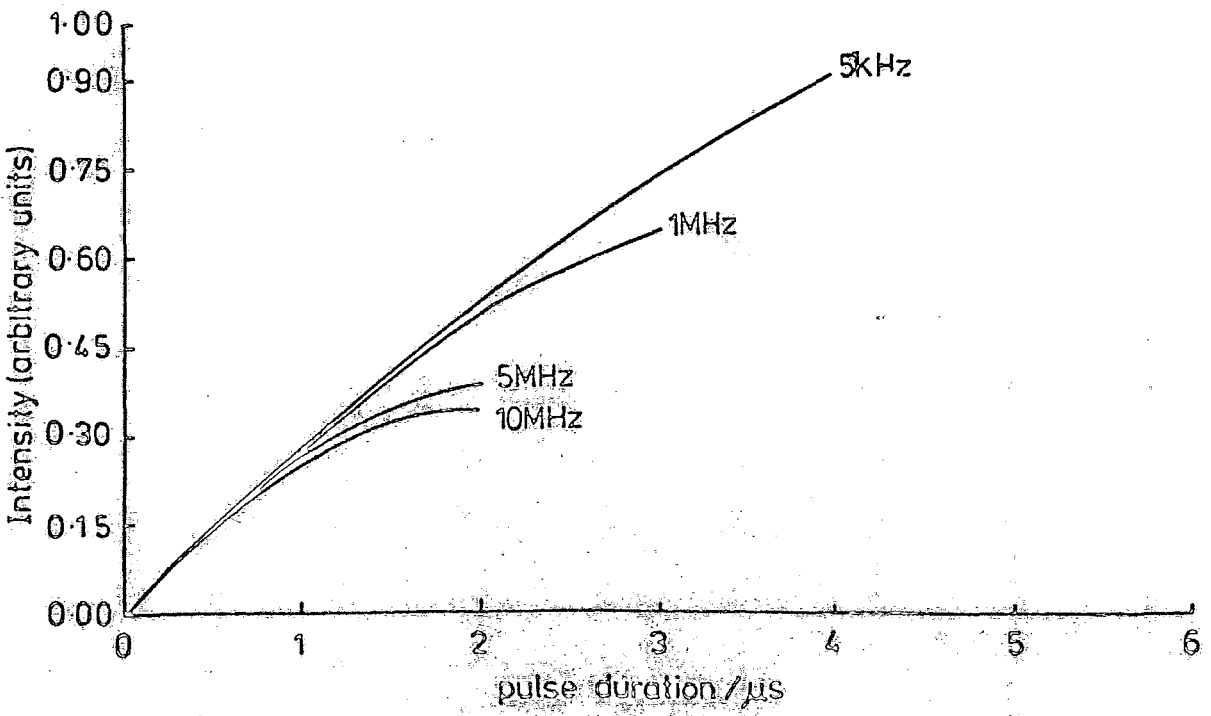

Figure 5.2: Intensity of central transition resonance as a function of the quadrupole coupling constant and pulse duration for $\omega_{rf} = 41^2/_3$ kHz and $I = {}^5/_2$.

above results for quantitative studies of half-integer spin quadrupolar nuclei is self-evident.

For crystalline powders, crystallite orientation typically ensures a whole range of ω_Q values. Given that equation (5.14) allows the calculation of the central transition signal intensity for arbitrary values of the quadrupole frequency, the powder line intensity may be calculated according to Haeberlen[14] from an integral equation where the line intensity is equalled to the statistically expected number of nuclei resonating within a certain limit, weighted by their orientation dependent excitation efficiency:

$$\int_{\omega_b}^{\omega_a} J(\omega)d\omega \propto b \int_0^{\pi/2}\int_0^{\pi/2} [A_{31}\sin\omega_{31}t_1 + A_{41}\sin\omega_{41}t_1 + A_{32}\sin\omega_{32}t_1 + A_{42}\sin\omega_{42}t_1] \times \sin\theta d\theta d\Phi \quad (5.20$$

The assumption of axial symmetry is made, and numerical integration methods give the intensity of the central transition powder pattern as a function of pulse duration (Figure 5.1), for the quadrupole coupling constants as indicated and an r.f. field strength of $41^2/3$ kHz. The intensities are normalised to be 0.393 for a pulse duration of $\pi/\omega_{rf(2(2I+1))}$. The normalisation condition ensures that the intensity of the central line for non-selective excitation is unity[2].

To produce the similar plot for the higher $I=5/2$ spin, it can be shown by a recurrent expansion of the density matrix using the fictitious spin operator formalism, that the central transition signal may be expressed as a function $J_I(\psi,\phi)$ of the quadrupolar flip angle ψ and a power series of the r.f. flip angle ϕ [4]:

$$J_{5/2}(\psi,\phi) \propto b^1 \langle \tfrac{1}{2}|\hat{I}_y|-\tfrac{1}{2}\rangle\langle -\tfrac{1}{2}|\hat{I}_y^{3/4}|\tfrac{1}{2}\rangle \times \left[3\phi + (12(\frac{\sin\psi - \psi\cos\psi}{\psi^3}) - \frac{9}{2})\phi^3 \ldots\right] \quad (5.21)$$

$\psi = 6\omega_Q t_p$ $\phi = \omega_{rf} t_1$ and ω_Q was defined previously.

The powder line intensity may be calculated in a similar fashion as for the I = $^3/_2$ spin to yield the results shown in Figure 5.2. The results for the I = $^5/_2$ spin are in excellent agreement for the range plotted with the results obtained by Fenzke[2] using numerical diagonalisation of the relevant Hamiltonian. The disagreement at long t_1 values results from violation of the condition $t_1\omega_{rf} \ll 1$ under which Lippmaa's result was derived, and is also due to the neglect of higher order expansion terms.

Figures 5.1 and 5.2 illustrate several points:

(1) If the complete central transition is excited, then the quadrupolar coupling constant may be calculated by measuring the signal intensity as a function of pulse duration; although the above results are subject to the constraint $t_1\omega_{rf} \ll 1$ in the case of the I=$^5/_2$ spin, the method is more than adequate for calculation of quadrupole coupling constants by initial variation in intensity as a function of pulse duration. The relevant graph may, of course, be plotted for values of the r.f. field strength other than the $41^2/_3$ kHz field used by Fenzke.

(2) The curves for small and large quadrupole coupling agree with the special cases of non-selective and selective excitation respectively - the ratio of the maximum intensities for the two extreme cases is close to the theoretical values of 2 and 3 in Figures 5.1 and 5.2 respectively.

(3) Comparison of intensities of nuclei with differing quadrupole coupling constants will lead to incorrect conclusions unless very short pulse durations are used, when the central transition signal intensity is proportional to the pulse duration (and the number of nuclei), and independent of the value of the quadrupole coupling. For an error of less than 5% in the signal intensity for the central transition, the effective spin flip angle must satisfy the condition[5]:

$$(I + {}^{1}/_{2})\omega_{rf}t_{1} \leq {}^{\pi}/_{6} \qquad (5.22)$$

In addition, if comparison is to be made with solution-state results, the intensity of, say, an aluminium signal in solution must be multiplied by a factor $^{9}/_{35}$ for quantitative comparison between solid and liquid samples[3]. For a solid, only the central transition is generally observed, while for a solution, all transitions contribute to the total. The $^{9}/_{35}$ factor results from the ratio of the central transition intensity to the total intensity.

5.3 Quantitative analysis of aluminium by ^{27}Al NMR

The above results form the basis of the method for quantitative analysis of aluminium in the zeolite samples studied. Quantitative analysis of aluminium is particularly useful in the case of dealuminated zeolites - dealumination being used to control the Brönsted acid site catalytic activity by control of the tetrahedral aluminium site density. After dealumination, ^{27}Al NMR allows a quantitative analysis of the amount of non-framework aluminium (both in six and four coordination) as well as the four-coordinate framework aluminium. Comparison of the total aluminium content measured by ^{27}Al NMR

with that of the aluminium content measured by XRF yields the proportion of aluminium invisible to ^{27}Al NMR. The aluminium is "invisible" as a consequence of it residing in an environment of low symmetry and gives rise to a signal that is too broad to be observed by NMR.

The aluminium quantitation work was performed on a Jeol GX400 spectrometer (aluminium frequency 104.22 MHz). Typically, a mordenite A material that had been fully characterised by XRF/AA was used as the reference sample. The assumption is made that all of the aluminium in a mordenite A sample may be detected by ^{27}Al NMR.

The finely ground samples are hydrated in a desiccator with saturated water vapour for at least 48 hours prior to the experiment. Some of the sample is then weighed in to a rotor and the remainder is sent for XRF analysis. The purpose of the hydration procedure is to make the aluminium sites as symmetrical as possible. Partial dehydration of the samples may result in broad or invisible lines. For the hydrated samples, the assumption is made that all of the four-coordinate framework aluminium sites contribute to the peak at ~55ppm. Using $\pi/11$ pulses and low radio frequency fields so that condition (5.22) is met, the central transition intensities of a series of materials fully characterised by XRF were obtained at Sunbury-on-Thames. The corresponding aluminium content was determined by comparison of the central transition signal of the material with that of the reference material for known weights of sample. The spinning rate was approximately 4 kHz, and the intensity rejection into spinning sidebands of the central transition was taken into account. The results are reproducible and are in excellent agreement with the XRF results,

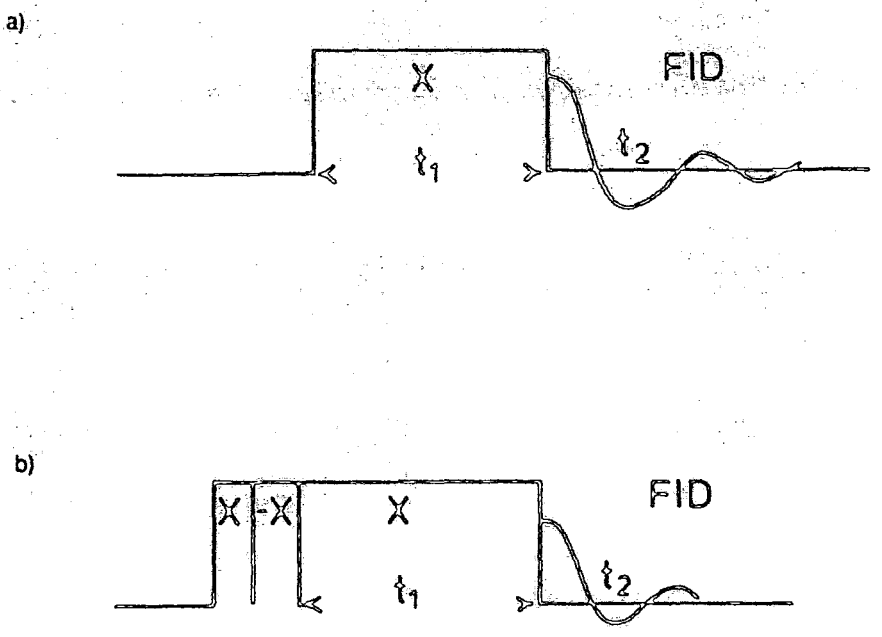

Figure 5.3: a) Quadrupole nutation experiment.
b) Rotary-echo nutation experiment.

implying that it is possible to accurately and reproducibly determine framework aluminium contents by ^{27}Al NMR. The short spin-lattice times of the aluminium species allow short recycle times to be used in the quantitation measurements. The deadtime was reduced as much as possible to ensure a flat baseline (∿13μs). However the presence of a finite deadtime ensures that the results can never be entirely quantitative, although this is only serious for very broad lines where the aluminium content is reported as observable aluminium. In principle, a very short deadtime could be produced by inserting non-magnetic resistors in series with the coil in order to spoil the quality factor (Q) for the circuit. This modification is typically made to the probehead in the case of ^{1}H CRAMPS experiments. Ideally, small sample volumes should also be used so that the r.f. field is homogeneous over the sample.

5.4 Nutation NMR[7,8,9,10]

Consideration of equation (5.9) suggests a simple two-dimensional experiment for the determination of the quadrupolar parameters. Free induction decays recorded after a r.f. pulse lengthened during the experiment by constant increments in t_1 (Figure 5.3(a)) results in a 2-D data array. During t_1, a low-field situation exists and the system evolves under the influence of both the first-order quadrupolar and r.f. field Hamiltonians. It can be seen from equation (5.10) that the initial intensity of the magnetisation in t_2 is modulated by the extent of excitation during t_1. Fourier transformation with respect to both the pulse duration and the duration of

the free induction decay results in a 2D data display; for a single crystal, projection on to the F_1 axis (excitation axis) leads to a maximum of four lines in the case of an $I=^3/2$ spin (equation (5.14)). The relative intensities of the lines will depend on the ratio $^{\omega}Q/\omega_{rf}$, and are given by A_{31}, A_{41}, A_{32} and A_{42} with excitation frequencies ω_{31}, ω_{41}, ω_{32} and ω_{42} respectively. For the extreme cases of selective and non-selective excitation, the previous results suggest that only one peak would be observed in the F_1 dimention at $2\omega_{rf}$ and ω_{rf} respectively. For a crystalline sample, the F_1 projection will be a powder pattern, the characteristics of which depend on the ratio $^{\omega}Q/\omega_{rf}$. For intermediate values of the ratio $^{\omega}Q/\omega_{rf}$, very complex projections may result in the F_1 dimension and computational methods are required to extract the quadrupolar parameters. The complexity results largely from the orientation dependence of ω_Q, which becomes much less important in the limits $\omega_Q >> \omega_{rf}$ and $\omega_{rf} >> \omega_Q$, when the powder pattern projection yields lines at $2\omega_{rf}$ and ω_{rf} respectively as in the case of a single crystal. The above results may be generalised to lines at $(I+\frac{1}{2})\omega_{rf}$ and ω_{rf} for a half-integer quadrupolar spin under conditions of selective and non-selective excitation. During t_2, the system evolves under the influence of the Zeeman, chemical-shift and second-order quadrupolar Hamiltonians. Consequently, the projection in the F_2 dimension yields a 1-D powder pattern resulting from chemical shift anisotropy and second-order quadrupolar interaction, complete with a second-order quadrupolar shift.

The 2-D experiment is particularly valuable in the case of synthetic zeolites where curve fitting of central transition

lineshapes is prevented by the observation of broad, featureless lines in ^{27}Al and ^{23}Na single-pulse spectra. The broadening may result from crystallographic inequivalence and/or a spread in quadrupole interactions. NQR is insensitive for the range of quadrupole interactions observed (0.05-5 MHz), and there is the additional problem of a wide frequency range to cover when searching for possible resonances.

5.5 Nutation development work

In an attempt to realise the difficulties inherent in the technique, a series of model compounds were investigated. Typically the radiofrequency pulse lengths t_1 were increased between the FID accumulations by 2μs increments from 2μs to 128μs (64 data points in the t_1 dimension), giving a spectral width of 250 kHz in the F_1 dimension. The 2D experiment is most conveniently carried out on-resonance with quadrature detection. On-resonance means at the Larmor frequency and not at the centre of gravity of the central transition powder pattern, which is shifted to low frequency of the Larmor frequency if second-order quadrupolar effects are significant (Chapter Two). To carry out the experiment on-resonance requires a knowledge of the second-order quadrupolar shift of the centre of gravity of the central transition lineshape, and thus a knowledge of the quadrupolar parameters. Often a trial experiment was performed to obtain an estimate of the quadrupolar parameters, and hence an estimate of the shift. Usually, the shift was of the order of several ppm and the

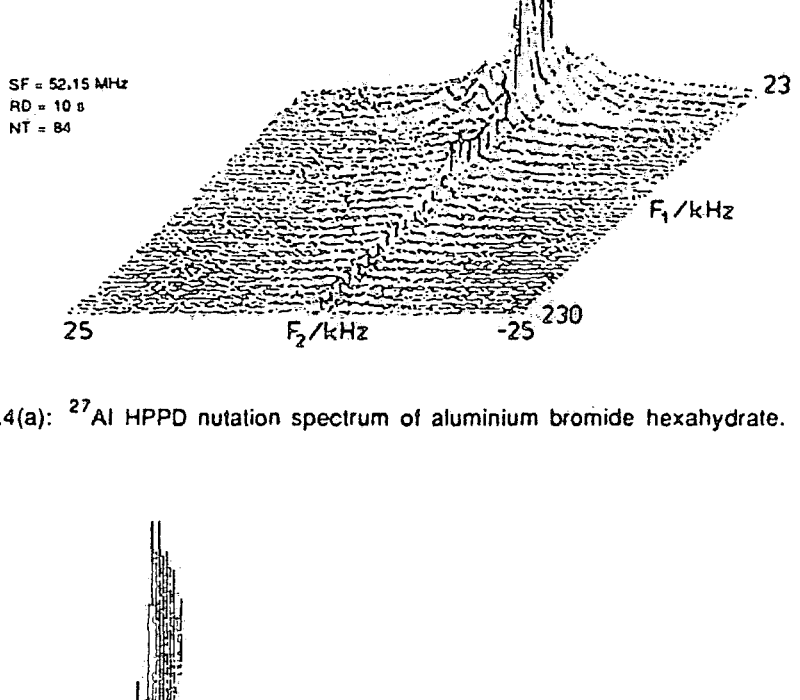

Figure 5.4(a): ^{27}Al HPPD nutation spectrum of aluminium bromide hexahydrate.

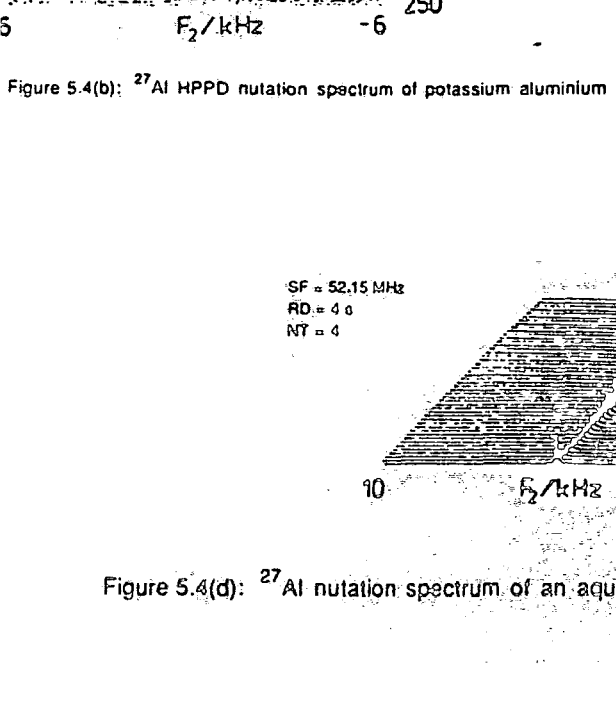

Figure 5.4(b): ^{27}Al HPPD nutation spectrum of potassium aluminium sulphate.

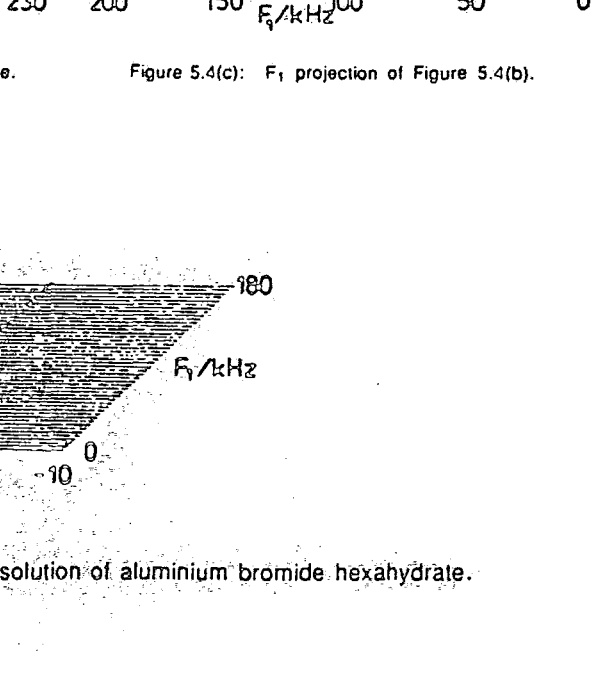

Figure 5.4(c): F_1 projection of Figure 5.4(b).

Figure 5.4(d): ^{27}Al nutation spectrum of an aqueous solution of aluminium bromide hexahydrate.

on-resonance position was well within the static lineshape of the central transition. If single-phase detection is used, any off-resonance effects complicate the results by introducing a shift in the position of the signal along the F_1 axis[7]. The strength of the radiofrequency pulses used varied between 60 and 70 kHz, and was determined either by a solution or the presence of a peak in the F_1 dimension at the relevant position. The FIDS were double Fourier transformed in the magnitude mode, and zero filling was used in both F_1 and F_2 dimensions.

5.5.1 ^{27}Al Nutation

5.5.1.1 (a) Aluminium bromide hexahydrate ($AlBr_3.6H_2O$)

The nutation spectrum of aluminium bromide hexahydrate ($AlBr_3.6H_2O$) is shown in Figure 5.4(a). The trivalent cation is surrounded by six water molecules in an octahedral arrangement[15], although the conventional static single-pulse experiment yields a first-order quadrupolar powder pattern suggesting that the aluminium is not situated in a completely symmetrical environment. The relevant quadrupole coupling constant is shown in Table 5.1, and was calculated from the closest symmetrical humps about the central peak corresponding to the $(\pm^3/_2, \pm^1/_2)$ transitions, given that the separation of the humps is $3e^2qQ/20h$ for axial symmetry. The nutation spectrum obtained in the presence of high-power proton decoupling indicates that the excitation proceeds almost exclusively at $\omega_{rf}/2\pi = 60$ kHz in accordance with the small ω_Q/ω_{rf} ratio of 1.0×10^{-2}. The results suggest that excitation is non-selective for such a small quadrupole coupling constant. The small $2\omega_{rf}$ component results from the recycle delay not being long enough for the system to return to

TABLE 5.1 Quadrupole coupling data for the samples studied

Sample	Nucleus studied	e^2qQ/h (MHz)	η	ω_Q/ω_{rf} (calculated using the experimental value of ω_{rf})	ω_Q/ω_{rf} (observed)
Aluminium bromide	^{27}Al	0.05 (a)	-	0.01	$\sim$0
Potassium aluminium sulphate	^{27}Al	0.395 (b)	0	8.2×10^{-2}	$0.05\leq\omega_Q/\omega_{rf}\leq0.15$
Sodium aluminium sulphate	^{27}Al	$\sim$1.92	$0.8\leq\eta\leq1$	-	$\sim$0.6
Sodium chloride	^{23}Na	$\sim$0	$\sim$0	-	$\sim$0
Borax (c)	^{23}Na	0.541, (b) 0.849 (b)	0.45, (b) 0.14 (b)	0.36, 0.57	$\sim$0.3, $0.3\leq\omega_Q/\omega_{rf}\leq0.6$
Sodium aluminium sulphate	^{23}Na	$\sim$1.2	$\sim$1	-	$\sim$0.8
Sodium perborate	^{23}Na	$\sim$0.45 (d)	$\sim$1 (d)	-	$\sim$0.3 (d)

(a) Calculated from the separation of the closest symmetrical humps about the central peak (with the assumption of axial symmetry).

(b) Obtained from published data.

(c) The two crystallographic sites are partially resolved in the static nutation spectrum.

(d) Value corresponds to an "average" value. The two crystallographic sites may not be distinguished by either nutation or conventional single-pulse experiments.

equilibrium before the next pulse, making the build-up of magnetisation along the z-axis incomplete. This disturbs the pure sine amplitude modulation of the FID and Fourier Transformation of a distorted $\sin\Omega_1 t$ wave gives a line at frequency Ω_1 plus harmonics at $2\Omega_1$, $3\Omega_1$, ... The number and amplitude of these harmonics depends on the distortion of the sine wave and they may easily be mistaken for components with a large quadrupole coupling, especially in the case of a spin $I=3/2$ nucleus[7].

Spurious peaks were observed at $F_1=0$ (not shown), and are due to off-resonance irradiation leading to a magnetisation component along the B_{eff} field in the rotating frame which does not evolve during t_1 (a type of $T_{1\rho}$ process)[5]. If these spurious peaks are sufficiently intense, the projection along F_2 is ruined and broadening occurs in the $F_1=0$ region. Investigations with aluminium bromide have shown that the intensity of the spurious peaks at $F_1=0$ may be significantly reduced by decreasing the strength of the B_1 field. Magic angle spinning experiments, as discussed later, also reduce the intensity of the peak at $F_1=0$. Previous research has shown that the intensity of the zero frequency peak may be significantly reduced by applying immediately after the strong excitation pulse, but before data acquisition, an additional $\pi/2$ phase-shifted weak radiofrequency pulse[5]. The unwanted spin-locked component of the magnetisation may be reduced close to zero by suitable choice of amplitude and duration of this phase-shifted pulse. However, for instrumental reasons, no additional weak pulses were used to avoid the build-up of spin-locked magnetisation for the results presented in this thesis.

Visual projection of the spectrum along F_2 gives the expected lineshape for the static single-pulse experiment. The broad underlying features in Figure 5.4(a) result from the presence of an aluminium background in the ^{31}P Andrew-Beams probe. The projection also reveals that a hole is burned in the 2D spectrum at the position of the carrier frequency in a way not dissimilar from that expected for an inhomogeneous line. Changing the position of the earlier frequency resulted in a corresponding change in frequency of the spike.

(b) Potassium aluminium sulphate ($KAl(SO_4)_2.12H_2O$)

Several alums were also investigated {$KAl(SO_4)_2.12H_2O$ and $NaAl(SO_4)_2.12H_2O$}. All alums crystallise in the space group Pa_3 and they may be classified into three different types[6]. The type depends on the size of the monovalent cation. If the cation is small, the γ form is produced. The β form is produced if the cation is large, and the α form results if the cation is of intermediate size. In all cases, the aluminium is surrounded by six water molecules in a nearly regular octahedron.

$KAl(SO_4)_2.12H_2O$ exists in the β-form[16], and the quadrupole coupling parameters for aluminium are shown in Table 5.1. The static nutation spectrum obtained in the presence of high-power decoupling is shown in Figure 5.4(b).

The excitation occurs predominantly at $\omega_{rf}/2\pi = 60$ kHz, but there is significant intensity at larger values of ω_{rf} suggesting that excitation is not completely non-selective. Comparison of the projection along F_1 (Figure 5.4(c)) with

the results published by Veeman *et al* (Appendix A) suggest that $0.05 \leqslant {}^{\omega}Q/\omega_{rf} \leqslant 0.15$ with $\eta = 0$. This is in good agreement with the data shown in Table 5.1.

A feature of both Figures 5.4(a) and 5.4(b) is the asymmetric nature of the peak at ω_{rf}; the intensity of the peak extending to low values of ω_{rf}. The homogeneity of the r.f. field is a potential source of linebroadening in nutation spectroscopy - the homogeneity of the r.f. coil is mapped out directly on the projection in the F_1 dimension. To distinguish whether the asymmetric feature is real or is a consequence of r.f. inhomogeneity, the experiment was repeated using aluminium bromide solution (Figure 5.4(d)). The nutation frequency spread is quite large, although most of the signal occurs at ω_{rf}. There should be a correlation between nutation frequency and sample position based on the assumption that the r.f. field drops off towards the ends of the coil. The effect of r.f. inhomogeneity cannot simply be described by a broadening function because a spread in ω_{rf} will cause a spread in the ratio ${}^{\omega}Q/\omega_{rf}$, and will thus change the whole nutation spectrum (albeit in a minor fashion given that the majority of the signal occurs at ω_{rf} in the solution spectrum)[7]. The effect of r.f. inhomogeneity may be reduced by using a smaller sample size situated at the centre of the coil. This may be achieved in several ways; either modification of the rotor design or packing of the sample between layers of an inert substance such as adamantane. Of course, either method will result in a loss of sensitivity due to the smaller sample volume. The ^{31}P double-bearing probe became available at this time, and solution studies revealed a similar nutation spectrum to that shown in Figure 5.4(d).

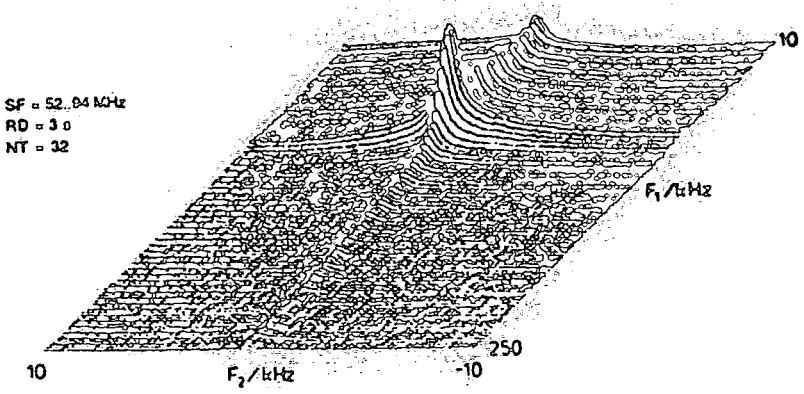

Figure 5.4(e): ^{23}Na nutation spectrum of NaY zeolite.

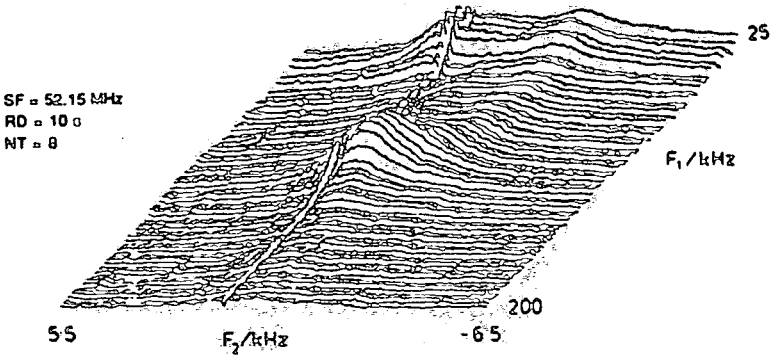

Figure 5.4(f): ^{27}Al HPPD nutation spectrum of sodium aluminium sulphate.

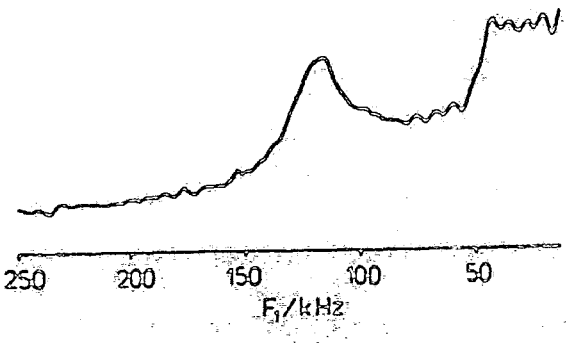

Figure 5.4(g): F_1 projection of Figure 5.4(f).

However, the ^{23}Na nutation spectrum of NaY (Figure 5.4(e)) packed between two layers of adamantane reveals a considerable improvement. Hydrated NaY zeolite was chosen because the sodium is very mobile and should give a liquid-like spectrum - the broad features in the F_2 projection result from the non-central transitions as discussed later. There is still a finite intensity to low values of ω_{rf} but there will of course be a contribution from the F_1=0 peak and the "feet" that appear on the peaks in the F_1 dimension due to Fourier Transformation in the magnitude mode.

For $KAl(SO_4)_2.12H_2O$, nutation allows a quick determination of the quadrupole coupling parameters - spinning sideband analysis would be difficult given the large range spanned by the first-order quadrupolar spinning sidebands and problems concerning uniform excitation may result. In addition to the need for complex refocusing sequences, similar problems would be encountered in trying to fit the first-order quadrupolar static lineshape. The size of the quadrupole coupling constant is such that the second-order contribution to the central transition lineshape is minimal, and curve fitting procedures will consequently be of little use.

(c) Sodium aluminium sulphate ($NaAl(SO_4)_2.12H_2O$)

$NaAl(SO_4)_2.12H_2O$ exists in the α-form[17], and the conventional single-pulse spectrum indicates a significant contribution of second-order quadrupolar effects to the central transition lineshape. The relevant static ^{27}Al nutation spectrum obtained in the presence of high-power decoupling is shown in Figure 5.4(f). Steps were taken to minimise r.f. inhomogeneity effects and the ^{31}P double-bearing probe

(aluminium free) was used. An r.f. field strength of 40 kHz was used in this case. Projection in the F_1 direction (Figure 5.4(g) reveals that excitation is in an intermediate region, there being peaks of significant intensity at both ω_{rf} and $3\omega_{rf}$. Comparison with Appendix A suggests that $\omega_Q/\omega_{rf} = 0.6 (e^2qQ/h = 1.9$ MHz) and $0.8 \leq \eta \leq 1$. The octahedral arrangement of the water molecules about the aluminium is clearly more distorted in $NaAl(SO_4)_2.12H_2O$ than in $KAl(SO_4)_2.12H_2O$.

5.5.2 ^{23}Na Nutation

After having established the setting up procedure on model aluminium containing compounds, attention was focused on ^{23}Na nutation spectroscopy. The projection in the F_1 direction may be used to determine whether or not the central transition is being selectively excited and this is an important consideration when investigating the refocusing effects of pulse sequences on the spectra of spin $I = 3/2$ quadrupolar nuclei. The effect of the CPMG pulse sequence on sodium chloride, sodium borates and sodium aluminium sulphate is discussed in detail in Chapter Seven. The nutation spectra of the above compounds are discussed below under identical r.f. conditions, and in relevant cases the effect of magic angle spinning and proton coupling is discussed.

5.5.2.1 (a) Sodium chloride

In sodium chloride, where the sodium is surrounded by six chlorines in an octahedral environment[18], the excitation proceeds nearly exclusively at ω_{rf}, with a very small $2\omega_{rf}$ component which resulted from too short a recycle delay. As expected, the excitation is non-selective.

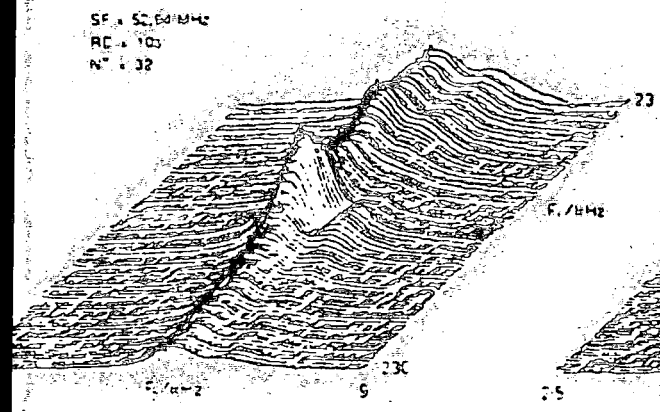

Static ^{23}Na nutation spectrum of Borax (r.f. strength = 62.5kHz.

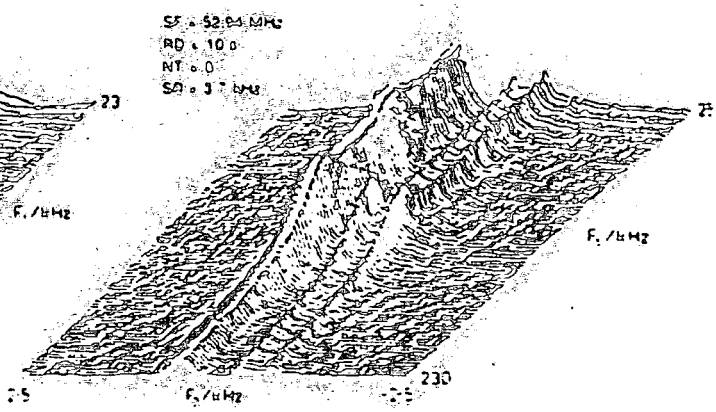

Figure 5.5(b): ^{23}Na MASNMR nutation spectrum of Borax (r.f. strength = 62.5kHz

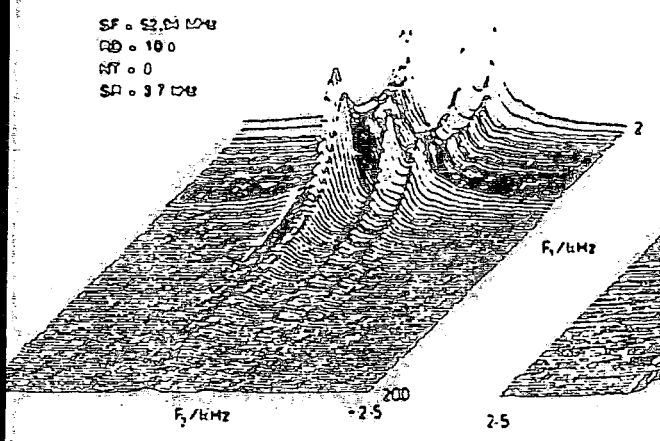

^{23}Na MASNMR nutation spectrum of Borax (r.f. strength = 26kHz)

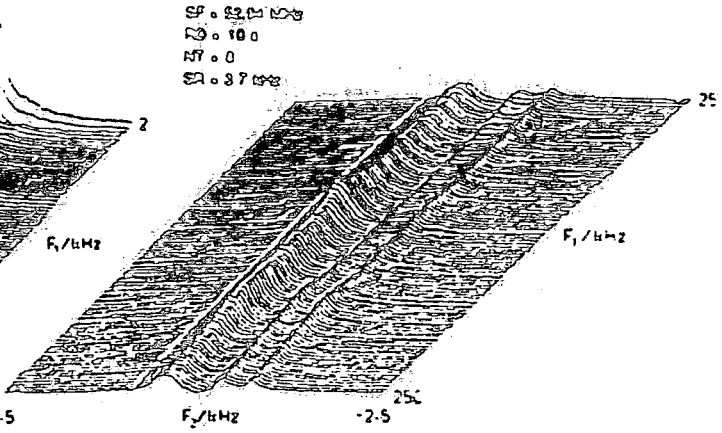

Figure 5.5(d): ^{23}Na MASNMR nutation spectrum of Borax (r.f. strength = 11·8kHz)

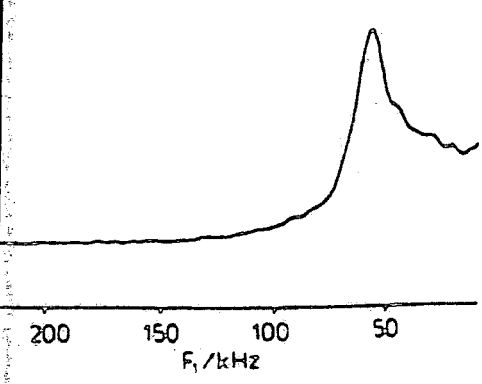

5(c) F_1 spectrum of Figure 5.5(c)

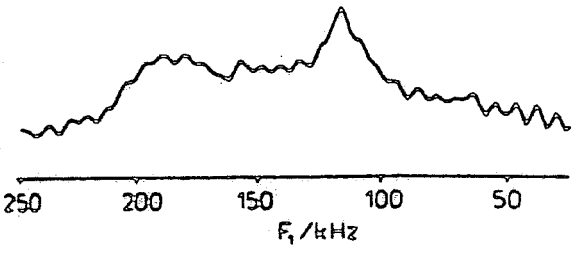

Figure 5.5(d): F_1 spectrum of Figure 5.5(d).

(b) Borax ($Na_2B_4O_7 \cdot 10H_2O$)

In borax, two crystallographically distinct sodium environments have been detected[19]. The sodium cations are surrounded by six water molecules in an arrangement close to octahedral symmetry. The solid-state NMR data is in agreement with the previous observation of two distinct sodium sites. Borax is a good sample with which to test the effectiveness of the nutation experiment. The static single-pulse spectrum consists of two overlapping featureless lines from which no accurate quadrupole interaction parameters could be obtained. The relevant quadrupolar coupling parameters are shown in Table 5.1, and the ability of the nutation experiment to separate chemical shift from quadrupole excitation effects is clearly illustrated in Figure 5.5(a). Given the r.f. field strength of 62.5 kHz used in this experiment, the higher frequency resonance suggests that $\omega_Q/\omega_{rf} \sim 0.3$ ($e^2qQ/h \sim 450$ kHz although it is difficult to estimate. The overlap makes it difficult to obtain a quadrupole coupling constant for the lower frequency peak but it is estimated to lie between 450 kHz and 900 kHz. It is clear from Figure 5.5(a) that excitation is neither selective nor non-selective for both types of crystallographically distinct site.

The borax sample is ideal for testing the effects of magic angle spinning on nutation spectra. If magic angle spinning could be used, it would certainly simplify matters by removing broadening effects in the F_2 dimension resulting from chemical shift anisotropy and any residual dipolar coupling. It would also narrow the broadening in the F_2 dimension resulting from second-order quadrupolar coupling by a theoret-

ical factor of 3.6, thus representing a significant gain in resolution and signal-to-noise ratio.

The magnetisation nutates in spin space at a rate vastly exceeding that of sample spinning so long as the condition $\omega_{rf} >> \omega_{rot}$ is obeyed, and this justifies the use of stationary energy levels in the calculation of the theoretical excitation spectra[5]. However, problems may arise due to changes in the orientation of the sample during the excitation period. This effect may be neglected if the r.f. pulses are short compared with the MAS period, although this approximation is unrealistic for nutation experiments where the longest pulse is 128μs (or 0.38 of a rotor period for a rotation rate of 3 kHz). The orientation dependence of ω_Q is relatively unimportant for selective and non-selective excitation, but may be of significance for experiments involving spinning when the excitation is intermediate. The former point has been demonstrated by Samoson and Lippmaa[4] in the ^{23}Na nutation study of a spinning mixture of $NaCl/NaNO_2$. For NaCl, the excitation proceeded nearly exclusively at ω_{rf}. whereas in $NaNO_2$, the excitation spectrum was more complex, but due to the much larger value of ω_Q/ω_{rf} (0.83), is mainly concentrated at $2\omega_{rf}$.

The ^{23}Na nutation spectrum of borax using a spin rate of 3.7 kHz obtained under otherwise identical conditions to those used in the static case is shown in Figure 5.5(b). The longest (128μs) pulse was shorter than the sample rotation period. For both resonances in the F_2 dimension, the corresponding excitation spectrum is in good agreement with the quadrupolar coupling parameters indicated in Table 5.1.

It is clear that the lower frequency peak corresponds to the more distorted of the two sodium environments. However, there are some differences between Figures 5.5(a) and (b). The F_1 projection of the higher frequency resonance is broadened in the spinning experiment, whereas the F_1 projection of the lower frequency resonance differs in that the ω_{rf} peak in the static experiment is reduced in intensity in the spinning experiment. It is, however, difficult to assess the contribution of shielding anisotropy to the excitation spectra in Figure 5.5(a), but it would seem that the excitation projections are slightly altered by MAS. To probe this matter further, the nutation experiment was repeated for several values of ω_{rf} using MAS. Given that two crystallographically distinct sites are present with different quadrupole coupling parameters, an opportunity is presented to compare the theoretical excitation projections in Appendix A with their MAS counterparts for a wide range of $^{\omega}Q/\omega_{rf}$ values. The ω_{rf} values were accurately determined by nutation experiments on sodium chloride solution.

The excitation projections, shown in Figures 5.5(e) and (f) are dominated by the higher frequency resonance in F_2. It should be remembered that the projections in the F_1 direction are subject to different scaling factors.

Figures 5.5(c) and (e) show the nutation spectrum and F_1 projection obtained with an r.f. field strength of 26 kHz and a spin rate of 3.7 kHz. The excitation is concentrated predominantly at $2\omega_{rf}$ for both sites as is expected given the $^{\omega}Q/\omega_{rf}$ values shown in Table 5.1. There is, however, in both cases a significant amount of intensity at lower values

of ω_{rf} that was not anticipated from the projections in Appendix A. It is difficult to assess the line-broadening influences arising from off-resonance peaks and finite r.f. inhomogeneity, although they are unlikely to account for the magnitude of the anomalous features observed. Figure 5.5 (d) and (f) show both the nutation spectrum and the F_1 projection obtained for an r.f. field strength of 118 kHz and spin rate of 3.7 kHz. The relevant ω_Q/ω_{rf} values are shown in Table 5.1, and the projections in F_1 are similar to those in Appendix A.

In conclusion, it would seem that the use of MAS gives similar results to the theoretical predictions of Veeman obtained assuming stationary energy levels. However, the above experiments suggest that some changes occur with MAS, most notably a linebroadening effect in the F_1 projection. Consequently, MAS was not used for the samples studied later, although this was not a serious loss because, for the samples studied, there was little to be gained by greater resolution along F_2. Comparison of Figures 5.5(a) and 5.5(b) does, however, indicate the significant gain in resolution in the F_2 direction that may result with MAS when several distinct sites are present. During the course of this work however, two papers were printed which involved, at least in part, the effect of MAS on the nutation spectrum[20,21]. Samoson and Lippmaa have shown that the projection in the F_1 direction is readily recognisable if strong r.f. pulses of duration $t_1 \leq \omega_{rot}^{-1}/4$ are applied and ω_Q is at least 5 to 10 times larger than ω_{rot}. This condition may still produce large deviations in the signal phase for some crystallites, although these contributions tend to cancel for a polycrystalline sample.

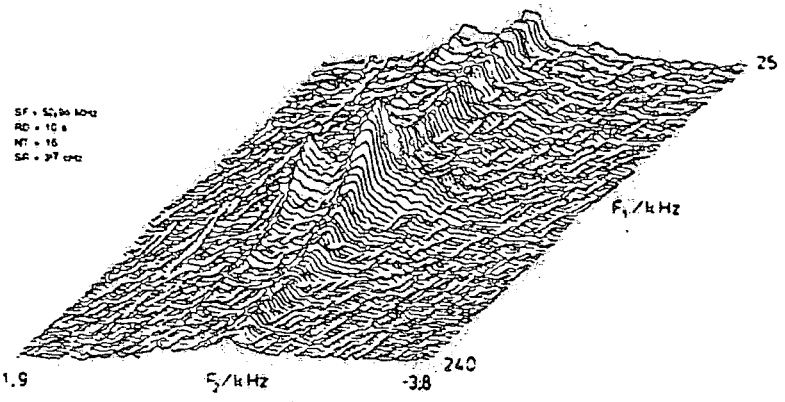

Figure 5.6(a) ^{23}Na MASNMR nutation spectrum of sodium aluminium sulphate

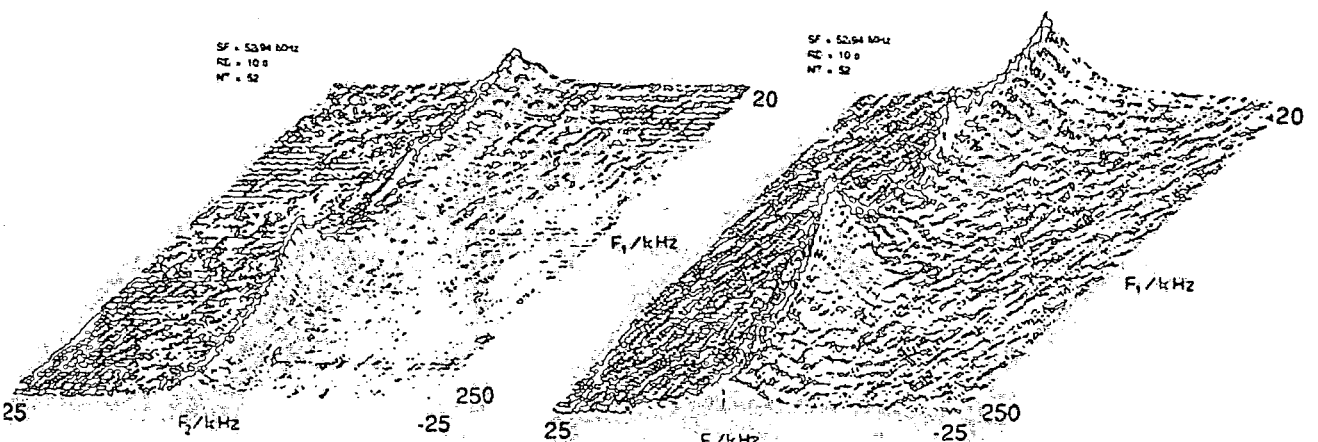

re 5.6(b): Static ^{23}Na HPPD nutation spectrum of sodium perborate.

Figure 5.6(c): Static ^{23}Na nutation spectrum of sodium perborate (without proton decoupling).

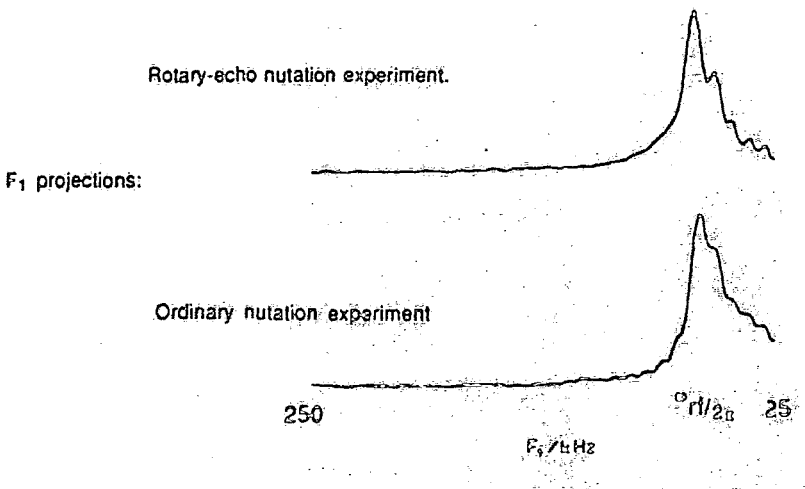

Figure 5.6(d): Effect of rotary-echo pulse pair on the nutation spectrum of hydrated NaY zeolite.

(c) Sodium aluminium sulphate ($NaAl(SO_4)_2.12H_2O$)

The structure of the alum was discussed earlier. The sodium cation is surrounded by six water molecules in a distorted octahedral arrangement. The ^{23}Na nutation spectrum obtained using an r.f. field strength of 62.5kHz and high-power proton decoupling reveals that excitation proceeds almost exclusively at $2\omega_{rf}$ both for spinning and static experiments (Figure 5.6(a)). The conclusion is that the central transition is selectively excited and that $^{\omega}Q/\omega_{rf} \sim 0.8$ ($e^2qQ/h \sim 1.2$ MHz) and $\eta \sim 1$.

(d) Sodium perborate ($Na_2BO_2.H_2O_2.3H_2O$).

Two crystallographically distinct types of sodium ion are present in sodium perborate[22]. Both sodium ions exist in a six-coordinate chain system, and the environments would be expected to be distorted from pure spherical symmetry. The nutation spectrum obtained using an r.f. field strength of 62.5 kHz and high-power proton decoupling reveals significant intensity in both the $2\omega_{rf}$ and ω_{rf} regions of the F_1 projection for the static experiment (Figure 5.6(b)) in agreement with the distortion from pure spherical symmetry predicted from crystallographic data. It was not however possible to resolve the crystallographically distinct sites even in the presence of magic angle spinning. However, the effect of heterodipolar coupling between the sodium and proton nuclei during the nutation experiment was investigated. The results shown in Figure 5.6(c) indicate that the F_2 projection of the nutation spectrum is broadened, as expected, although the excitation projection is unaltered. The magnitude of the

dipolar coupling between the sodium and proton nuclei was estimated to be about 650 Hz on the basis of standard bond lengths. This is expected to exceed the magnitude of similar interactions between quadrupolar nuclei and protons in zeolites and the nutation response for the zeolite samples investigated in the remainder of this chapter was examined in the absence of high-power proton decoupling.

5.5.3 Linebroadening in nutation spectroscopy

Three mechanisms may contribute to the width of the lines in the excitation projection: Distributions of the quadrupolar parameters e^2qQ/h and/or η, relaxation effects and inhomogeneous r.f. fields. Neglection of terms in the rotating frame Hamiltonian (equation 5.3) due to chemical shift and dipolar interactions is a reasonable approximation in zeolites, although chemical shift interactions may still affect the nutation spectrum by off-resonance effects[23]. Broadening due to r.f. inhomogeneity may be minimised as outlined above but is in any case small because the spectral width in the excitation projection is usually much larger than the r.f. inhomogeneity[23].

The two most important causes of linebroadening are thus a distribution of quadrupole parameters (static) and relaxation effects (dynamic)[24]. For some zeolites, severe linebroadening is observed in the ^{27}Al and ^{23}Na nutation spectra. In order to distinguish between the two probable linebroadening mechanisms, a simple extension of the nutation experiment may be used where the nutation pulse is preceded by two r.f. pulses of equal duration but opposite phase[24] (Figure 5.3(b)). The rotary echo that precedes the nutation

pulse is the rotating frame analogue of the Hahn echo. The idea is simply to use such a rotary echo sequence before the nutation experiment to study relaxation behaviour of the quadrupolar spins in the rotating frame. Veeman *et al* have shown that the rotary echo sequence refocuses the magnetisation at time 2τ along the z-axis only for the two limiting situations $\omega_Q >> \omega_{rf}$ and $\omega_Q << \omega_{rf}$ in the case of sodium. Given that the same result may be derived by using the fact that in the respective cases, the relevant rotating frame Hamiltonian may be approximated by $\hat{H}=(I+\frac{1}{2})\omega_{rf}\hat{I}_x$ and $\hat{H}=\omega_{rf}\hat{I}_x$, the result for sodium may be generalised to any half-integer quadrupolar spin. For intermediate ratios of ω_Q/ω_{rf}, the signal and the nutation spectrum depend on the duration of the rotary echo pulse pair even in the absence of relaxation effects. In the limiting cases, the only effect the rotary echo pulse pair can have on the nutation spectrum is due to relaxation in the rotating frame, which may attenuate the formation of the rotary echo at the time the nutation pulse begins. The characteristic time constant that governs the attenuation of the rotary echo and hence the nutation signal is $T_{2\rho}$. If $T_{2\rho}$ relaxation processes are important, the attenuation of the rotary echo manifests itself as an absence of broad features in the F_1 projection. Given that the splitting of the rotating frame energy levels is of the order of 100 kHz, molecular motion in this frequency range will lead to a short $T_{2\rho}$ value and consequential broadening in the F_1 projection which may be removed by the rotary echo.

As an example, the rotary echo spectrum of hydrated NaY zeolite is shown in Figure 5.6(d) and was obtained using rotary echo pulses of 2μs duration. The sodium cations

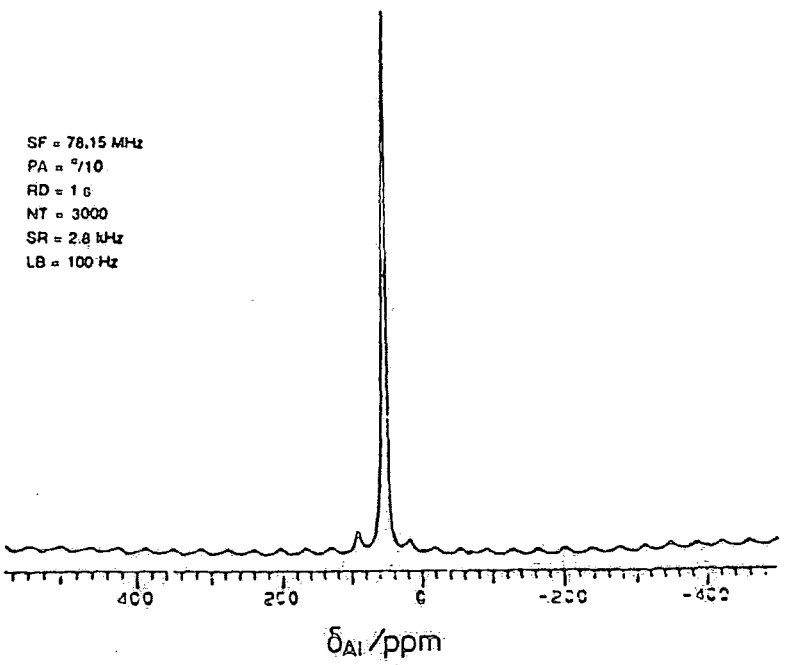

Figure 5.7: ^{27}Al SP MASNMR spectrum of hydrated NH_4^+-ZSM-5.

are mobile and the conventional nutation experiment yields a single peak at ω_{rf}. The rotary echo experiment clearly has little effect indicating that the molecular motion experienced by the sodium cations is in a different frequency range from that required to give rise to efficient $T_{2\rho}$ relaxation processes. A slight narrowing is however observed in the F_1 projection.

5.6 ^{27}Al NMR Studies of NH_4^+-ZSM-5

The hydrated form of NH_4^+-ZSM-5 yields an interesting single-pulse ^{27}Al MASNMR spectrum in the sense that both the $(\pm 3/2, \pm 1/2)$ and $(\pm 5/2, \pm 3/2)$ satellite transitions are observed in addition to the central transition signal (part of the spectrum is shown in Figure 5.7), unlike the situation for most zeolites where non-central transitions are often broadened beyond detection. Previous reports have suggested that for most zeolites, the aluminium environment is of such low symmetry that the non-central transitions are spread over too wide a frequency range to be observable[25]. Variation of pulse duration for constant r.f. field strength shows that the central transition intensity reaches a maximum before the spinning sideband manifold associated with the satellite transitions reaches its maximum, as expected. High-power proton decoupling was observed to have a negligible effect on the single-pulse ^{27}Al MASNMR spectrum.

Quantitative ^{27}Al MASNMR and XRF data are shown in Table 5.2.

TABLE 5.2

	NH_4^+-ZSM-5
Four-coordinate aluminium, % wt (NMR)	3.36
Six-coordinate aluminium, % wt (NMR)	0
Asymmetric aluminium, % wt (NMR)	0
Total aluminium, % wt (XRF)	3.60
Invisible aluminium	0.24

Thus, the vast majority of the aluminium present (93%) resides in an environment of sufficiently high-symmetry that it may be detected by NMR.

5.6.1 Evaluation of quadrupole coupling parameters for hydrated NH_4^+-ZSM-5

It is important to realise that only average quadrupole coupling parameters may be measured due to both the inhomogeneity in the zeolite structure and crystallographic inequivalence. This in itself renders comparison of the experimentally observed ($\frac{1}{2} \leftrightarrow -\frac{1}{2}$) transition lineshape with the calculated MASNMR powder pattern lineshape completely unsuitable.

The variation with magnetic field of the centre of gravity of the central transition may be used to obtain average values for the true isotropic chemical shift and the quadrupole coupling constant.

The centre of gravity (δ_{CG}) of the central transition lineshape is shifted from the true isotropic chemical shift (δ_{CS}) by the second-order quadrupolar shift (δ_{QS}).

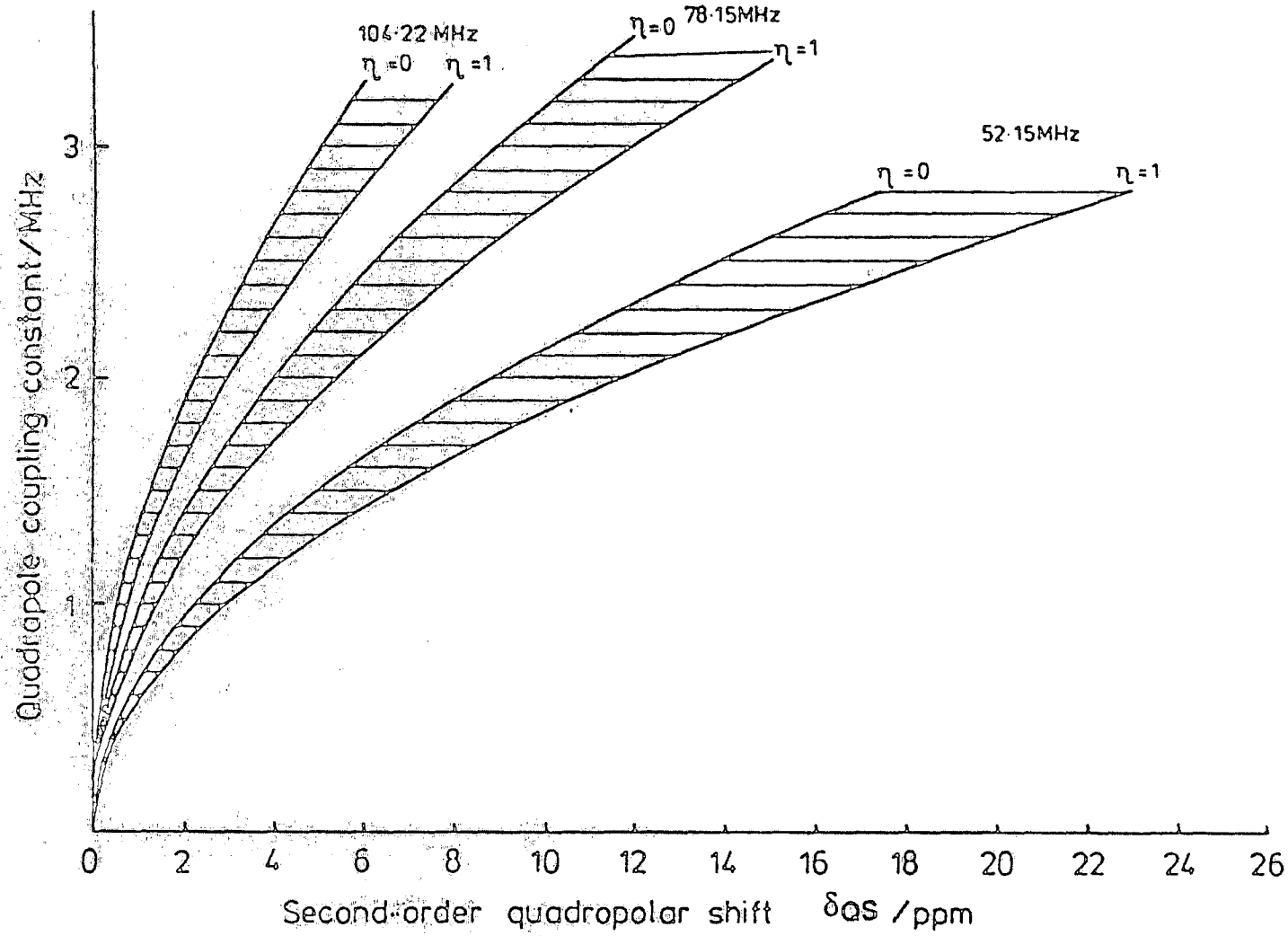

Figure 5.8: Second-order quadrupolar shift as a function magnetic field strength and quadrupole coupling constant.

$$\delta_{CG}(m) = \delta_{CS} + \delta_{QS}(m) \qquad (5.23)$$

For the ^{27}Al MASNMR spectrum central transition ($I=5/2$ and $m=\frac{1}{2}$ for equation 2.41):

$$\delta_{QS}(\tfrac{1}{2}) = -6000\ (\frac{e^2qQ}{h\nu_L})^2(1+\eta^2/3) \qquad (5.24)$$

Thus the quadrupolar shift diminishes with the second power of the Larmor frequency ν_L. A plot of the shift as a function of quadrupole coupling constant for the magnetic fields used in this thesis is shown in Figure 5.8.

The presence of crystallographic inequivalence means that Lippmaa's treatment must be modified. The centre of gravity of a system of peaks is defined as:

$$\delta^*_{CG} = \frac{\sum_i I_i \delta_{CG}(i)}{\sum_i I_i} \qquad (5.25)$$

where $\delta_{CG}(i)$ is the centre of gravity of a peak with intensity I_i. The assumption of the same asymmetry parameter for all of the sites and substitution of 5.23 and 5.24 into 5.25 leads to:

$$\delta^*_{CG} = \frac{\sum_i I_i \delta_{CS}(i)}{\sum_i I_i} - \frac{6000(1+\eta^2/3)}{\nu_L^2} \cdot \frac{\sum_i I_i (e^2qQ/h)_i^2}{\sum_i I_i} \qquad (5.26)$$

Clearly, if the observed peak maximum is considered to be a reasonable approximation of δ^*_{CG}, then a plot of δ^*_{CG} against $1/\nu_L^2$ will lead to a weighted mean isotropic chemical shift and a mean square quadrupole coupling constant. The observed peak maximum will be a poor approximation to the centre of gravity of the spectrum if the peaks characterising each individual site differ greatly either in width at half height or in chemical shift. The assumption that the ratios of the intensities of the peaks remain quantitative for

each of the variable field measurements is of course implicit. The data obtained from a variable field study performed on fully hydrated NH_4^+-ZSM-5 are shown in Table 5.3:

TABLE 5.3

^{27}Al frequency/MHz	δ_{CG}/ppm	$\Delta\nu_{\frac{1}{2}}$/Hz
52.15	53.80	335
78.15	54.68	440

Simultaneous solution of equation (5.26) leads to a value of the root mean square quadrupole coupling constant between 734 kHz (η=1) and 848 kHz (η=0) with a weighted isotropic chemical shift of 55.4 ppm.

The samples were compared in identical states of hydration and a very dilute solution of aluminium chloride was used as reference material. The linewidth was observed to increase with magnetic field suggesting that the distribution of chemical shifts is a more dominating linebroadening influence than the second-order quadrupolar effects at 52.15 MHz.

An attempt was made to compare the above values with the values calculated from the second-order quadrupolar shift of the centre of gravity of the ($\pm^3/2$, $\pm^1/2$) transition. In this case, the true isotropic chemical shift is given by[5]: $\delta_{CG} = \delta_{CG}(^3/2) - {}^1/9\,[\delta_{CG}(^3/2) - \delta_{CG}(^1/2)]$. Unfortunately, the satellite transition centreband is obscured by the centreband of the ($\frac{1}{2} \leftrightarrow -\frac{1}{2}$) transition and the value obtained for the true isotropic chemical shift (and hence quadrupole coupling parameters) using the average position of the second pair of spinning sidebands is very sensitive to the accuracy of the measurement making the method unsuitable. The first pair of spinning sidebands was not used due to the contribution of

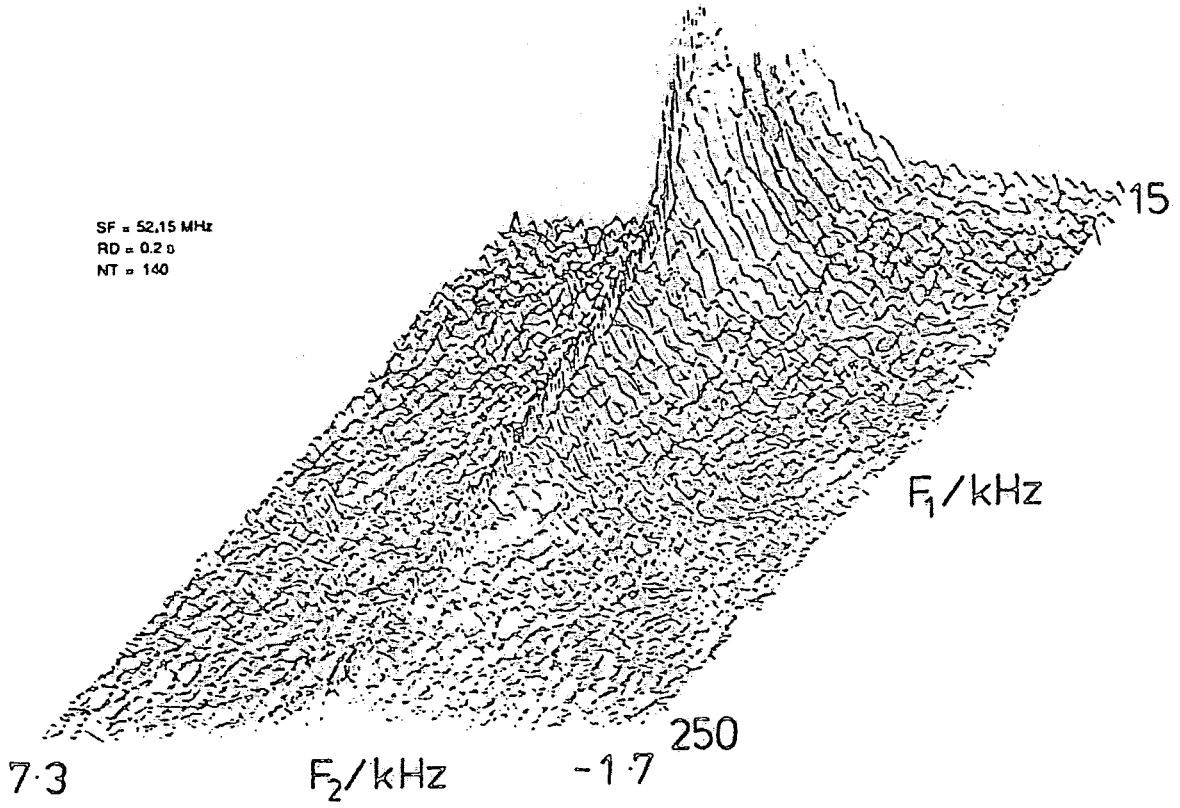

Figure 5.9(a): ^{27}Al nutation spectrum of hydrated NH_4^+-ZSM-5.

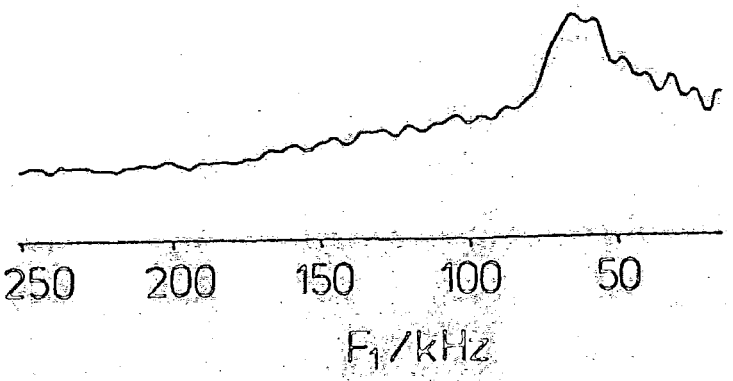

Figure 5.9(b): F_1 projection of Figure 5.9(a).

shielding anisotropy.

The relevant nutation spectrum obtained by 2D Fourier Transformation of the data obtained for a static sample in magnitude mode is shown in Figure 5.9(a). The length of the r.f. pulse was increased by 2μs increments up to 128μs and the amplitude of the r.f. field used was 62.5 kHz.

The nutation spectrum indicates that the situation is more complex than suggested by the single-pulse data, and contrasts with the results of Veeman who studied H-ZSM-5 as a function of dehydration. In that case, peaks were only observed at ω_{rf} and $3\omega_{rf}$ in the F_1 dimension, the relative intensities depending on the state of hydration[11].

The quality of the spectrum is surprisingly good given the Si/Al ratio of 12 (Figure 5.9(a)). Projection in the F_1 direction (Figure 5.9(b)) is in agreement with a value of ω_Q/ω_{rf} between 0.15 and 0.3 (750 kHz$\lesssim e^2qQ/h\lesssim$1.5 MHz) with η=1. The value of e^2qQ/h is much closer to the 750 kHz end of the range. The broad component centred on ω_{rf} is more intense and extends further than expected for the relevant projections of ω_Q/ω_{rf}. Such broadening could arise from $T_{2\rho}$ relaxation processes, and experiments to corroborate this are discussed at a later stage.

5.6.2 Dehydration studies of NH_4^+-ZSM-5

Partial dehydration of NH_4^+-ZSM-5 by heating at 353 K for 12 hours results in a broadening of both the first-order quadrupolar spinning sidebands and the central transition resonance (Figure 5.10(c)). An increase in the quadrupole coupling constant is implied by a shift to lower frequency of the central transition and a corresponding increase

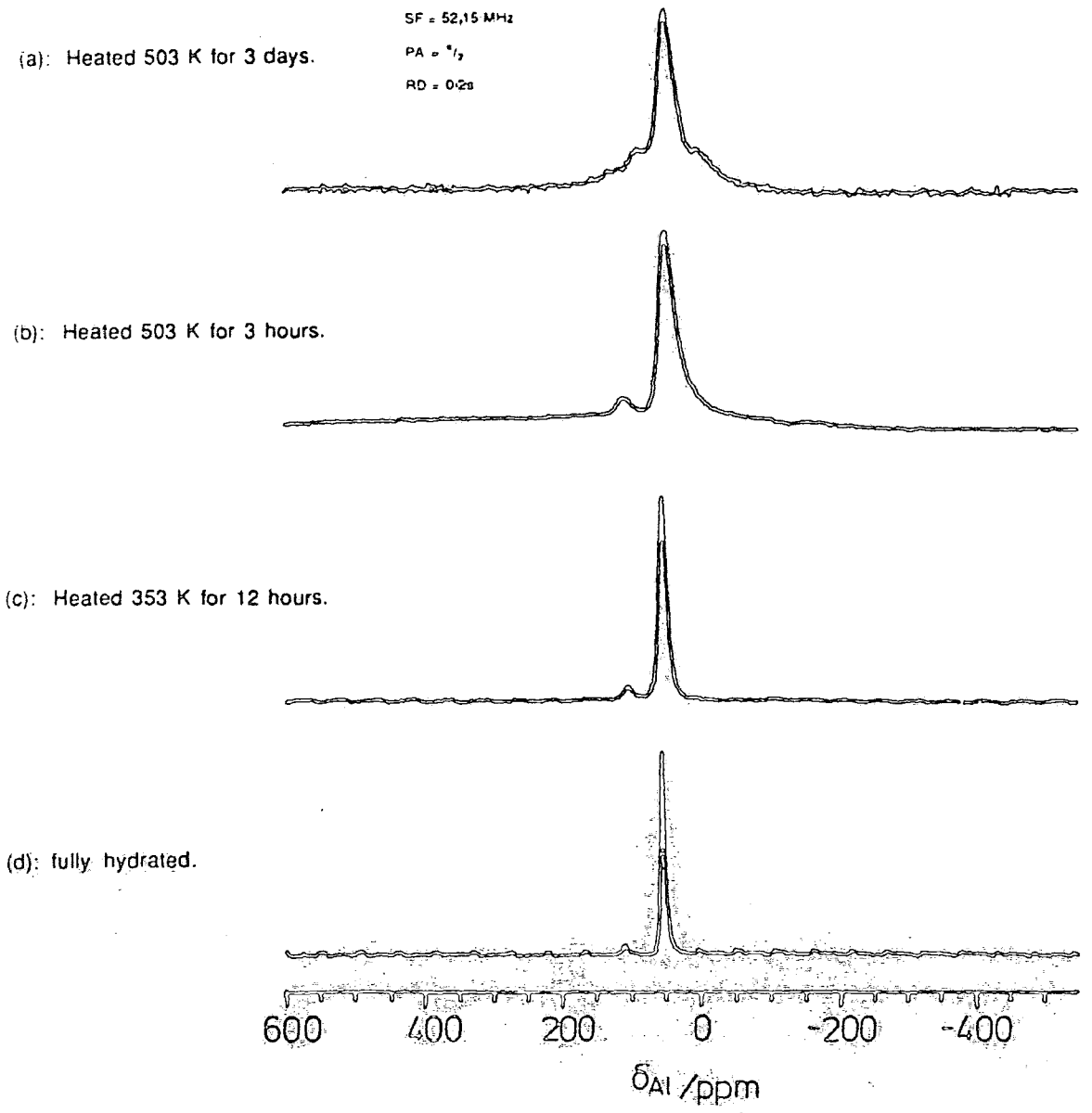

Figure 5.10: ^{27}Al SP MASNMR spectra of NH_4^+-ZSM-5 as a function of dehydration conditions.

in broadening. A decrease in the intensity of the first-order spinning sidebands would be expected given the increase in magnitude of the quadrupole coupling constant (Table 5.4). An increase in width might also be expected given the increased contribution of the shielding anisotropy and second-order quadrupolar effects to the spinning sideband manifold, but the observed increase in linewidth is quite remarkable given the rather modest increase in the quadrupolar coupling constant.

Dehydration for several hours at 503 K resulted in Figure 5.10(b). The first-order spinning sideband pattern has been removed and a broad underlying peak is visible. This is more clearly reflected in Figure 5.11 which is representative of a sample in a slightly lower state of hydration than Figure 5.10(b). The loss of intensity of the first-order spinning sidebands is surprising because although a decrease in intensity of a particular sideband would be expected, the shift to low frequency of the central transition suggests a quadrupole coupling constant of the order of 1.70 MHz, whereas albite shows non-central transition spinning sidebands under similar conditions and is subject to a stronger quadrupole coupling (e^2qQ/h = 3.29 MHz)[26]. The increase in the quadrupole constant was independently confirmed by measuring the central transition intensity as a function of pulse duration and comparing the observed behaviour with the fully hydrated case. Figure 5.12 shows that maximum transverse magnetisation is obtained for shorter pulse duration in the case of the partially dehydrated sample in agreement with the expected behaviour for larger quadrupole coupling predicted in Section 5.2. This result confirms that the observed broadening of

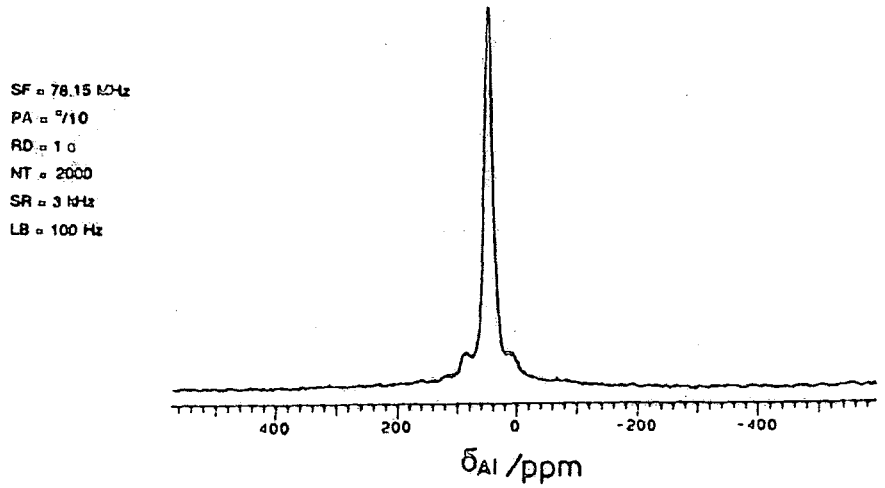

Figure 5.11: ^{27}Al SP MASNMR spectrum of partially dehydrated NH_4^+-ZSM-5. The broad underlying resonance is clearly visible.

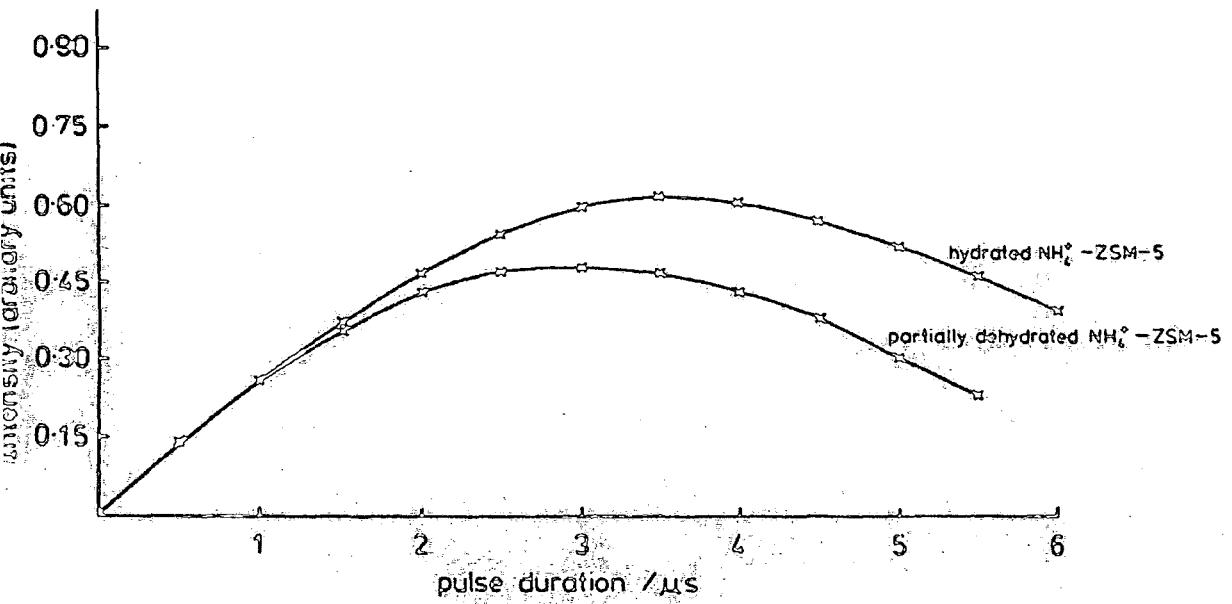

Figure 5.12: Intensity of ^{27}Al central transition resonance as a function of pulse duration for hydrated and partially dehydrated NH_4^+-ZSM-5 ($\omega_{rf} = 41^2/_3$ kHz).

the central transition does not result from an increase in shielding anisotropy, although the remaining spinning sidebands would certainly be expected to contain such a contribution. The possibility of partial decomposition of NH_4^+-ZSM-5 to H^+-ZSM-5 was shown to be irrelevant in this case on account of Figure 5.10(d) being reproduced on rehydration.

Dehydration for 3 days at 503 K results in a further shift to low frequency of the central transition resonance (Figure 5.10(a)). A broad peak is observed due to the overlap of broad spinning sidebands whilst close inspection reveals the presence of a very broad underlying peak. This is more clearly illustrated in Figure 5.16. Rehydration studies suggest that the dehydration process accompanying heating of the sample for 3 days at 503 K is not fully reversible. The rehydrated sample spectrum is more similar to Figure 5.10(c) than (d). There is even a new resonance of low intensity in the six-coordinate aluminium region indicating that slight dealumination has occurred. On complete rehydration, the linewidth of the central transition resonance is increased by 100 Hz relative to the untreated form.

TABLE 5.4 Chemical shift, linewidth and quadrupole coupling constant information as a function of dehydration

Dehydration conditions	δ_{cs}/ppm	$\Delta\nu_{\frac{1}{2}}$/Hz	r.m.s. e^2qQh/MHz
none	53.8	335	0.73
heated 353 K for 12 hours	53.0	700	0.95
heated 503 K for 3 hours	48.6	1358	1.70
heated 503 K for 3 days	46.8	1460	1.93

The r.m.s. e^2qQ/h values were calculated using the value of 734 kHz calculated from the variable field study on the hydrated form (η=1 from the nutation experiment) and

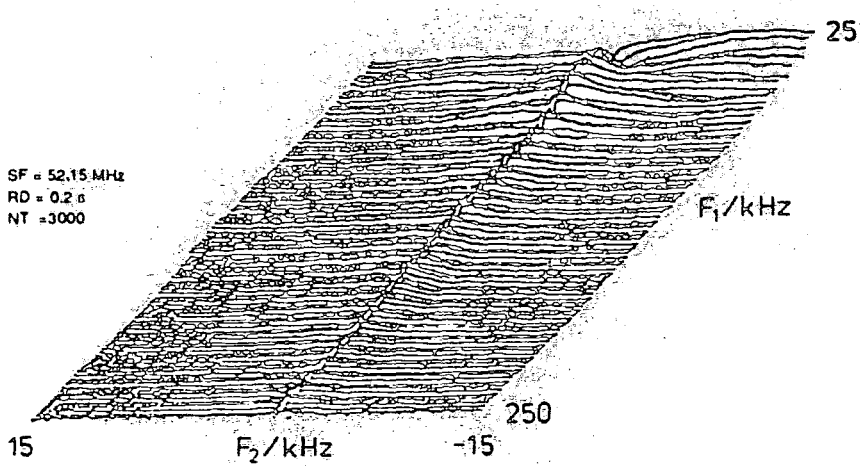

Figure 5.13(a): ^{27}Al nutation spectrum of NH_4^+-ZSM-5 after heating at 503K for 3 hours.

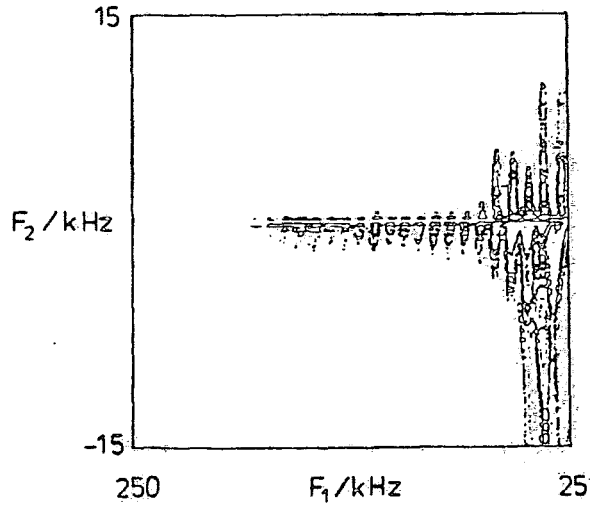

Figure 5.13(b): F_1 projection of Figure 5.13(a).

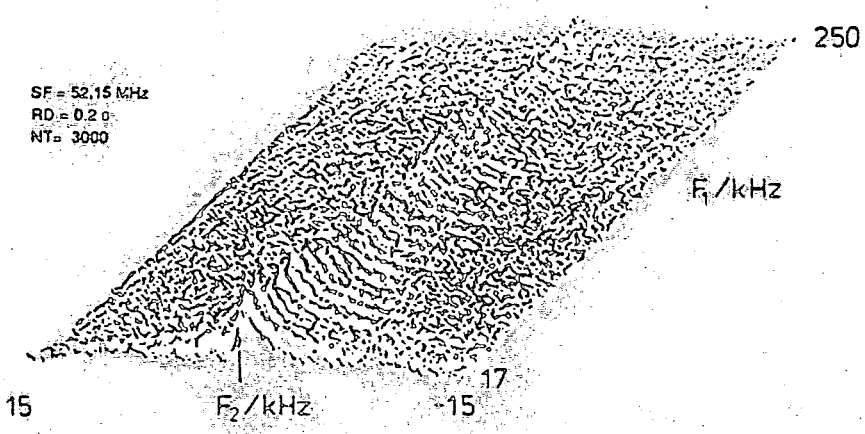

Figure 5.13(c): ^{27}Al nutation spectrum of NH_4^+-ZSM-5 after heating at 503K for 3 days.

subsequent simultaneous solution of equation (5.26) using the lower frequency shift of the thermally treated form. The assumption is made that the true isotropic chemical shift is not altered by dehydration.

Nutation experiments were performed in an attempt to assign the various spectral features to aluminium in different chemical environments for various stages of dehydration.

The ^{27}Al nutation spectrum of the sample heated at 503 K for 3 hours obtained under identical conditions to the spectrum of the hydrated material discussed earlier is shown in Figure 5.13(a). The quality is somewhat reduced with respect to Figure 5.9(a) on account of the broadening in the normal single-pulse experiment but Figure 5.13(a) clearly shows that the broad underlying peak is situated at ω_{rf} and not $3\omega_{rf}$ in the excitation projection as might have been expected. (This is more clearly illustrated in the contour plot shown in Figure 5.13(b)). It necessarily follows that this broad peak does not result from aluminium species in a low symmetry environment, although the contribution of shielding anisotropy to the broadening is difficult to assess. The 2D spectrum is distorted by off-resonance effects at low frequency in the excitation projection. The broadening in the excitation projection is increased with respect to the hydrated case, although the increase is difficult to quantify.

The ^{27}Al nutation spectrum of the sample heated at 503 K for 3 days is shown in Figure 5.13(c). The excitation projection indicates that, as before, the broad contribution to the single-pulse spectrum does not result from aluminium

species in sites of low symmetry. The nutation spectrum is strongly distorted by off-resonance effects but the above observation and pronounced broadening in the F_1 dimensions are clear. The relevant point is that although the peak at $3\omega_{rf}$ becomes more intense on dehydration, the spectra are different to Veeman's results for dehydration of H-ZSM-5, the excitation projection being significantly broadened in the present study.

In conclusion, it was decided that there was sufficient evidence for motional effects from the dehydration studies to justify probing the system further. The decision was based on the facile removal of the first-order quadrupolar spinning sideband pattern for modest increases in the quadrupole coupling constant and the emergence of a broad underlying resonance which may not be attributed to aluminium species in a low symmetry environment. The motional effects are likely to be attributed to the ammonium cations and associated water molecules. Partial dehydration may result in the lowering of the correlation time describing the motion to a value comparable with the rotation frequency of the sample with a consequential broadening of the already reduced first-order quadrupolar spinning sideband manifold[27].

This corresponds to an intermediate situation - further reduction of the correlation time would eventually result in a full first-order quadrupolar spinning sideband manifold ($as\ \tau_C \rightarrow 0$). The increased broadening in the excitation projection of the nutation experiments on increased dehydration is indicative of the increased efficiency of $T_{2\rho}$ processes which are sensitive to motion in the 100 kHz region. Such broadening may also result from a distribution of quadrupolar

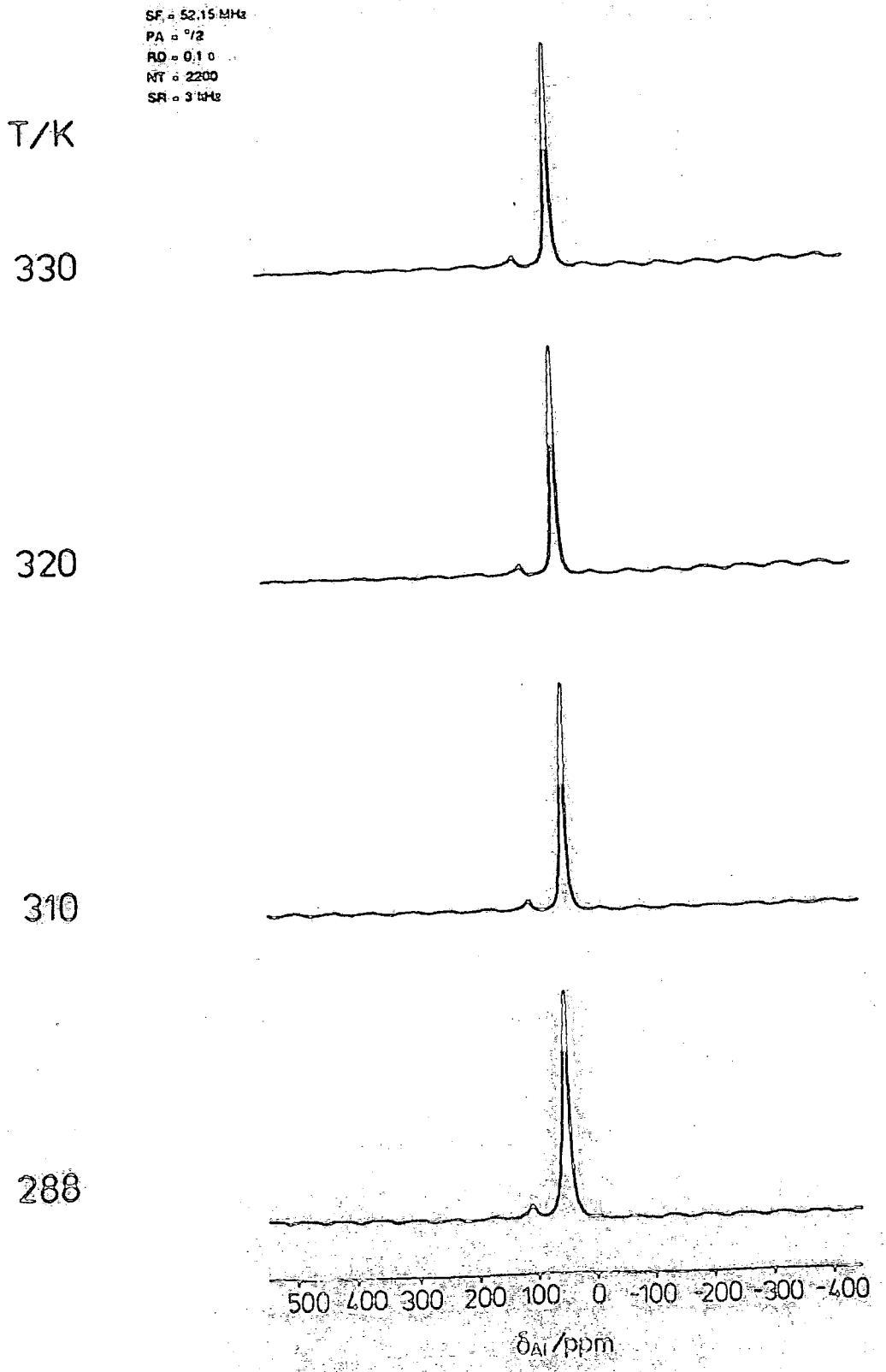

Figure 5.14: ^{27}Al SP MASNMR spectra of NH_4^+-ZSM-5 after heating at 353K for 12 hours as a function of temperature.

parameters and further experiments were implemented to provide evidence for motional effects.

The important point is that if certain cationic motional regimes lead to a collapse of the first-order quadrupolar spinning sideband pattern to a broad hump, then quantitative aluminium studies may lead to an incorrect assignment of the broad hump to non-framework aluminium species.

(A) Temperature dependence of spectra

A sample was prepared in a similar state of hydration to that corresponding to Figure 5.10(c) and the effects of temperature changes are shown in Figure 5.14 and Table 5.5.

TABLE 5.5 Variation of central transition linewidth with temperature

T/K	$\Delta\nu_{\frac{1}{2}}$/Hz
288	700
310	496
320	486
330	473

There is a clear narrowing of the central transition resonance on raising the temperature from 288 to 310 K, in addition to the change in appearance of the first-order spinning sidebands. Increasing the temperature further to 320 and 330 K results in only a slight decrease in width of the central transition resonance, although there is a clear decrease in the intensity of the spinning sideband pattern on the high frequency side of the central transition resonance. A slight shift in the centre of gravity of the central transition resonance from 53.8 ppm at 288 K to 54.7 ppm at 330 K is also observed (Figure 5.15). Reducing the temperature back to 288 K results in a restoration of the broader central transition resonance and the

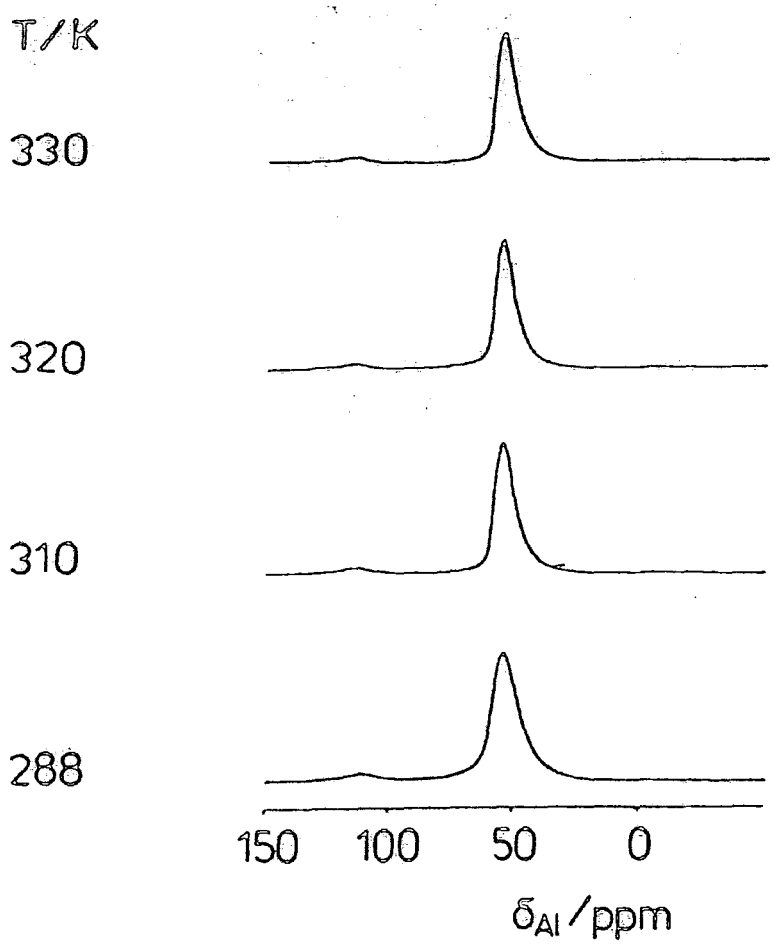

Figure 5.15: Scale expansion of Figure 5.14 to show the effect of temperature variation on the central transition resonance.

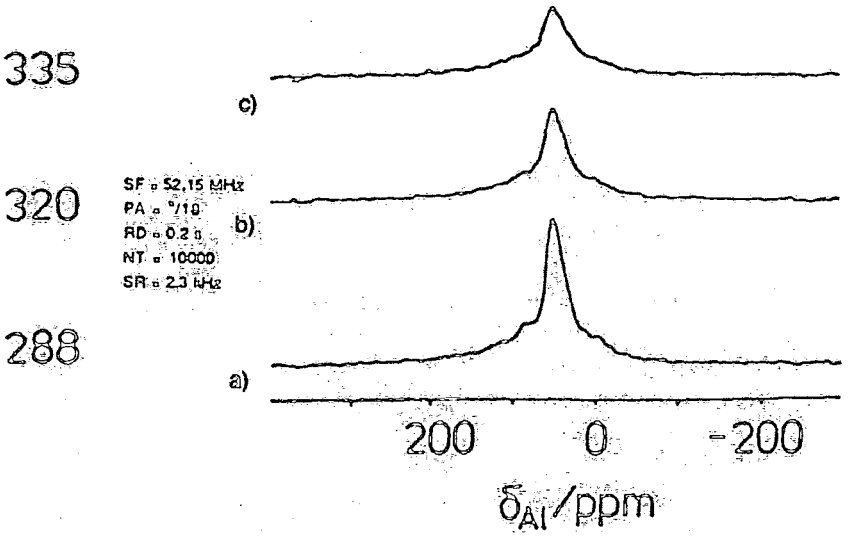

Figure 5.16: ^{27}Al SP MASNMR spectra of NH_4^+-ZSM-5 after heating at 503K for 3 days as a function of temperature.

spinning sideband pattern. Figure 5.10(a) is also sensitive to variation in temperature. Raising the temperature under quantitative conditions results in a loss in intensity of the central transition signal and its associated spinning sidebands. This presumably results from intensity transfer to the very broad resonance which is believed to be broadened beyond detection at higher temperature. The results are shown in Figures 5.16(a)-(c) and Figure 5.16(a) is reproduced on cooling the sample from 335 to 288 K.

Phase changes from the monoclinic to the orthorhombic form have been reported for temperature variation of highly siliceous samples of ZSM-5[28]. The presence of aluminium is known to stabilise the orthorhombic form, and for a Si/Al ratio of 12, the phase transition should have occurred below 272 K, thus ruling out the possibility of a phase transition accounting for the observed temperature dependent spectra. It should however be noted that the first-order quadrupolar spinning sideband manifold would be expected to be very sensitive to even small changes in geometry and it may be that the structure is flexible. In an attempt to distinguish between temperature induced structural fluctuations and cationic motion, further evidence was sought for motion at constant temperature.

(B) Rotary-echo nutation experiment

The excitation projection of the untreated form of NH_4^+-ZSM-5 exhibits a broad peak centred on ω_{rf}. Such broadening may result from either a distribution of quadrupolar parameters or relaxation effects. The linebroadening mechanisms may be distinguished by the use of a rotary echo before the nutation pulse. If $T_{2\rho}$ processes are important, the

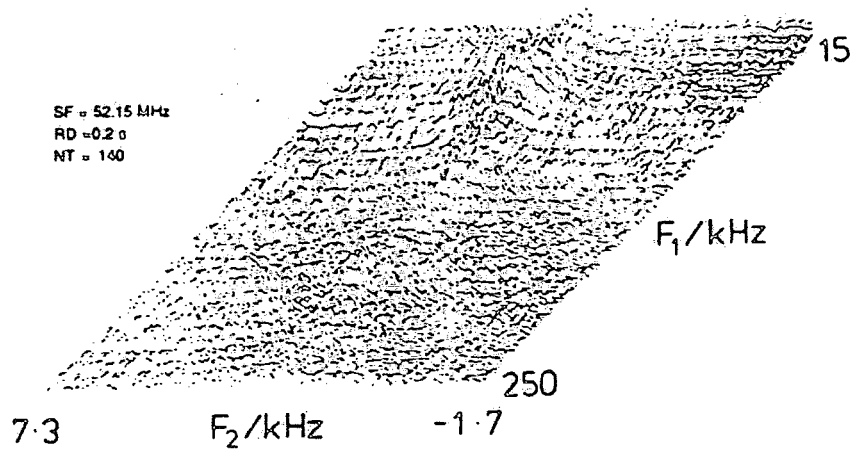

Figure 5.17(a): Rotary-echo ^{27}Al nutation spectrum of hydrated NH_4^+-ZSM-5.

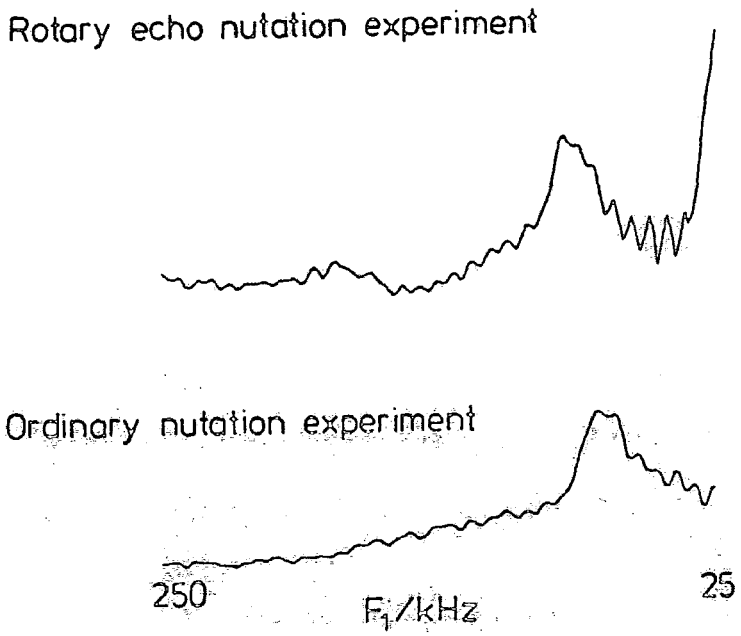

Figure 5.17(b): F_1 projections of rotary-echo and conventional nutation experiments.

attenuation of the rotary echo by relaxation processes leads to an absence of broad features in the excitation projection as explained earlier.

It should be noted that the experiment is only useful for the limiting cases of ω_Q/ω_{rf} (≫ or ≪ 1). For intermediate cases, the signal and nutation spectrum depend on the duration of the rotary echo pulse pair even in the absence of relaxation effects. This effect is neglected here because most of the nutation intensity is found at ω_{rf}. Thus, the only effect the rotary-echo pulse pair can have on the nutation spectrum is due to relaxation in the rotating frame which may prevent the formation of a rotary echo at the time the nutation pulse begins.

The duration of the rotary echo pulses used was 2μs and Figure 5.17(a) indicates that this was sufficient to remove most of the intensity centred on ω_{rf}. In addition, a faint peak at $3\omega_{rf}$ is observed which is due to aluminium in sites of low symmetry - this was formerly concealed by the broad peak. In fact, the excitation projection (Figure 5.17(b)) may be considered to consist of a peak due to aluminium with a quadrupole coupling constant of 710 kHz (η=1) in addition to the peak considered above. Fluctuations of the electric field gradient are the most likely reason for such a linewidth effect. Repeating the ordinary nutation experiment at 320 K resulted in a decrease in the S/N ratio in the excitation projection, suggesting that the broad component was broadened even further by the temperature change.

The increase in broadening in the excitation projection on lowering of water content would thus seem to suggest an increase in the efficiency of $T_{2\rho}$ processes. Maximum effic-

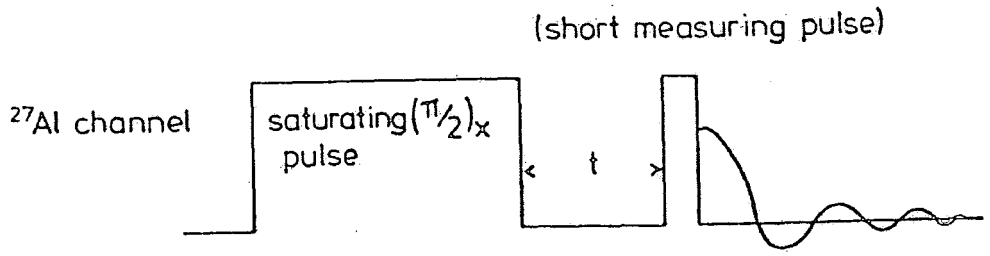

Figure 5.18(a): Determination of ^{27}Al T_1 using a soft pulse to selectively excite the central transition.

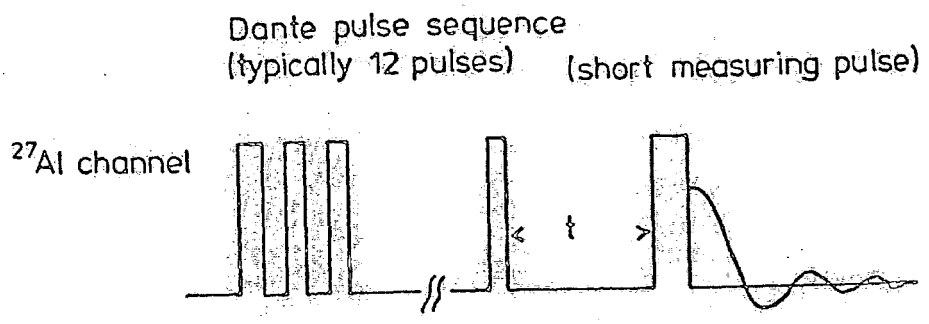

Figure 5.18(b): Determination of ^{27}Al T_1 using a Dante sequence to selectively excite the central transition.

iency would be expected for a fluctuation rate of $\sim 10^5 s^{-1}$.

(C) ^{27}Al T_1 Measurements

In an attempt to provide further details on the nature of the motion, it was decided to measure the aluminium T_1 as a function of hydration. The assumption was made that motional effects influence the T_1 processes of all possible transitions, and the measurements were made on the central transition resonance.

Relaxation of the spins between different levels in a quadrupole split system has been considered from two different initial conditions[29]. One is to start with equal populations in all levels (following the application of a non-selective $\pi/2$ pulse). The other condition is to equalise the populations of the $m=\pm\frac{1}{2}$ levels without altering the populations of the other levels (following the application of a selective $\pi/2$ pulse on the central transition).

Haase *et al*[30] have used the latter method (Figure 5.18(a)) in which selective excitation of the central transition was obtained by the application of a resonant r.f. pulse provided that its amplitude B_1 and duration τ satisfy the condition:

$$\gamma_{Al} B_1 \tau = \pi/2 \qquad (5.27)$$

After a delay time t_1, a short measuring pulse of amplitude B_{1m} and duration τ_m is applied in order to measure the difference in occupancy of the two central levels:

$$\gamma_{Al} B_{1m} \tau_m \leq \pi/12 \qquad (5.28)$$

Due to instrumentation problems, it was not possible to apply a saturating r.f. pulse of the required duration for selective excitation and a saturating Dante sequence was used

to replace the soft pulse (Figure 5.18(b)). Application of a resonant Dante sequence to the central transition would be expected to influence the populations of the $m=\pm\frac{1}{2}$ levels considerably more than the populations of the other levels. The data obtained by use of the pulse sequence shown in Figure 5.18(b) could always be fitted to an exponential decay and a T_1 of 4.4 ms was obtained for the hydrated form of NH_4^+-ZSM-5. This contrasts with a value of 13 ms obtained using an inversion-recovery sequence. For the inversion-recovery experiment, it was unclear whether or not the recovery of the magnetisation was exponential. It is however clear that the two experiments are measuring different physical processes.

For the Dante sequence, 12 equally spaced (7μs) pulses of 0.5μs duration were typically used and the selective saturating pulse was set on the sample using a Dante sequence. The frequency selectivity of such a pulse sequence should be equivalent to that of soft pulse of the same overall duration. The T_1 value obtained was found to be insensitive to accurate setting of the saturating pulse applied to the static sample. In addition, an identical value was observed using a Dante sequence with six 1μs duration pulses spaced at 14μs intervals. Occasionally, unusual behaviour was observed for very small values of t and this was attributed to inaccuracies in the setting of the saturating pulse.

Previous work by Haase *et al*[30] suggests that the controlling mechanism for T_1 relaxation of aluminium in hydrated zeolites is the quadrupole interaction of ^{27}Al with the crystal electric field gradients modulated by the motion of polar

sorbate molecules and/or charge compensating cations. The theoretical T_1 value calculated for such a relaxation mechanism is 2.2 ms in excellent agreement with the observed T_1 value, although the Sternheimer antishielding factor was neglected. Dehydration for several hours at 503K resulted in an increase of the T_1 value to 5.5 ms. It seems that if motional processes are responsible for the removal of the first-order quadrupole spinning sideband pattern after dehydration for several hours at 503 K then the ^{27}Al T_1 value for the central transition is relatively insensitive to these processes. Observation of the ^1H MASNMR spectrum before and after the dehydration procedure is consistent only with the removal of some of the physisorbed water. Evidence for increased rigidity in the system is found after heating at 503 K for 30 hours when spinning sidebands accompany the predominant NH_4^+ resonance observed at 7 ppm in the ^1H MASNMR spectrum. The short ^{27}Al T_1 values for both the hydrated and partially dehydrated forms suggest that an efficient T_1 relaxation pathway is provided by motion in the megahertz region. T_1 measurements on dehydrated zeolites have indicated T_1 values in the 1s region.

The opportunity was also taken to see how the ^{27}Al T_1 value varied for a series of the ZSM-5 samples with different sorbate molecules. The results for the samples shown in Table 5.6 were obtained using air as a cooling gas. It is surprising to observe similar T_1 values for such different systems (difference in mobility of template if present, amount of adsorbed water, and paramagnetic oxygen).

2D Exchange NMR

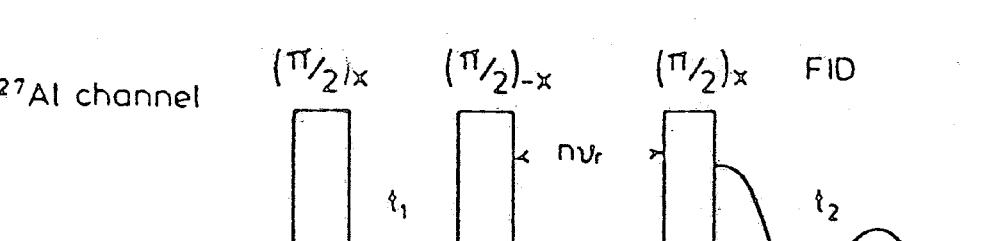

Figure 5.19(a): Conventional 2D experiment used to probe for motion in NH_4^+-ZSM-5.

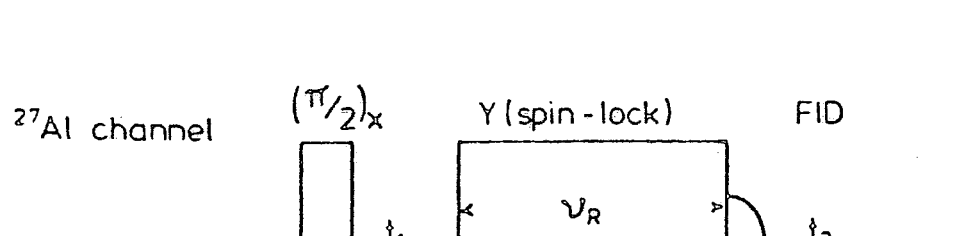

Figure 5.19(b): Exploratory pulse sequence used to probe for motion in NH_4^+-ZSM-5.

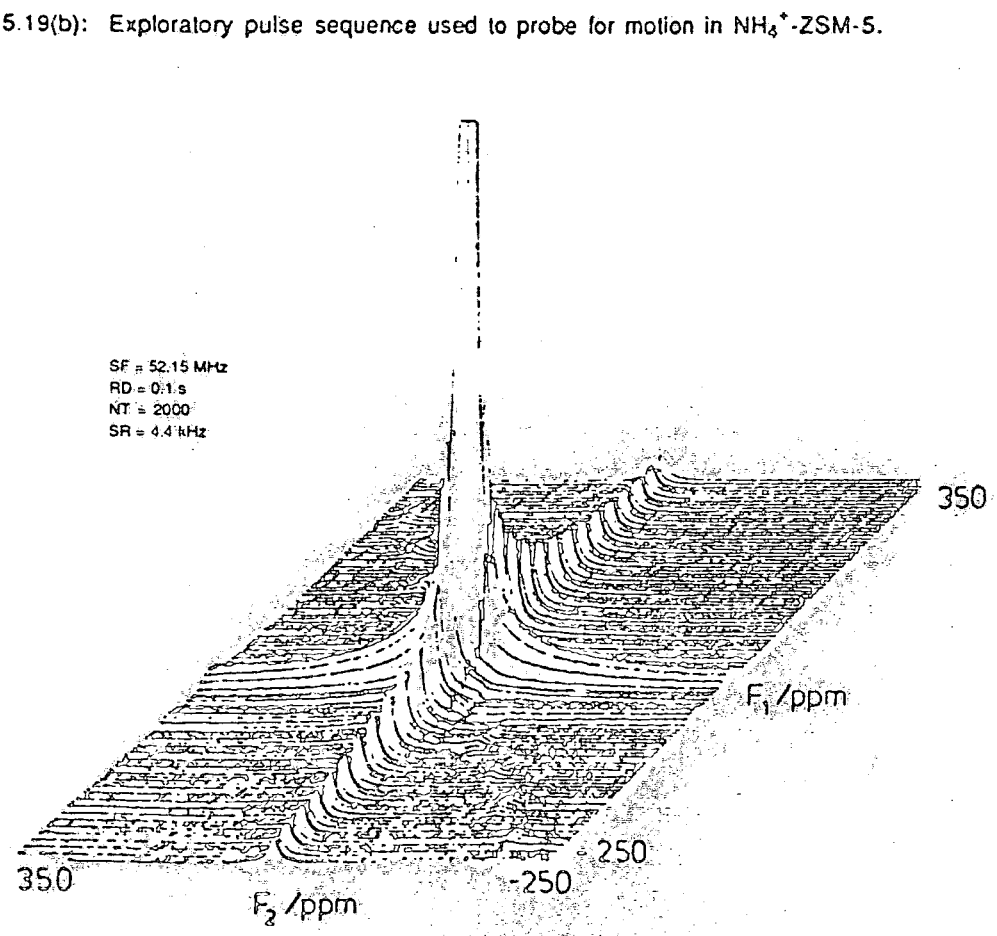

Figure 5.19(c): Control experiment on NH_4^+-ZSM-5 using ν_R = 0ms.

TABLE 5.6 ^{27}Al T_1 values as a function of composition

Compound	T_1/ms
Na, TPA^+-ZSM-5	3.50
Na, K, DEA^+-ZSM-5	1.94
NH_4^+-ZSM-5	4.40

The tetrapropylammonium cation completely fills the channels and excludes the possibility of paramagnetic oxygen contributing to the relaxation mechanism. Given that oxygen is accessible to the channels in NH_4^+-ZSM-5, it seems that oxygen is not the major source of spin-lattice relaxation for aluminium in zeolites. (The work performed by Haase *et al* was performed using nitrogen as the cooling gas).

(D) 2D Exchange NMR

The 2D exchange experiment involves combining the usual two dimensional procedures used for detecting spin exchange and diffusion processes with a MAS experiment as shown by De Jong *et al*[31]. In that case, very slow molecular re-orientations were studied by analysis of the cross-peaks associated with spinning sidebands (shielding anisotropy). The experiment was extended to the case under consideration and the pulse scheme shown in Figure 5.19(a) was used.

The experiment consists of three parts:

(1) an evolution period during which the aluminium spins are labelled with their precession frequency ω_1.

(2) a mixing period (τ_m) in which molecular motion may take place. If any molecular motion has taken place during τ_m, the orientation of the quadrupole tensor may be different in t_1 and t_2.

(3) a detection period, during which the aluminium spins are labelled with a precession frequency ω_2. If molecular motion has occurred during t_1 this would be expected to lead to cross peaks at (ω_1, ω_2) for the non-central transition spinning sidebands.

The mixing time must be synchronised with the rotor period otherwise the aluminium spins will start at another precession frequency at the beginning of t_2, and off-diagonal peaks will be observed even in the absence of motion. In fact, the pulse sequence shown in Figure 5.19(a) was found to be of little value - no peaks were observed from the non-central transition spinning sidebands in the 2D spectrum, which was presumably due to the fact that the quadrupolar nucleus is being treated as a spin-½ nucleus. The condition for refocusing along the z-axis depends on the ratio ω_Q/ω_{rf}.

In an attempt to get around this problem, the exploratory pulse sequence shown in Figure 5.19(b) was used. The mixing time was chosen to be one rotor period (225μs) which was significantly shorter than the measured ^{27}Al T_1 value. Only axial peaks are observed for experiments of this type if the mixing time is longer than T_1. For zero mixing time, no cross peaks were observed as expected (Figure 5.19(c)), although large feet associated with peaks on the diagonal which were not removed by phase cycling were observed. It is probable that their origin lies in the fact that the 2D Fourier Transformation was performed in magnitude mode. No cross-peaks were observed for a mixing time of 227μs and exaggeration of the vertical scale suggested the absence of low intensity cross-peaks. It seems that if motional processes are responsible for the broadening of the first-order quadrupolar

spinning sideband pattern after dehydration for several hours at 353 K then they do not occur on a timescale of 227μs. It was not possible to probe for slower molecular motion because the spinning sideband intensity became too feeble at longer spin-locking times. For the above experiment, the maximum lengths of t_1 and t_2 exceed τ_m and may have led to a linebroadening in both dimensions had any motion occurred during these periods, which was not observed[32,33].

(E) Variable spinning rate experiments

The spinning sideband pattern associated with the partially hydrated form was observed as a function of spin rate in an attempt to probe lower frequency motions (<4.4kHz). The spinning sideband pattern collapsed to yield a broad underlying peak at slow spin rates. Unfortunately, this experiment cannot distinguish between motional effects at slow spin rates and the fact that the broad spinning sidebands may merge into one another. A positive result could only be claimed if the spinning sidebands disappeared on increasing the spin rate between the situation outlined above and 4.4 kHz.

- - - - - - - - - - - - - - -

In conclusion, the previous sections illustrate the experimental techniques available for probing a wide range of motional regimes in quadrupolar systems. In some cases, caution must be exercised in concluding that motional processes alone account for the experimental observations. Less significance should be attached to the 2D exchange experiment with respect to the other techniques due to its exploratory nature.

Evidence for motional processes is unambiguously provided by the short ^{27}Al T_1 values observed for both the hydrated and

partially dehydrated forms of NH_4^+-ZSM-5. It is interesting to note that the motional effects of the adsorbed species do not yield off-diagonal elements in the 2D exchange experiment which points to the probability that either the cross-peaks in the 2D exchange experiment are too faint to be observed or that the motion of the adsorbed species corresponds to small angle fluctuations of the axes defining the principal tensor components of the electric field gradient in the vicinity of the aluminium nuclei. The theoretical effect of fast small angle oscillations on the spectra of the quadrupolar nuclei is considered in the next section.

T_1 relaxation is sensitive to motion in the megahertz region and the similarity of the ^{27}Al T_1 values for hydrated and partially dehydrated form of ZSM-5 suggests similar motional regimes in both cases. However, if the broadening/disappearance of the first-order quadrupolar spinning sideband pattern that occurs on partial dehydration of NH_4^+-ZSM-5 is to be attributed to motional effects in the same way that the broadening/disappearance of spinning sidebands resulting from shielding anisotropy is explained, then the motion must correspond to a much slower regime. The most likely explanation is that partial dehydration of the fully hydrated NH_4^+-ZSM-5 sample results in a slight modification of the motion in NH_4^+-ZSM-5 which leads to a very efficient relaxation pathway for the non-central transitions. However, the possibility of the production of a range of motional regimes on partial dehydration may not be discounted and novel experiments to probe lower frequency regimes are required. The 2D exchange experiment (subject to the constraints discussed above) suggests that the frequency of such motion must be less than 4.4 kHz.

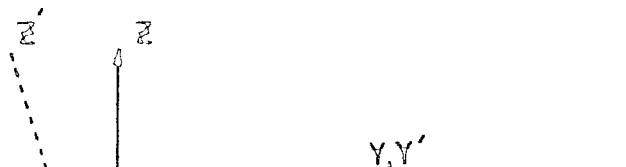

Figure 5.20: Coordinate frame used for the calculation of the effect of small angle fluctuations on the quadrupolar Hamiltonian.

It seems that hydrated NH_4^+-ZSM-5 and natural zeolites such as albite represent limiting cases for which non-central transition spinning sidebands may be observed. In the former case, the solvated NH_4^+ ion is unusually mobile[34], whereas in the case of albite, the counterbalancing ions/associated water molecules constitute a more rigid system as indicated by ^{23}Na and ^{1}H NMR experiments. Partial dehydration of hydrated NH_4^+-ZSM-5 presumably reduces the correlation time for motion to an intermediate regime which is similar to that observed for most ZSM-5 samples for which no spinning sideband pattern is observed.

While the conclusions drawn about the motion have been of a general nature, it is clear that motional processes that lead to a cancellation of the first-order quadrupolar spinning sideband pattern and its subsequent replacement by a broad underlying peak may complicate the assignment of spectral features to particular aluminium moieties during quantitative aluminium NMR work. For instance, broad resonances could be wrongly assigned to aluminium in environments of low symmetry when they could result from slow motion/transition-dependent relaxation processes. Finite deadtime constraints may prevent the resolution of this problem by comparison with other quantitative aluminium techniques (*e.g.* XRF).

5.6.3 Theoretical effect of small angle oscillations of EFG tensor components on ^{27}Al spectra

A simple model is used for the description of the fast molecular motion which leads to the calculation of the averaged electric field gradient tensor components in the coordinate frame shown in Figure 5.20. The theoretical effect

of small angle torsional oscillations on quadrupolar nuclei has been discussed by Bayer[35]. In the case of zeolites, the hydrated cations are a significant distance from the framework aluminium species and are thus expected to have a minor perturbing influence on the electric field gradient experienced by the aluminium spins. It is assumed that in the molecular frame, the field gradient has cylindrical symmetry about an axis OZ' and that the motion of this frame due to the mobility of adsorbed species is a small angle toggle of OZ' about OZ in a plane perpendicular to an axis OY in the coordinate frame shown. Given the averaged tensor components in the coordinate frame, the nuclear spin Hamiltonian in the laboratory frame may be calculated and hence a qualitative comparison may be made with the static case. The effect of temperature variation is also considered.

In the molecular frame, the tensor components are given by:

$$V_{ZZ'} = eq. \quad V_{XX'} = V_{YY'} = -eq/2 \tag{5.29}$$

After a toggle of θ about OZ, the tensor components in the OXYZ frame are given by the usual formulae:

$$V_{ZZ} = \frac{eq}{2} (3\cos^2\theta - 1) \tag{5.30}$$

$$V_{XX} = \frac{eq}{2} (3\sin^2\theta - 1) \tag{5.31}$$

$$V_{YY} = \frac{-eq}{2} \tag{5.32}$$

$$V_{XZ} = \frac{-3eq}{2} \sin\theta\cos\theta \tag{5.33}$$

also $V_{YZ} = V_{XY} = 0$

Now the average values of $\cos^2\theta$ and $\sin^2\theta$ are given by:

$$\langle\cos^2\theta\rangle=\tfrac{1}{2}(\cos^2\theta+\cos^2-\theta)=\cos^2\theta \simeq 1-\theta^2 \text{ for small } \theta \qquad (5.34)$$

$$\langle\sin^2\theta\rangle=\tfrac{1}{2}(\sin^2\theta+\sin^2-\theta)=\sin^2\theta \simeq \theta^2 \text{ for small } \theta \qquad (5.35)$$

Similarly, $\langle\sin\theta\rangle=\tfrac{1}{2}(\sin\theta+\sin-\theta)=0$ (5.36)

Thus, the averaged tensor components are given by:

$$\bar{V}_{ZZ} \simeq eq(1-3\theta^2/2) \quad \bar{V}_{YY} = -eq/2 \quad \bar{V}_{XX} \simeq \frac{eq}{2}(3\theta^2-1) \qquad (5.37)$$

and the averaged principal components lie along the axis of the coordinate frame defining the principal axis system for the static case. In the static case, the Hamiltonian for the quadrupole interaction in the principal axis system of the electric field gradient tensor is[1]:

$$\hat{H}_Q = \frac{eQ}{4I(2I-1)} [V_{ZZ}(3\hat{I}_Z^2-\hat{I}^2) + (V_{XX}-V_{YY})(\hat{I}_X^2 - \hat{I}_Y^2)] \qquad (5.38)$$

$$= \frac{e^2qQ}{4I(2I-1)} (3\hat{I}_Z^2 - \hat{I}^2) \qquad (5.38a)$$

The averaged Hamiltonian in the principal axis system for the motion described above is given by:

$$\bar{\hat{H}}_Q = \frac{eQ}{4I(2I-1)} [eq(1-3\theta^2/2)(3\hat{I}_Z^2-\hat{I}^2) + \frac{3\theta^2 eq}{2} (\hat{I}_X^2-\hat{I}_Y^2)] \qquad (5.39)$$

$$= \frac{e^2qQ}{4I(2I-1)} (1-3\theta^2/2) \{ (3\hat{I}_Z^2-\hat{I}^2) + \frac{3\theta^2}{2-3\theta^2} (\hat{I}_X^2-\hat{I}_Y^2) \} \qquad (5.39a)$$

The second term in the above equation represents a small departure from axial symmetry. However, in the presence of a strong magnetic field, it is more appropriate to consider the Hamiltonian in the laboratory frame. In the laboratory axis system, the average Hamiltonian may be expressed as:

$$\bar{\bar{H}}_Q = \frac{3e^2qQ(1-3\theta^2/2)}{4I(2I-1)} \{ 3\hat{I}_z^2\cos^2\beta + 3\hat{I}_x^2\sin^2\beta + 3\sin\beta\cos\beta(\hat{I}_z\hat{I}_x+\hat{I}_x\hat{I}_z) - \hat{I}^2+(\frac{\theta^2}{4-6\theta^2}).[\cos2\phi(\hat{I}_y^2-\hat{I}_x^2)\sin2\phi(\hat{I}_x\hat{I}_z+\hat{I}_y\hat{I}_x)]\} \quad (5.40)$$

where β and ϕ are the polar angles describing V_{ZZ} relative to the z-axis.

Comparison with standard formulae reveals that the first-order corrections to the transition frequencies are given by:

$$\nu_{m\leftrightarrow m-1} = \nu_L - \frac{3e^2qQ(1-3\theta^2/2)}{4I(2I-1)h} [(3\cos^2\beta-1)+(\frac{3\theta^2}{2-3\theta^2})\sin^2\beta\cos2\phi] (m-\tfrac{1}{2}) \quad (5.41)$$

Thus, for an $I=5/2$ spin ($e^2qQ/h=1$MHz), the frequency of the $(-3/2\leftrightarrow-1/2)$ transition is reduced by 6,854 Hz (for $\beta=0$) relative to the static case. A maximum value of $\pi/18$ was used for θ for which $\sin\theta\simeq\theta$. Second-order effects have been neglected in the calculation.

The effect of the above motion on the non-central transition lineshapes will be to scale them by the factor $(1-3\theta^2/2)$ with an accompanying slight distortion in appearance due to the departure from axial symmetry relative to the static case for which $\theta=0$. Increasing the temperature would be expected to result in an increase in θ and a corresponding increase in scaling and deviation from axial symmetry.

The corresponding correction to the frequency of the central transition is given by:

$$\nu_{\frac{1}{2}\leftrightarrow-\frac{1}{2}} = \nu_L - (\frac{3e^2qQ(1-3\theta^2/2}{2I(2I-1)h})^2 \frac{1}{6\nu_L} (I(I+1)-3/4) [A(\phi)\cos^4\beta+B(\phi)\cos^2\beta+ C(\phi)] \quad (5.42)$$

where $A(\phi) = \frac{-27}{8} + (\frac{9}{4})(\frac{3\theta^2}{2-3\theta^2})\cos 2\phi - (\frac{3}{8})(\frac{3\theta^2}{2-3\theta^2})^2 \cos^2 2\phi$ (5.42(a))

$B(\phi) = \frac{30}{8} - \frac{1}{2}(\frac{3\theta^2}{2-3\theta^2})^2 - 2(\frac{3\theta^2}{2-3\theta^2})\cos 2\phi + (\frac{3}{4})(\frac{3\theta^2}{2-3\theta^2})^2 \cos^2 2\phi$ (5.42(b))

$C(\phi) = \frac{-3}{8} + \frac{1}{3}(\frac{3\theta^2}{2-3\theta^2})^2 - (\frac{1}{4}).(\frac{3\theta^2}{2-3\theta^2}).\cos 2\phi - (\frac{3}{8})(\frac{3\theta^2}{2-3\theta^2})^2 \cos^2 2\phi$ (5.42(c))

For $\beta=\phi=0$ and an $I=5/2$ spin ($e^2qQ/h = 1$ MHz), a shift to higher frequency of 0.2 Hz would be expected relative to the static case assuming a value of $\pi/18$ for θ. Clearly, the energy levels of the central transition are affected by a combination proportional to θ^4/ν_L (neglecting higher order terms in θ) which makes the second-order shift negligible with respect to the first-order interaction experienced by the non-central transitions.

The motion described above will scale the central transition lineshape by a factor proportional to $(1-3\theta^2/2)^2/\nu_L$ and there will be a slight distortion from axial symmetry as in the case of the non-central transitions. Again, increased departure from axial symmetry and increased scaling should result on raising the temperature.

If the slight deviation from axial symmetry is ignored, the shift in the centre of gravity of the powder pattern of the central transition from the unperturbed frequency ν_L is given by:

$$\nu_L - \nu_{CG} = (\frac{3e^2qQ(1-3\theta^2/2)}{2I(2I-1)h})^2 \frac{1}{120\nu_L}(2I-1)(2I+3) \qquad (5.43)$$

For the conditions described above, the motion will result in a shift to higher frequency of 105 Hz of the centre of gravity.

Although the above equations were derived assuming

a stationary Hamiltonian, the qualitative features of the above results for temperature variation should be applicable to the case where sample spinning is used. However, the changes observed in the ^{27}Al spectrum of partially dehydrated NH_4^+-ZSM-5 on temperature variation are inconsistent with the conclusions deduced above. It is felt that an explanation may be sought in a more sophisticated model that takes account of the possibilities of; a fluctuation frequency less than the frequencies of the spin Hamiltonian for which the theoretical derivation would not be valid, relaxation phenomena, and large angle fluctuations which might result from a flexible framework.

5.7 ^{23}Na Studies of NaY zeolite

The NaY sample was initially studied by ^{23}Na NMR in an attempt to see if the different cation sites could be distinguished in the NMR spectrum. All of the cations are located in one of three sites: I, I′, or II (Figure 4.10), and site II′ may only be occupied by adsorbed molecules such as water. The adjacent sites I and I′ are not simultaneously occupied. Thus, the potential for probing sodium cation distributions exists, with the possibility of extending the results to the case where H^+ is the cation.

For rapid molecular rotational diffusion ($\omega_o\tau_c << 1$, where ω_o is the Larmor frequency and τ_c is the rotational correlation time) all the transitions are degenerate and exponential T_1 and T_2 relaxation behaviour is observed. For slower motion ($\omega_o\tau_c \geq 1$) as in micelles, membrane vesicles, or biological macromolecules, the widths and frequencies of the various transitions may be different[36].

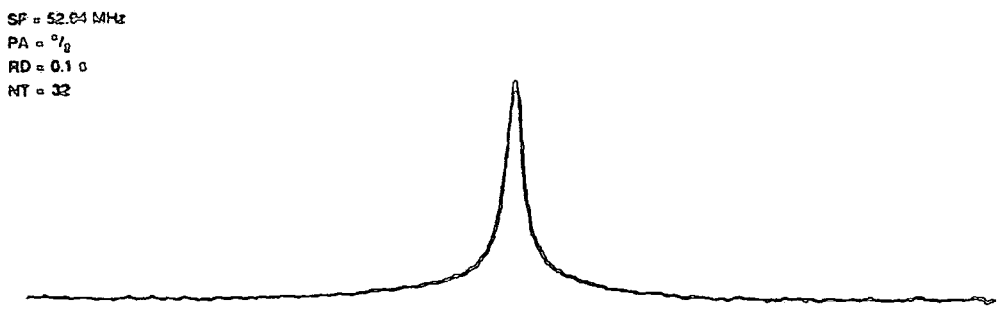

Figure 5.21: ^{23}Na SP NMR spectrum of hydrated NaY zeolite.

The single-pulse ^{23}Na MASNMR spectrum of the fully hydrated form is disappointing in that only one symmetric resonance was observed with no spinning sidebands suggesting that the Na^+ ions are located in high-symmetry sites, coordinated to water molecules. However, the spectrum was difficult to phase and the static spectrum shown in Figure 5.21 reveals the presence of a broad underlying peak in addition to the relatively narrow resonance. It was impossible to phase the spectrum so that both the broad and narrow component have the same chemical shift. The ^{23}Na nutation spectrum is shown in Figure 5.4(e) and the excitation projection reveals a signal at ω_{rf} only which confirms that the broad resonance does not result from the presence of sodium ions in a low symmetry environment.

It would seem that $\omega_o \tau_c$ is greater than 1 (slow tumbling of Na^+ ions), in which case for an $I=^3/_2$ nucleus, the lineshape consists of two components: 60% of the signal intensity characterised by a large linewidth and 40% of the total signal intensity characterised by a relatively smaller linewidth[36]. The two components have different Larmor frequencies, but the second-order dynamic frequency shift is often difficult to detect because its value is small relative to the linewidth of the broad component.

However, the experimental demonstration that this is the case is not straightforward. Attempts were made to simulate the spectrum using two Lorentzian peaks. Such an approach of course assumes that the spectrum is phased correctly and that quadrupolar interactions do not introduce asymmetry in the lineshapes. In addition, it is assumed that the hydrated sodium ions exist in very similar environments. It was not

possible to simulate the spectrum using two Lorentzian peaks although a good fit was obtained using peaks of mixed Gaussian-Lorentzian character. The ratio of the intensities of the narrow component to that of the broad component was 60:40 which is the wrong way around in so far as the theory is concerned. However, it should be remembered that a significant proportion of the intensity of the broad component is lost in the 13μs deadtime. More convincing evidence is provided by the fact that the linewidth at half height (which is overwhelmingly dominated by the narrow component) is reduced on increasing the magnetic field strength which would be expected in the slow motion regime[37]. The linewidth (in Hz) should be reduced by a factor of $^{2}/_{3}$ which is close to the reduction observed.

It is of course possible that there could be two chemically distinct types of sodium present. During the course of this work, results were published that suggested that the very broad species resulted from sodium ions existing at site 1 in the hexagonal prisms[38]. Two other substantially narrower resonances were also observed which were assigned to sodium in sites I′ and II. However, no proof was presented which suggested that the motion of the sodium cations corresponded to the extreme narrowing region, which is necessary for such an assignment. In addition, no explanation was given for the large linewidth for the site 1 species which presumably indicates a shorter T_2 for these species relative to sites I′ and II.

If the extreme narrowing region obtains in the present case, then the broad component would be expected to have a significantly shorter T_1 value than the narrow component.

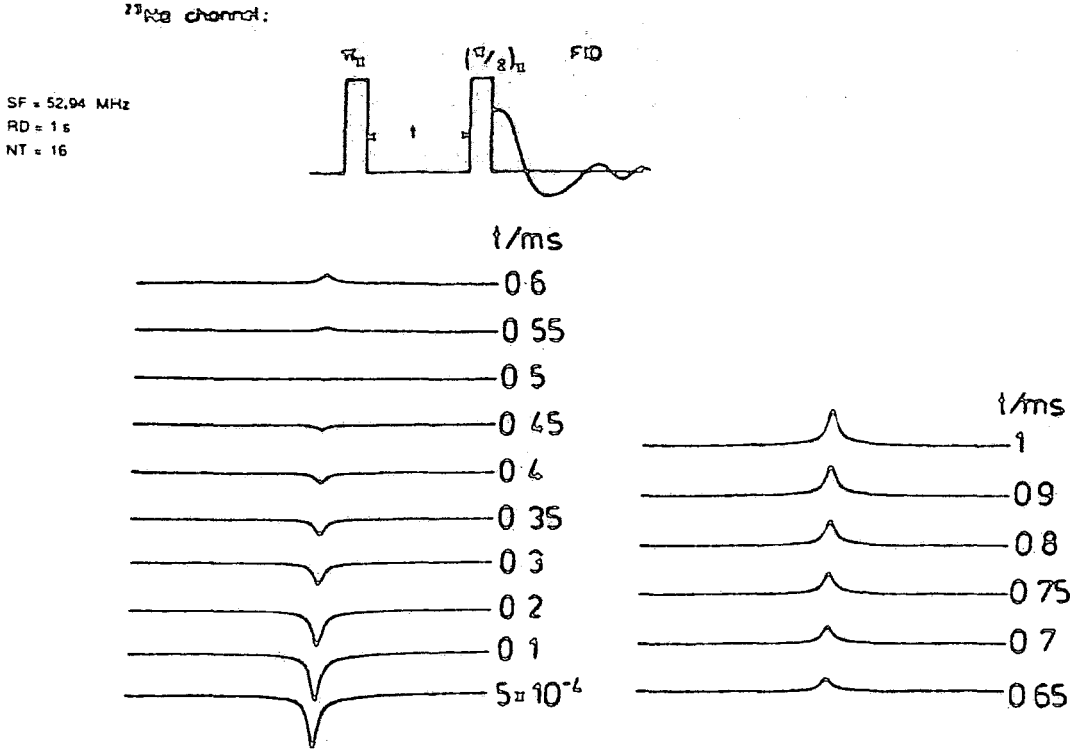

Figure 5.22: Application of the conventional inversion recovery pulse sequence to NaY zeolite.

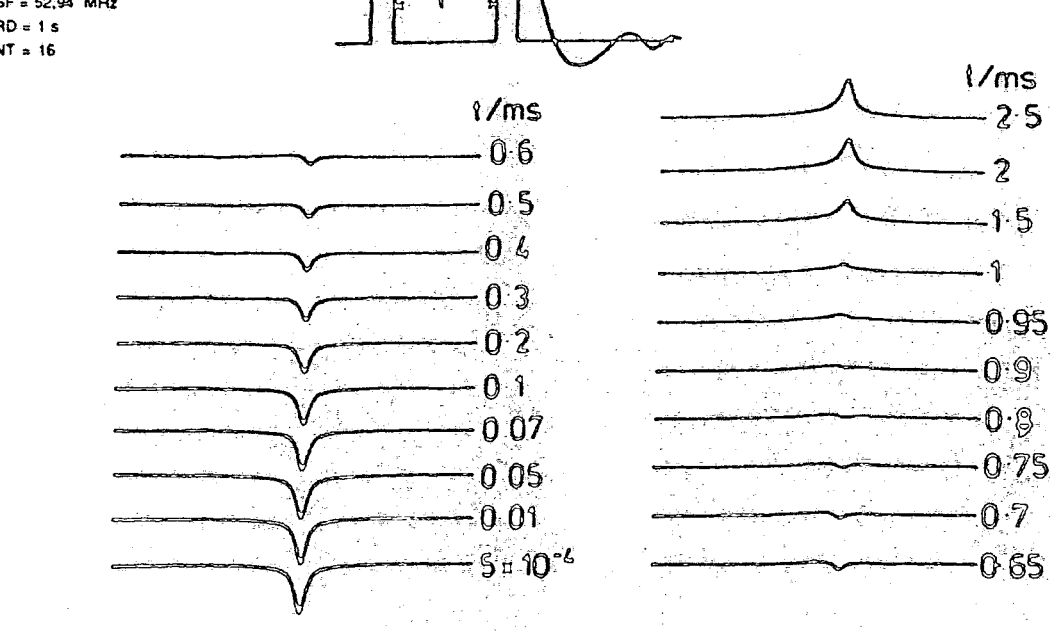

Figure 5.23: The effect of using a short measuring pulse in the inversion recovery sequence.

However, application of the usual $\pi-\tau-(\pi/2)$ inversion recovery sequence does not distinguish between the two components (Figure 5.22). This behaviour would be expected in the slow motion regime because a $\pi/2$ sampling pulse will mix the two longitudinal recovery rates[39]. The $\pi-\tau-(\pi/18)$ inversion recovery experiment clearly resolved the longitudinal relaxation of the broad and narrow component peaks (Figure 5.23) as expected if a second-order dynamic frequency shift of the non-central transitions is present. Theoretical calculations have shown that the broad component should decay exponentially and with a time constant shorter than that of the narrow component[39]. A T_1 value of 4.3×10^{-4}s is estimated from the null point of the broad component which compares with a T_1 value of 1.3×10^{-3}s estimated for the narrow component assuming simple exponential recovery in both cases. The relaxation measurements thus provide conclusive evidence that the motion corresponds to the slower regime and that a second-order dynamic frequency shift is being observed. The results also clearly illustrate the care that must be exercised when using ^{23}Na NMR as an analytical tool for providing information on the cation distribution.

Interesting behaviour is observed on temperature variation (Figure 5.24). The width of the narrow component as a function of temperature is summarised in Table 5.7.

TABLE 5.7 Width and shift of the narrow resonance as a function of temperature at a sodium frequency of 52.98 MHz.

T/K	$\Delta\nu_{\frac{1}{2}}$(Hz)	δ/ppm
286	712	-0.3
315	850	-3.2
330	674	-4.4

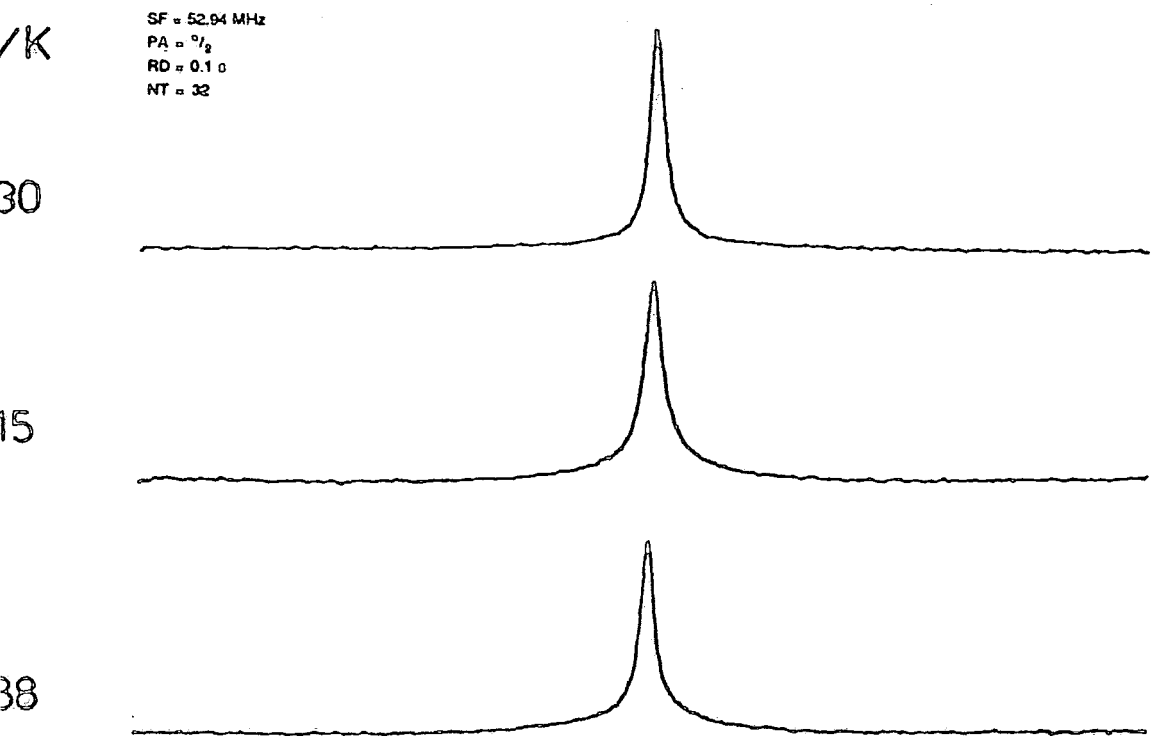

Figure 5.24: ^{23}Na SP NMR spectra of NaY zeolite as a function of temperature.

The results are reversible in all cases. Theory predicts that the linewidth of the narrow component increases as the temperature is raised in the slow motion limit and then decreases with temperature in the fast-motion limit[37]. The data are thus consistent with a change in motional regime over a fairly modest temperature range. Complex changes in the linewidth of the broad species are observed on temperature variation. Under quantitative conditions it seems that there is a transfer of intensity from the broad component to the narrow component until at 330 K, the non-Lorentzian character of the spectrum has almost disappeared. This result is also in agreement with the change in motional regime outlined above. The shift to low frequency of the narrow resonance with increasing temperature is, however, more enigmatic. Usually, such a shift would be interpreted in terms of an increase in second-order quadrupole coupling. However, there is no noticeable increase in asymmetry of the lineshapes at higher temperatures and the linewidths are not consistently broadened as the temperature is increased. Incidentally, the change in chemical shift between 286 and 330 K would suggest a gain in the quadrupole coupling constant of approximately $\sim$700 kHz which is certainly not observed in the excitation projections of the nutation spectra discussed below. Temperature perturbations of the system might be expected to lead to a rearrangement of the cation positions, but the shift is significant and this seems an unlikely interpretation of the data over such a modest temperature range. It seems more likely that the shift corresponds to some motional effect. If this interpretation is correct, then care would have to be taken in assigning various narrow sodium shifts to specific cation

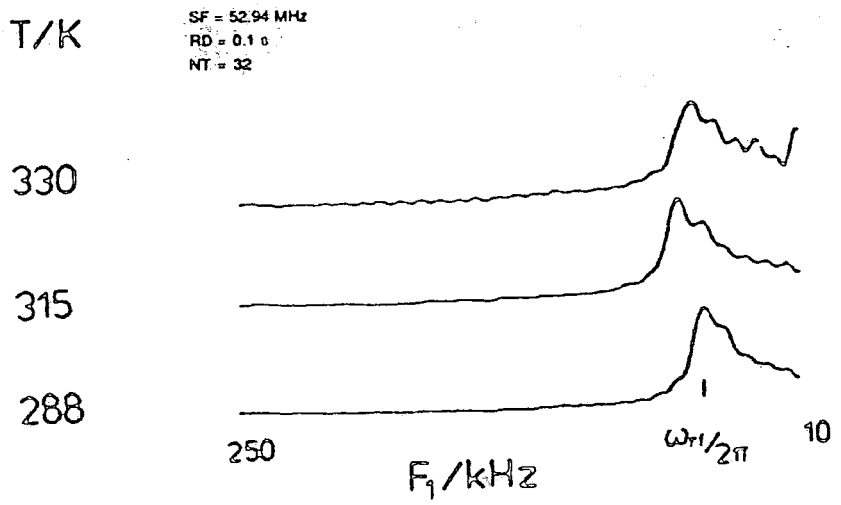

Figure 5.25(a): F_1 projection of ^{23}Na nutation spectrum of hydrated NaY zeolite as a function of temperature.

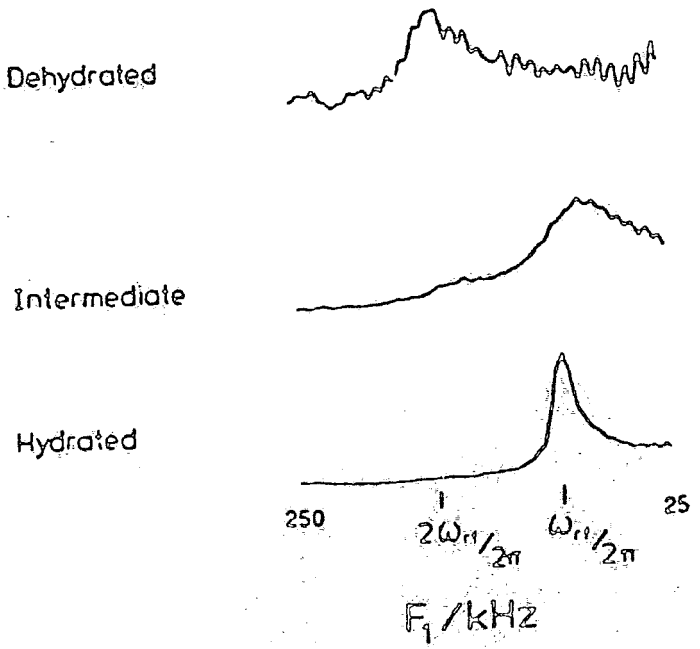

Figure 5.25(b): F_1 projection of ^{23}Na nutation spectrum of hydrated NaY zeolite as a function of dehydration.

locations because fluctuations in the positions of the water molecules (in a local sense) could result in the observation of more than one sodium resonance.

The excitation projection of the ^{23}Na nutation spectrum suggests a quadrupole coupling constant between 0 and 75 kHz at 286 K (closer to the 75 kHz end of the range), and on raising the temperature from 286 to 330 K, a perceptible increase in linebroadening is observed (Figure 5.25(a)). The increase in excitation linewidth is consistent with a gain in the efficiency of $T_{2\rho}$ relaxation processes. Similar observations have been reported for the zeolite NaA[24], but in that case the maximum excitation linewidth was observed at 253 K. It seems that the mobility of the sodium ions or the water molecules must possess a higher energy barrier to motion in the present case because of the higher temperature required to reach maximum relaxation efficiency. Only a slight reduction in the linewidth of the excitation projection of the nutation spectrum measured at 286 K is observed when the nutation pulse is preceded by a rotary echo pair of both 2 and 4 μs durations, showing that the influence of $T_{2\rho}$ relaxation processes on the linewidth is small at 286 K. The linebroadening influence on the excitation projection at 330 K is more significantly reduced on using a rotary echo before the nutation pulse, confirming the importance of $T_{2\rho}$ relaxation processes. A temperature-dependent shift of the major peak in the excitation projection is observed, which corresponds to an effective different radio-frequency field strength in the experiments (which is surprising given that the experiments were performed under identical radio-frequency field strength conditions).

The temperature dependence of the results is quite distinct from the changes that occur on dehydration of the NaY sample (Figure 5.25(b)). Partial dehydration of the zeolite leads to a shift (4 ppm) of the narrow component of the sodium resonance to lower frequency with a gain in linewidth suggesting an increase in the quadrupole coupling constant. Assuming that the isotropic chemical shift is unaffected by the dehydration procedure, the shift to low frequency corresponds to a gain in the quadrupole coupling constant of ∿650 kHz which is in reasonable agreement with the nutation projection shown. Realistically, it is to be expected that a distribution of quadrupolar coupling parameters results on partial dehydration, which will have a broadening influence on the excitation projection. Greater dehydration results in a shift to low frequency of 17 ppm, and a considerable increase in linewidth. The shift is consistent with a gain in quadrupole coupling constant of 1.4 MHz, which is in agreement with the excitation projection of the nutation spectrum.

5.8 General conclusion

This chapter has been principally concerned with the application of radiofrequency pulses to quadrupolar spin systems. The results of a density matrix calculation for the case where a single r.f. pulse is applied to a system of $I=^3/_2$ nuclei has been used to illustrate the differences between selective and non-selective excitation for half-integer spin quadrupolar nuclei and also the conditions for quantitivity. The expression for the coherence detected between the $m=\frac{1}{2}$ and $m=-\frac{1}{2}$ states leads to the concept of the 2D nutation

experiment which is a valuable tool in the study of quadrupolar spin systems in the solid state as is indicated by the study of a series of model compounds. In addition to information concerning the quadrupole coupling parameters, it is possible to obtain information about the selectivity of excitation of the central transition and molecular motion.

The second part of the chapter has been concerned with the investigation of complex quadrupolar spin systems. In the case of NH_4^+-ZSM-5, changes observed in the single-pulse ^{27}Al MASNMR spectrum on partial dehydration have been interpreted in terms of fast transition-dependent relaxation, although further experiments are required to exclude the unlikely possibility of very slow motion accounting for the observations. Changes observed in the single-pulse ^{27}Al MASNMR spectrum on temperature variation may not be interpreted in terms of a simple model representing small angle fluctuations of the axis defining the principal tensor components, and a more sophisticated theoretical treatment is required to account for the probable effect of motion relaxation processes. The effects observed on the partial dehydration and temperature variation would be expected to complicate the interpretation of quantitative ^{27}Al work.

Studies on the NaY sample suggest that the sodium ions are tumbling slowly and this serves to complicate the interpretation of the spectrum. The results suggest that a knowledge of the sodium cation mobility is required before ^{23}Na NMR may be used as an analytical tool for providing information on the cation distribution. This has important implications for the NMR of ^{7}Li and ^{133}Cs which are often used as charge-compensating cations in zeolites.

REFERENCES - CHAPTER FIVE

1. A. Abragam, "The Principles of Nuclear Magnetism", Oxford University Press, London and New York (1961).

2. D. Fenzke, D. Freude, T. Fröhlich and J. Haase, Chem.Phys. Lett., 111, 171 (1984).

3. V.H. Schmidt, Phys.Rev.B., 7, 4145 (1973).

4. A. Samoson and E. Lippmaa, Phys.Rev.B, 28, 6567 (1983).

5. E. Lippmaa, A. Samoson and M. Mägi, J.Am.Chem.Soc., 108, 1730 (1986).

6. A. Samoson, E. Lippmaa, G. Engelhardt, U. Lohse and H.-G. Jerschkewitz, Chem.Phys.Lett., 134, 589 (1987).

7. A.P.M. Kentgens, J.J.M. Lemmens, F.M.M. Overts and W.S. Veeman, J.Magn.Reson., 71, 63 (1983).

8. P.P. Man, J.Magn.Reson., 67, 78 (1984).

9. A. Samoson and E. Lippmaa, Chem.Phys.Lett., 100, 205 (1983).

10. P.P. Mann, H. Theveneau and P. Papon, J.Magn.Reson., 64, 271 (1985).

11. F.M.M. Geurts, A.P.M. Kentgens and W.S. Veeman, Chem. Phys.Lett., 120, 206 (1986).

12. A.P.M. Kentgens, K.F.G.J.Scholle and W.S. Veeman, J.Phys.Chem., 87, 4337 (1983).

13. L. Pandey, S. Towta and D.G. Hughes, J.Chem.Phys., 85, 6923 (1986).

14. U. Haeberlen, "High Resolution NMR in Solids, Selective Averaging", (Academic Press, New York, San Francisco, London 1976).

15. A.J. Banister, Private Communication.

16. Strukturbericht III, 456, 1933-1935.

17. H. Lipson, Proc.Roy.Soc., (London), A151, 347 (1963).

18. N.N. Greenwood and A. Earnshaw, "Chemistry of the Elements", Pergamon Press Ltd., 1984.

19. J.D. Cuthbert and H.E. Petch, J.Chem.Phys., 39, 1247 (1983)

20. G. Engelhardt, J-Ch Buhl, J. Felsche and H. Foerster, Chem.Phys.Lett., 153, 332 (1988).

21. A. Samoson and E. Lippmaa, J.Magn.Reson., 79, 255 (1988).

22. A. Hanson, Acta Chem.Scand., 15, 934 (1961).

23. R. Jansen and W.S. Veeman, J.Chem.Soc., Faraday Trans.1, 84, 3747 (1988).

24. R. Jansen, G.A.H. Tijink and W.S. Veeman, J.Chem.Phys., 88, 518 (1988).

25. K.F.M.G.J. Scholle, Ph.D. Thesis (University of Nijmegen), 1985.

26. J. Kirkpatrick, R.A. Kinsey, K.A. Smith, D.M. Henderson and E. Oldfield, Am.Mineral., 70, 106 (1985).

27. M.M. Maricq and J.S. Waugh, J.Chem.Phys., 70, 3300 (1979).

28. G. Debras, A. Gourge, J.B. Nagy and G. De Clippeleir, Zeolites, 6, 161 (1986).

29. E.R. Andrew and D.P. Tunstall, Proc.Phys.Soc., 78, 1 (1962).

30. J. Haase, H. Pfeifer, W. Oehme and J. Klinowski, Chem.Phys.Lett., 130, 189 (1988).

31. A.F. De Jong, A.P.M. Kentgens and W.S. Veeman, Chem. Phys.Lett., 109, 337 (1984).

32. D.L. Turner, J.Magn.Reson., 61, 28 (1985).

33. R. Jansen, G.A.M. Tijink, W.S. Veeman, Th.L.M. Maeson and J.F. van Lent, J.Phys.Chem., 93, 899 (1989).

34. C.L. Perrin and R.K. Gipe, Science, 238, 1393 (1987).

35. H. Bayer, Z.Phys., 130, 227 (1951).

36. A.G. Marshall, T-C.L.Wang, C.E. Cottrell and L.G. Werbelow, J.Am.Chem.Soc., 104, 7665 (1982).

37. L. Lerner and D.A. Torchia, J.Am.Chem.Soc., 108, 4264 (1985).

38. L.B. Welsh and S.L. Lambert, ACS Symp.Ser., 368 (Perspect.Mol.Sieve Sci.), 33 (1988).

39. L.G. Werbelow and A.G. Marshall, J.Magn.Reson.,43, 443 (1981).

CHAPTER SIX

MULTINUCLEAR MAGNETIC RESONANCE STUDY OF HIGH-SILICA THETA-1

6.1 Introduction

The use of probe molecules to provide information concerning both the microporosity and acid sites of zeolites is well established. The presence of Brönsted and Lewis acid sites has been inferred[1,2,3] from ^{1}H, ^{13}C and ^{15}N NMR, the ^{15}N studies being particularly valuable as a consequence of both the large nuclear shielding range of ^{15}N and the direct interaction of the nitrogen atom with the active site. Information concerning the dimensions of cavities and channels, short-distance crystallinity, and the nature of the structural defects may be examined from ^{129}Xe spectra [4].

In the following study, the diethylamine template present in as-synthesised high-silica theta-1 is used as a probe molecule. The high-silica form of theta-1 is characterised by high-resolution ^{13}C and ^{29}Si MASNMR, additional complementary information being sought by ^{1}H NMR. The ^{13}C spectra are interpreted as showing the presence of both neutral and protonated template molecules. These observations are discussed in terms of the possible presence of acid sites and their spatial distribution. The ^{29}Si NMR results are consistent with the template molecule occupying the 10-T channels only, and the spin-lattice relaxation behaviour of both the ^{13}C and ^{29}Si spins are interpreted in terms of restricted motions of the template molecules. Changes in the ^{29}Si NMR spectra on calcination indicate the possibility of a minor framework rearrangement.

6.2 Characterisation by non-NMR techniques

Powder X-ray diffraction analysis of the as-synthesised sample indicates a very high degree of crystallinity and purity. There is no trace of α-cristobalite which often accompanies the preparation of high-silica theta-1. Data obtained by microanalysis, X-ray fluorescence, atomic absorption and thermal gravimetric analysis are shown in Table 6.1. Aluminium is present as an impurity and presumably results from trace impurities in the Ludox AS40 silica solution.

TABLE 6.1 Microanalysis, X-ray fluorescence, atomic absorption and thermal gravimetric analysis data for high-silica as-synthesised theta-1 zeolite

	$Si^{(a)}$	$Al^{(a)}$	$C^{(b)}$	$N^{(b)}$	$Na^{(c)}$	$H_2O^{(d)}$
% mass	41.3	∿0.0	3.1	1.0	0.1	0.2
atoms/unit cell$^{(e)}$	24.0	∿0.0	4.2	1.2	0.1	0.2

(a) X-Ray fluorescence.

(b) Microanalysis.

(c) Atomic Absorption (correction being made for background signal).

(d) Thermal gravimetric analysis. The value was calculated by assuming that inter-channel water accounted for the mass loss between 303 and 423 K.

(e) The quoted composition of the unit cell assumes that all the impurity aluminium present is in a tetrahedral environment. The results suggest approximately 1 template molecule per unit cell.

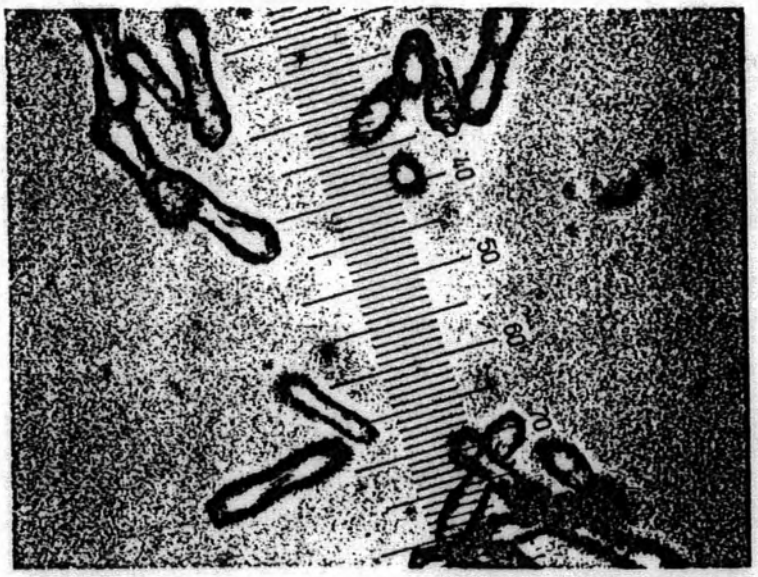

Figure 6.1: As-synthesised high-silica theta-1 (x 40). 1 small division = 3 μm.

A photograph of the crystallites magnified by a factor of 40 is shown in Figure 6.1. It can be seen that the crystallites radiate from either side of a central nucleus to produce a wheatsheaf type aggregate. Close inspection reveals that each wheatsheaf head consists of approximately 10 crystallites, thus suggesting an individual crystallite diameter of approximately 0.3μm. The wheatsheaf aggregates result from secondary nucleation which is caused by either the temperature rising too high during the reaction or the presence of too much diethylamine[5]. The regular nature of the aggregates suggests that they do not result from the adhesive effect of diethylamine between the crystallites.

6.3 ^{13}C NMR Studies of as-synthesised high-silica theta-1

Cross-polarization (^{1}H-^{13}C) MASNMR was used to study the microporosity of theta-1. The ^{13}C NMR shift is highly sensitive to the environment of the nucleus and as such potentially provides important information on the structure and position of the diethylamine template. In addition, complementary information was obtained by (a) delayed contact cross-polarization to carbon experiments and (b) carbon T_1 measurements obtained by the Torchia proton-enhancement method[6].

Figure 6.2(a) shows the cross-polarization ^{13}C MASNMR spectrum of as-synthesised high-silica theta-1. It is surprising to observe three major peaks, given the inherent equivalence of the two carbon chains in diethylamine. The observed spectrum is consistent with a mixture of physisorbed and protonated diethylamine (the relevant chemical shift

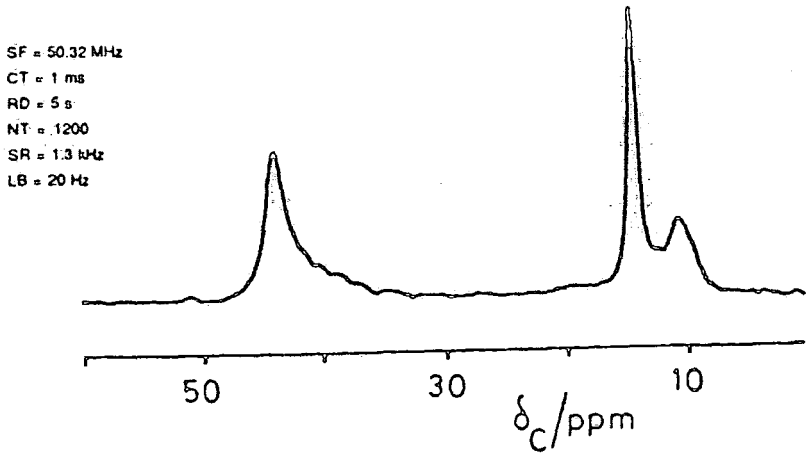

Figure 6.2(a): ^{13}C CP MASNMR spectrum of as-synthesised high-silica theta-1.

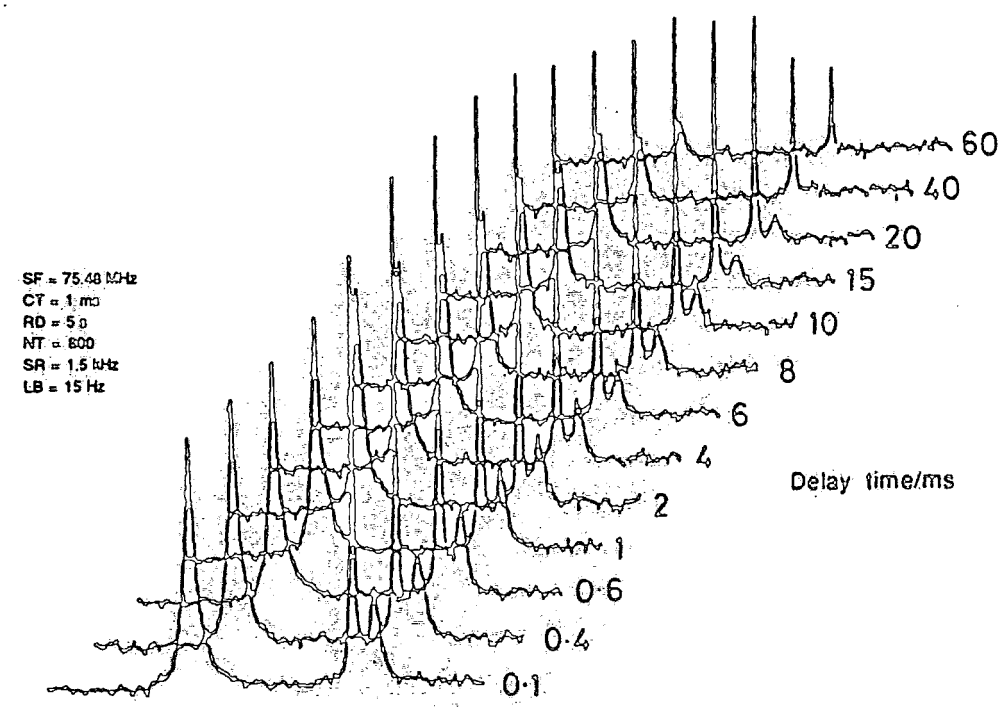

Figure 6.2(b): Variable spin-lock delay ^{13}C CP MASNMR spectrum of as-synthesised high-silica theta-1.

information[7] is shown in Table 6.2). The two methylene resonances are not clearly resolved due to a combination of the similarity in chemical shifts expected for the protonated and physisorbed environments and spectral perturbations caused by (^{13}C, ^{14}N) dipolar coupling.

TABLE 6.2 Carbon chemical shifts for the diethylamine template

	Methylene δ/ppm	Methyl δ/ppm
free diethylamine[7]	44.2	15.4
protonated diethylamine[7]	43.6	12.2
observed in zeolite theta-1	43.9, ∿42	14.2, 10.7

It has been suggested that the different channels present within a zeolite influence the ^{13}C chemical shift of otherwise equivalent carbons in the zeolite ZSM-5[8]. In high-silica theta-1, twinning results in the production of two types of 10-T channel[9], but it is felt that the difference in chemical shift of the methyl groups of the respective forms is too large to reflect the influence of two very similar channels. Another possibility is that both surface and channel template may be present. Thorough washing of the sample with water (1g in 500 ml of water) resulted in no perceptible change in the spectrum. Fearing that water might not wet the zeolite surface, the washings were repeated with methanol but a similar result was obtained. Diethylamine is extremely soluble in alcohols and soluble in water[10].

ESCA was also used to eliminate the possibility of surface template. The ESCA analysis was complicated by the fact that it was necessary to initially establish whether the

zeolite powder covered the surface of the sample tape after evacuation, there being poor adhesion between the tape and the zeolite. Fortunately, the tape contained both carbon and silicon and so it was possible to compare the silicon/carbon ratio of the tape with zeolite with just the silicon/carbon ratio in the tape. In the latter case, the silicon/carbon ratio is extremely low. The results indicated that there was no nitrogen signal and that the silicon/carbon ratio was very high - the small amount of hydrocarbon observed resulted from regions of the tape not completely covered by the zeolite. Thus no template is present on the zeolite surface. The only other explanation is that the surface template was removed on evacuation. However, the sample chamber pressure was monitored as a function of evacuation time, the pressure dropping almost instantly to high-vacuum. Usually, if volatile species are present, approximately half an hour is required to reach high-vacuum. Fast removal of surface diethylamine species would contradict the washing studies outlined earlier.

Microanalysis results (Table 6.1) are in agreement with previous density measurements[9] and X-ray refinement techniques[9], which indicate that high-silica theta-1 contains approximately one diethylamine molecule per unit cell (in accordance with the short repeat distance in the c-direction).

The single-pulse ^{29}Si MASNMR spectrum of the calcined form suggests the presence of four crystallographically distinct sites only (see later) and rules out the presence of either clathrasils or zeosils which occasionally accompany the synthesis of high-silica theta-1, such species trapping the diethylamine molecules during synthesis[9]. Finally, there is no obvious

decomposition product that would account for the chemical shifts, and similar studies on a fresh sample yielded identical results, suggesting that the smaller peaks in the cross-polarization ^{13}C MASNMR spectrum do not result from impurities.

The results of a spin-locked delayed-contact cross-polarization to carbon experiment are shown in Figure 6.2(b). The intensity of a particular peak decays with a proton $T_{1\rho}$ value characteristic of the proton bath used to effect cross-polarization. A complete description of this experiment is given in Chapter Three. Figure 6.2(b) indicates that the protonated species are characterised by a shorter $T_{1\rho}$ value than the free diethylamine. A likely explanation for the observation is that there are two physically distinct domains with different NMR properties and that for $T_{1\rho}$ (^1H) relaxation, spin diffusion is unable to average out these heterogeneities [11]. Ideally, it would be preferable to compare the above observation with the direct measurement of proton T_1 and $T_{1\rho}$, but the presence of a finite amount of surface and channel water would certainly complicate the interpretation. The spin-lattice relaxation behaviour of the protons was, however, investigated by the usual saturation recovery pulse sequence applied to the ^1H nuclei on resonance. The resultant relaxation behaviour was fitted by a least squares method to a double exponential decay (T_1[51.5%]-0.65 s, T_1[48.5%]-0.16 s, ν_H = 200.13 MHz). Given the small amount of structural/occluded water (Table 6.1), it is speculated that for T_1 relaxation processes of the free and protonated diethylamine, spin diffusion is unable to average out the heterogeneities. This in turn leads to the conclusion that the domains are fairly large on the molecular scale. It should be noted that this

interpretation of the ^{1}H T_1 data is highly speculative - ^{1}H T_1 relaxation for some molecules containing methyl groups has been observed to be double exponential in character due to coupling of the Zeeman and rotational polarization reservoirs[12].

The intensity variation illustrated in Figure 6.2(b) may be used to estimate the relative amounts of the protonated and free diethylamine. The intensity of a peak (I(t)) after a spin-locked delayed-contact time t is given by equation (6.1):

$$I(t) = KI(o)\exp(^{-t}/T_{1\rho}) \qquad (6.1)$$

A derivation of this equation and a precise expression for K are given in Chapter Three, suffice it to say here that K depends on the cross-relaxation time (T_{IS}), the proton $T_{1\rho}$ and the contact time. Although K differs for the two species, calculated values using an estimated value for T_{IS} of 0.5 ms show that the ratio of the K values is almost unity for the 1ms contact time used ($^{K}free/K_{protonated} = 0.98$).

The proton $T_{1\rho}$ values and approximate values for the signal intensities were obtained by approximating the peak height to the intensity and fitting it to the function $A=A_o\exp(^{-t}/T_{1\rho})$. Although the signal intensities are crude, the results in Table 6.3 allow us to estimate a lower limit on the protonated diethylamine concentration.

TABLE 6.3 Proton $T_{1\rho}$ and intensity information for peaks in Figure 6.2(b)

δ/ppm	$T_{1\rho}$/ms	I_o
43.9	26	52.6
14.4	30	99.7
10.7	14	18.6

ν_H = 300.13 MHz, ν_{1H} = 38.46 kHz

Approximately one in every six template molecules is protonated. In such a silica-rich system, residual hydroxyl ions or acidic internal silanol groups must be present. The traces of aluminium present are not sufficiently abundant to counterbalance the cationic charge of the protonated diethylamine. It is likely that acidic internal silanol groups provide the balance to the protonated diethylamine.

Figure 6.2(b) implies the existence of domains and hence localised regions of defects. A defect site concentraction of $7.2 \times 10^{19} g^{-1}$ may be calculated with the further assumption of mutual exclusivity with respect to the sodium defect sites. This compares with a value of $4.0 \times 10^{19} g^{-1}$ calculated for the concentration of surface silanol groups, n (using the expression[13] $n = 1.2 \times 10^{19}/d$, where d denotes the diameter of the crystallites in μm).

Convincing evidence for the existence of internal silanol groups in highly siliceous ZSM-5 and Y zeolites has been provided in the literature[14,15,16,17,18,19,20]. Initially, there was some argument concerning the arrangement of silanol groups in the zeolite. Dessau[17] proposed an arrangement whereby the silanol groups are isolated but trimethylsilation experiments have concluded that ZSM-5 zeolites without prolonged heat treatment contain $\equiv Si\text{-}O^{-}Na^{+}$ or $\equiv Si\text{-}OH$ moieties with at least one or two $\equiv Si\text{-}OH$ groups at distances suitable for formation of bi- and tridentate linkages[18]. It has been suggested that high-silica ZSM-5 typically contains clusters

of four terminal groups each where T atoms are missing from the lattice. Lippmaa *et al*[21] have shown that an increase in ^{1}H chemical shift of the silanol resonance occurs on exchange of Na^{+} cations at the defect sites with H^{+} (1.4 ppm to 2.2 ppm). The chemical shift change was taken to indicate a rearrangement to a neighbouring location of silanol groups in a geminal [=Si(-OH_2)] or vicinal [≡Si-OH HO-Si≡] arrangement. The accompanying increase in linewidth was interpreted in terms of the expected increase in homonuclear magnetic dipolar interaction. Using Pfeifer's[22] concept of the ^{1}H NMR chemical shift scale as an acidity scale, it may be concluded that the internal silanol clusters are more acidic than isolated silanol species.

6.3.1 Spin-lattice relaxation times for ^{13}C nuclei of the template

Carbon T_1 measurements were made using the proton enhancement method of Torchia[6]. The T_1 of the methyl group of the non-protonated form at 286 K (1.0 s) is less than that of the methylene group (2.4 s). The result is surprising in the sense that the methyl group is expected to be more mobile than the methylene group. (The temperature dependence of the T_1 values is shown in Table 6.4).

TABLE 6.4 Carbon-13 spin-lattice relaxation times for the template in theta-1

Temperature/K	$10^3/T\ K^{-1}$	T_1 (a) (methyl)/s	$\ln(T_1/s)$	T_1 (a) (methylene)/s	$\ln(T_1/s)$
286	3.50	0.97	-0.03	2.34	0.85
303	3.30	1.45	0.37	2.87	1.10
321	3.12	2.03	0.71	4.07	1.40
340	2.91	2.36	0.86	5.20	1.65

(a) ν_c = 50.32 MHz

The increase in T_1 value for both the methylene and methyl groups implies that the motion characterising the methyl and methylene groups corresponds to the high temperature side of the minimum. The situation could, of course, be complicated by the presence of more than one predominant mode of motion, leading to more than one minimum in the plot of log (T_1) against correlation time. The most likely explanation for the shorter spin-lattice relaxation time of the methyl group

is that the close-packed arrangement of the template molecules, as suggested by the microanalysis study, results in hindered methyl group rotation. The situation may be contrasted with that observed in ZSM-5 with the tetrapropylammonium cation as the template. In that case, the methyl resonance is split into two components of approximately equal intensity, the explanation being that the cation is located in the cross-section of the two non-equivalent channels, with propyl groups lodged in each channel[8]. The methylene group adjacent to the methyl group is characterised by a T_1 value of 0.25 s whereas the methyl group resonances were characterised by T_1 values of 1.2 s (higher frequency peak) and 0.75 s. These measurements reflect detailed differences in the behaviour of the two systems. Assuming that the predominant mode of motion corresponds to the high temperature side of the minimum, the spin-lattice relaxation times suggest that for ZSM-5, the template molecules are not close enough to allow methyl group interaction. The implication of the data is that the higher frequency methyl group resonance resides in the larger of the two channels.

For the as-synthesised form of theta-1, a plot of $\ln T_1(^{13}C)$ against $^1/T$ yields a quasi-linear plot for both the methyl and methylene groups of the non-protonated form. If a single correlation time with an Arrhenius-type temperature dependence is assumed, the gradient of the plot is $^{+}E_a/R$, where E_a is the activation energy for the process[23] (rotational motion of the diethylamine molecules being the most likely mode of

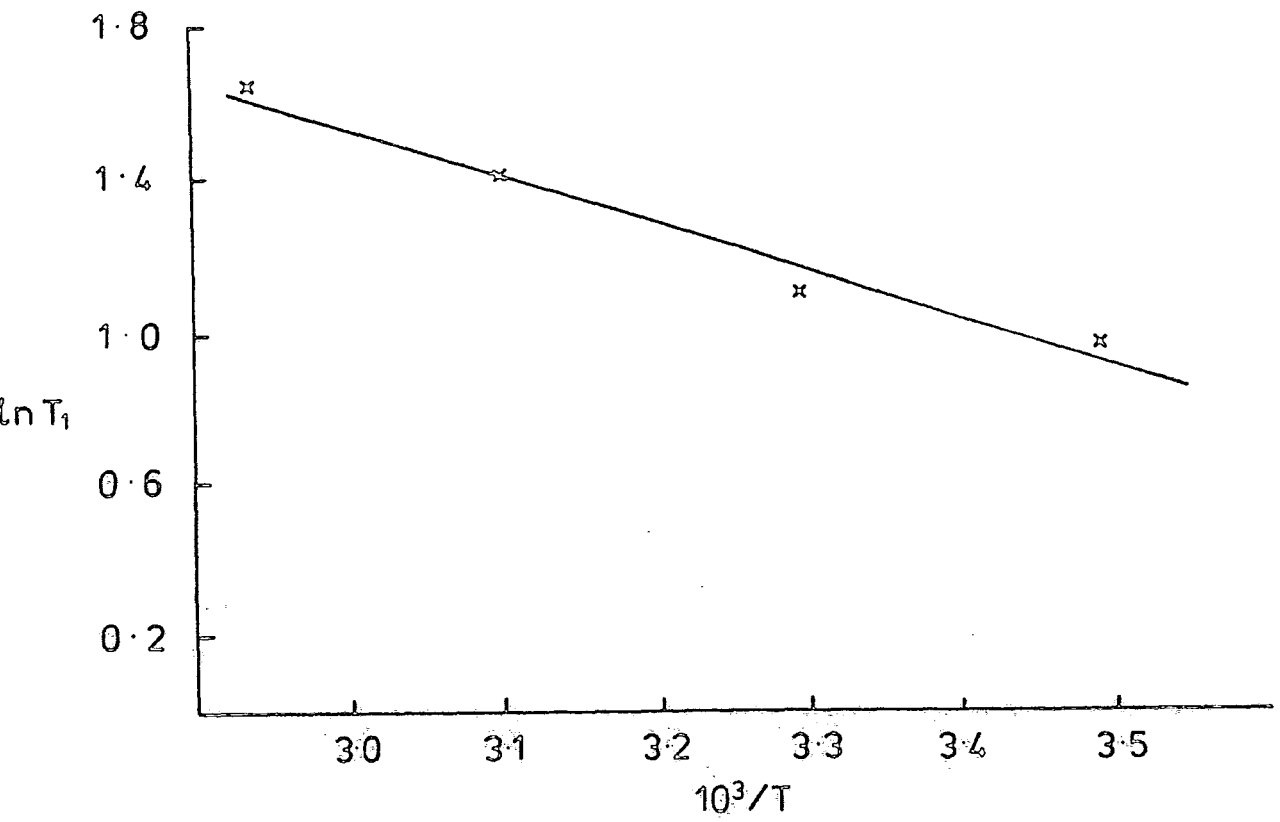

Figure 6.3: Plot of $\ln T_1$ against 1/T for the methyl group of diethylamine in high-silica theta-1.

motion). The slope of the plot in Figure 6.3 yields an activation energy of ~12 $kJmol^{-1}$ for the motion in the 286 to 340 K region for the methyl group (the methyl and methylene values have the same E_a value within experimental error). The value obtained is within the range of activation energies calculated for benzene undergoing small angle rotation ($<\pm 10^{o}$), where the longest axis of benzene is assumed to lie parallel to the theta-1 channel direction [24].

Although ^{13}C T_1 values could not be accurately measured for the protonated form, it is clear that they do not differ significantly from those of the non-protonated form. This is not surprising given the similarity of the indirectly measured proton $T_{1\rho}$ values of the respective forms. The conclusion is that the template mobility of both forms is similar. Because the size of the diethylamine molecule (4.6 x 4.2 Å) closely matches the diameter of the 10-T channels (5.5 x 4.7 Å), it might have been expected that small changes in geometry expected at defect sites would affect the mobility of the template. The results are, however, in agreement with the defect sites occurring in the channels rather than a more open arrangement.

As an aside, it was noticed that the ^{13}C NMR chemical shifts were not affected over the temperature range studied, suggesting that no structural changes occur in the high-silica theta-1 framework over this temperature range, the ^{13}C NMR chemical shift being highly sensitive to the environment of the nucleus.

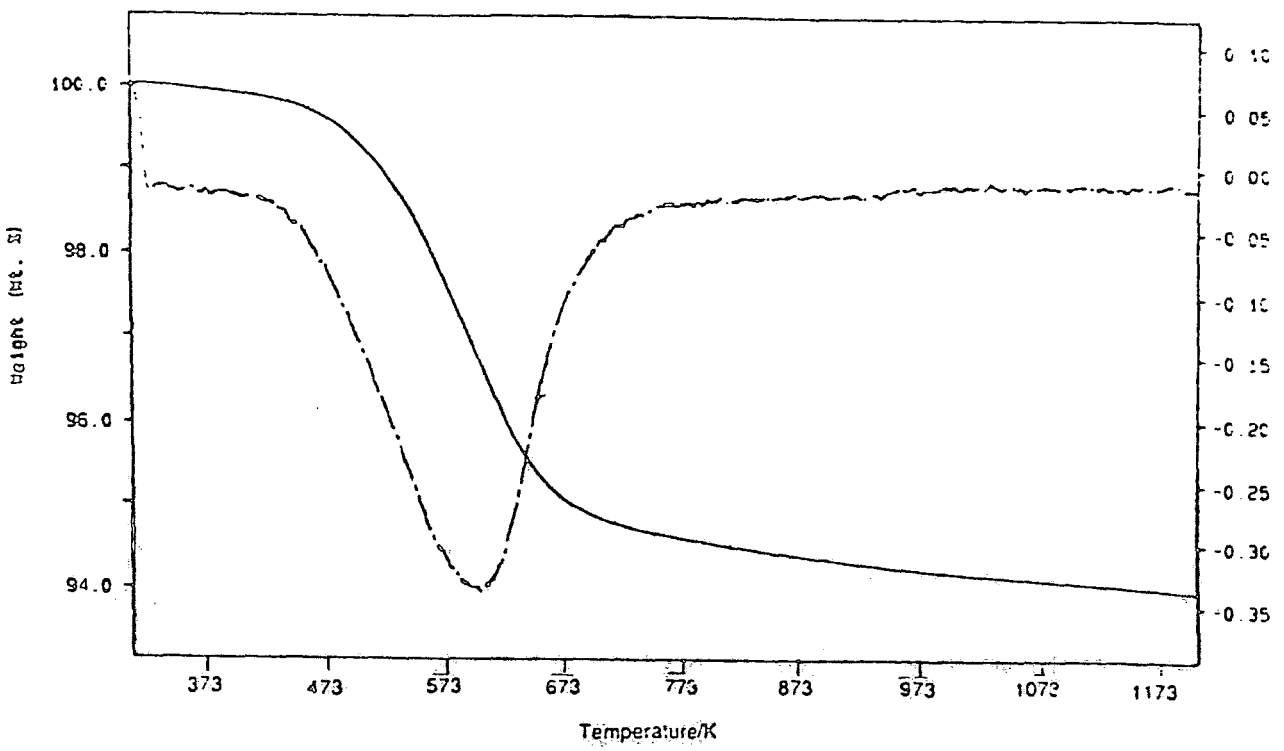

Figure 6.4: TGA trace for as-synthesised theta-1 (diethylamine template).

6.4 Thermal gravimetric analysis of as-synthesised high-silica theta-1

Figure 6.4 shows the TGA trace for the as-synthesised sample. The first derivative plot is also shown. Given the presence of free and protonated diethylamine, it would be expected that the protonated species desorb at a higher temperature. The results in Chapter Seven certainly indicate that the strongest acid sites desorb a prescribed base at the highest temperature. The main feature of Figure 6.4 is a mass loss between 473 and 673 K which corresponds to the loss of the diethylamine. The considerable breadth of this peak points to kinetic hindrance of the removal of diethylamine from the 10-T channels and this prevents the straightforward observation of a double peak description profile. The first derivative plot does indicate a second peak in the 753 to 993 K region, but on the basis of ^{29}Si studies presented later, this peak is believed to result from dehydroxylation of silanol moieties at defect sites. The assignment is in disagreement with previous results which indicate that dehydroxylation occurs in the 973-1173 K region [25]. However, given the absence of a peak in the 973-1173 K region of the first derivative plot, the assignment is not unreasonable and points to a more favourable arrangement of the silanol defects for condensation type reactions. The relevant point is that for typical calcination procedures at 823 K the removal of diethylamine will be accompanied by silanol condensation. Assuming that the loss in weight in the 753 to 993 K region results solely from condensation of internal silanol groups and assuming a condensation reaction of the form: $-Si - OH + -Si - OH \rightarrow -Si - O - Si + H_2O$, the concentration of silanol moieties that participate in the

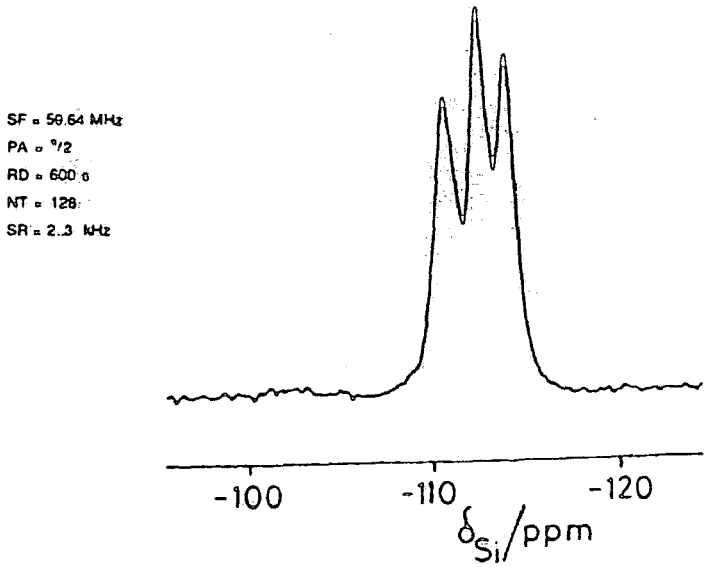

Figure 6.5: ^{29}Si SP MASNMR spectrum of as-synthesised high-silica theta-1.

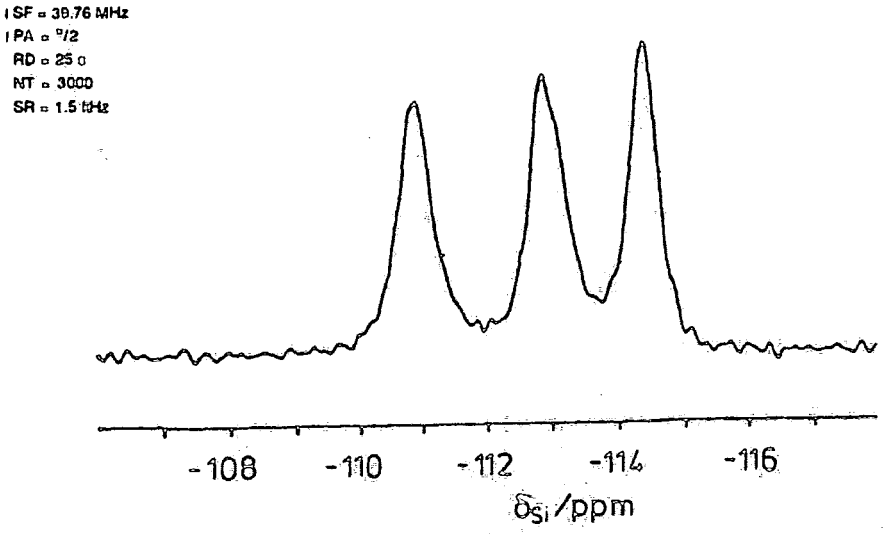

Figure 6.6: ^{29}Si SP MASNMR spectrum of calcined theta-1 (with resolution enhancement).

condensation reaction is 30.4 x $10^{19} g^{-1}$. This exceeds the estimated concentration of the protonated diethylamine by a factor of 4.2.

Losses in weight between 303 and 423 K are assumed to be due to removal of occluded water. The assignments are limited because loss of occluded water or the dehydroxylation may occur simultaneously with the removal of diethylamine, and thus the weight loss due to diethylamine may be an overestimate and the weight loss due to water may be too low. However, calculations indicate that the weight loss between 423 and 753 K is in excellent agreement with the %wt of carbon and nitrogen determined by microanalysis suggesting that the assignments are not unreasonable.

6.5 ^{29}Si NMR Studies of the as-synthesised form of high-silica theta-1

6.5.1 Single-pulse studies

Results presented in Chapter Seven suggest that the diethanolamine template causes structural modifications of theta-1 prepared with a Si/Al ratio of 25.8. Unfortunately, the resolution was poor due to quadrupolar broadening by aluminium and the distribution of aluminium about the ^{29}Si nuclei in terms of second and further nearest neighbour interactions.

In an attempt to ascertain the effect of the template on the framework of theta-1, the single-pulse ^{29}Si MASNMR spectrum of as-synthesised high-silica theta-1 was recorded. The quantitative single-pulse spectrum is shown in Figure 6.5. Good samples of theta-1 exhibit 3 peaks of equal intensity but in the best samples, the central resonance may be partially resolved into 2 peaks [26]. Comparison of the observed ^{29}Si

chemical shifts with literature values for the calcined form suggests that the diethylamine template does not cause a significant Si-O-Si bond angle distortion. However, the increased linewidths relative to the calcined case point to a greater range of Si-O-Si bond angles caused by minor structural strain introduced by the template molecules closely fitting the free channel parameters. Powder X-ray diffraction studies performed on the as-synthesised form suggest that the d-spacings are similar to those of H-theta-1 unlike the case when diethanolamine is the template, when the d-spacings are significantly larger than those of H-theta-1. This difference is apparently reflected in the single-pulse ^{29}Si MASNMR experiment for the two forms. Results in the literature[27] suggest that the presence of absorbed organic molecules is not, in itself, a reason for an increase in linewidth of the silicon species. Calcination and subsequent resolution enhancement reveal that the central peak is indeed a composite (Figure 6.6). The untreated single-pulse spectrum is fitted more accurately to four rather than three Lorentzian peaks (Table 6.5).

TABLE 6.5 Lorentzian peak fitting of Figure 6.6

δ/ppm	width/Hz	% area	Normalized intensity (N=24)
-110.87	30.9	35.1	8.4
-112.79	23.8	16.1	3.9
-113.03	26.5	16.3	3.9
-114.35	24.6	32.5	7.8

6.5.2 Cross-polarization studies

In addition to enhancement of intensity on the Q^3 region (-98 to -105 ppm arising from silanol moieties), the

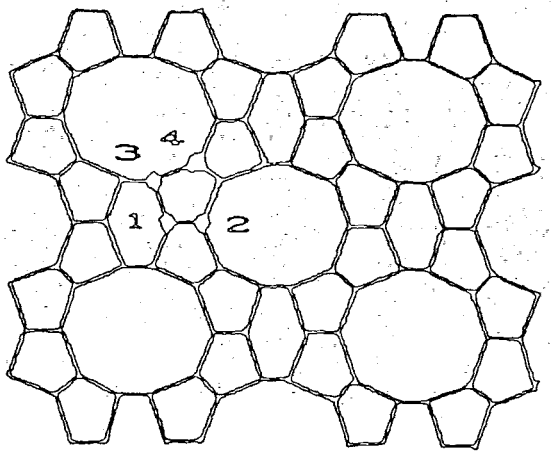

Figure 6.7: Projection of theta-1 in the c-direction. The four crystallographically distinct sites are indicated.

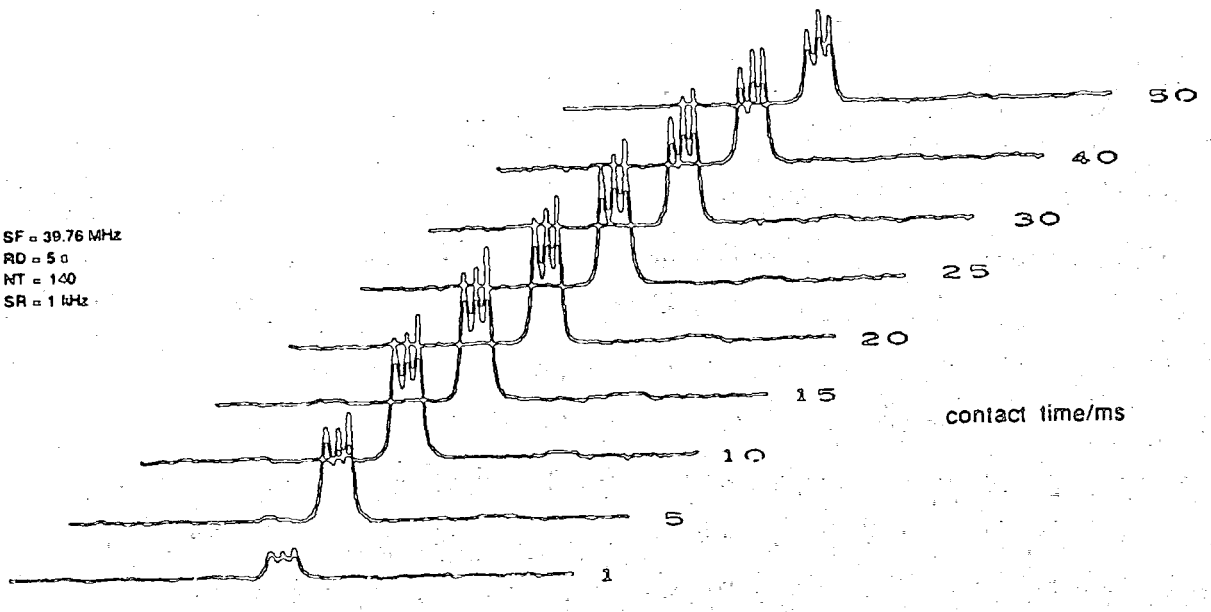

Figure 6.8: Variable contact time ^{29}Si CP MASNMR spectrum of as-synthesised high-silica theta-1.

^{1}H-^{29}Si cross-polarization ^{29}Si MASNMR spectrum of the as-synthesised form reveals a decrease in intensity of the middle Q^4 peak relative to the two outer Q^4 peaks in the single-pulse spectrum for short contact times. Cross-polarization is a discriminating technique, and for short contact times, polarization transfer may preferentially occur from the template protons to the silicon sites facing directly onto the 10-T channels. The assumption is made that any water present in the 6-T channels does not contribute significantly to the signal - the close packing of the template in the 10-T channels virtually eliminates the possibility of water residing in the 10-T channels. The unit cell information given in Table 6.1 certainly justifies the assumption that the template protons make the most significant contribution to the cross-polarization signal. Consideration of the unit cell projection of theta-1 in the c-direction (Figure 6.7) indicates that site 1 faces only onto the 6-T channels and is thus the furthest site from the template. Increasing the contact time eventually results in an increase in intensity of the middle peak with respect to the two outer peaks as expected (Figure 6.8).

The cross-polarization dynamics of the three observable peaks were analysed by simulating the spectrum obtained for each contact time with three peaks of equal Lorentzian/Gaussian character. Values for the proton $T_{1\rho}$ and the cross-relaxation time (T_{IS}) were obtained for each peak by fitting the peak intensity as a function of contact time to the formula [28]:

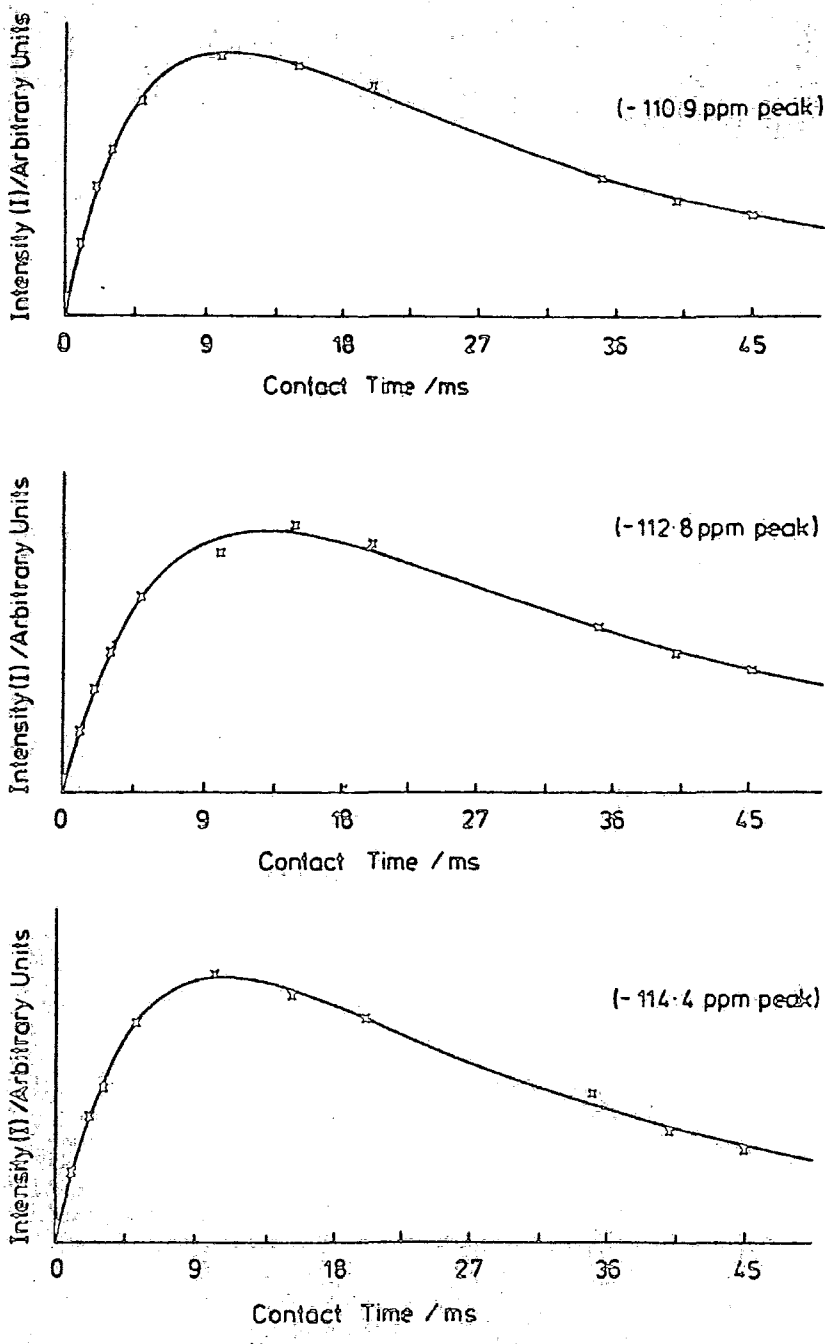

Figure 6.9: Peak intensities as a function of contact time for the spectra shown in Figure 6.8.

$$I(\tau) = \frac{\gamma_H}{\gamma_{Si}} \left(\frac{I_o}{T_{IS}}\right) \left[\exp(-\tau/T_{1\rho}) - \exp(-\tau/T_{IS}) \right] \Bigg/ \left[\frac{1}{T_{IS}} - \frac{1}{T_{1\rho}}\right] \quad (6.2)$$

τ = contact time

I_o = quantitative intensity

T_{IS} = cross-relaxation time

$T_{1\rho}$ = proton spin-lattice relaxation time in the rotating frame

γ_H = gyromagnetic ratio of proton

γ_{Si} = gyromagnetic ratio of silicon

The above equation may be derived assuming a vanishing heat capacity of the silicon spins and $T_{1\rho}$ relaxation of only the proton spins [29]. These conditions are met by the dilution of the silicon spins and a matched Hartmann-Hahn situation. Additionally, an exponential proton $T_{1\rho}$ and non-composite peaks are assumed. Plots of peak intensity against contact time for each peak are shown in Figure 6.9. Typically, the signal rises exponentially as the contact time is increased to approach asymptotically an "equilibrium" value which is itself falling exponentially to zero with a time constant $T_{1\rho}(^1H)$. Since $T_{1\rho}(^1H)$ is longer than the T_{IS} values measured, there is no difficulty in separating the two processes. The values obtained for T_{IS} and $T_{1\rho}$ (Table 6.6) should be treated with caution due to phase instabilities in the proton spin-locking field [30] (which would tend to make the $T_{1\rho}$ results shorter than the real values), but the relative magnitudes are relevant.

Of course, it may be that the analysis of cross-polarization dynamics is complicated by the highly disordered arrangement of diethylamine molecules present in the 10-T

TABLE 6.6 T_{IS} and proton $T_{1\rho}$ values obtained by peak fitting of intensity of ^{29}Si CPMAS spectrum as a function of contact time

δ/ppm	L/G ratio	T_{IS}/ms	$T_{1\rho}$/ms (a)	Normalised intensity (N=24)
-110.87	0.15	4.80	29.7	8.76
-112.70	0.15	6.46	32.0	7.43
-114.31	0.15	5.16	28.6	7.81

(a) ν_{1H} = 62.5 kHz.

---

channels (as suggested by X-ray diffraction data)[9] as well as by cross-polarization to identical but more distant crystallographic sites at longer contact times. A simplistic deduction from Table 6.6 is that the longer T_{IS} value observed for the central peak results from the composite nature of the peak, cross-polarization to site 1 becoming more efficient as the efficiency of cross-polarization to site 2 is decreasing; site 1 species only existing in the second coordination sphere of the template. Similar $T_{1\rho}$ values are observed for all the peaks suggesting that cross-polarization is occurring from only one proton bath. For a more quantitative discussion, a Madelung-type summation would have to be performed. The quantitative ratio of the intensities of the peaks is 8.7:7.4:7.8 (in order of decreasing frequency) in reasonable agreement with the theoretical ratio of 8:8:8. Systematic errors will be introduced by assumptions about the Lorentzian/Gaussian character of the peaks and by the assumption that the two central peaks may adequately be described by a single peak.

Perhaps the largest assumption in equation (6.2) has been that of significant I-I and I-S dipolar interactions.

Calculations indicate a weak dipolar interaction between the template (∿915 Hz). Magic-angle spinning is therefore likely to suppress the heteronuclear ^{1}H-^{29}Si interaction, and this may be demonstrated by comparing a ^{29}Si single-pulse proton-decoupled experiment with just the single-pulse experiment. This interaction remains active in the magnetisation-transfer process as explained by Stejskal *et al.*[31] who pointed out that in an I-S spin system with weak I-I and S-S interactions, transfer takes place when the mismatch of the Hartmann-Hahn condition is a multiple of the MAS frequency. The results imply that for an isolated I-S pair, CP matching is achieved at mismatch frequencies of $\pm\Omega$ and $\pm 2\Omega$ (Ω=MAS spin frequency) with relative transfer efficiencies of 1 and $1/\sqrt{2}$ in powders, while no polarization may be transferred at the exact Hartmann-Hahn condition. Studies by Vega[32] indicate that the cross-polarization dynamics of hydrated zeolites follow the model of isolated ^{1}H-^{29}Si pairs. However, in the case of the diethylamine template, the protons will mutually interact, and more sidebands including the centreband (in the plot of transfer rate ($1/T_{IS}$) against Hartmann-Hahn mismatch frequency) are activated by additional modulations of the spin system. In the limit of strong I-I interactions, there should be no strong dependence of signal intensity on small Hartmann-Hahn mismatches [31]. For a rigid solid such as benzene,[33] the second moment of the proton signal is of the order of 3.1 Gauss^2. This corresponds to a proton linewidth of the order of $\sqrt{3.1}$ Gauss (or 47.3 kHz). For the case where diethylamine is encapsulated within the zeolite framework and closely packed, the predominant mode of motion is likely to be rotation of the diethylamine about its long axis. If the reorientation

is anisotropic about a fixed axis, the linewidth is reduced by a factor $(3\cos^2\theta-1)/2$, where θ is the angle between the direction of the interaction and the axis of rotation [33]. In the present case, $\theta=\pi/2$ and the motion will lead to a linewidth of the order of $\sqrt{3.1}/2$ Gauss (or 23.7 kHz). Theoretically, in the presence of such a significant I-I interaction, the previously mentioned plot of transfer rate against Hartmann-Hahn mismatch should be a broad peak centered on zero mismatch. The presence of additional motion to that described above is not likely to produce discernible sidebands as in the plot of transfer rate against Hartmann-Hahn mismatch for adamantane [31], but rather to reduce transfer rates for zero mismatch and increase them for Hartmann-Hahn mismatches. If this is the case, then the assumption is that cross-polarization transfer in the above experiment is taking place from the centreband. However, crude experiments involving the observation of signal intensity as a function of ^{29}Si r.f. field strength suggest that the plot of transfer rate against mismatch is a broad peak. The qualitative features of the variable contact time experiment, as indicated in Figure 6.8, are reproducible, similar results being obtained for both setting the Hartmann-Hahn match on the compound and by using trimethylsilyl-1-propane sulphuric acid as the matching standard. The assumptions made above are apparently vindicated by the agreement between the experimental results in Table 6.6 and theoretical expectation. Ideally, the strength of the I-I interaction could easily be checked by a ^1H wideline experiment, although in this case the interpretation was more complex than expected. It should be noted that the results of any proton wideline or for that matter ^1H MASNMR experiment may be misleading because narrow

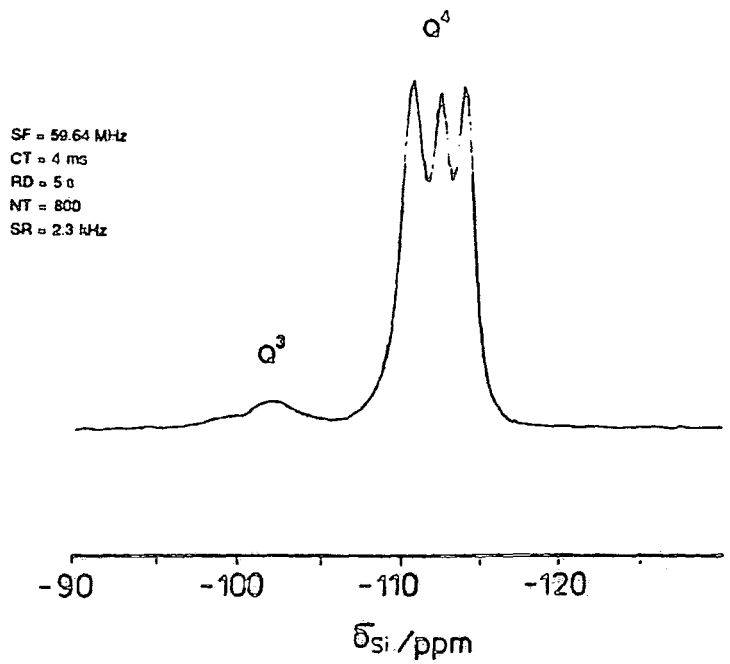

Figure 6.10: Q^3 and Q^4 regions of ^{29}Si CP MASNMR spectrum of as-synthesised high-silica theta-1.

components often dominate,whilst significant loss of intensity of the broad component may occur in the finite dead time. The results of this experiment are discussed later (in addition to ^{1}H MAS and CRAMPS results).

The importance of the above discussion is that corroborating evidence for a further removed crystallographic site from the main channel of theta-1 is provided. Taken in conjunction with *ab-initio* calculations performed by Dwyer *et al* [34],which indicate that aluminium is favourably positioned in sites 1 and 4 (Figure 6.7), this result may have important mechanistic implications in catalysis.

6.5.3 Silanol moiety investigation

Close inspection of Figure 6.8 at short contact times reveals that the Q^3 region is composed of at least two peaks (Figure 6.10). These originate from $(HO)-Si-(O-Si)_3$ units which have previously been reported in ZSM-5 and zeolite Y [19,20]. Typically, shifts of -101 to -104 ppm are observed for these species. In the present case, shifts are observed at -102.5 ppm (predominant peak) and -98 ppm. For samples of ZSM-5 containing both isolated silanols and silanols in vicinal arrangements, peaks are only observed at -103 ppm. Peaks at -98 ppm in highly siliceous ZSM-5 have previously been assigned to $Si-O^{-}Na^{+}$ defects but are naturally only visible in the single-pulse ^{29}Si MASNMR spectrum [35]. It is possible that the peak at -98 ppm in the cross-polarization ^{29}Si MASNMR spectrum of as-synthesised high-silica theta-1 results from $Si-O^{-}$ $[diethylamine]^{+}$ defects. If this is the case, then a longer cross-relaxation time would be expected for the Si atoms contributing to the -98 ppm peak relative to those contributing to

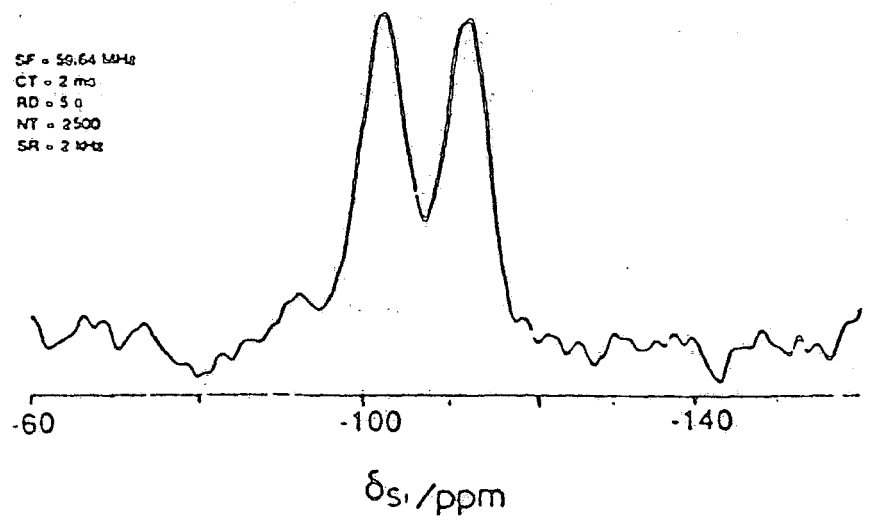

Figure 6.11(a): ^{29}Si CP MASNMR spectrum of partially hydrated calcined high-silica theta-1(2ms contact time).

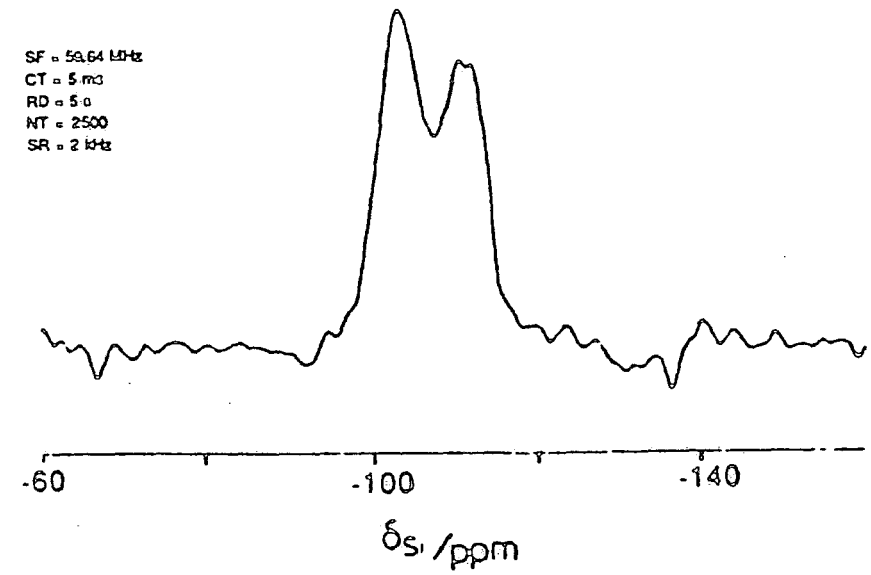

Figure 6.11(b): ^{29}Si CP MASNMR spectrum of partially hydrated calcined high-silica theta-1 (5ms contact time).

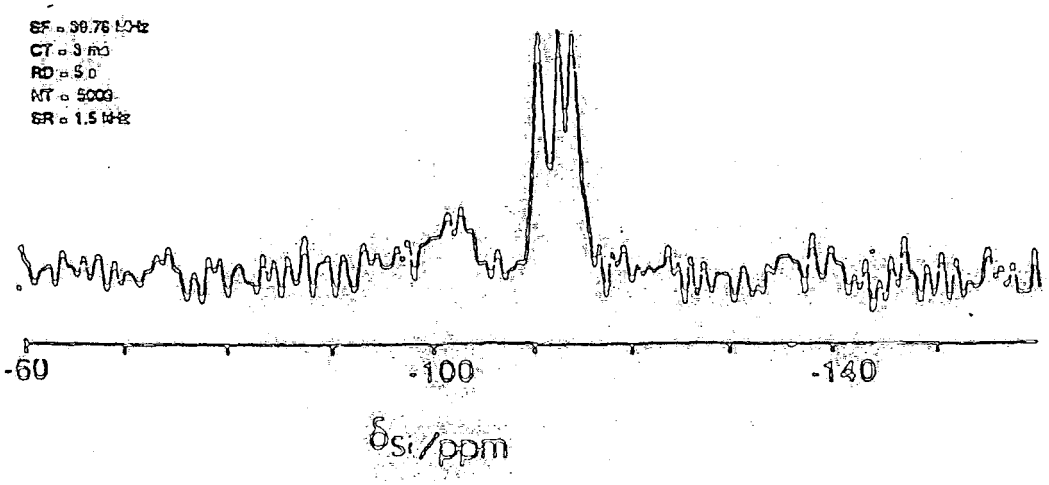

Figure 6.11(c): ^{29}Si CP MASNMR spectrum of fully hydrated calcined theta-1(3ms contact time).

-102.5 ppm. A variable contact $^{1}H-^{29}Si$ cross-polarization experiment was performed but unfortunately the results were inconclusive. This is due to a range of Q^3 environments with varying cross-polarization characteristics between -98 and -105 ppm making a qualitative description impossible. The nature of these defect sites was probed further by analysis of the calcined form.

Approximately 1.5 g of as-synthesised theta-1 were calcined in a tube furnace in a flow of air for 12 hours at 823 K, the calcined sample being transferred quickly to a sealed bottle. The calcined sample was pure white, suggesting that calcination had been complete. Previous reports in the literature[25] have implied that the channels in theta-1 are partially blocked preventing clean calcination of the sample and giving rise to a black sample even after heating for 18h at 1173 K. For the dehydrated calcined form, it proved very difficult to obtain a $^{1}H-^{29}Si$ cross-polarization spectrum - saturation occurring even for very long recycle times. Unfortunately, the protons were so low in abundance that it proved impossible to obtain a value for the proton T_1. Presumably the protons are rigidly bound to the lattice and are insufficiently mobile to allow proton-proton dipolar relaxation. It might be expected that hydration would lower the proton T_1 at the silanol defect sites due to water promoted spin exchange. On partial hydration, the proton T_1 was significantly reduced to allow acquisition of $^{1}H-^{29}Si$ cross-polarization spectra measured at contact times of 2 and 5ms for the partially hydrated sample. Signals are observed at -113ppm $\{Si-OSi)_4\}$ and -102.5ppm $\{(HO)-Si-(O-Si)_3\}$, and for longer contact time, an increase in the $Si-(O-Si)_4$ signal is obtained,

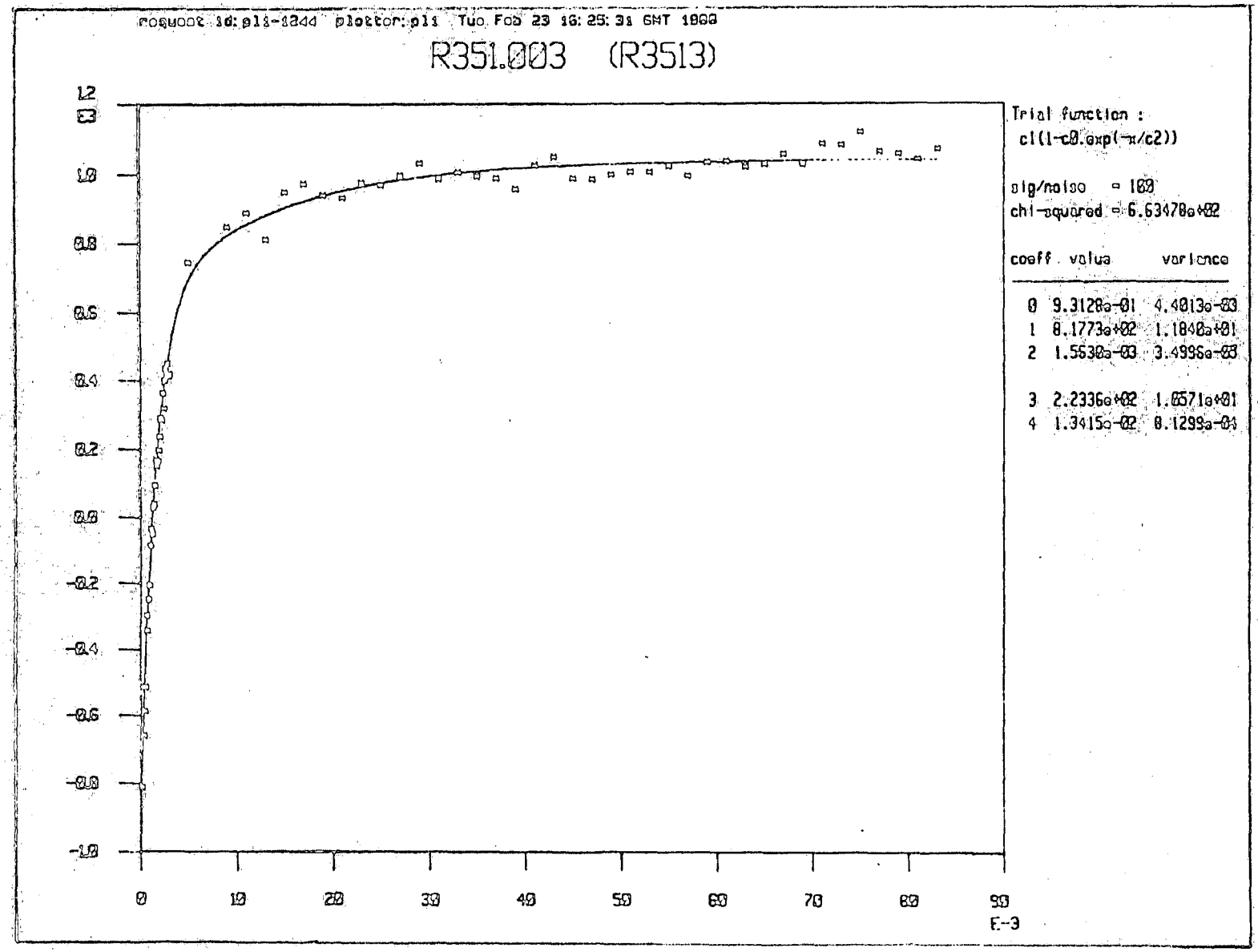

Figure 6.12: ^{1}H T_1 determination for partially hydrated calcined high-silica theta-1.

suggesting a longer cross-relaxation time for these Si atoms from channel water (compare Figures 6.11(a) and (b)). The proton T_1 was measured for the partially hydrated sample by inversion-recovery and the growth of magnetisation was observed to be non-exponential (Figure 6.12, T_1 (80%) = 1.6 ms, T_1 (20%) = 1.3 ms). This is interpreted in terms of the channel water and the protons at defect sites constituting two physically distinct domains. Further hydration results in a dramatic improvement in the intensity of the Q^4 peak relative to the Q^3 peak. In addition, the resolution in the Q^4 region is significantly enhanced and Figure 6.11(c) suggests that interchannel water cross-polarizes as efficiently as the template. Unfortunately, the resolution in the Q^3 region after calcination is such that it is not possible to compare, even in a qualitative sense, the effect of calcination on the Q^3 region.

6.5.4 Evidence for minor framework rearrangement

However, a decrease in resolution of the single-pulse ^{29}Si MASNMR spectrum of the calcined form is initially observed with respect to that of the as-synthesised form (Figure 6.13). On hydration/standing, the resolution is improved, and eventually is greatly improved with respect to that of the as-synthesised form (Figure 6.14). The initial increase in dispersity of the ^{29}Si chemical shifts on calcination is indicative of Si-O-Si bond angle distortion[36]. Taken in conjunction with subtle changes in the Q^3 region of the single-pulse ^{29}Si MASNMR after calcination, the results are consistent with slow structural healing or a minor framework rearrangement following calcination. Cross-polarization ^{29}Si MASNMR

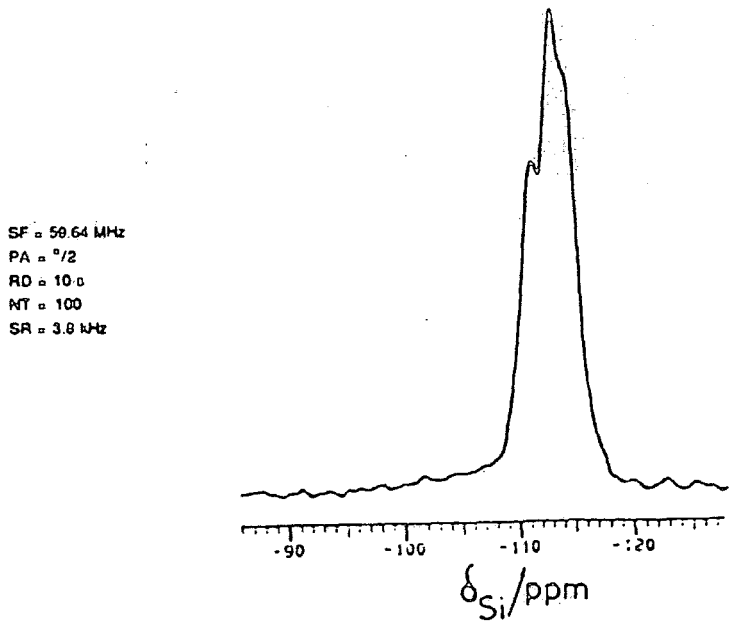

Figure 6.13: ^{29}Si SP MASNMR of freshly calcined high-silica theta-1.

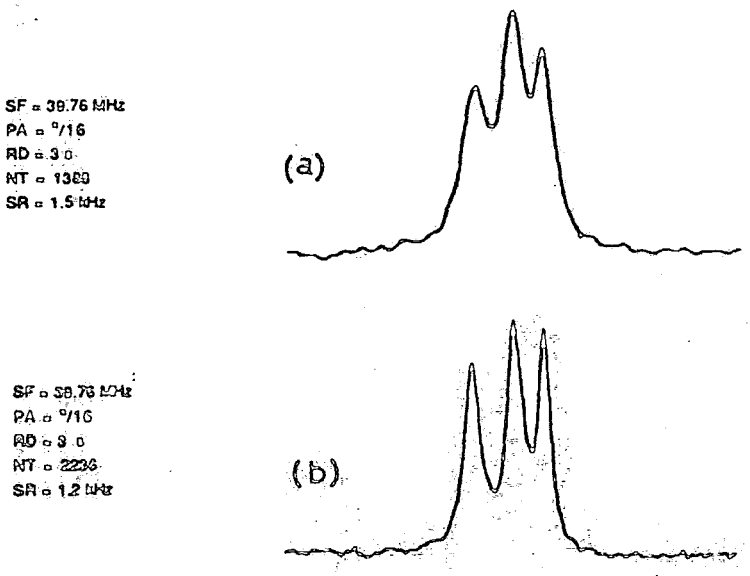

Figure 6.14(a): ^{29}Si SP MASNMR spectrum of as-synthesised high-silica theta-1.

Figure 6.14(b): ^{29}Si SP MASNMR spectrum of calcined high-silica theta-1 after hydration/standing.

results are also in agreement with this conclusion. For the sample exhibiting either a partially or poorly resolved single-pulse ^{29}Si MASNMR spectrum, the corresponding cross-polarization ^{29}Si MASNMR spectrum was also poorly resolved in the Q^4 region. However, for similar contact times, the sample giving rise to a highly resolved spectrum in the single-pulse studies also gave a highly resolved spectrum by cross-polarization. Given the weight loss between 753 and 993 K in the TGA plot (Figure 6.4), it seems likely that the silanol condensation reaction is initiated by the calcination process. It appears that the structural healing/rearrangement is incomplete after calcination and that its conclusion may be followed by improvement in resolution in the Q^4 region. In addition, the use of exponential linebroadening reveals the presence of a faint broad peak underlying the Q^4 region of the single-pulse ^{29}Si MASNMR spectrum of the as-synthesised form. The results are in agreement with the hypothesis that calcination results in the production of additional silanol groups *via* the reaction:

$$- SiO^- \ [\text{diethylamine}]^+ \xrightarrow{\Delta} - Si\text{-}OH + \text{organic products}$$

and that the newly formed silanol group becomes part of an unstable hydroxyl nest which may be removed either by simple condensation reactions or insertion of silica into the hydroxyl nest (involving condensation) *via* lattice transformations and silica transport. The latter mechanism has been suggested for removal of hydroxyl nests during hydrothermal dealumination of zeolites [37]. Of course, from the present data it is not possible to differentiate between these two mechanisms. While no evidence has been suggested for the latter mechanism, results by Maciel *et al*[38] show that vicinal(hydrogen-bonded) silanols

condense on evacuation at temperatures as low as 773 K in the case of silica gels. The ease of this condensation reaction will depend on the arrangement of the vicinal groups. Loss of resolution and small chemical shift changes accompanying dehydration have been reported in the Q^4 region of the single-pulse ^{29}Si MASNMR spectra of zeolites Y[39] and rho[36]. This was attributed to both distortions at Si-O-Si bond angles and also from the asymmetric localisation of the charge balancing cations, distorting equivalence in the lattice. The recovery of resolution on hydration was explained by solvation which separated the counterions from the framework resulting in restoration of framework symmetry. Also, the increased molecular mobility averages out remaining inequivalences. Dehydration at 503 K for 20 hours of the fully hydrated sample of theta-1 resulted in no perceptible change in the single-pulse ^{29}Si MASNMR spectrum implying that the time-dependent effects outlined above for calcined theta-1 do not arise simply as a consequence of hydration after calcination. This is not surprising given the small number of counterbalancing cations relative to the cases outlined above for zeolites Y and rho.

6.5.5 Investigation of ^{29}Si T_1 relaxation mechanisms for framework silicon species

For the present sample of theta-1 in which air is displaced from the 10-T channels by the diethylamine template, a potentially powerful opportunity is presented to obtain further information on the ^{29}Si relaxation mechanism(s) in zeolites. This is aided by the ability to distinguish the crystallographically inequivalent sites by ^{29}Si MASNMR.

Previous reports in the literature have suggested that the paramagnetic oxygen molecule is the dominant source of ^{29}Si spin-lattice relaxation in zeolites[40,41], although contributions to the relaxation process have been reported which involve ^{29}Si-^{1}H dipolar relaxation *via* water molecules present in hydrated samples[42,43].

Using nitrogen as the drive gas, silicon T_1 measurements were made using the cross-polarization method of Torchia[6]. The sample was spun in nitrogen for 24 hours prior to the experiment. The results shown in Table 6.7 were obtained by assuming an exponential recovery of the longitudinal magnetisation in all cases. Relaxation measurements were made using both air and nitrogen as the drive gas.

TABLE 6.7 ^{29}Si T_1 values as a function of the drive gas and the state of the sample.

	T_1/s		
δ/ppm	N_2 (as-synthesised)[(a)]	Air (as-synthesised)[(b)]	Air (calcined)[(b)]
-110.87	122	19.6	4.60
-112.70	138	20.0	5.52
-114.31	119	18.3	3.80

(a) ν_{Si} = 59.82 MHz

(b) ν_{Si} = 39.758 MHz

Within experimental error, the T_1 values for the differing crystallographic sites in as-synthesised theta-1 using N_2 as the drive gas are equivalent. The values are the same order of magnitude as those observed in the as-synthesised form of ZSM-5 containing the tetrapropylammonium cation as the template, although no information was supplied on the nature of the drive gas[44].

Given the 8 ms contact used, the measured T_1

value for the central resonance is likely to be dominated by the site 2 silicon species. Although previous reports in the literature have provided evidence that the ^{29}Si T_1 values of crystallographically distinct sites in mordenite and silicalite differ considerably within the same sample under oxygen [41], the present results are not surprising. Making the simplifying assumption that any oxygen present will have been replaced by nitrogen, the predominant mode of relaxation will be ^{29}Si-^{1}H dipolar relaxation. Strictly speaking, the effect of any cations present should also be taken into consideration. However, a silicon T_1 value of ~140 s was measured for a sample of theta-1 containing a much greater proportion of sodium, potassium and aluminium (and a diethanolamine template). Although none of the crystallographically inequivalent sites could be clearly resolved, the T_1 value seems to indicate that the presence of cations does not have a significant effect on the ^{29}Si T_1 value. The crystallographic sites observed in the present study are all in the first coordination sphere of the diethylamine template and thus similar T_1 values would be expected given a ^{29}Si-^{1}H dipolar relaxation mechanism. The situation is confused by the fact that the similarity of the T_1 values observed could well depend on the timescale of the experiment. Chemical shift correlation experiments performed on p-dimethoxybenzene show the presence of cross-peaks due to ^{13}C-^{13}C spin diffusion in the presence of magic-angle spinning after a mixing period of 90 s [45]. In the present experiment, seven out of the eight times used for longitudinal recovery of the silicon magnetisation corresponded to values between 70 s and 432 s. Although the ^{29}Si spins are spatially dilute, their natural abundance

is 4.2 times that of carbon. However, the large distance between the ^{29}Si spins and the use of magic angle spinning are likely to suppress any ^{29}Si coupling in this fashion, although the possibility of T-atom jumps may not be ruled out. It should be noted that both of these rather abstruse mechanisms may lead to deviation from a simple exponential decay of the silicon magnetisation in the z-direction due to the range of timescales being traversed.

The possibility of spin diffusion between the ^{29}Si spins *via* mutual spin flips can be shown to be unimportant by reduction of the recycle time in a single-pulse ^{29}Si experiment to a value much less than $5T_1$, when only a minor reduction in intensity of the central resonance relative to the outer two resonances is observed. This suggests that spin diffusion processes do not play an important role in equalising the T_1 values for the sites. The slight decrease in intensity of the central resonance would be expected given the contribution of site 1 which is furthest from the template protons. T-atom jumps on such a short timescale are also unlikely.

After exposure of the sample to air, the ^{29}Si T_1 measurements were repeated using air as the drive gas and an inversion-recovery sequence. The T_1 values were obtained by fitting the data to an exponential recovery and were found to be reduced by a factor of six relative to the case where nitrogen was used as the drive gas. Assuming that ^{29}Si-^{1}H dipolar relaxation is still the dominant mode of relaxation, then a reduction in T_1 value might be expected because the measurements made using nitrogen as the drive gas were obtained

at a higher magnetic field strength. However, the template ^{13}C T_1 values (for which ^{13}C-^{1}H dipolar interactions are the dominant mode of relaxation) are equivalent within experimental error at these two field strengths suggesting that the correlation time for template motion is small enough for T_1 to be independent of the magnetic field strengths used. The reason for the drop in T_1 is thus most probably due to the presence of paramagnetic oxygen in the drive gas.

Given that the 6-T channels are accessible to water, then they will also be accessible to molecular oxygen. These paramagnetic species contribute to the relaxation of the ^{29}Si spins most probably by dipolar couplings of the silicon spins to the unpaired electrons of the molecular oxygen [46]. The presence of approximately one template per unit cell eliminates the possibility of molecular oxygen penetrating the 10-T channels. It is therefore particularly surprising to note the similarity in the T_1 values of the outer resonances (corresponding to sites 3 and 4 in Figure 6.7) given their difference in distance from the 6-T channel, and also given that the above-mentioned relaxation process is strongly distance dependent [46]. It may be that a spin diffusion type process operates between the ^{29}Si spins *via* the paramagnetic oxygen.

Deviations from pure exponential behaviour could result from gaps in the communication network. A more quantitative discussion is not warranted without the use of complex statistical methods. Suffice it to say that distance-dependent relaxation effects cannot by themselves account for the observed behaviour. Deviations from exponential behaviour may also result from the presence of more than one spin-

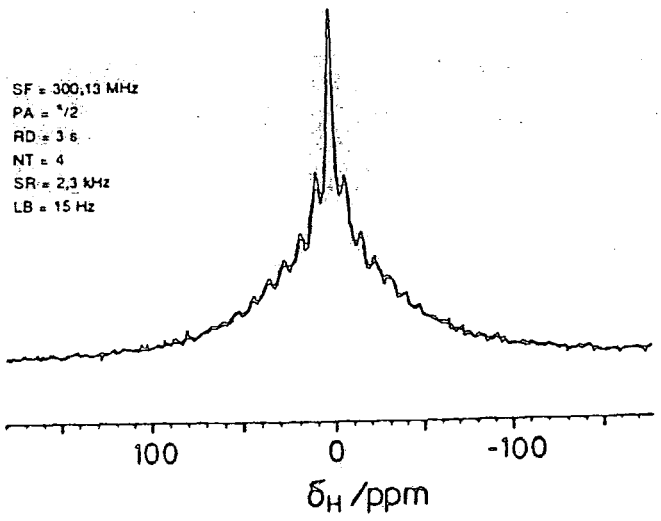

Figure 6.15(a): ^{1}H MASNMR spectrum of as-synthesised high-silica theta-1.

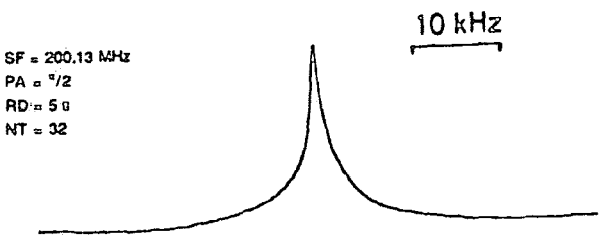

Figure 6.15(b): ^{1}H wideline spectrum of as-synthesised high-silica theta-1.

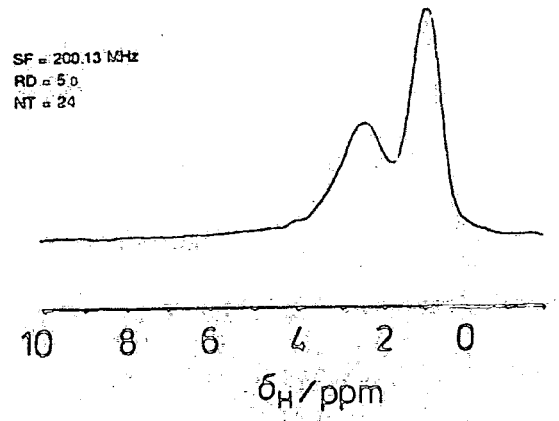

Figure 6.15(c): ^{1}H CRAMPS of as-synthesised high-silica theta-1.

lattice relaxation mechanism.

Calcination leads to a further reduction in the T_1 values. Also,the best fit is then observed for a single - exponential recovery. A further reduction in the T_1 values is to be expected due to the accessibility of the lO-T channels to molecular oxygen and a corresponding increase in oxygen content. The T_1 values are all the same order of magnitude and subtle differences in their values may be accounted for by the different affinities of molecular oxygen for the crystallographic sites, the shorter timescale of the experiment preventing any indirect communication between the silicon species as outlined above. It should be noted that the template protons in the as-synthesised form may also be able to play an indirect part in communication between distant silicon species.

6.6 ^{1}H NMR Studies of as-synthesised form of high-silica theta-1

The ^{1}H MASNMR spectrum of the as-synthesised form is shown in Figure 6.15(a). It is surprising to observe dipolar spinning sidebands for a cluster of more than two interacting spins due to the expected homogeneous nature of the interaction. Vega has observed inhomogeneous spinning sideband behaviour in rotating NH_4^+ groups in NH_4^+-ρ-zeolite[32], in $-CH_3$ groups in a deuterated sodium acetate matrix[32] and in $-Si-(CH_3)_3$ groups in a surface silyl residue[47], and Zimbulyadis has observed similar behaviour in the ^{19}F NMR spectrum of CF_3CO_2Ag[48]. Oldfield *et al*[49] have observed similar behaviour in ^{1}H NMR studies of liquid crystalline phases. The fact that a ^{1}H MASNMR spectrum breaks up into narrow sidebands is unusual for a cluster of more than two interacting spins because their static dipolar Hamiltonian

$$\sum_{i>j} D_{ij}(\emptyset)\,(3\hat{I}_{zi}\hat{I}_{zj} - \hat{\underset{\sim}{I}}_i\hat{\underset{\sim}{I}}_j) \qquad (6.3)$$

does not commute with itself at different rotor orientations, so no line narrowing is achieved unless the spinning rate exceeds the interaction strength D_{ij}. In the case of NH_4^+ exchange or methyl group rotation, all ^1H nuclei become equivalent so that the static dipolar Hamiltonian becomes

$$D(\emptyset) \sum_{i<j} (3\hat{I}_{zi}\hat{I}_{zj} - \hat{\underset{\sim}{I}}_i\hat{\underset{\sim}{I}}_j) \qquad (6.4)$$

which does commute with itself at different rotor orientations[32]. Of course, this situation differs greatly with that expected for the template molecules in theta-1. In addition, calculations indicate that the proton-proton dipolar interaction is of the order of 24 kHz, which vastly exceeds the 2.2 kHz spin rate. However, the present situation is not profoundly different from that of liquid crystalline systems. The unidimensionality of theta-1 ensures that a parallel arrangement of diethylamine molecules along their long axes ('director axis') results in each crystallite of theta-1. In order to account for the dipolar spinning sidebands, it is necessary to bring the angle dependence of the Hamiltonian outside the summation so that the Hamiltonian may commute with itself at different rotor orientations. This will be the case if the intermolecular dipole-dipole interactions are negligible and the diethylamine molecules are undergoing fast axial rotation (so that the projections of all proton-proton vectors onto the lamellar plane average to zero over times which are short on the NMR timescale). This results in a Hamiltonian of the form[50]

$$\tfrac{1}{2}(3\cos^2\theta-1)\sum_{i<j} D^{o}_{ij}[3\hat{I}_{zi}\hat{I}_{zj} - \hat{\underset{\sim}{I}}_i\hat{\underset{\sim}{I}}_j] \qquad (6.5)$$

where θ = angle between director and B_o and $D^{o}_{ij} = \gamma_H^2\hbar^2/r_{ij}^3$

which is similar to equation (6.4) above. The important point is that the angular dependence is the same for all proton pairs, unlike the usual case for protons in a solid sample. The absorption curve is independent of θ and the effect of a variation in θ is only a change in the frequency scale since the couplings between all protons are multiplied by the same factor $(3\cos^2\theta-1)$. This will result in a super-Lorentzian lineshape which is indeed observed[50] (Figure 6.15(b)). A super-Lorentzian lineshape was also observed for theta-1 synthesised with diethanolamine as the template, although the spectrum was more complex because of a mobile component resulting from diethanolamine on the surface. The unusually intense wings present in the spectrum confirm the presence of a super-Lorentzian component.

The application of a CRAMPS sequence (MREV-8) results in a considerable increase in resolution of the ^1H MASNMR spectrum (Figure 6.15(c)). Peaks are observed at 0.9 and 2.5ppm which are assigned to methyl and methylene protons respectively. There may of course be a contribution to the resonance at 0.9 ppm from silanol moieties. A broad resonance centered on 4.5 ppm is assigned to protons directly bound to nitrogen. Unfortunately, the resolution is not sufficient to indicate the presence of both free and protonated diethylamine which was the initial aim of the experiment.

6.7 Suggestions for further work

Deuterium labelling in the methyl group would be valuable in so far as providing evidence for hindered methyl group rotation in the as-synthesised form of theta-1 is concerned. The ^{2}D first-order quadrupolar parameters would allow easy determination of the template motion which could also be studied as a function of temperature. In addition, labelling with ^{15}N would allow us to prove the existence or otherwise of the protonated template species. Unfortunately, the ^{15}N or ^{2}D labelled samples of diethylamine are very expensive in the quantities required for the standard synthesis, and the possibility of reducing the amount of template used in the synthesis was investigated, as well as the possibility of a small-scale synthesis. The synthesis was performed using the amounts outlined in Chapter Three and the template mass was varied. Unfortunately, for lower levels of template, no crystalline solid was produced over the 3-day reaction period. The possibility of a straightforward small-scale synthesis were prevented by the large pressure vessel volume, and attempts to reduce the sample volume by a plastic insert were also unsuccessful, the sample volume still being too large. It is probable that a more subtle approach involving the variation of template, sodium and water content is required before a crystalline phase may be successfully produced.

REFERENCES - CHAPTER SIX

1. L. Petrakis and F.E. Kiviat, J.Phys.Chem., 80, 606, (1976).

2. W.H. Dawson, S.W. Kaiser, P.D. Ellis and R.R. Inners, J.Am.Chem.Soc., 103, 6780, (1981).

3. J.A. Ripmeester, J.Am.Chem.Soc., 105, 2925, (1983).

4. J. Fraissard, in "Some Applications of ^{129}Xe-NMR of Adsorbed Xenon for the Determination of Surface Properties", BRSG and CISG NMR in Colloid and Interface Science (1988).

5. S. Barri, Private Communication.

6. D.A. Torchia, J.Magn.Reson., 30, 613, (1978).

7. J.E. Sameski, H.L. Surprenant, F.K. Molen and C.N.Reilley, Analytical Chemistry, 47, 13, (1975).

8. G. Boxhoom, R.A. van Santen, W.A. van Erp., G.R. Huis and D.Clague, J.Chem.Soc., Chem.Commun., 264, (1982).

9. B. Marler, Zeolites, 7, 393, (1987).

10. R.C. Weast, "CRC Handbook of Chemistry and Physics", CRC Press Inc., Boca Roton, Florida.

11. K.J. Packer, J.M. Pape and M.E. Cudby, J.Polym.Sci., Polym.Phys.Ed., 22, 589, (1984).

12. R.A. Wind, S. Emid, J.F.J.M. Pourquie and J. Smidt., J.Chem.Phys., 67, 2435, (1977).

13. D. Freude, M. Hunger and H. Pfeifer, Chem.Phys.Lett., 128, 62 (1986).

14. A.W. Chester, Y.F. Chu, R.M. Dessau, G.T. Kerr and C.T. Kresge, J.Chem.Soc., Chem.Commun., 5, 289,(1985).

15. S.G. Fegan and B.M. Lowe, J.Chem.Soc., Chem.Commun., 437, (1984).

16. G.L. Woolery, L.B. Alemany, R.M. Dessau and A.W. Chester, Zeolites, 6, 15, (1986).

17. R.M. Dessau, K.D. Schmitt, G.T. Kerr, G.L. Woolery and L.B. Alemany, J.Catal., 104, 484, (1987).

18. B. Kraushaar, J.W. De Haan and J.H.C. Van Hooff, J.Catal., 109, 470,(1988).

19. G.J. Ray, A.G. Nerherm and J.A. Donohue, Zeolites, 8, 458, (1988).

20. M. Hunger, J. Kärger, H. Pfeifer, J. Caro, B. Zibrowius, M. Bülow and R. Mostowicz, J.Chem.Soc., Faraday Trans.1, 83 , 3459, (1987).

21. E. Lippmaa, A. Samōson, V.V. Brei and Y.I. Gorlov, Fiz.Chim., 259, 403, (1981).

22. D. Freude, T. Fröhlich, M. Hunger, H. Pfeifer and G. Scheler, Chem.Phys.Lett., 98, 263, (1983).

23. C.A. Fyfe, 'Solid State NMR for Chemists', C.F.C.Press, Ontario, (1983).

24. A.K. Nowak, A.K. Cheetham, S.D. Pickett and S. Ramdas, Molecular Simulation, 1, 67 (1987).

25. K.R. Franklin and B.M. Lowe, Zeolites, 8, 508, (1988).

26. C.A. Fyfe, H. Strobl, G.T. Kokotailo, C.T. Pasztor, G.E. Barlow and S. Bradley, Zeolites, 8, 132, (1988).

27. C.A. Fyfe, H. Strobl, G.T. Kokotailo, and G. Barlow, J.Am.Chem.Soc., 110, 3373, (1988).

28. Bruker Simfit Routine, see Bruker Applications Note.

29. M. Mehring, 'Principles at High Resolution in NMR in Solids', Springer-Verlag, Berlin, (1983).

30. W.L. Earl, TAMU New Letter, December 22, 1983.

31. E.O. Stejskal, J. Schaefer and J.S. Waugh, J.Magn.Reson., 28, 105 (1977).

32. A.J. Vega, J.Am.Chem.Soc., 110, 1049, (1988).

33. C.P. Schlichter, "Principles of Magnetic Resonance, Springer-Verlag, Berlin, (1978).

34. P.J. O'Malley and J. Dwyer, Zeolites, 8, 132, (1988).

35. G. Engelhardt, B. Fahlke, M. Mägi and E. Lippmaa, Z.Phys.Chem.(Leipzig), 266, 239 (1985).

36. Z. Luz, and A.J. Vega, J.Phys.Chem., 91, 374 (1987).

37. G. Engelharat and D. Michel, "High-Resolution Solid-State NMR of Silicates and Zeolites", J.Wiley and Sons, (1987).

38. C.F. Bronnimann, R.C. Zeigler and G.E. Maciel, J.Am.Chem. Soc., 110, 2023 (1988).

39. S. Hayashi, K. Hayamizu, and O. Yamamoto, Bull.Chem.Soc. Jpn., 60, 105, (1987).

40. D.J. Cookson and B.E. Smith, J.Magn.Reson., 63, 217 (1985).

41. J. Klinowski, T.A. Carpenter and J.M. Thomas, J.Chem.Soc., Chem.Commun., 956, (1986).

42. R.D. Farlee, D.R. Corbin and A.J.Vega, in Proceedings of the 25th Rocky Mountain Conference, Denver (1983).

43. P.F. Barron, P. Slade and R.L. Frost, J.Phys.Chem., 89, 3305, (1985).

44. L.J.M. van de Ven, J.G. Post, J.H.C. van Hooff and J.W. van de Haan, J.Chem.Soc., Chem.Commun., 214 (1985).

45. N.M. Szeverengi, M.J. Sullivan and G.E. Macrel, J.Magn. Reson., 47, 462, (1982).

46. A. Abragam, "Principles of Nuclear Magnetism", Oxford University Press, London and New York (1961).

47. J. Köhler, D.B. Chase, R.D. Farlee, A.J. Vega, J.J.Kirkland, J.Chromatogr., 352, 275, (1985).

48. N. Zumbulyadis, private communication with E. Oldfield.

49. J. Forbes, C. Husted and E. Oldfield, J.Am.Chem.Soc., 110, 1059, (1988).

50. H. Wennerström, Chem.Phys.Lett., 18, 41 (1973).

CHAPTER SEVEN

MULTINUCLEAR MAGNETIC RESONANCE STUDY OF LOW-SILICA THETA-1

7.1 Introduction

After a brief discussion concerning the composition of the zeolites investigated in this chapter, a multinuclear magnetic resonance study of the as-synthesised and calcined forms of the zeolites is presented. The discussion is mainly about the zeolite theta-1, but some reference is made to the zeolite ZSM-5 and its gallium analogue. For the as-synthesised form of theta-1 (diethanolamine template), the results are interpreted by paying particular attention to modifications in the ^{29}Si MASNMR spectra arising as a result of the presence of the diethanolamine template, the use of the diethanolamine template as a probe for the investigation of both surface and bulk acid sites, and the nature of the template interaction with the surface. ^{1}H MASNMR is used to characterise the surface template species, and the experiments used may be extended to other systems where the mobility of the organic species simplifies the ^{1}H MASNMR spectrum.

The Brönsted acid sites are observed directly by ^{1}H NMR. The experimental procedure is discussed, and a ^{1}H MASNMR study of the zeolites H-theta-1 and H,Na-Ga-ZSM-5 in various stages of dehydration is presented. Temperature programmed desorption of ammonia was used to further characterise the acid sites present in H-theta-1 and H,Na-Ga-ZSM-5.

The catalytic activity of zeolites is accounted for by Brönsted acid sites associated with framework aluminium and Lewis acid sites associated with non-framework aluminium. The catalytic activity may be controlled by hydrothermal dealumination, the mechanism of which was investigated in the case of theta-1 by quantitative aluminium studies. Temperature programmed desorption of ammonia was used to characterise

the acid sites present as a function of dealumination time. The nature of the non-framework aluminium giving rise to broad resonances on dealumination was investigated by variable magnetic field studies, high-power proton decoupling experiments,and variable pulse duration experiments. Broad resonances are also observed on the dehydration of Na-ZSM-5 and NaY zeolites. The application of multiple-pulse type experiments to the solution of linebroadening mechanisms in quadrupolar nuclei is considered, with a theoretical treatment given in the case of the CPMG pulse sequence, (see Appendix B).

7.2 Composition of the zeolites

7.2.1 (a) As-synthesised theta-1 (diethanolamine template)

Data obtained by microanalysis, X-ray fluorescence, atomic absorption, ESCA, thermal gravimetric analysis, and quantitative ^{27}Al MASNMR analysis are shown in Table 7.1.

Powder X-ray diffraction analysis of the sample indicates a high degree of crystallinity and purity. There may be a trace of α-cristobalite present which often accompanies the preparation of theta-1.

The above results suggest that 4,4 diethanolamine molecules are present per unit cell, which is not possible given the short repeat distance in the c-direction (∿5 Å) of the unidimensional zeolite. A significant proportion of the template must thus reside at the surface. After very thorough washing of the zeolite with water (0.5 g in 2000 cm^3 of water), repeated analysis suggests approximately 1 diethanolamine molecule per unit cell. ESCA studies suggest that the surface atomic Si/Al ratio is less than the bulk atomic

TABLE 7.1

	Si[a]	Al(4)[b]	Al(6)[b]	Al(invisible)[b][c]	C[c]	N[c]	K[d]	Na[d]	H_2O[e]
% mass	29.1	1.0	0.0	0.2	10.1	2.7	1.0	0.6	0.8
	Si	Al(4)	Al(6)	Al(invisible)	C	N	K	Na	H_2O
atoms/ unit cell	23.2	0.9	0.0	0.2	18.7	4.3	0.6	0.6	1.0

Bulk Atomic	Si/Al	Si/k	Si/Na
Ratios	23	41	40
Surface Atomic[f]	18	19	11

(a) X-Ray fluorescence.

(b) X-Ray fluorescence and ^{27}Al MASNMR. (4),(6) denote four- and six-coordinate aluminium.

(c) Microanalysis.

(d) Atomic Absorption.

(e) Thermal gravimetric analysis. The value was calculated by assuming that inter-channel water accounted for the mass loss between 303 and 403 K.

(f) ESCA.

Si/Al ratio implying an inhomogeneous distribution of the aluminium in the structure. It is of course impossible to distinguish between an inhomogeneous distribution of framework aluminium and an inhomogeneous distribution of non-framework aluminium which may be present as an extraneous species. The extraneous species may take the form of $NaAlO_2$ and/or Al_2O_3 on the surface[1]. The ESCA studies indicate a range of aluminium environments.

The above results indicate a surfeit of positive charge, suggesting the presence of silanol defect sites. ESCA was also used to probe the homogeneity of the distribution of the sodium and potassium cations. The results suggest that both types of cation are inhomogeneously distributed. It seems that the cations are more favourably situated close to the surface, the sodium ions more so than the potassium ions.

(b) As-synthesised ZSM-5 (diethanolamine template)

Data obtained by microanalysis, X-ray fluorescence, atomic absorption and ^{27}Al NMR are shown in Table 7.2:

TABLE 7.2	Si[(a)]	Al(4)[(b)]	Al(6)[(b)]	Al(invisible)[(b)]	C[(c)]	N[(c)]	K[(d)]	Na[(d)]
% mass	36.7	2.7	0.0	0.1	3.0	0.8	1.1	0.6
	Si	Al(4)	Al(6)	Al(invisible)	C	N	K	Na
atoms/ unit cell	89.2	6.8	0.0	0.3	17.1	3.9	1.9	1.8

(a) X-Ray fluorescence.

(b) X-Ray fluorescence and ^{27}Al MASNMR. (4),(6) denote four- and six-coordinate aluminium.

(c) Microanalysis.

(d) Atomic Absorption.

Powder X-ray diffraction studies suggest that the sample is pure. The results indicate that the sodium and potassium cations are not sufficiently abundant to counterbalance the negative charge on the framework aluminium species and, consequently, a significant proportion of the diethanolamine template must be protonated. Approximately four diethanolamine molecules are present per unit cell. This is similar to the situation when tetrapropylammonium hydroxide is used in the synthesis, when roughly four tetrapropylammonium cations and a variable number of sodium ions are present per unit cell in ZSM-5 [2].

Again, an inhomogeneous distribution of aluminium is suggested by the fact that the surface atomic Si/Al ratio (10) is less than the bulk atomic Si/Al ratio (12.6).

(c) As-synthesised Ga-ZSM-5 (diethanolamine and tetrapropylammonium cation templates

The powder X-ray diffraction studies of both forms of as-synthesised Ga-ZSM-5 indicate that the materials are highly crystalline and pure. Minor differences in the traces are attributed to the presence of different template molecules. In particular, the d-spacings in the Ga-ZSM-5 sample synthesised with tetrapropylammonium hydroxide are larger than those for the sample synthesised with diethanolamine, indicating a slightly larger unit cell. This increase in the unit cell parameters on replacing diethanolamine with the tetrapropylammonium cation probably reflects the strain associated with the distorted tetrapropylammonium cations existing at the channel intersections.

Data obtained by microanalysis, X-ray fluorescence, and atomic absorption are shown in Table 7.3 for Ga-ZSM-5 synthesised with tetrapropylammonium hydroxide.

TABLE 7.3	Si[a]	Ga[a]	Al[a]	Na[b]	C[c]	N[c]	Ca[a]
% mass	37.2	5.8	∿0.0	0.8	7.3	0.8	0.2
	Si	Ga	Al	Na	C	N	Ca
atoms/ unit cell	90.3	5.7	∿0.0	2.4	41.5	3.9	0.5

(a) X-ray fluorescence.

(b) Atomic absorption.

(c) Microanalysis.

The data obtained in a similar fashion for Ga-ZSM-5 synthesised with diethanolamine are shown in Table 7.4:

TABLE 7.4	Si[a]	Ga[a]	Al[a]	Na[b]	C[c]	N[c]	Ca[a]
% mass	36.9	6.1	∿0.0	0.2	4.9	1.5	0.3
atoms/ unit cell	90.0	6.0	∿0.0	0.6	28.0	7.3	0.5

(a) X-ray fluoresence.

(b) Atomic absorption.

(c) Microanalysis.

Assuming that all the gallium present is in the framework, the analytical data of Table 7.4 suggest that the charge on the gallium is overwhelmingly compensated by protonated template. This further assumes that the calcium is present as a surface impurity (if not, the protonated diethanolamine accounts for ∿73 % of the gallium species).

In the case of Ga-ZSM-5 synthesised with tetrapropylammonium hydroxide,a larger proportion of the gallium charge

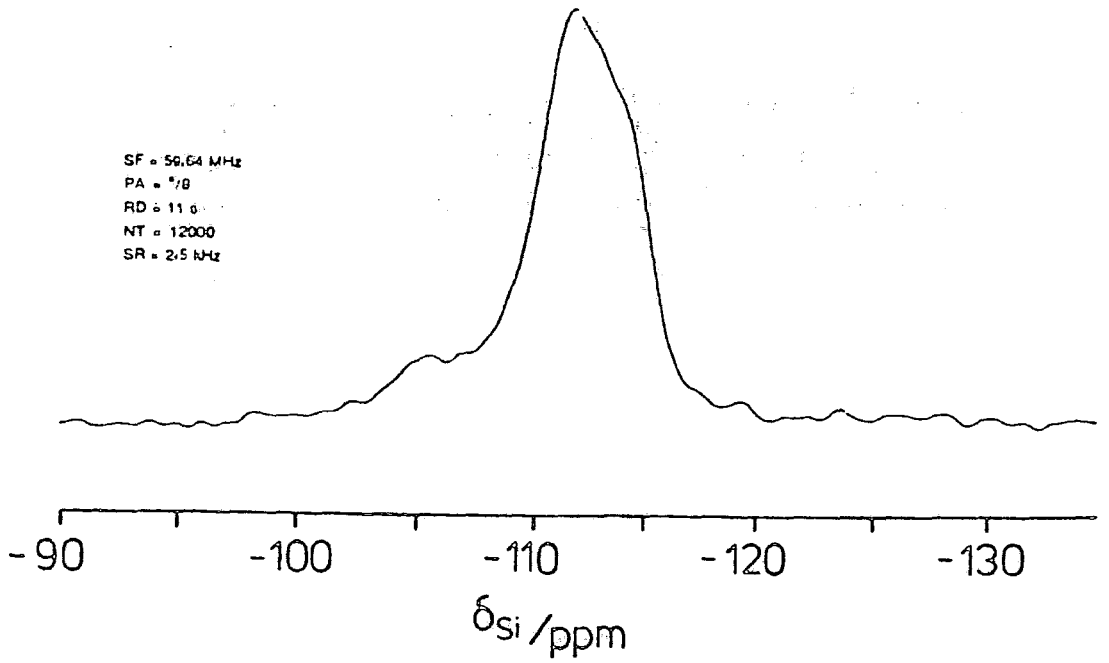

Figure 7.1(a): ^{29}Si SP MASNMR spectrum of as-synthesised theta-1.

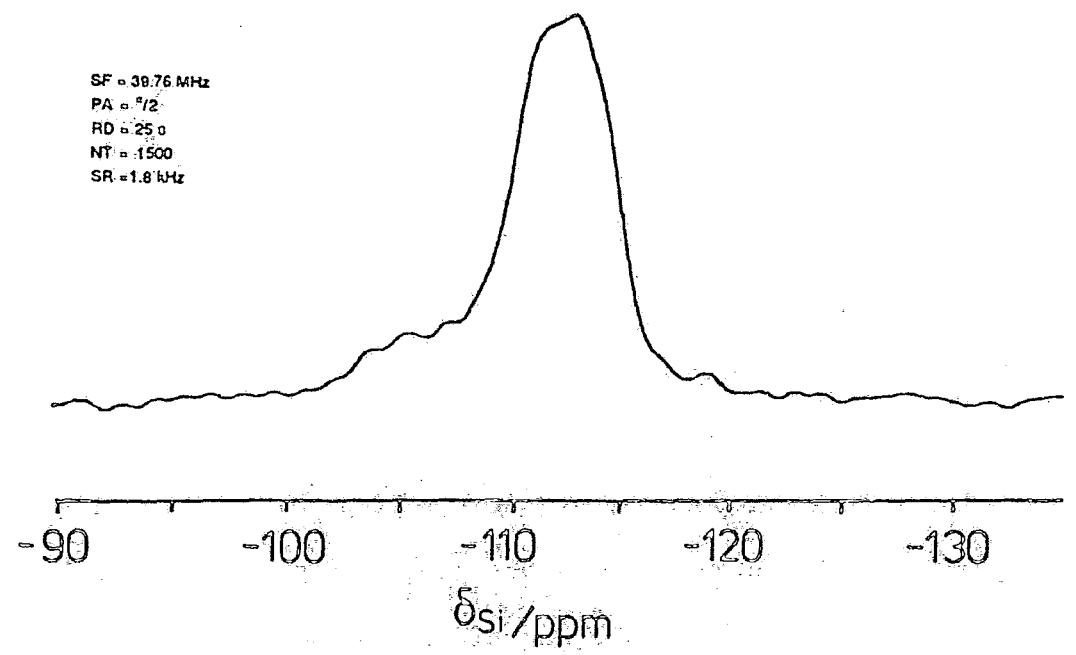

Figure 7.1(b): ^{29}Si SP MASNMR spectrum of calcined theta-1.

is compensated for by sodium cations. As with the aluminium analogue, approximately four TPA^+ cations are present per unit cell.

Trace amounts of iron, cerium and titanium were detected in both samples (% masses <0.03, <0.09 and <0.02 respectively) by X-ray fluorescence.

7.3 ^{29}Si MAS Studies of as-synthesised theta-1

7.3.1 (a) Single-pulse studies

In Chapter Four, the spectral changes that occur in the ^{29}Si NMR spectrum of ZSM-5 on loading the zeolite with organic molecules were discussed. The ^{29}Si MASNMR spectrum of ZSM-5 depends critically on the sorbate molecule[3,4,5], the change being attributed to either a reorganisation of the framework structure or to a possible crystallographic change from the orthorhombic to monoclinic form, as suggested by X-ray diffraction measurements. The change is also influenced by the Si/Al ratio, the presence of aluminium in the zeolite framework stabilising the orthorhombic form[6].

Both ZSM-5 and theta-1 may be constructed from the same so-called 5-1T secondary building units, and single-pulse ^{29}Si MASNMR spectra of the as-synthesised and calcined forms of theta-1 were recorded in order to see if theta-1 displays the same structural sensitivity as ZSM-5.

The single-pulse ^{29}Si MASNMR spectrum of the as-synthesised form of theta-1 is shown in Figure 7.1(a). The spectrum was recorded using small flip angles (<25^{o}), with a 16 s delay between the pulses so that the Ernst angle condition was satisfied for a ^{29}Si T_1 value of 140 s. The spectral resolution

in the Q^4 region is such that it is not possible to resolve the individual crystallographic sites, but the results of the previous chapter suggest that the ^{29}Si T_1 values for crystallographically distinct sites in theta-1 synthesised with diethylamine are similar. The spectrum was however recorded using a variety of recycle delays to ensure that no spectral distortion due to T_1 saturation occurred. It has been shown that for a given structure[7], T_1 varies little between the silicon environments Si(nAl).

The asymmetric nature of the Q^4 region shown in Figure 7.1(a) would not be expected to result simply by the broadening of the resonances observed for calcined high-silica theta-1 due to distribution of aluminium about the ^{29}Si nuclei in terms of second and further nearest neighbour interactions. The interpretation is complicated somewhat by the spectral overlap of the Q^4 and Q^3 regions.

Figure 7.1(b) shows the single-pulse ^{29}Si MASNMR spectrum of the calcined sample. The sample was calcined in air for 12 hours at 823 K using a ramp rate of 15 K/min. Figure 7.1(b) was obtained under quantitative conditions using the ^{29}Si T_1 data for calcined high-silica theta-1 presented in the previous chapter. Superposition of Figures 7.1(a) and (b) reveals that the overlap between the Q^3 and Q^4 regions is identical. The differences between the spectra thus result purely from the removal of the template.

Clearly, the single-pulse ^{29}Si MASNMR spectra depend on the physical state of the sample and this change may be attributed to either a reorganisation of the framework structure or to a possible crystallographic change, although the

possibility that it is due either to bulk susceptibility effects of the template molecules replacing water in the zeolite, or due to template-framework interactions may not be ruled out. X-ray diffraction studies were performed in an attempt to resolve this problem and the results shown in Table 7.5 eliminate the possibility of a major crystallographic symmetry change.

TABLE 7.5 d-spacings for theta-1 samples

h	k	l[8]	as-synthesised/Å	calcined/Å
1	1	0	10.81(m)	10.78(vs)
0	2	0	8.71(w)	8.66(w)
2	0	0	6.95(w)	6.91(w)
2	2	0	5.42(w)	5.40(w)
1	3	0	-	-
1	1	1	-	-
3	1	0	-	-
0	2	1	-	-
0	4	0	4.36(s)	4.36(s)
2	2	1	-	-
2	4	0	-	-
1	3	1	3.69(vs)	3.68(s)
3	3	0	3.62(s)	3.61(s)
4	0	0	3.48(m)	3.47(m)

vs = very strong
s = strong
m = medium
w = weak

Table 7.5 suggests that the sample containing diethanolamine has larger d-spacings for smaller values of 2θ. This indicates that the presence of diethanolamine increases the dimensions of the unit cell. Also significant is the difference in intensity of some of the peaks, notably the |110| reflection. It is possible that the differences in intensities between the two patterns result from orientation effects[8], although this is unlikely given the small size of the crystallites. In addition, other research at Sunbury-on-Thames has suggested that calcination results in a change of intensity of the |110| reflection when reasonable precautions were taken to avoid orientation effects.

The situation is in contrast to that observed for theta-1 synthesised with diethylamine, where the single-pulse ^{29}Si MASNMR spectra of both the as-synthesised and calcined forms are similar and the d-spacings of the as-synthesised form are similar to those of calcined theta-1.

It seems that the diethanolamine template interacts more strongly with the zeolite framework than the diethylamine template due to the enhanced facility for hydrogen bonding. This hydrogen bonding should result in an increased valency of some of the framework oxygens and a corresponding increase in the local Si-O bond distance. The overall result should be a minor reorganisation of the framework structure with a corresponding change in the ^{29}Si MASNMR spectrum. Similar changes in the single-pulse ^{29}Si MASNMR spectrum are noticed for NH_4^+-theta-1.

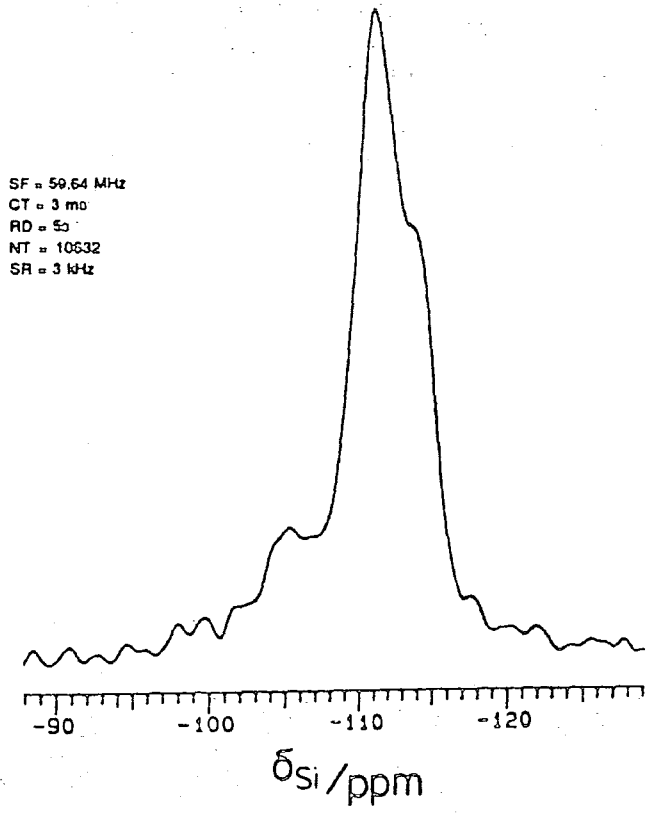

Figure 7.2: ^{29}Si CP MASNMR spectrum of as-synthesised theta-1.

(b) Cross-polarization studies

The analysis outlined earlier suggests that the diethanolamine template which exists solely in the 10-T channels is the major source of protons for cross-polarization experiments. Figures 7.1(a) and (b) suggest that the chemical shifts of the crystallographically distinct silicon species of the as-synthesised form are slightly modified with respect to the calcined form. In an attempt to simplify the Q^4 region, the ^{1}H-^{29}Si cross-polarization ^{29}Si MASNMR spectrum of the as-synthesised form was obtained using a 3ms contact time. The results of Chapter Six suggest that the resulting cross-polarization signal should be dominated by three crystallographically distinct sites in the first-coordination sphere of the template. Figure 7.2 is not conclusive,but suggests that the signals from sites 2 and 3 overlap to produce a peak at ∿-111.9ppm, whereas site 4 contributes to the peak at -114.4 ppm (see Figure 6.7).

Increasing the contact time to 35ms results in a spectrum similar to Figure 7.1(a), presumably due to the contribution of site 1 to the centre of the spectrum at longer contact times. It is thus reasonable to suggest that the framework topology of sites 2 and 3 are more similar in the presence of a diethanolamine template than without it.

7.4 ^{13}C NMR Studies of as-synthesised theta-1

The multinuclear magnetic resonance study of theta-1 was continued by using the template as a probe for acid sites. NMR has the potential to distinguish between amine adsorbed at different acid sites in the zeolite, and additionally, the mode of bonding to the acid sites may be determined[9,10]. The

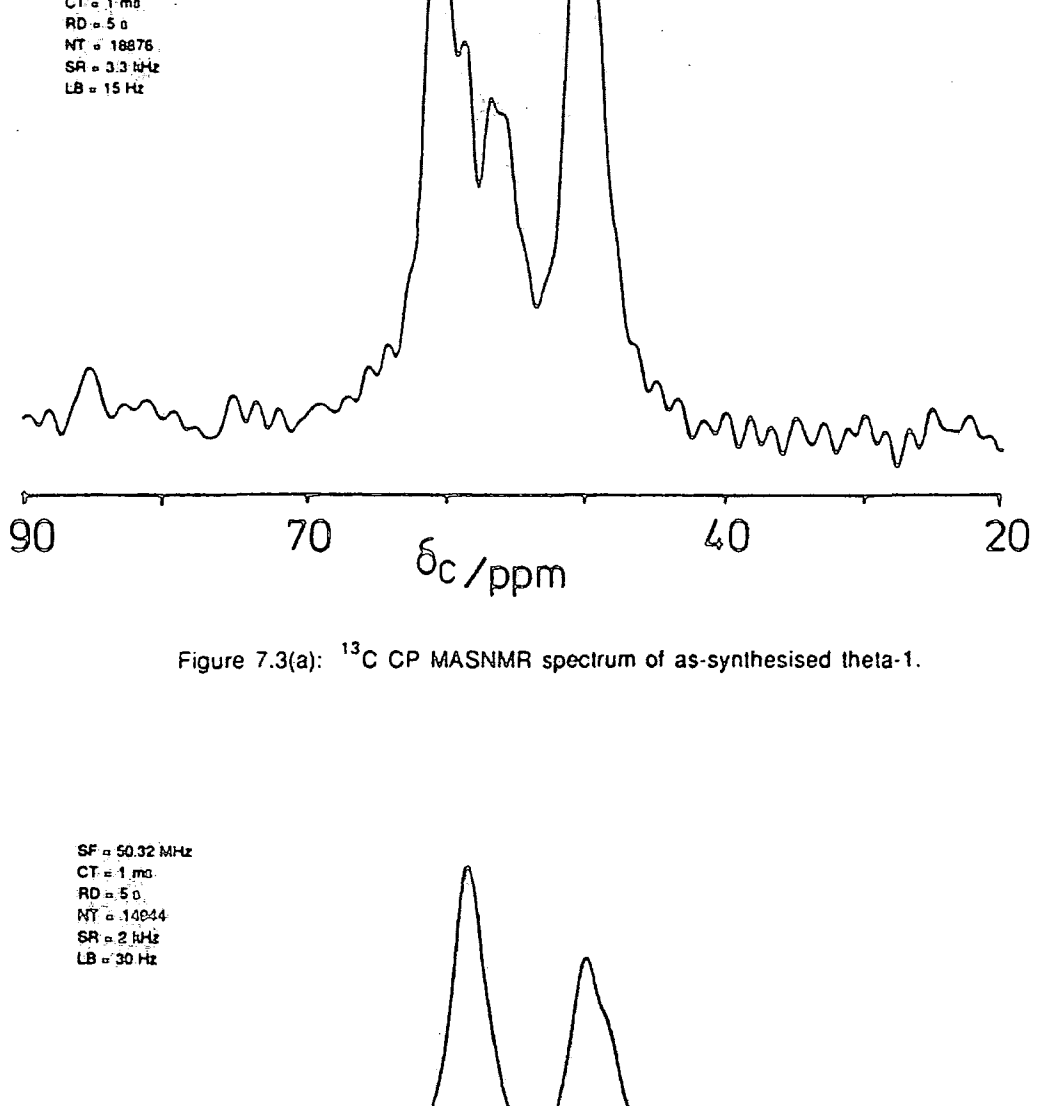

Figure 7.3(a): ^{13}C CP MASNMR spectrum of as-synthesised theta-1.

Figure 7.3(b): ^{13}C CP MASNMR spectrum of as-synthesised theta-1 after thoroughly washing with water

analytical data shown in Table 7.1 suggest the presence of both Brönsted and Lewis sites. The Lewis acidity is associated with the non-framework aluminium species, and there may be some contribution from sodium and potassium cations. In addition, the possibility of hydrogen bonding with surface hydroxyls, interchannel oxygen or physisorbed water exists. There may also be interaction with internal silanol groups of the type found in high-silica theta-1.

Three major peaks were observed in the cross-polarization ^{13}C MASNMR spectrum of as-synthesised theta-1 (Figure 7.3(a)). These peaks are further split suggesting that a range of species correspond to each major peak. It was felt that the major peaks corresponded to the protonated and non-protonated forms of the template - the peak at 50.5 ppm being a composite. The solution state studies shown below suggest that this is the case (Table 7.6), protonation of the amine giving rise to a diamagnetic shift of the carbon resonances. Measurement of the shifts in water reveals that the hydrogen-bonded shifts correspond closely to those of the non-protonated form.

TABLE 7.6 ^{13}C Chemical shifts of free and protonated diethanolamine[a] (δ/ppm)

	Free diethanolamine	Protonated diethanolamine[b]	(As-synthesised theta-1
$HN(CH_2\underline{C}H_2OH)_2$	60.2	55.8	(∿60, ∿56.3)
$HN(\underline{C}H_2CH_2OH)_2$	49.8	48.5	(∿50.5, with shoulder on low frequency side)

(a) The solvent used was chloroform.

(b) Ethanoic acid was used to protonate the diethanolamine.

The peak at ∿60ppm and part of the signal at 50.5ppm are reduced in intensity on washing with water. To confirm that some of the template had been removed, microanalysis studies were performed to eliminate the possibility of a change in cross-polarization dynamics on washing. Clearly, the peak at 60 ppm and part of the peak at 50.5ppm result from template physisorbed at the surface (physisorbed in this sense refers to the ease of removal). The template is surprisingly difficult to remove - many protracted water washings are necessary to remove the surface species. The spectrum of the thoroughly washed sample is shown in Figure 7.3(b). The remaining signal corresponds to the chemisorbed species, the shifts implying that the template is protonated. Given the coincidence in the molar ratio of nitrogen to framework aluminium of 1.2 for the thoroughly washed sample, the results suggest that the template is the counterbalancing cation for the anionic aluminium charge. The ^{13}C chemical shifts are in good agreement with the shifts observed for diethanolamine present in ZSM-5 and Ga-ZSM-5,where the template must be protonated to compensate for the anionic charge. The lower frequency peak is broader and exhibits a shoulder as a consequence of being directly bound to nitrogen. There is also a broad underlying peak of indeterminate nature, which probably accounts for the excess of chemisorbed template with respect to framework aluminium.

For a given number of transients, the signal-to-noise ratio for as-synthesised theta-1 containing diethanolamine as the template molecule (both physisorbed and chemisorbed species) is considerably worse than that observed when diethylamine is

the template in spite of the fact that the %wt. carbon is greater by a factor of 3.26 in the former case. It seems that not all of the diethanolamine template is detected in a cross-polarization experiment. The single-pulse ^{13}C MASNMR spectrum of the diethanolamine form reveals a dramatic increase in the intensity of the physisorbed/chemisorbed diethanolamine ratio relative to that observed in the cross-polarization ^{13}C MASNMR spectrum. The possibility that differences in mobility between different types of adsorbed diethanolamine species make a significant proportion of diethanolamine sensitive to the Hartmann-Hahn match was discounted by variation of the ^{13}C r.f. field strength in successive cross-polarization experiments.

For ZSM-5 containing the diethanolamine template, single-pulse ^{13}C MASNMR studies reveal that the template is predominantly protonated, in agreement with the microanalysis results of Table 7.2, although the precise determination of the chemical shifts is made difficult by the broad background from the rotor cap. A cross-polarization ^{13}C MASNMR experiment reveals a very feeble signal which was not improved by variation of the mismatch parameter. Given that the template is predominantly confined within the channels, it is surprising to see such a feeble signal. The %wt. carbon is similar to that observed for theta-1 synthesised with diethylamine. Although the channels in ZSM-5 are larger than those of theta-1, it seems unlikely that the diethanolamine template could execute isotropic motion.

It was felt that motional effects might be responsible for the observation in the cross-polarization ^{13}C MASNMR spectrum and consequently, the cross-polarization ^{13}C MASNMR spectrum

was recorded at 265 and 330 K. The spectrum was essentially unaltered at 265 K but the result at 330 K was an improvement, albeit with very broad peaks. It seems likely that motion is occurring at either the decoupling or spinning frequency[11].

Figure 7.3(a) suggests the presence of a range of species associated with the protonated amine region. It may be that in addition to counterbalancing the framework aluminium charge, there may be some contribution from diethanolamine species protonated at silanol defect sites or interacting with electron-deficient non-framework aluminium species. The contribution from hydrogen-bonded amine may be ruled out on the basis of its ^{13}C chemical shifts in water. It is however clear that water has a greater affinity for these sites than diethanolamine.

The possibility of surface acid sites was further probed by ^{1}H NMR and ESCA. For the ^{1}H MASNMR studies, it was anticipated that the physisorbed species present at the surface would be very mobile and consequently would be selectively observed in a ^{1}H MASNMR experiment with respect to the bulk species. ^{1}H NMR relaxation measurements were also performed with a view to simplifying the ^{1}H MASNMR spectrum. The interaction of amines with acid surfaces is an area of considerable interest, and an unambiguous description of the nature of the adsorption complexes has not yet emerged.

7.5 ^{1}H NMR Studies

Measurement of the spin-lattice relaxation time of the protons in the rotating frame at 200.13 MHz was carried out using the usual spin-locking sequence applied to the ^{1}H nuclei on-resonance. For the as-synthesised form, where the observed

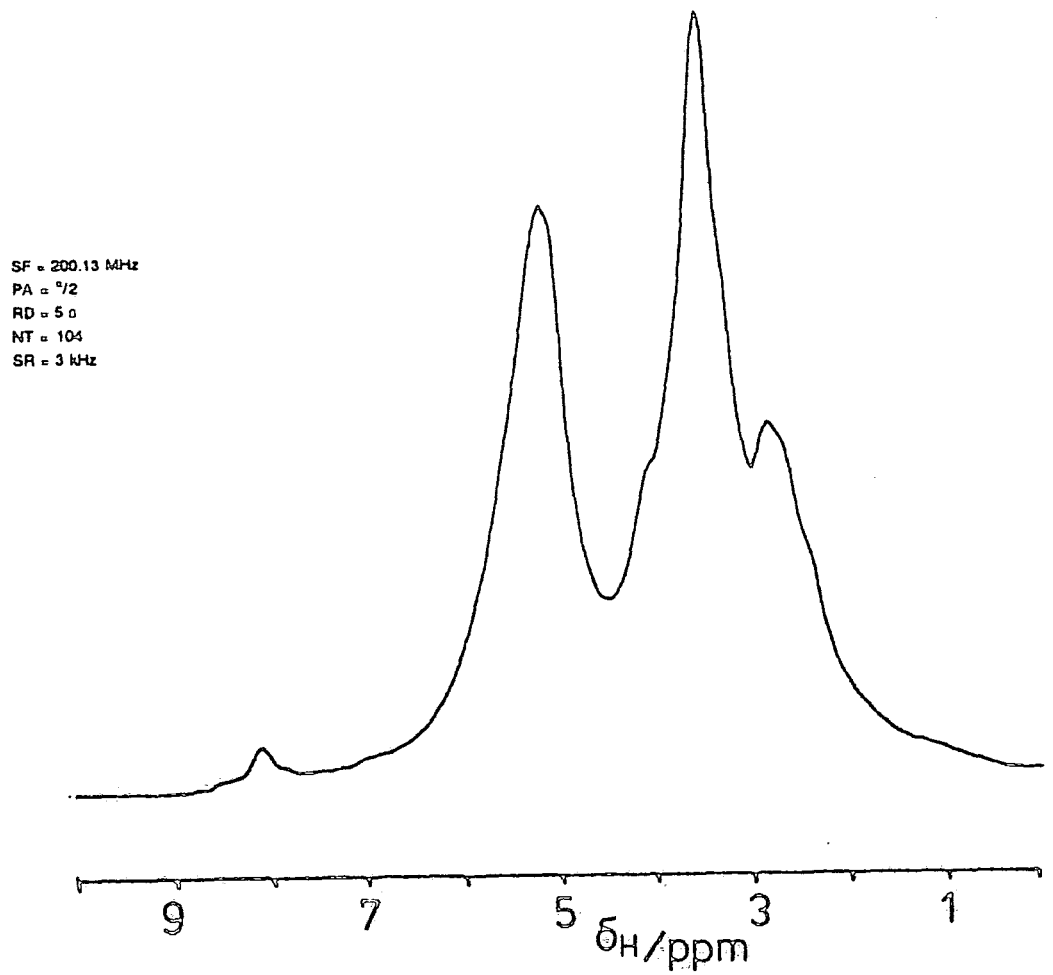

Figure 7.4: ^{1}H MASNMR spectrum of as-synthesised theta-1.

signal corresponds mainly to the physisorbed form, the data were fitted to two exponential components (Table 7.7). The most likely explanation is that at least two physically distinct regions with different NMR properties exist at the surface and that for $T_{1\rho}$ (^1H) relaxation, spin diffusion is unable to average out these heterogeneities, unlike the case for T_1 where an exponential decay was observed (Table 7.7).

TABLE 7.7. ^1H T_1 and $T_{1\rho}$ data for as-synthesised theta-1

T_1/S	%	$T_{1\rho}$/ms	%
0.49	100	2	24.6
		8.8	75.4

ν_H = 200.13 MHz, ν_{1H} = 125 kHz

Experiments exploiting the non-exponential decay of $T_{1\rho}$ were thus employed to simplify the ^1H MASNMR spectrum.

The ^1H MASNMR spectrum is shown in Figure 7.4. The spectrum is well resolved due to molecular motion averaging out the ^1H homodipolar coupling and shielding anisotropy. Application of the MREV-8 pulse sequence with MAS confirms the absence of significant ^1H homodipolar coupling, the only difference being the appearance of a new peak of low intensity at 1.3ppm. The peak at 5.3ppm is believed to result from the presence of physisorbed water on the basis of D_2O vapour exchange experiments and the chemical shift. The rest of the peaks are attributed to the surface template. Dramatic reduction of the recycle delay to 0.1s results in only a

^1H channel:

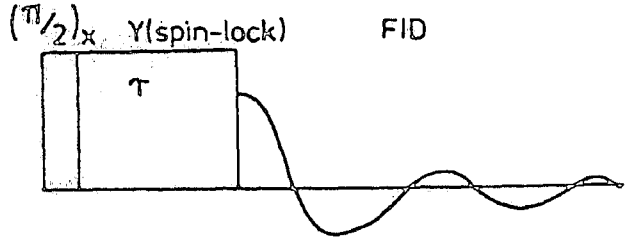

Figure 7.5(a): Spin-locking experiment used to simplify conventional ^1H SP MASNMR experiment.

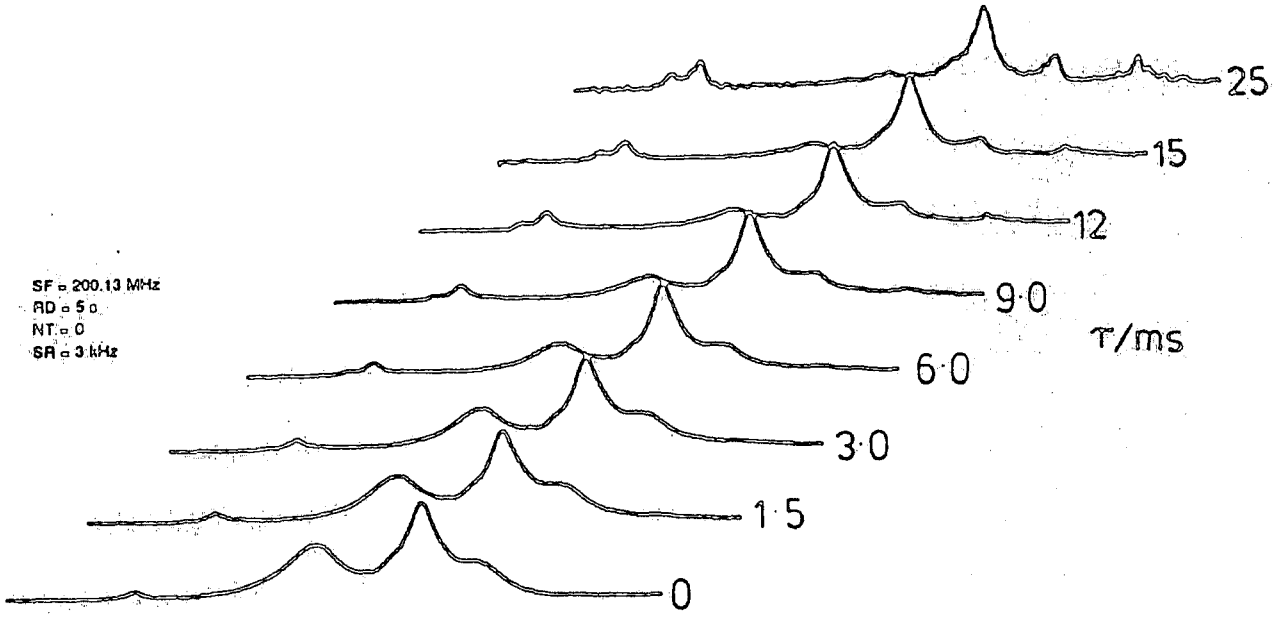

Figure 7.5(b): Application of the pulse sequence shown in Figure 7.5(a) to as-synthesised theta-1.

reduction in sensitivity - the relative intensities of the peaks are identical to those of Figure 7.4 in agreement with Table 7.7. Clearly, the proton exchange rate of the protons giving rise to the resonances at 8.1-8.6 ppm and 1.3 ppm with the water is slow on the NMR timescale ($\sim<1.6\times10^{-3}s^{-1}$ and $<1.3\times10^{-3}s^{-1}$ respectively).

It was decided that the $T_{1\rho}$ values were sufficiently different to justify the use of the spin-locking experiment shown in Figure 7.5(a). The spectra obtained as a function of τ are shown in Figure 7.5(b). The data confirm that the template is not spread homogeneously across the surface, and at least three physically distinct surface domains may be distinguished. The two-component $T_{1\rho}$ obtained by direct measurement corresponds to an approximation of a very complex situation. The physisorbed water is identified as the component with the shortest $T_{1\rho}$. The $T_{1\rho}$ values for the various peaks were estimated from the variation of peak intensity as a function of contact time and are shown in Table 7.8.

TABLE 7.8 Proton $T_{1\rho}$ as a function of chemical shift

δ/ppm	$T_{1\rho}$/ms
1.3	11
2.8	6
3.7	6
5.3	4.5
8.1	11
8.6	11

ν_H = 200.13 MHz, ν_{1H} = 62.6 kHz.

---

^{1}H channel :

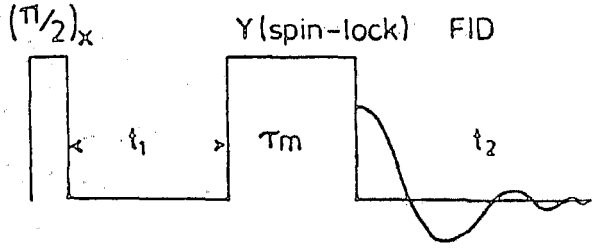

Figure 7.6(a): Homonuclear 2D proton experiment used for the investigation of spin exchange.

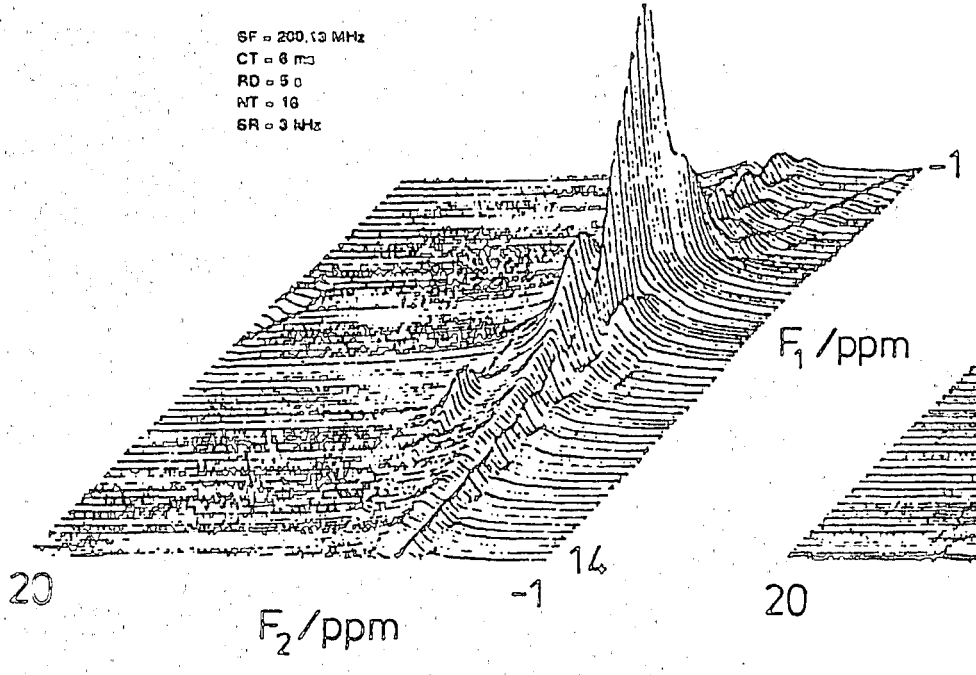

Figure 7.6(b): As-synthesised theta-1 with τ_m = 6ms.

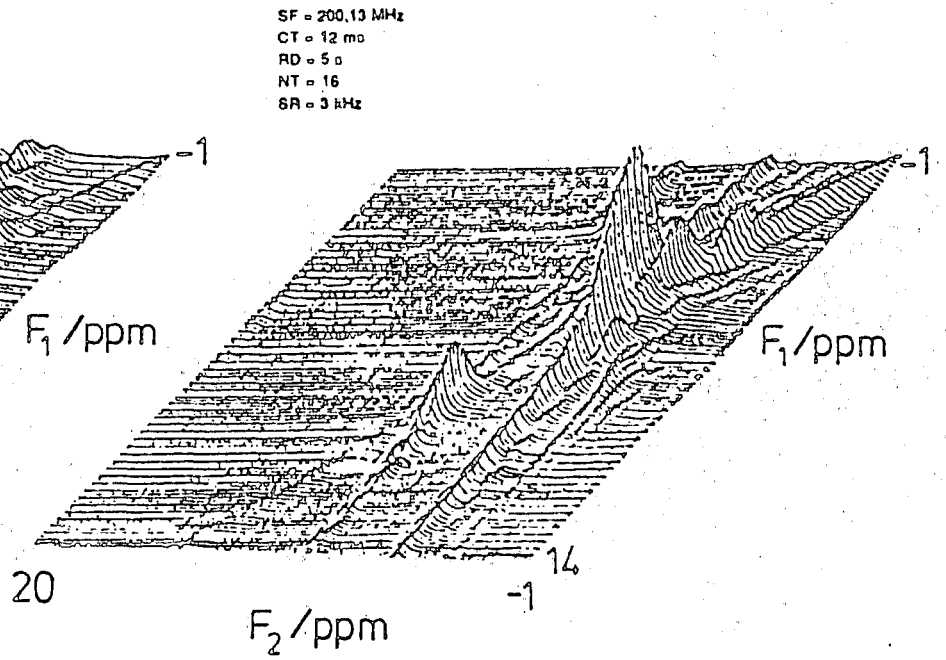

Figure 7.6(c): As-synthesised theta-1 with τ_m = 12ms.

A new peak is observed at 1.3 ppm when the spin-lock time exceeds 9 ms. This presumably corresponds to the peak observed when the CRAMPS sequence was applied. The ^{1}H MASNMR spectrum of pure liquid diethanolamine suggests that the peaks at 3.7 and 2.8 ppm result from protons attached to the carbon atoms next to the oxygen and nitrogen atoms respectively. These shifts correspond to hydrogen-bonded diethanolamine. The ^{1}H MASNMR spectrum of liquid diethanolamine exhibits a third peak at 4.9 ppm resulting from exchange between alcoholic and amine protons - the alcohol proton typically resonating at higher frequency than the amine proton. The shoulders to the high frequency side of the main peaks at 3.7 and 2.8 ppm, in conjunction with peaks in the 8.1-8.6 ppm region suggest the possibility of protonated amine which in turn implies the existence of surface acid sites.

The system was analysed further by examining the possibility of slow exchange between species with similar $T_{1\rho}$ values. 2D NMR spectroscopy is a valuable method for the study of spin-exchange processes such as those resulting from chemical exchange or spin diffusion. A pulse scheme for analysing such exchange processes was outlined in Chapter Three, and the homonuclear 2D proton experiment[12] used is shown in Figure 7.6(a). As a consequence of the insignificant homodipolar proton interaction in the surface template, no MREV-8 sequence was applied during t_1 and t_2. 64 FIDS were obtained with t_1 increments of 60μs and the 2D Fourier Transformation was performed in magnitude mode. There was no need to synchronise the spin-lock time with the rotor period due to an absence of spinning sidebands[12]. The value

of the 2D experiment is greatly enhanced by the effective "handle" the experimentalist has on the intensity of the peaks - a suitable choice of τ_m potentially simplifies a complex spectrum. It was accepted of course that given the narrow ^1H chemical shift range, the observation of cross peaks would be a difficult task. In fact, the assignment was made all the more complex by the dispersion wings of the absolute-value diagonal peaks.

The result for a spin-lock time of 6 ms is shown in Figure 7.6(b). The situation was more complex than expected due to modulation in the F_1 dimension. The effect was reduced by alternating the phase of the spin-locking pulse and subtracting the alternate FIDS to minimize the effect of artefacts. Although the resolution is limited, it is possible to see that no exchange is occurring between the water peak at 5.3ppm and the resonances at 8.6, 8.1 and 1.3ppm. This could have been predicted from Table 7.8 where different $T_{1\rho}$ values for the relevant peaks are observed. The onset of exchange between the species in the 8.1-8.6ppm range and the 1.3ppm species is just observable. Table 7.8 suggests that the proton exchange rate of the two species is less than $7.1 \times 10^{-4} s^{-1}$ and Figure 7.6(b) suggests that the exchange rate is of the order of $6.0 \times 10^{-3} s^{-1}$.

Figure 7.6(c) shows the result obtained using a spin-lock time of 12 ms. The water peak has a very low intensity in this case and the exchange between the above mentioned species is now more apparent. For all of the above results, both the rotor cap and rotor were soaked in D_2O to eliminate any spurious proton signals.

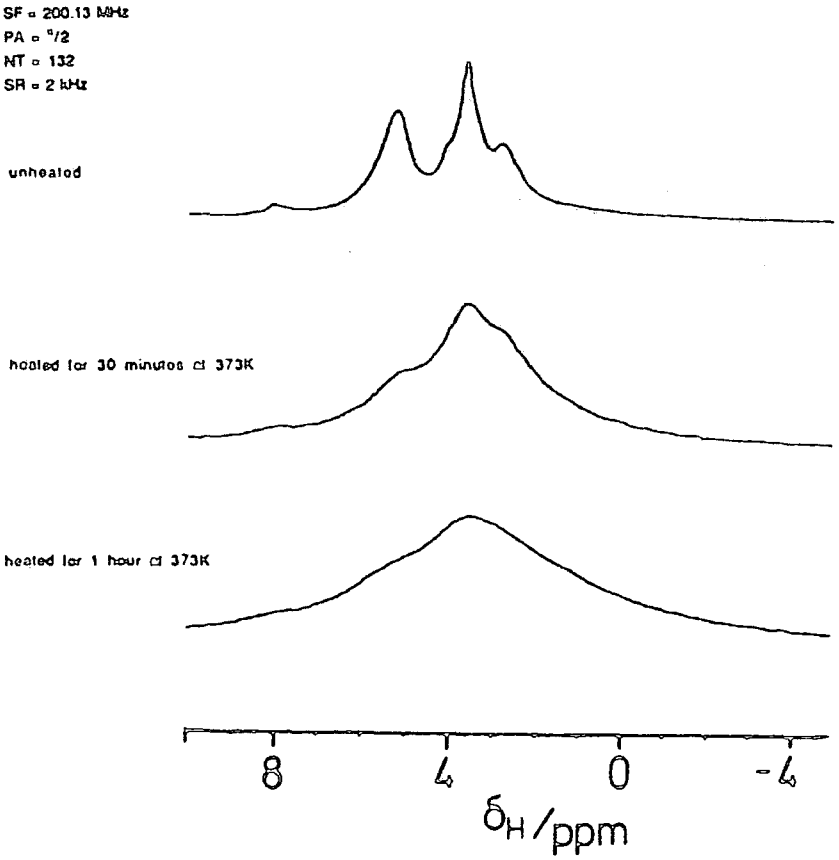

Figure 7.7: ^{1}H MASNMR spectra of as-synthesised theta-1 as a function of heat treatment.

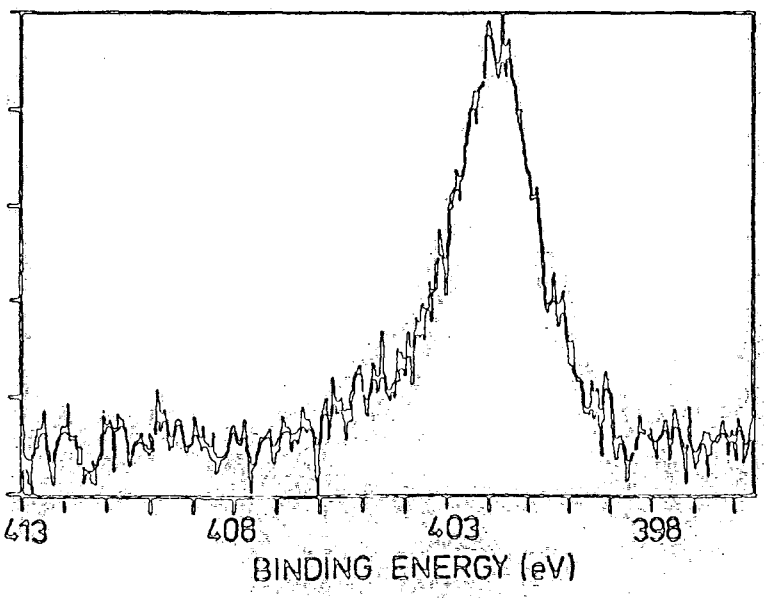

Figure 7.8: Nitrogen ESCA spectrum for as-synthesised theta-1.

It would thus seem that the protonated amine or amine complex is in close contact with the 1.3 ppm species which is probably a silanol moiety close to the surface acid site.

The ^{1}H MASNMR studies, for which the surface species are selectively observed, are in agreement with the ^{13}C NMR studies. The bulk of the signal originates from the non-protonated species. The surface species are all physisorbed in the sense that they may be removed by thorough washing. This corresponds to the removal of the 60ppm peak in the ^{13}C NMR studies in addition to the removal of some of the protonated species. The fact that the surface species may be removed by thorough washing indicates that water either interacts more strongly with the surface sites and/or that the surface sites are extraneous species (or contain an extraneous component).

Heating the sample at 373 K results in a time-dependent broadening of the ^{1}H MASNMR spectrum (Figure 7.7). This is believed to result from the increased homodipolar ^{1}H interaction that occurs if the template becomes more strongly adsorbed at the surface as the water is removed. Surface dehydration is also accompanied by an increase in the signal-to-noise ratio in the cross-polarization ^{13}C MASNMR spectrum. A broad component is observed in addition to the physisorbed and chemisorbed species.

In conclusion, the experiments outlined in the ^{1}H NMR section provide a novel method for characterising the nature of the diethanolamine interaction with the surface. The

experiments could be extended to probe catalytic reactions where the mobility of the surface organic species results in a similar simplification of the ^{1}H MASNMR spectrum due to the averaging of the homodipolar proton interaction. ^{1}H MASNMR allows the selective observation of surface organic species due to the restricted motion of the channel species.

7.6 ESCA Studies of as-synthesised theta-1

The nitrogen signal shown in Figure 7.8 confirms both the presence of protonated and non-protonated diethanolamine template. The protonated template accounts for the shoulder observed at 2-3eV to the high binding energy side of the major peak. Although the surface of the zeolite may be selectively observed by the use of ESCA, the technique suffers from the drawback that the actual penetration depth is poorly defined. Given that the technique is sensitive to a depth of 30 Å, and that the crystallite size is approximately 0.1x2μm,[13,14], in addition to the fact that a significant proportion of the diethanolamine resides between the crystallites, it seems probable that Figure 7.8 results from nitrogen-containing species at the crystallite surface (recall that no nitrogen signal was observed for the as-synthesised form of high-silica theta-1). This observation adds weight to the arguments presented above for the existence of surface acid sites. The results would not be expected to be quantitative however because some loosely bound template would be removed on evacuating down to high-vacuum.

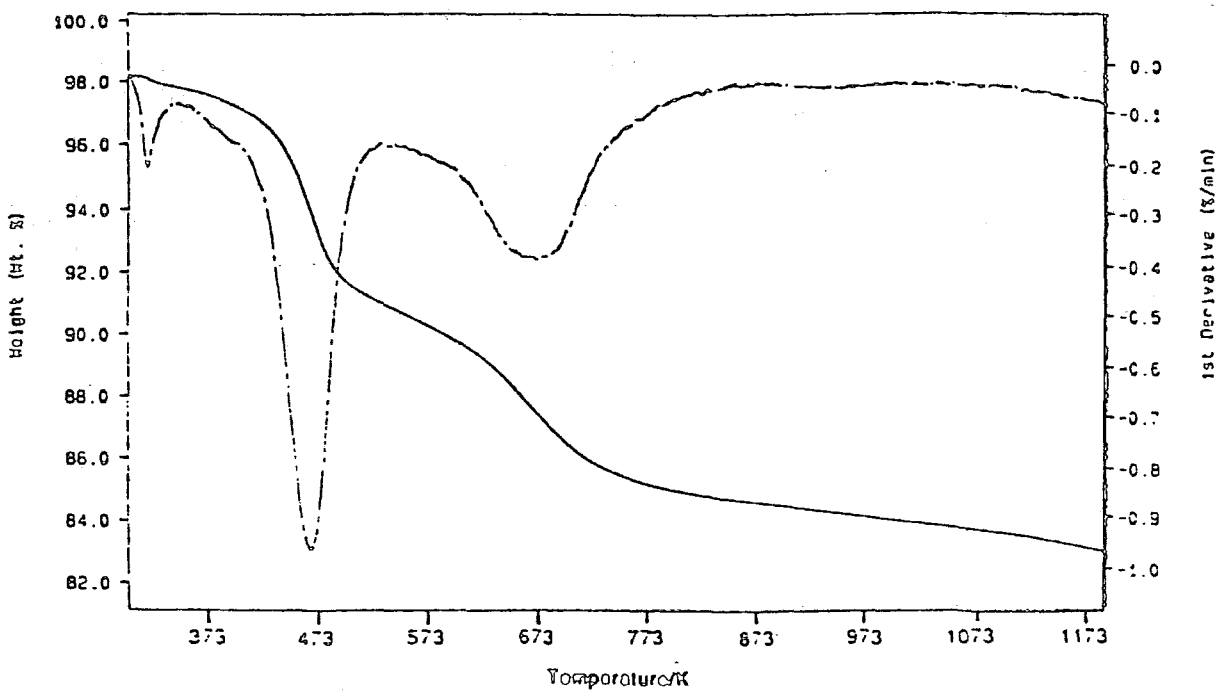

Figure 7.9(a): TGA trace for as-synthesised theta-1.

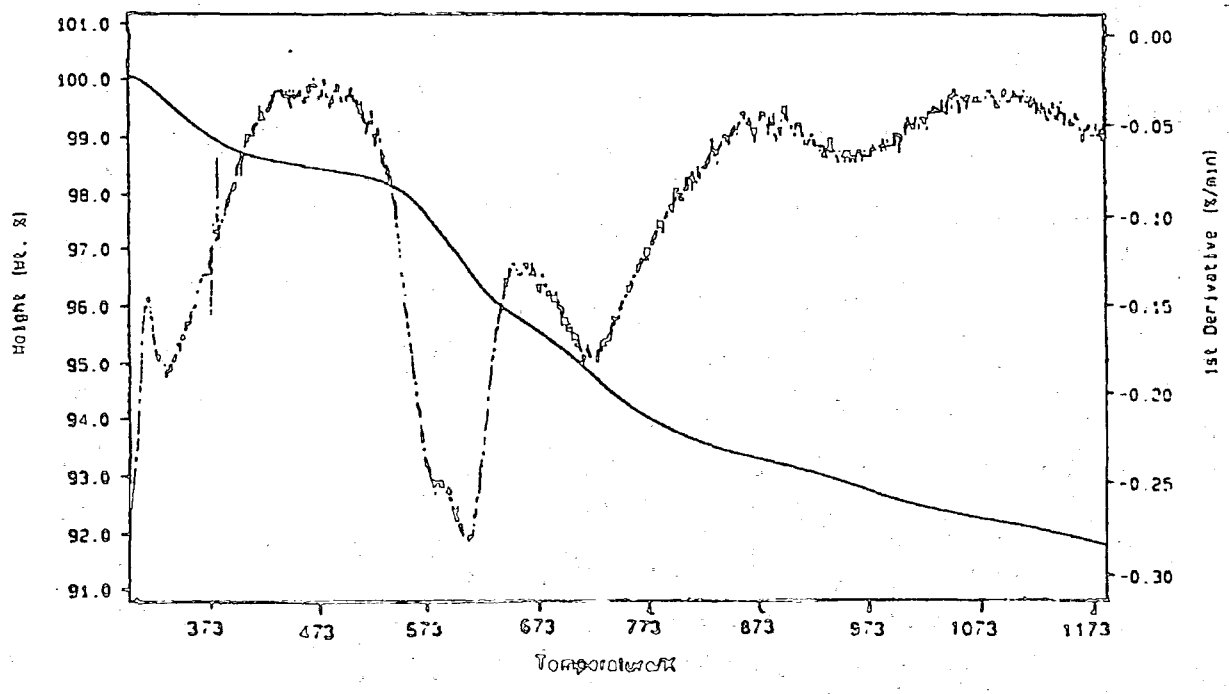

Figure 7.9(b): TGA trace for as-synthesised ZSM-5.

7.7 Thermal gravimetric analysis of as-synthesised theta-1 and ZSM-5

Figures 7.9(a) and (b) show the TGA traces for the as-synthesised samples. The strongest acid sites typically desorb a presorbed base at the highest temperature. On the basis of the above results, a range of desorption temperatures would be expected for theta-1, whereas a smaller range would be expected for ZSM-5 given that no mobile surface template was detected by ^{1}H MASNMR. The data resulting from the differential plots are shown in Table 7.9.

TABLE 7.9 Peak temperatures and widths for the first derivative plot

	Peak Temperature/K				Peak Width/K			
	Peak 1	Peak 2	Peak 3	Peak 4	Peak 1	Peak 2	Peak 3	Peak 4
Theta-1	diffuse	468	313	923	diffuse	44	98	102
ZSM-5	diffuse	593	703	943	diffuse	71	~102	102

The diffuse peaks that are observed in both Figures 7.9(a) and (b) between 303 and 423 K result from the desorption of surface water. Two major desorption peaks are observed for theta-1 as expected. The 468 K desorption peak is believed to result from the desorption of surface template and the 673 K desorption peak is probably associated with the protonated template that counterbalances the anionic aluminium charge. For ZSM-5, no 468 K peak is observed, in agreement with the ^{1}H NMR data, but peaks at 593 and 703 K are seen. These peaks may indicate the presence of framework Brönsted acid site inhomogeneity but care must be exercised due to the possible contribution of kinetic factors.

Peaks are observed in the 873-973 K range in both cases and may be associated with the condensation of silanol groups and/or dealumination of some of the framework aluminium (both processes involve the loss of water from the zeolite framework). There may also be a peak in the 1173 K region which would almost certainly result from dehydroxylation.

7.8 ^{27}Al Studies of theta-1

In the work discussed below, a variable magnetic field study was performed on the as-synthesised and H-forms of theta-1. In addition to information concerning the co-ordination of the aluminium species present, the variation with field of the centre of gravity of the central transition may be used to obtain the true isotropic chemical shift and the quadrupole coupling constant[15]. The true isotropic chemical shift in turn provides information on the mean Al-O-Si bond angle at the Brönsted acid site[16]. Of course, there are a maximum of four crystallographically distinct aluminium sites which cannot be resolved in the ^{27}Al central transition MASNMR spectrum for the magnetic fields used, and so the values calculated for the true isotropic chemical shift and the quadrupolar coupling constants correspond to weighted means as discussed in Chapter Five.

The improvement in quality of the spectrum of as-synthesised theta-1 on going from an aluminium frequency of 52.15 MHz to a frequency of 104.22 MHz involves increased symmetry as well as a reduction in the width of the peak which is observed in the four-coordinate aluminium region. These effects were expected and are due to the reduced contribution to the spectrum of the second-order quadrupolar term at higher magnetic field,

as is the shift to high frequency of the centre of gravity of the central transition lineshape (Table 7.11). Similar effects have been observed for NaA[17]. It is clear that second-order quadrupolar broadening is more important than chemical shift broadening at 52.15 MHz. Proton decoupling had no effect on the linewidth of the as-synthesised form of theta-1 at 52.15 MHz, showing that magic-angle spinning alone is sufficient to suppress any ^{1}H-^{27}Al dipolar broadening.

The spectrum of H-theta-1 shows similar improvements to those discussed for the as-synthesised form. Again, second-order quadrupolar broadening is the dominant factor at 52.15 MHz and the results at 104.22 MHz suggest that even higher magnetic fields must be used to resolve the crystallographically distinct sites. Exposing a sample of H-theta-1 to water vapour results in a significant narrowing of the tetrahedral peak, and this is indicative of chemisorbed water averaging out the electric field gradient in the vicinity of the aluminium-oxygen tetrahedra[18].

Interestingly, quantitative aluminium measurements on fully hydrated samples of both as-synthesised and H-theta-1 indicate that a significant proportion of the aluminium is invisible (Table 7.10).

TABLE 7.10 Quantitative ^{27}Al MASNMR data and XRF analysis for indicated samples

	H-theta-1	As-synthesised theta-1
Four-coordinate aluminium, %wt (NMR)	1.10	1.04
Six-coordinate aluminium, %wt (NMR)	0.00	0.00
Asymmetric aluminium, %wt (NMR)	0.00	0.00
Total aluminium %wt (XRF)	1.43	1.27
Aluminium invisible to NMR	0.33	0.23

It would seem that in both cases a significant proportion of aluminium exists in such a low symmetry environment that it is invisible to ^{27}Al NMR at 104.22 MHz.

The linewidth and chemical shift data obtained for the samples at both field strengths are shown in Table 7.11. The samples were in similar states of hydration for both of the measurements and a dilute solution of aluminium chloride was used as reference material in both cases.

TABLE 7.11 Linewidth and chemical shift data for indicated samples

	52.15 MHz		104.22 MHz	
	δ/ppm	$\Delta\nu_{\frac{1}{2}}$/Hz	δ/ppm	$\Delta\nu_{\frac{1}{2}}$/Hz
as-synthesised theta-1	49.9	900	54.8	760
H-theta-1	49.9	900	54.1	660

Simultaneous solution of equation 5.26 leads to the data shown in Table 7.12.

TABLE 7.12 Root mean square quadrupole interaction constants, true isotropic weighted mean chemical shifts and weighted mean Si-O-Al bond angles for the samples indicated. Axial symmetry was assumed in the calculation.

	r.m.s. e^2qQ/h(MHz)	<Si-O-Al>/^{o}	δ_{cs}/ppm
as-synthesised theta-1	1.72 ± 0.3	151.2 ± 2.8	56.4 ± 1.4
H-theta-1	1.59 ± 0.3	153 ± 2.8	55.5 ± 1.4

The weighted mean Si-O-Al bond angles were calculated using the relationship between the true isotropic chemical shift and mean <Si-O-Al> bond angle as derived by Lippmaa[16]: δ_{cs}(Al) = -0.50 + 132 ppm. Unfortunately, the difference in chemical shift at 104.22 MHz is not sufficient to justify a

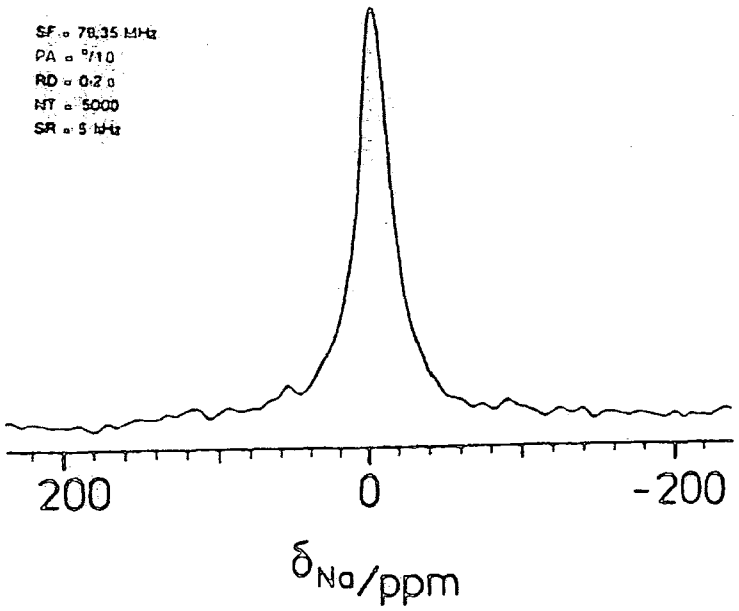

Figure 7.10(a): ^{23}Na SP MASNMR spectrum of as-synthesised theta-1.

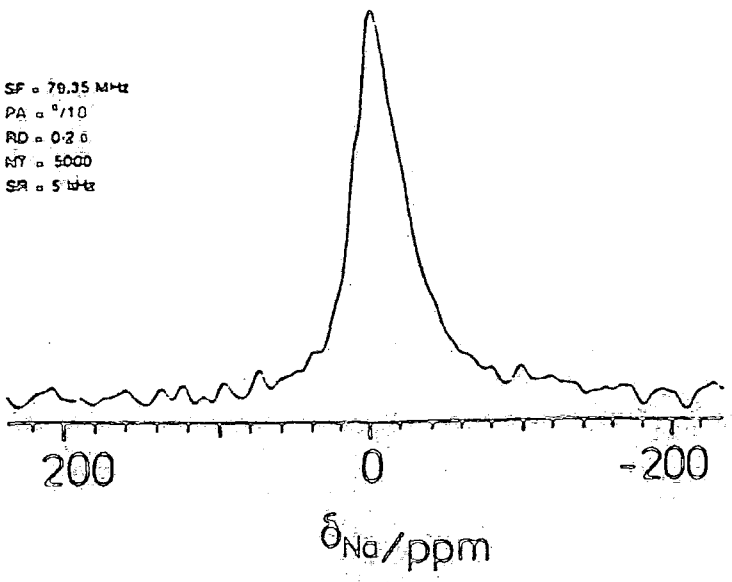

Figure 7.10(b): ^{23}Na SP MASNMR spectrum of as-synthesised high-silica theta-1.

claim that the geometry of the zeolite is affected by the presence of the diethanolamine template in spite of the observations in the single-pulse ^{29}Si MASNMR spectra of the two forms.

The "average" quadrupole coupling constants observed compare with values of 2.0 and 1.1 MHz measured for the hydrated forms of NaY and NaA respectively[19], although only one crystallographic site exists for the aluminium in these cases. The quadrupole interaction for theta-1 leads to corrections (6.5 ppm and 5.6 ppm) for the apparent chemical shift values (both 49.9 ppm) measured at 52.15 MHz for the as-synthesised and H-forms of theta-1.

7.9 ^{23}Na Studies of theta-1

The single-pulse ^{23}Na spectrum is shown in Figure 7.10(a). The sample was fully hydrated and the flip angle was short enough to ensure quantitivity. The peak at $\sim$-7.8 ppm results from hydrated sodium species - the lack of structure probably resulting from a distribution of η and e^2qQ/h values, in addition to the mobility of the sodium cation.

The single-pulse ^{23}Na spectrum of the high-silica form of theta-1 is shown in Figure 7.10(b). The major peak is observed at $\sim$-7.0 ppm and is very similar to the shift for the sample containing aluminium. Previous results[20] have suggested that the sodium resonance is sensitive to the nature of the counterbalancing anion and a simplistic deduction from these data is that sodium cations do not participate in the charge balancing of the anionic aluminium for as-synthesised theta-1 samples prepared with a diethanolamine template.

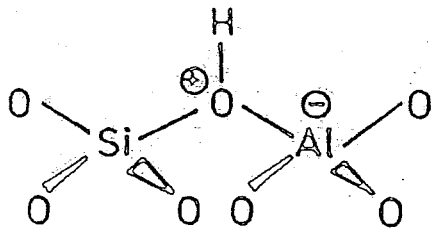

Figure 7.11(a): Linkage of SiO_4 and AlO_4^- groups to produce a structural (Bronsted) acid site.

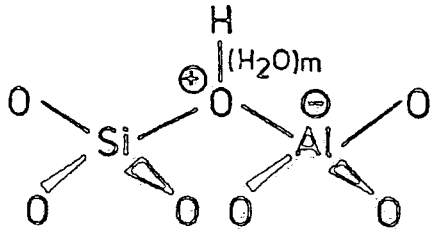

Figure 7.11(b): Hydrated Bronsted acid site.

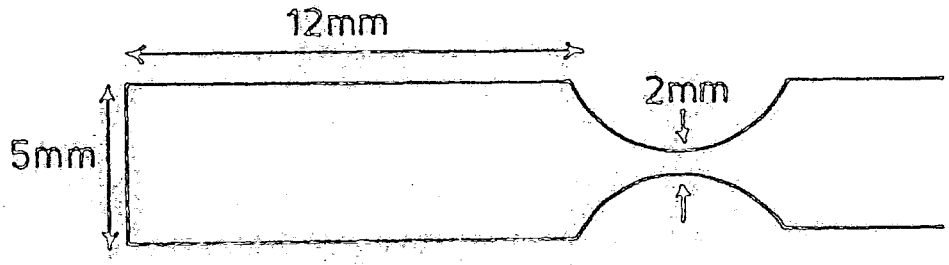

Figure 7.11(c): Configuration of pyrex NMR tube used for sealed samples.

7.10 ^{1}H NMR Studies

In addition to termainal silanol species at the surface of the crystallite and at lattice defects, aluminosilicates may contain hydroxyl groups in the bridged arrangement shown in Figure 7.11(a) - the so-called structural -OH groups[21]. These Brönsted acid sites usually have water associated with them in the absence of activation and are more correctly described as in Figure 7.11(b).

Recently, the concept of superacidity in zeolites has been advanced[22]. It is proposed that superacidity in zeolites may arise from the interaction of Bronsted acid sites and extra-lattice Lewis sites of the type $(AlO)^{+}$. The latter species may be formed locally on the steaming of H-zeolites. Acid hydroxyls have also been observed in amorphous silica-aluminas in which there is an "interphase" of silica and alumina[23].

Thus protons play an important part in the catalytic activity of aluminosilicates, both in the structural hydroxyl groups and in physically or chemically adsorbed water. High-resolution ^{1}H MASNMR is the most advanced tool for the measurement of zeolitic activity, which is essential for the understanding of the mechanisms underlying many zeolitic-mediated catalytic reactions[24]. The proton-proton distances in dehydrated zeolites are relatively large and therefore the homonuclear interactions, whose removal requires the use of multiple-pulse line-narrowing techniques, are not generally significant. However, there are many other problems. The major difficulties are the strong heteronuclear interactions, the narrow proton chemical shift range and, in the case of zeolites which are hygroscopic, the need to dehydrate the sample thoroughly to avoid the signal from adsorbed water. There is also a re-

quirement to use spinners which do not contain protons[24].

Initially, in order to provide both an idea of the scope of the problem and a possible simplification, the zeolites were heated in an oven and then transferred to the rotor (*via* a glovebag). This method relies on the fact that at high Si/Al ratios (as in theta-1), the zeolite is hydrophobic and sealing may not be necessary.

At a more advanced stage in the studies, vacuum dehydration was performed by transferring a small amount of the zeolite to an 18 mm tube equipped with a stopcock which was attached to a vacuum system of about 10^{-3} torr residual pressure. The sample temperature was then raised to the relevant value (ramp rate 4 K/min),and then kept constant for a specified length of time - the sample then being transferred to a dry glovebox/glovebag for rotor packing.

A similar method to the vacuum dehydration was used for the sealed samples. A pyrex 5 mm NMR tube was modified to yield the configuration shown in Figure 7.11(c). The tube was then attached to the vacuum line; the potential sample tube being accommodated in a lagged hole in an aluminium heating block. After heating for the relevant time, the aluminium block was removed and, after cooling, the sample tube was lowered into a nitrogen dewar and then sealed. Teflon tape was used to support the sample tube in a KEL-F rotor. The success of this method depends on the nature of the symmetry of the seal and very careful glassblowing techniques are required to stand the slightest chance of the sample spinning in the Andrew-Beams probe.

The pioneering work on the application of ^{1}H MASNMR to zeolites was performed by Pfeifer, Freude and Hunger. In the first study, Freude *et al*[25] measured the ^{1}H MASNMR spectra at 60 MHz of CaNaY zeolite, dealuminated NaHY zeolite and H-mordenite. The samples were carefully dehydrated and measured in sealed glass ampoules spun at 2.5 kHz. Two broad but well resolved signals were observed with maxima in the ranges 1.5-1.8 and 8.6-9.9 ppm. The shift of the low frequency signals was attributed to weakly acidic terminal Si-OH groups and to Al-OH groups in non-framework aluminium species. The high frequency signal at about 9 ppm was assigned to strongly acidic hydroxyl groups in the zeolites.

Considerable improvement in resolution was achieved in a subsequent study by Freude *et al*[26], where use was made of a higher magnetic field (270 MHz proton frequency) and MAS in combination with the WAHUHA pulse sequence. Peaks were observed in the ranges 2.0, 4.2-5.0 and 6.8-8.0 ppm. In this work, the line at 2 ppm was assigned to terminal Si-OH and Al-OH groups and the two other lines were attributed to acidic hydroxyl groups in the dealuminated HY zeolites.

A further increase in resolution was observed in a third study by Freude *et al*[27] in which the same technique was used and the same species were studied as above. The chemical shifts were assigned as below:

(a) 1.8 ppm - due to terminal Si-OH groups at the surface and at defects, and Al-OH groups attached to non-framework aluminium.

(b) 3.9-4.6 ppm) both due to bridging Si(OH)Al hydroxyl

(c) 4.8-5.6 ppm) groups of the zeolite framework.

(d) 7.0 - 7.5 ppm - due to residual NH_4^+ cations.

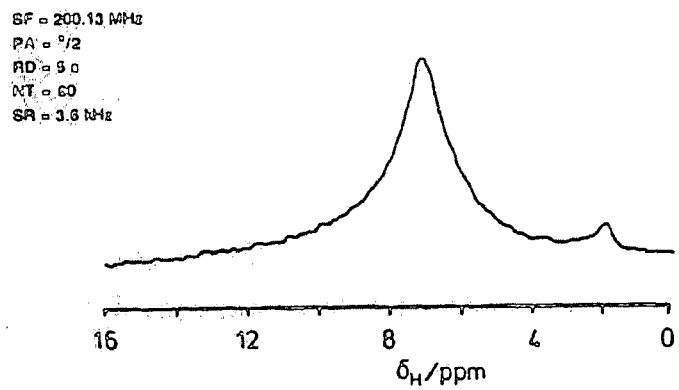

Figure 7.12(a): ^{1}H SP MASNMR spectrum of hydrated theta-1.

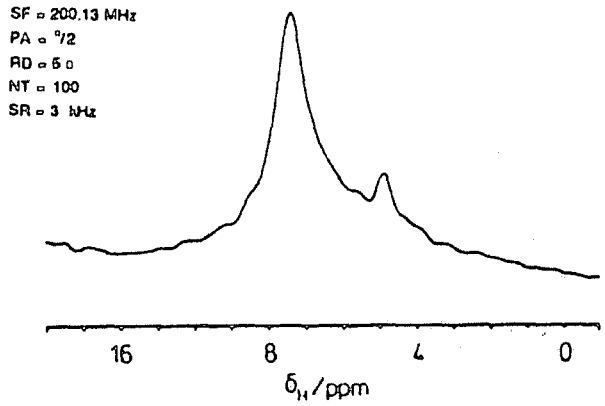

Figure 7.12(b): ^{1}H CRAMPS spectrum of hydrated theta-1.

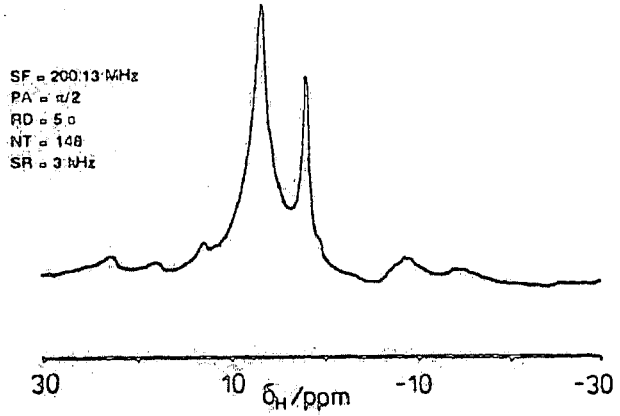

Figure 7.12(c): ^{1}H SP MASNMR spectrum of partially hydrated theta-1.

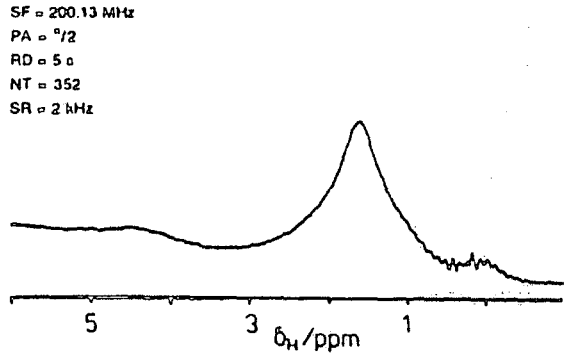

Figure 7.12(d): ^{1}H SP MASNMR spectrum of dehydrated theta-1.

The two types of bridging hydroxyl groups were interpreted in terms of hydroxyl groups existing in both the larger α-cage (line(b)) and the smaller cage (line(c)) of the faujasite structure. Studies of ZSM-5[28,29] reveal that the bridging hydroxyl group resonates at 4.0 ppm, although studies by Scholle *et al*[30] suggest a value for the chemical shift of the bridging hydroxyl group that is inconsistent with the above data.

In conclusion, it is less than clear why there should be a range of reported values for the structural hydroxyl group resonance (even taking into account the small range expected due to variation in Si/Al ratio), and the study below was performed with a view to providing a fuller understanding of this, in addition to the characterisation of the acid sites present in H-theta-1 and the gallium analogue of H-ZSM-5.

7.10.1 H-theta-1

A hydrated sample of H-theta-1 was investigated by both straightforward ^{1}H MASNMR and CRAMPS (MREV-8) and the results are shown in Figures 7.12(a) and (b) respectively. The sample had already been fully characterised by ^{27}Al MASNMR (Table 7.10). In the ^{1}H NMR spectra, two main resonances are observed. The lower frequency resonance at 1.9 ppm was assigned to -OH groups of low acidity such as terminal Si-OH groups. The higher frequency resonance was observed at 6.9 ppm and is at higher frequency than would be expected for free physisorbed water. This signal was assigned to protons at Brönsted acid sites and water molecules chemisorbed at these sites. The physisorbed water signal is believed to contribute to the region between the 6.9 and 1.9 ppm resonance, and this is more clearly indicated in the CRAMPS spectrum although there

is no major improvement in resolution. The 6.9 ppm peak was shown to consist of a significant proportion of water by heating the sample at 498 K for 48 hours (sample transferred to rotor *via* globebag under dry nitrogen) and observing a decrease in intensity of this peak with respect to the silanol moiety peak. An increase in the number of spinning sidebands is observed in the ^{1}H MASNMR spectrum (Figure 7.12(c)) which results from an appreciable anisotropic inhomogeneous interaction, but dipolar interaction of the protons with the neighbouring aluminium nuclei at the Brönsted acid sites (as suggested by Luz and Vega[31]) is an unlikely mechanism given that spinning sidebands accompany both the Brönsted acid peak and the silanol moiety peak. The presence of the spinning sidebands may indicate that partial dehydration has reduced the fast molecular motions which average out the ^{1}H-^{1}H dipolar interactions.

The ^{1}H MASNMR spectrum of a thoroughly dehydrated sample of H-theta-1 is shown in Figure 7.12(d). The sample was activated by heating in air at 673 K for 12 hours followed by heating under vacuum for a further 12 hours at 673 K; the tube being opened in a glovebox for sample transfer to the rotor. Previous studies had shown that samples of dehydrated H-Mordenite prepared under similar conditions for both the sealing and glovebox techniques gave similar results and so sealed samples were not considered to be absolutely necessary. H-Mordenite was used on account of its low Si/Al ratio and hence greater hydrophilicity with respect to theta-1. The presence of a hydrogen background results in a poor quality spectrum and the spike removal routine was used to remove a very sharp peak at ~0.4 ppm. A broad peak is observed at

~4.4 ppm and is assigned to the dehydrated Brönsted acid resonance on the basis of the chemical shift data presented by Freude[27]. A silanol moiety peak is observed at 1.8 ppm, although the low frequency peak has a contribution from the background. The result is not easy to reproduce; peaks are often preferentially observed at 7 ppm with respect to the peak at 4.4ppm even for very small loadings of water.

When water is present, it is probable that the Brönsted acid proton is hydrated, possibly as H_3O^+ or $H_7O_3^+$, and at higher levels of hydration, chains of hydrogen bonded water molecules extending through the unidimensional channel system may be envisaged. Such chains of water molecules have been reported for the natural zeolite bikitaite[32]. It is well known from solution studies and from wide-line NMR studies of other zeolite water systems that the protons of water adsorbed at an adsorption site and the proton of the adsorption site exchange very rapidly and consequently, the chemical shift of the fast exchange species must be intermediate between that of free liquid water and the chemical shift of the adsorption site alone.[33] The observed chemical shift of 7 ppm is outside the predicted 5-4.4 ppm range, suggesting that the situation cannot be explained by a simple exchange model. In the case of hydrogen bonding between the water molecules, the constraint of the zeolite framework would be expected to disrupt hydrogen bonding relative to the normal liquid phase[34] which would result in a shift to low frequency and thus this cannot account for the observation. The most likely explanation would seem to be strong hydrogen bonding between the framework oxygen and the water. Interactions such as these have been suggested

by Mank *et al*[35]. Given that the 7 ppm peak exists for both small and more significant levels of hydration, it would seem that the water molecules preferentially interact with the framework rather than each other even for more significant loadings of water.

During the course of this work, Hunger *et al* published a paper[36] suggesting that strong Lewis acid sites associated with non-framework aluminium accounted for a peak at 6.5 ppm for small loadings of water. The quantitative ^{27}Al MASNMR data for the sample (Table 7.10) studied above suggests neither the presence of hexaaqua complexes nor non-framework four-coordinate aluminium species, although ∿20% of the aluminium is NMR-invisible. However, the absence of a peak at ∿3.0 ppm due to non-framework Al-OH moieties in the ^{1}H MASNMR spectrum suggests that the 'invisible' aluminium is in a high enough state of condensation for Lewis acid effects to be insignificant.

The acid sites present in zeolite theta-1 were further examined by temperature programmed desorption of ammonia. The experimental details for NH_3-TPD measurements are given in Chapter Three. Two peaks are usually observed in the plot of desorption rate as a function of temperature. The lower temperature peak is usually attributed to the desorption of ammonia from the silanol groups (weak acid sites), whereas the high temperature peak is usually attributed to the desorption of ammonia from the framework Brönsted acid sites[37,38]. The assignment of the low temperature peak is, however, a matter of some controversy[39].

The H-theta-1 sample used in the ^{1}H MASNMR studies was dehydrated at 823 K for 3 hours before exposure to

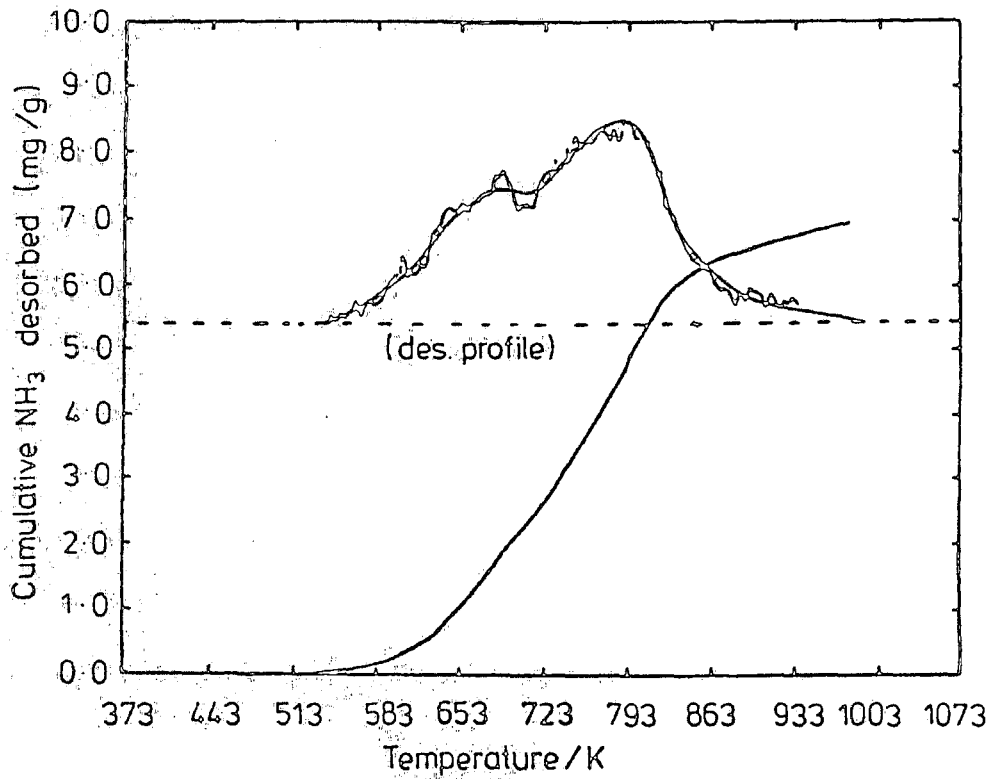

Figure 7.13: NH_3-TPD curve for H-theta-1.

ammonia. Figure 7.13 indicates the presence of two types of strong acid site. There is no indication of the low temperature peak in the derivative plot usually associated with the silanol moieties, suggesting that either the ammonia was accessible to only a small number of silanol groups or that the starting temperature (513 K) was already sufficiently high enough to desorb the ammonia molecules from these sites. The concentration of acid sites detected by this technique is in excellent agreement with the concentration of tetrahedral framework aluminium sites measured by ^{27}Al NMR (Table 7.13). The assumption of one acid site per ammonia molecule is made. A cynic might observe that aluminium invisible to ^{27}Al NMR is also invisible to NH_3-TPD!

TABLE 7.13 Characterisation of theta-1 samples by NH_3-TPD and ^{27}Al NMR

	NH_3-TPD		aluminium concentration/g^{-1}		
	acid site concentration /g^{-1}	T_{max}/K	Framework	Non-framework (visible)	(invisible)
H-theta-1 (used in ^{1}H MASNMR)	2.51×10^{20}	(673,793)	2.45×10^{20}		7.4×10^{19}
NH_4^+-theta-1	3.29×10^{20}	(673)	2.27×10^{20}	5.13×10^{19}	
NH_4^+-theta-1 (steamed 6h,973 K)	1.98×10^{20}	(537,745)	1.45×10^{20}	2.1×10^{20}	
NH_4^+-theta-1 (steamed 18h, 973 K)	2.05×10^{20}	(499,660)	1.11×10^{20}	2.21×10^{20}	2.45×10^{19}
NH_4^+-theta-1 (steamed 68h,973 K)	1.38×10^{20}	(503,632)	8.02×10^{19}	2.03×10^{20}	1.11×10^{20}

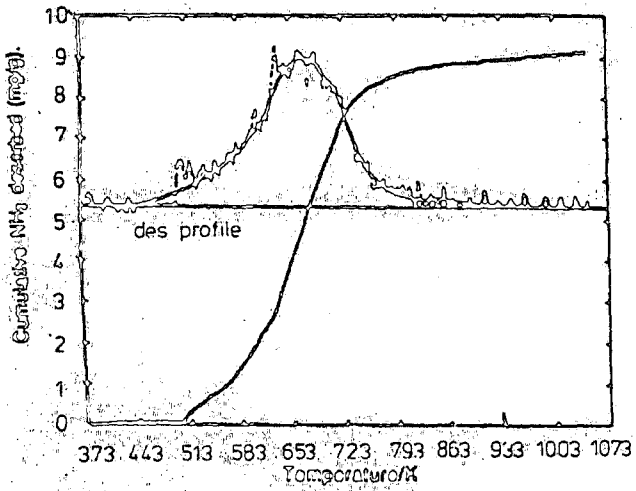

Figure 7.14(a): NH_3-TPD curve for NH_4^+-theta-1.

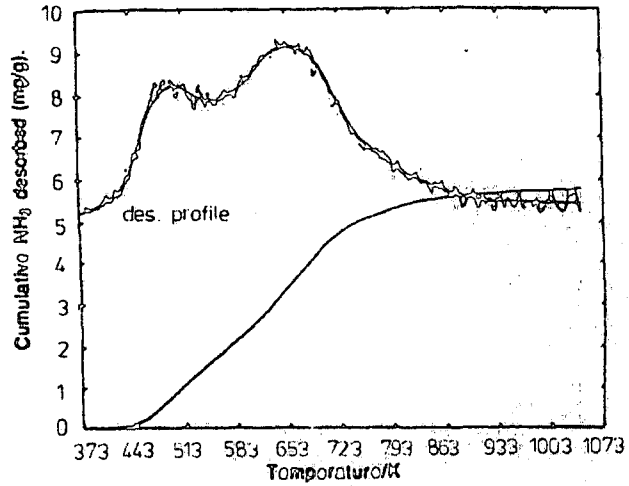

Figure 7.14(c): NH_3-TPD curve for NH_4^+-theta-1 (steamed 973K for 18 hours).

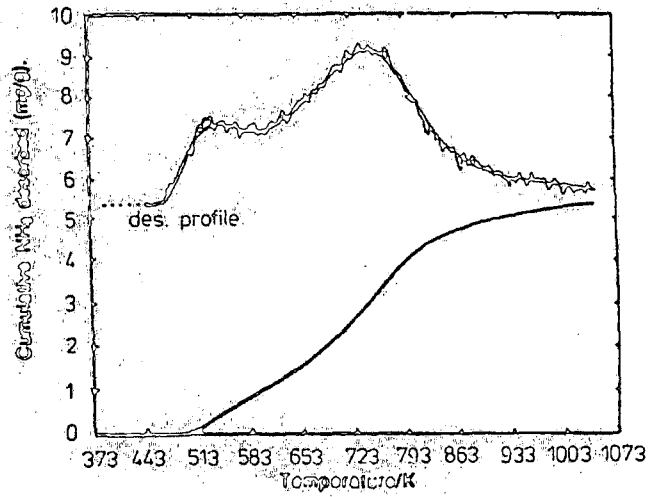

Figure 7.14(b): NH_3-TPD curve for NH_4^+-theta-1 (steamed 973K for 6 hours).

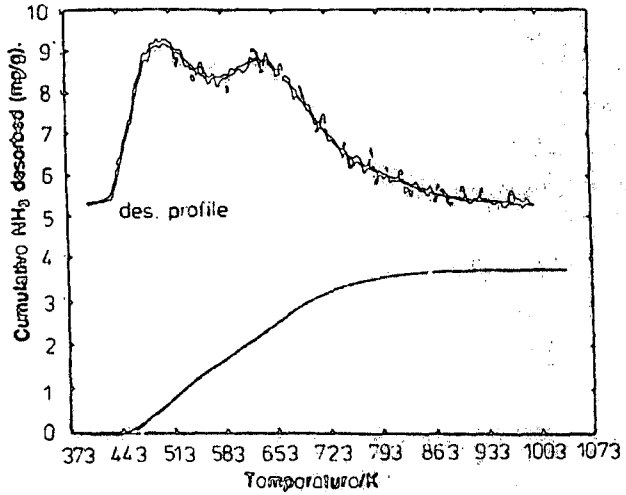

Figure 7.14(d): NH_3-TPD curve for NH_4^+-theta-1 (steamed 973K for 68 hours)

The presence of more than one peak in the derivative plot is indicative of Brönsted acid site inhomogeneity, and this may be a contributing factor to the width of the Brönsted acid resonance in the ^{1}H MASNMR spectrum. The peak at $\sim$ 773 K is indicative of acid sites of greater strength than usually observed for framework acid sites in TPD experiments. Caution must however be exercised in the interpretation due to the possibility of either kinetic factors or the enhancement of Brönsted acidity by neighbouring non-framework aluminium.

A series of samples in various stages of hydrothermal dealumination were studied in an attempt to investigate the influence of non-framework aluminium on the TPD profile. The full details of the analysis by ^{27}Al NMR are given in Section 7.12.1. Analysis by NH_3-TPD and quantitative ^{27}Al NMR yielded the results shown in Figures 7.14(a),(b),(c) and (d) and Table 7.13. TPD analysis of the starting material (NH_4^+-theta-1) failed to reproduce the peak observed at 773 K for the sample discussed above. In addition, the concentration of acid sites detected by TPD exceeds the aluminium concentration suggesting that silanol moieties contribute to the TPD profile if the assumption of one aluminium acid site per desorbed ammonia molecule is made. The silanol moieties presumably contribute to the low temperature side of the main peak accounting for its lop-sided nature (Figure 7.14(a)). Hydrothermal dealumination initially results (Figure 7.14(b)) in an increase in acidity of the strong acid peak which presumably results from an interaction between the Brönsted acid site and the Lewis acid sites associated with non-framework aluminium. The possibility that it results from a decrease

in the concentration of the framework aluminium may be discounted because the strong acid peak becomes less acidic at higher levels of dealumination (Figures 7.14(c) and (d)). It is interesting to note that catalytic measurements on ZSM-5 have indicated an optimum steaming time[40], and that microcalorimetry analysis of ZSM-5 mirrors the above results observed for theta-1[41]. It seems that the presence of non-framework aluminium can dramatically effect the position of the strong acid peak, and interactions between framework and non-framework aluminium may well account for the observation of the very strong acid peak in Figure 7.13. Shoulders are observed on the high temperature side of the strong acid peak on dealumination and these are attributed to the interaction between ammonia and Lewis acid sites. The concentration of acid sites detected by NH_3-TPD always exceeds the concentration of aluminium which indicates the adsorption of ammonia onto sites like silanol groups. These groups probably account for the low temperature peak that eventually becomes more intense on increasing the steaming time than the peak characterising the strong acid sites. The position of the silanol peak is also sensitive to the hydrothermal dealumination conditions.

7.10.2 H, Na-Ga-ZSM-5

The as-synthesised sample prepared using a tetrapropylammonium hydroxide template was calcined under nitrogen (773 K for 12 hours) and then heated at 773 K for 12 hours in air. This calcination procedure minimizes the possibility of gallium being removed from the framework when the template is removed. The sample was used without any further treatment

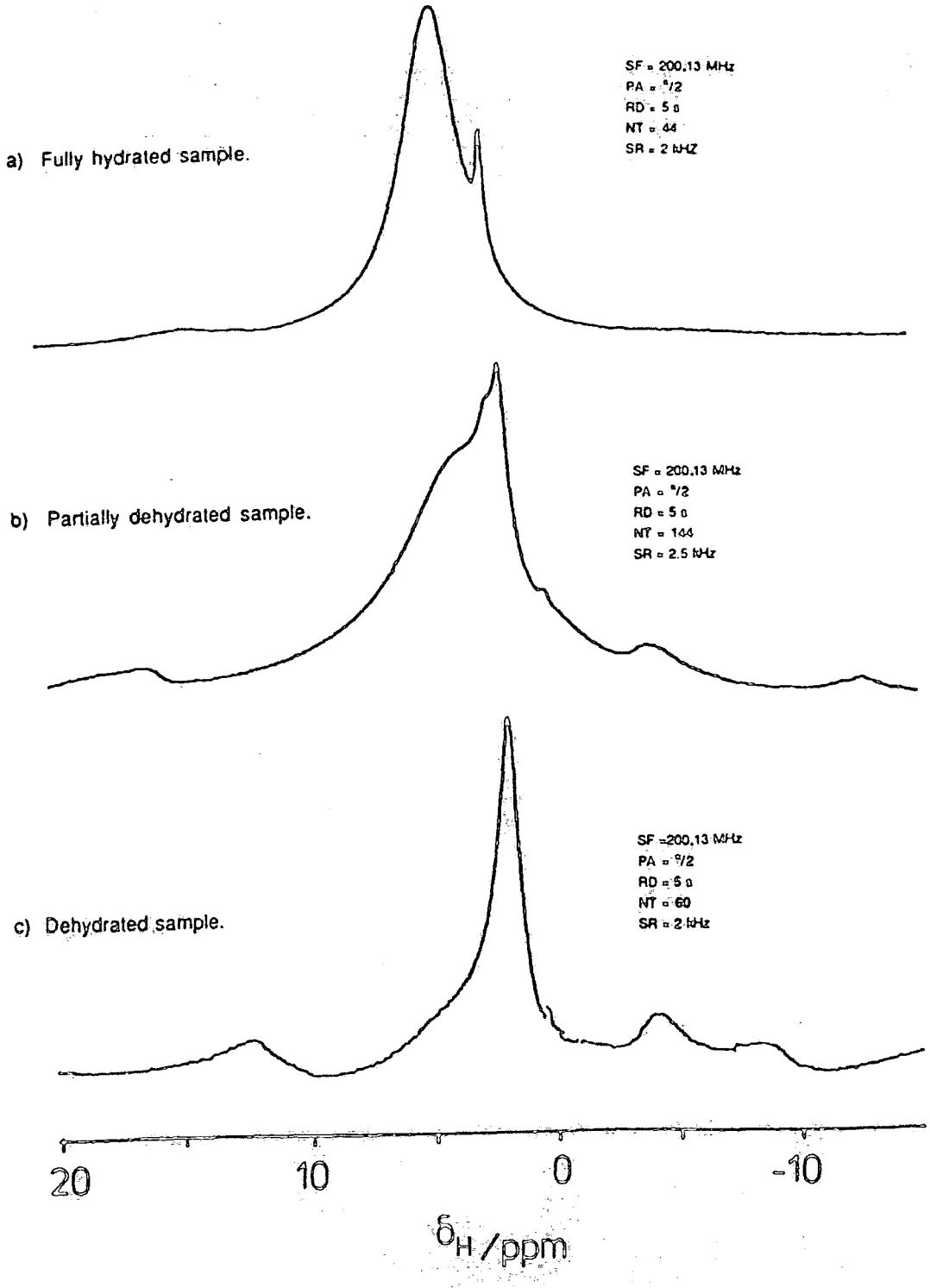

Figure 7.15: ^{1}H SP MASNMR spectra of H,Na-ZSM-5 as a function of hydration.

for ion exchange. Chemical analysis of the sample is shown in Table 7.3 and reveals that if all the gallium exists in the framework, then approximately 60% of the anionic charge associated with gallium is counterbalanced by H^+ and the remaining 40% by Na^+.

Figure 7.15(a) shows the ^1H MASNMR spectrum of the fully hydrated sample. Two peaks are observed (4.8 and 2.1 ppm). These were assigned to hydrated Brönsted acid sites and water coordinated to sodium respectively. If proton exchange is occurring between the two sites, then the exchange rate must be less than $1.85 \times 10^{-3} s^{-1}$. Partial dehydration at 488 K for several hours results in Figure 7.15(b). Three peaks are now observed, presumably water chemisorbed at Brönsted acid sites (4.8 ppm), water coordinated to sodium (2.1 ppm), and silanol moieties (1.7 ppm). The spinning sideband intensity is dramatically increased on partial dehydration due to the decrease in mobility of the protons. Figure 7.15(c) shows the fully dehydrated form of the zeolite. The sample was dehydrated at 673 K for 6 hours under vacuum and the rotor was packed in a glovebox. The Brönsted acid peak maximum is estimated to lie between 4 and 4.3 ppm - the precise shift being difficult to determine given its broad nature and partial overlap with the peak at 1.7 ppm. The broad silanol peak could reflect the presence of non-framework Ga-OH species. The Brönsted acid peak is in the region associated with similar acid sites in the aluminium analogue. It is now possible to suggest an acidity sequence for the Group III elements that have so far been substituted into the ZSM-5 framework based on NMR data alone:

$$Al \sim Ga > B \text{ (in order of increasing acidity)}$$

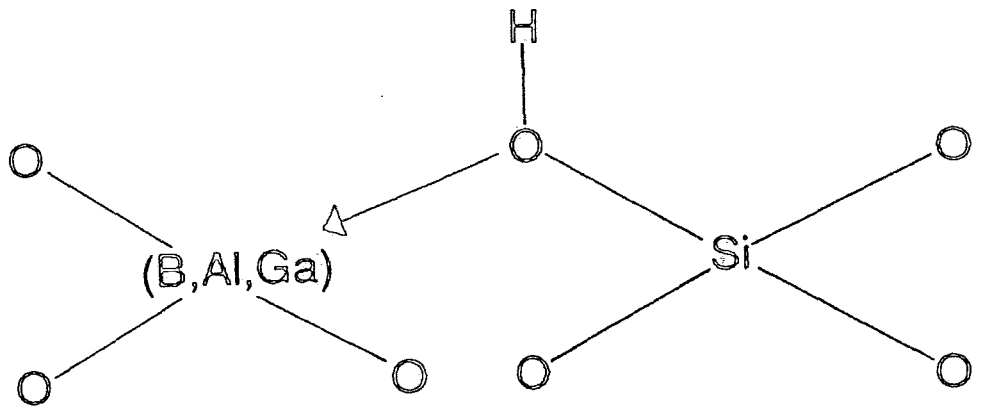

Figure 7.16: Coordination of $(B,Al,Ga)O_4^-$ unit to SiO_4 unit via p-orbitals of oxygen.

Previous studies[33,42] have shown that the "acid" sites associated with boron in ZSM-5 are in fact non-acidic (their chemical shift (2.4 ppm) only slightly exceeds that of the silanol species). The presence of acid sites on Ga-ZSM-5 that are significantly more acidic than the silanol species is independently confirmed by the fact that for the sample of Ga-ZSM-5 prepared *via* a diethanolamine template, chemical analysis confirms that the template must be predominantly protonated.

It is easy to rationalise the observed acidity sequence using the qualitative electrostatic valence model of Pauling[43]. The strength of the O-H bond at a Brönsted acid site depends on the electronegativity of the anionic species. According to the model, a (B,Al,Ga)-O bond in a Si-OH(B,Al,Ga) bridge is coordinated *via* the p-orbitals of oxygen as shown in Figure 7.16[43].

The strengthening of the (B,Al,Ga)-O bond with decreasing electronegativity will result in a weakening of the corresponding O-H bond and, hence, higher acidity. The Pauling electronegativities of aluminium, gallium and boron are 1.5, 1.6 and 2.0 respectively[44], showing that the above argument is in good agreement with the experimental data. The similarity of the Pauling electronegativities of aluminium and gallium results in an indistinguishable difference on the ^{1}H MASNMR acidity scale given the resolution of Figure 7.15(c).

So far, the fact that approximately 40% of the gallium is counterbalanced by sodium cations has been ignored. According to the Sanderson intermediate electronegativity model[45], the presence of the sodium should result in a decreased positive charge on the hydrogen and would be expected

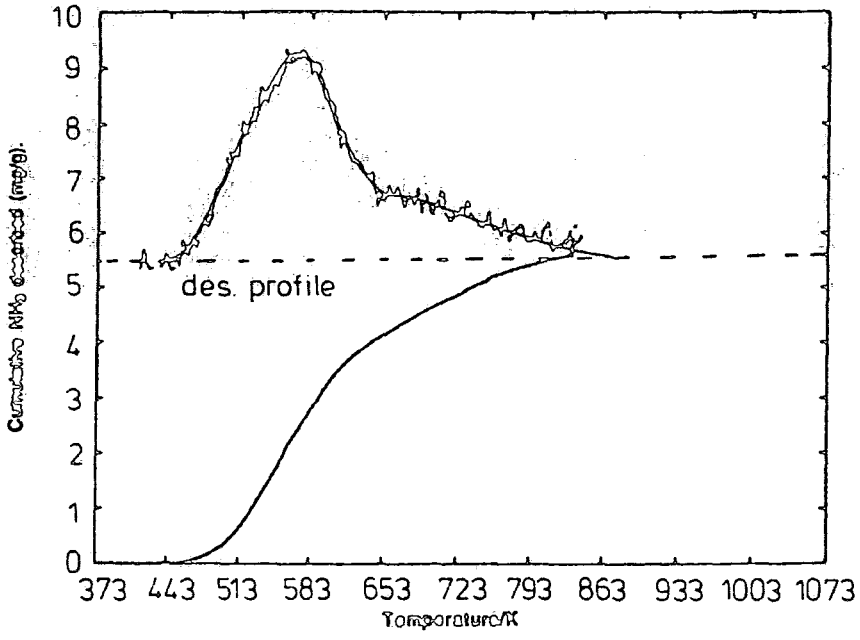

Figure 7.17(a): NH_3-TPD of Na,H-Ga-ZSM-5.

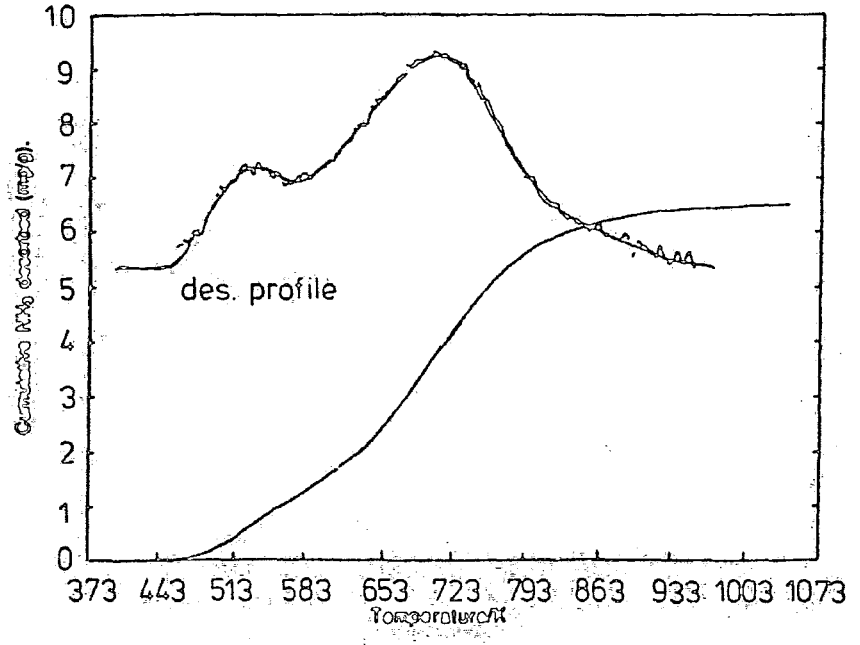

Figure 7.17(b): NH_3-TPD of NH_4^+-ZSM-5

to shift the Brönsted acid resonance to low frequency of the sodium-free form. The presence of calcium has been ignored in this treatment - the presence is attributed to surface impurities, but if the calcium is participating in the charge balancing, there would be a further reduction of the positive charge on hydrogen.

It may even be that the pure H- form of Ga-ZSM-5 is more acidic than the corresponding H- form of Al-ZSM-5 in agreement with deprotonation energies of $(OH)_3SiOHAl(OH)_3$ and $(OH_3)SiOHGa(OH)_3$ aggregates calculated using pseudopotential methods[46]. It should be noted that the Brönsted acidity sequence calculated from NMR data alone is in disagreement with acidity sequences based on IR and TPD studies which suggest Al>Ga>B (in order of increasing acidity), although aluminium and gallium are close to one another on the respective scales[47,48].

The sample of H,Na-Ga-ZSM-5 was further investigated by temperature programmed desorption of ammonia. The sample was dehydrated at 673 K for 3 hours before exposure to ammonia. The plot of NH_3 desorption rate as a function of temperature is shown in Figure 7.17(a). Both weak and strong acid sites are present. The weaker acid sites ($T_{max} \simeq 553$ K) are associated with silanol moieties and sodium cations. The stronger acid sites ($T_{max} \simeq 693$ K) are believed to be due to Brönsted acid sites, and the estimated peak maximum is in a similar region to that associated with Brönsted acid sites in the aluminium analogue of ZSM-5 for similar heating rates (Figure 7.17(b)). A greater number of strong acid sites are present in the aluminium analogue due to an ion

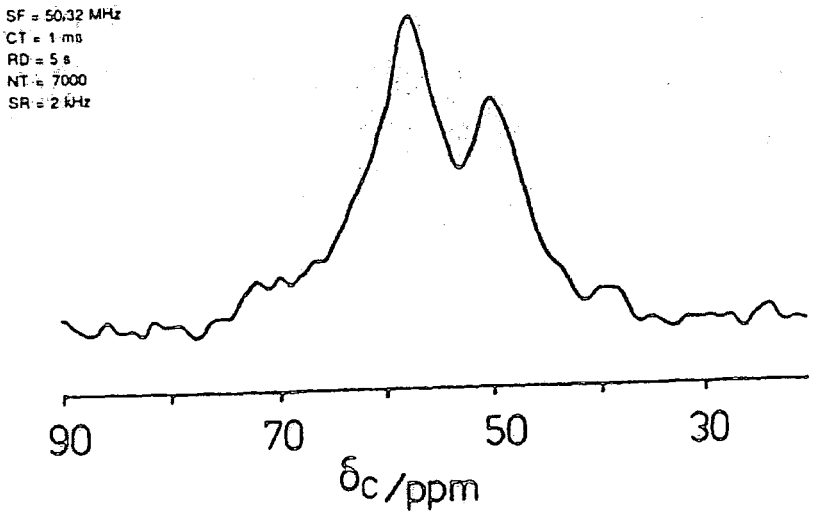

Figure 7.18(a): ^{13}C CP MASNMR spectrum of theta-1 containing the diethanolamine template.

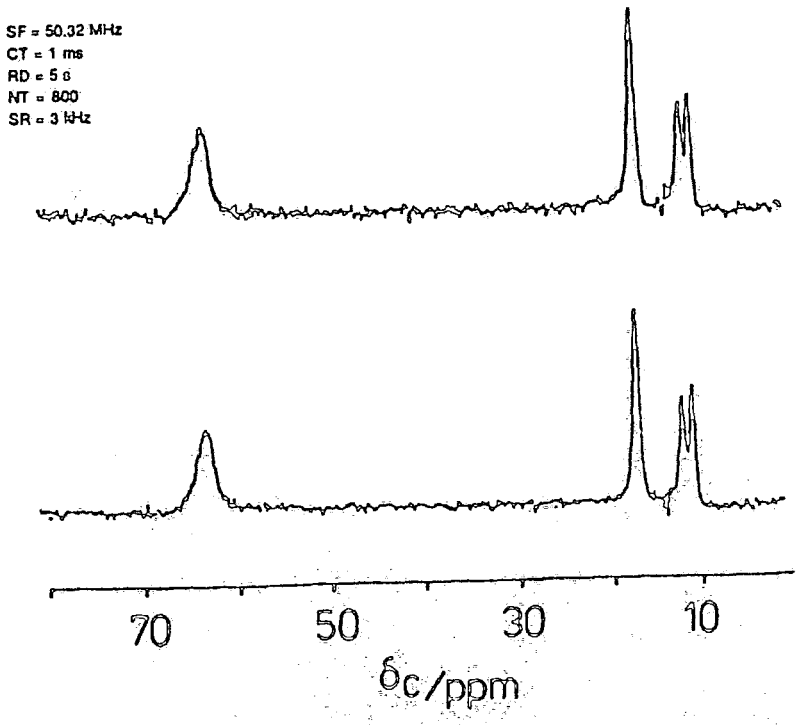

Figure 7.18(b) ^{13}C CP MASNMR spectra of the tetrapropylammonium cation occluded in ZSM-5 (upper) and its gallium analogue (lower).

exchange procedure to remove the sodium ions unlike the situation for the gallium analogue. The broadness of the high temperature peak and the corresponding broad ^{1}H MASNMR resonance in the dehydrated sample point to a range of strong acid sites.

7.11 ^{13}C Studies of as-synthesised Na,Ga-ZSM-5

The as-synthesised forms were investigated by cross-polarization ^{13}C MASNMR in order to investigate the state of the template and probe possible template-framework interactions.

The result for the diethanolamine form is shown in Figure 7.18(a). Peaks are observed at ~57 ppm and 49.5 ppm, with some peaks of lower intensity also being present. Comparison with Table 7.6 suggests that the template is protonated in agreement with the analytical data in Table 7.4. Table 7.4 suggests an excess of template with respect to gallium sites and this is reflected in the lower intensity peaks of Figure 7.18(a). The other species potentially include hydrogen-bonded amine and amine coordinated to Lewis acid sites. The broadness of the major resonances may result from motion in the kHz region or a distribution of protonated diethanolamine environments. The shifts of the maxima correspond to the shifts observed for the protonated amine in theta-1, implying that the template does not interact strongly with gallium/aluminium.

Further evidence for weak interactions between the framework metal anion and the template is given in Figure 7.18(b). Clearly the shifts are not affected by the sub-

stitution of aluminium by gallium. The narrowness of the lines suggests a different motional regime or higher crystallinity with respect to Figure 7.18(a).

7.12 ^{27}Al NMR Studies of the hydrothermal dealumination of theta-1 and ZSM-5

The hydrothermal dealumination of the zeolite theta-1 was investigated by ^{27}Al MASNMR. During the hydrothermal treatment, which is used to enhance the stability and activity of a zeolite, aluminium is dislodged from the framework but retained in the structure. ^{27}Al MASNMR may be used to quantify the framework and extra-framework aluminium present. Measurement of the framework aluminium concentration as a function of steaming time potentially provides important information of the dealumination mechanism. Dealumination was performed at 873 K and 973 K, and a comparison was made with ZSM-5.

The aluminium removed from the framework was initially considered to be converted into six-coordinate aluminium-oxygen species located in the channels[49] (the relevant line occurs at 0 ppm in the ^{27}Al MASNMR spectrum). More recently, broad lines accompanying the dealumination of zeolite Y have been interpreted in terms of the presence of polymeric aluminium species[50]. Boehmite and pseudo-Boehmite aluminium clusters have been detected by XRD in zeolite Y and are believed to be produced by condensation of Al-OH groups[51]. Results have also shown that a loss of ^{27}Al intensity may occur on dealumination due to extra-framework aluminium existing in an environment of low symmetry[52]. The "invisible" aluminium could be present as $Al(OH)_3$, $Al(OH)^{2+}$, $Al(OH)_2^{+}$, or

some distorted polymeric aluminous species. Freude *et al*[53] have suggested that non-framework aluminium gives rise to only two peaks in the ^{27}Al NMR spectrum. In addition to the six-coordinate aluminium discussed above, the presence of four-coordinate non-framework aluminium gives a broad line at ≈50ppm. Two types of isolated non-framework aluminium complexes were invoked[53]: $Al(H_2O)_6^{3+}$ and AlOOH. It was proposed that the AlOOH molecule is associated with two framework oxygens giving a four-coordinate arrangement about the aluminium. The evidence however is less than convincing, and it seems that the true nature of the non-framework species is far from clear. In addition to the dealumination studies outlined below, the linebroadening mechanism of the non-framework aluminium species was investigated in an attempt to provide further information on the nature of the non-framework species.

7.12.1 Hydrothermal dealumination of theta-1

The dealumination studies were performed on the NH_4^+ form of theta-1 which was prepared by ion exchange of a Na, NH_4^+-theta-1 sample with ammonium nitrate as described in Section 3.3. Prior to the dealumination study, the sample was dried at 373 K for 18 hours, and its structural integrity was confirmed by powder XRD.

For the dealumination studies, approximately 5 g of zeolite was spread finely over a glass boat (shallow bed conditions) and placed in a horizontal tubular furnace. The sample was heated at 4 K/min to 473 K under a flow of dry N_2 gas and held at this temperature for several hours, after which the sample was heated at the same rate to the dealumination

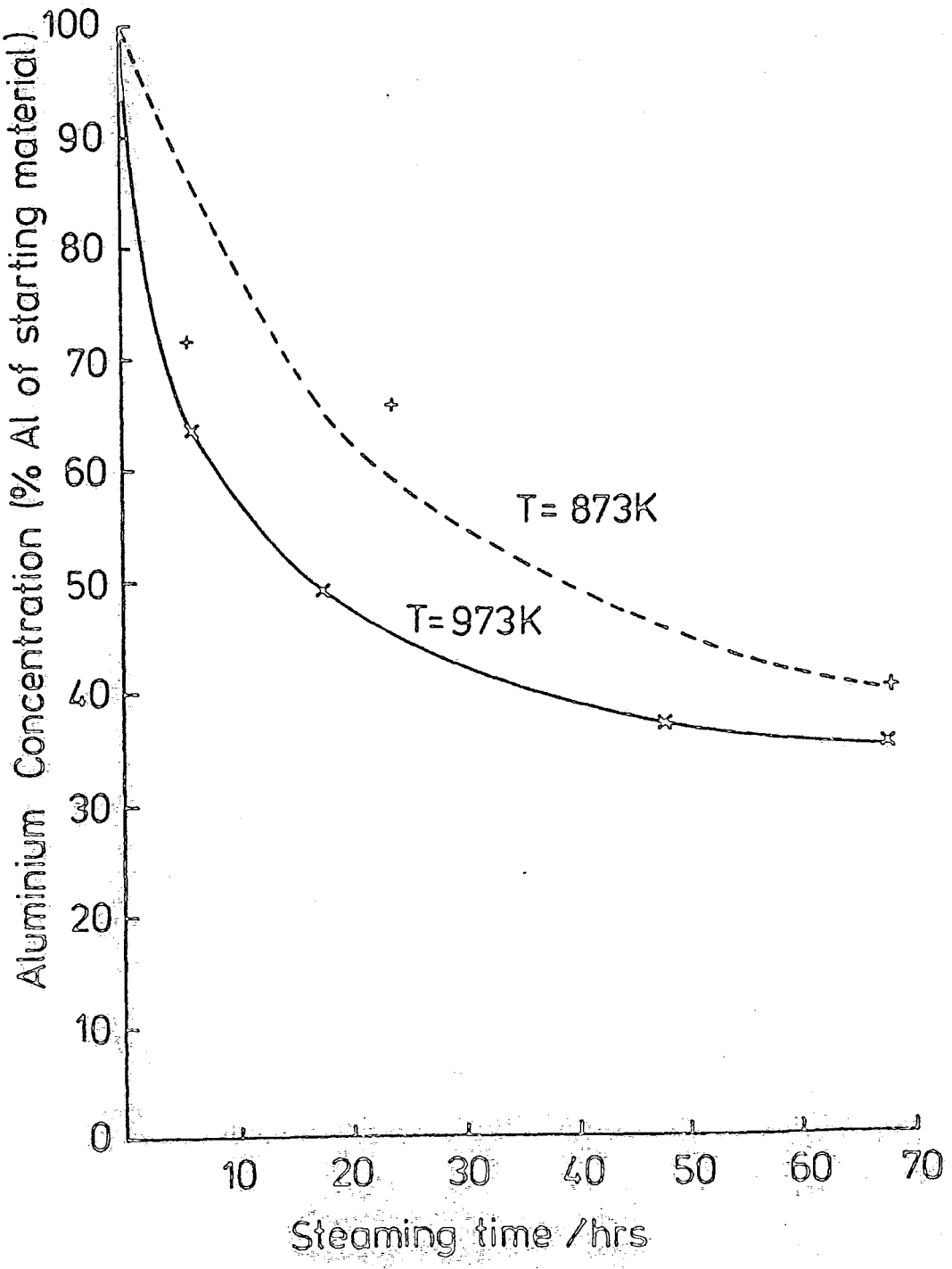

Figure 7.19: Concentration of framework aluminium in theta-1 as a function of steaming time.

temperature. Dealumination was effected at atmospheric pressure by bubbling the nitrogen through water prior to entering the furnace. Calcination of NH_4^+-theta-1 should occur before the dealumination temperature is reached so that the ^{27}Al MASNMR studies reflect the hydrolytic removal of aluminium atoms from the framework at Brönsted acid sites.

The quantitative aluminium measurements were made at 104.22 MHz using a converted solution-state probe, built free of an aluminium background. Qualitative measurements were made on an aluminium-free double-bearing probe at 52.15 MHz. For quantitative accuracy, short radiofrequency pulses with small flip angles satisfying the conditions of Chapter Five were used.

The results obtained by ^{27}Al MASNMR and XRF studies for both dealumination temperatures in shown in Tables 7.14 and 7.15, and a plot of framework aluminium concentration as a function of steaming time is shown in Figure 7.19. It is clear that dealumination proceeds at a faster rate at higher temperatures. The loss in intensity of the framework aluminium species peak at 55 ppm is accompanied by the appearance of a very broad peak centred on the tetrahedral region. Thus the aluminium lost from the framework does not go into sites of sufficiently high symmetry to contribute to the framework tetrahedral resonance - see Figure 7.20, where the relative intensities of the framework tetrahedral peak are plotted in absolute intensity mode as a function of dealumination for similar masses and states of hydration. Comparison of Figures 7.21(a) and (b) clearly reveals that a broad species is produced in the single-pulse ^{27}Al MASNMR spectrum on de-

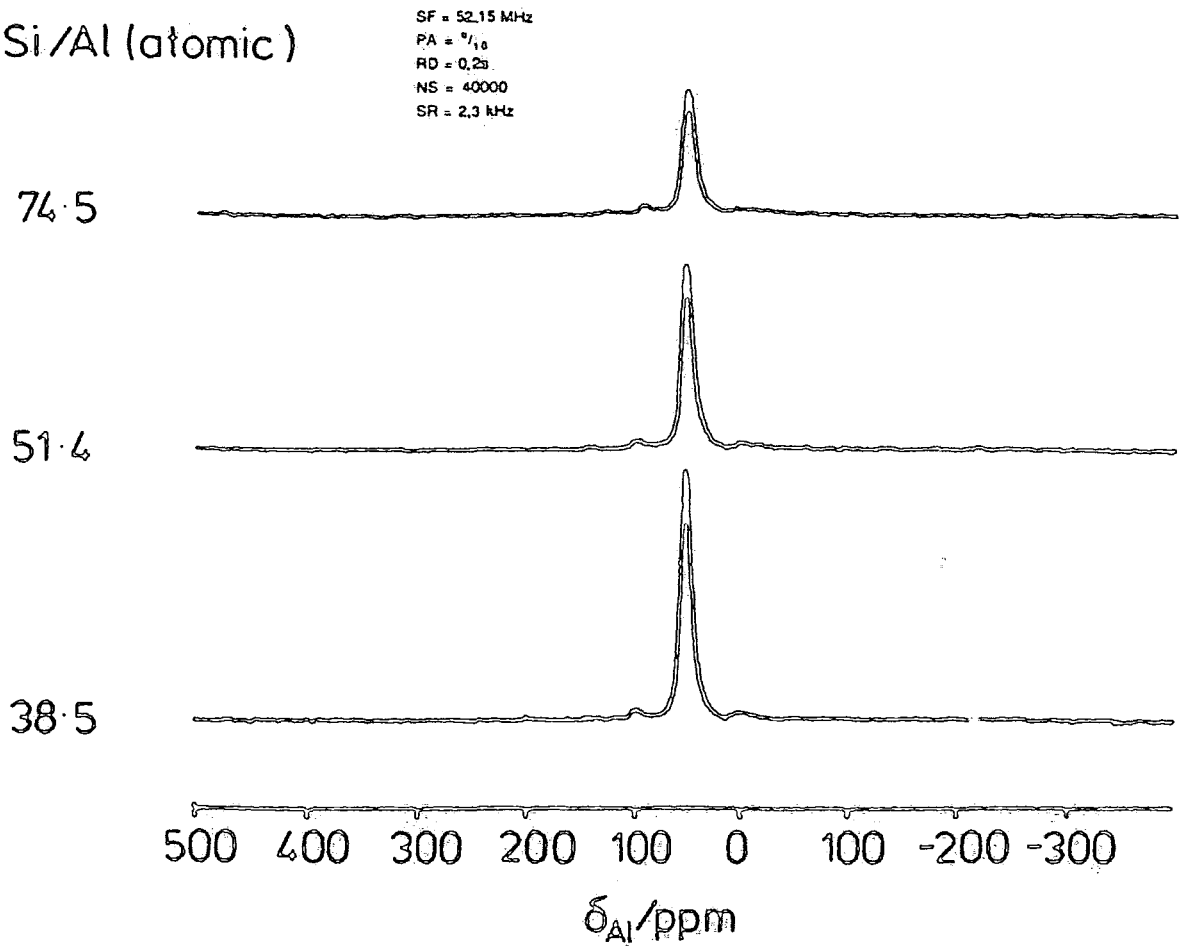

Figure 7.20: Intensity of framework four-coordinate aluminium resonance as a function of dealumination.

TABLE 7.14 Hydrothermal dealumination of NH_4^+-theta-1 at 373 K (atmospheric pressure)

	Steaming time/hrs.			
	0	6	24	68
Four-coordinate Al, %wt. (NMR)	1.02	0.73	0.67	0.41
Six-coordinate Al, %wt. (NMR)	0.00	0.00	0.00	0.00
Asymmetric Al observed by NMR, %wt. (NMR)	0.23	0.85	0.92	1.20
Asymmetric Al invisible to NMR, %wt. (XRF,NMR)	0.00	0.00	0.00	0.00
Total Al, %wt. (XRF)	1.25	1.58	1.59	1.61
Total Si, %wt. (XRF)	34.2	42.5	43.8	43.4
Bulk Si/Al atomic ratio (XRF)	26.3	25.8	26.4	25.9
Framework Si/Al ratio (XRF,NMR)	32.2	55.7	62.9	101.3

TABLE 7.15 Hydrothermal dealumination of NH_4^+-theta-1 at 973 K

	Steaming time/hrs.				
	0	6	18	48	68
Four-coordinate Al, %wt. (NMR)	1.02	0.65	0.50	0.38	0.36
Six-coordinate Al, %wt. (NMR)	0.00	0.03	0.07	0.05	0.06
Asymmetric Al observed by NMR, %wt. (NMR)	0.23	0.90	0.92	0.59	0.65
Asymmetric Al invisible to NMR, %wt. (XRF,NMR)	0.00	0.00	0.11	0.46	0.5
Total Al %wt. (XRF)	1.25	1.58	1.60	1.48	1.56
Total Si %wt. (XRF)	34.2	43.5	44.0	41.2	41.5
Bulk Si/Al atomic ratio (XRF)	26.3	26.4	26.4	26.7	25.6
Framework Si/Al atomic ratio (XRF,NMR)	32.2	64.4	84.8	105.2	111.9

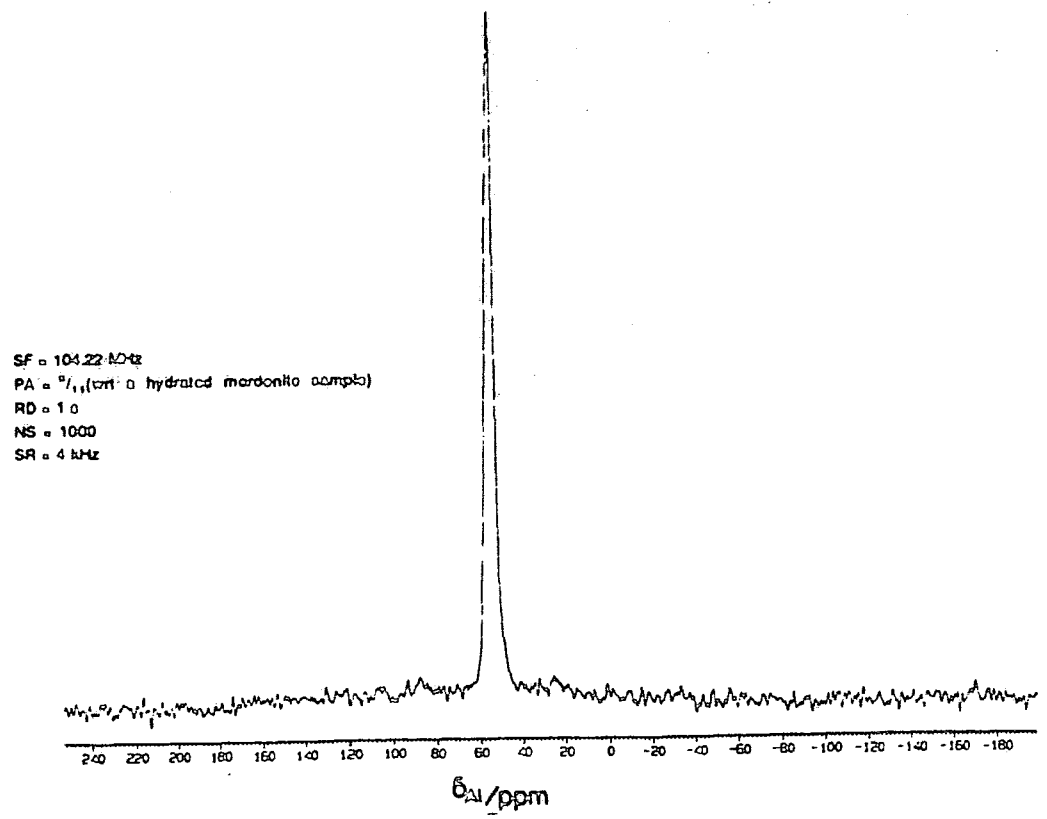

Figure 7.21(a): ^{27}Al SP MASNMR spectrum of NH_4^+-theta-1.

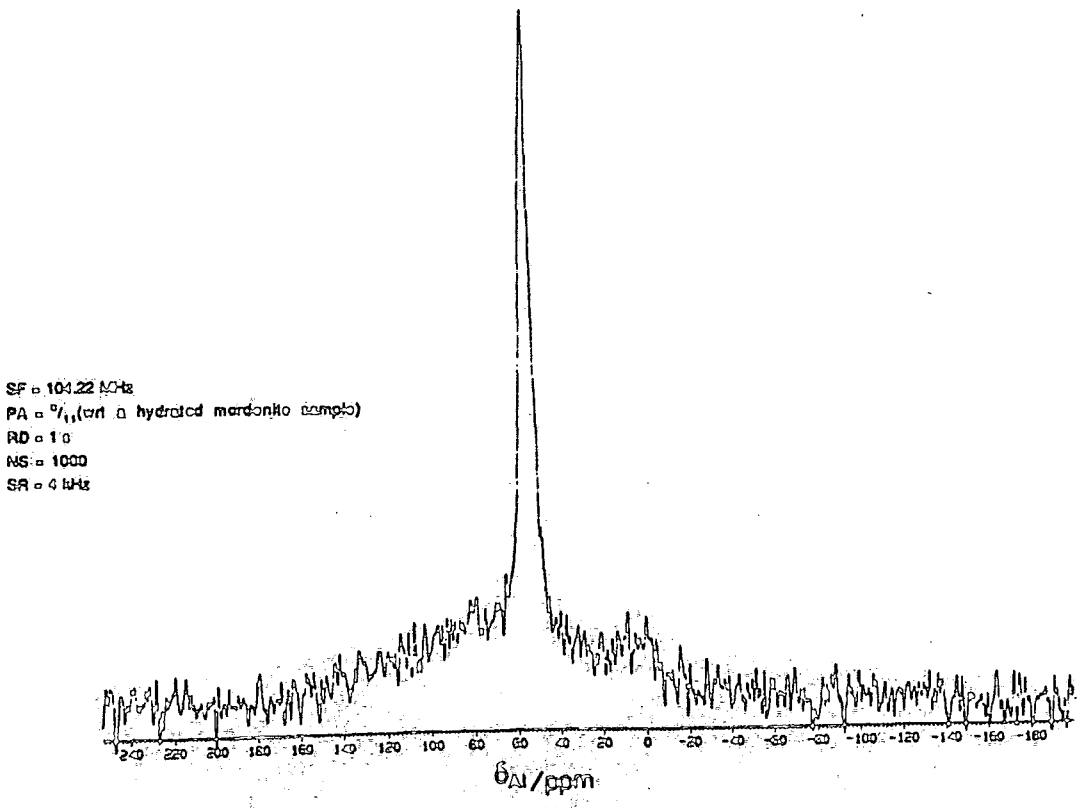

Figure 7.21(b): ^{27}Al SP MASNMR spectrum of NH_4^+-theta-1 steamed at 973K for 18 hours.

alumination. Figure 7.21(b) is typical of the spectra produced on dealumination at 973 K. Inspection of the broad species reveals that there are contributions to the non-framework aluminium signal in both the six- and four-coordinate aluminium regions although the four-coordinate signal is the dominant. The intensity of the six-coordinate aluminium species increases with dealumination time. It may be that this represents degradation of some of the four-coordinate or polymeric aluminium species to Al_2O_3 on increased severity of steaming. The linewidth of the broad non-framework four-coordinate aluminium species remains essentially unaltered ($\sim$11.7 kHz) throughout the dealumination process. The situation is in contrast to the ^{27}Al MASNMR results for dealumination at 873 K. In this case, the linewidth of the broad species is greater ($\sim$16 kHz), and the evidence for any non-framework six-coordinate aluminium peak at any stage of dealumination is unconvincing.

Figure 7.19 suggests that the final degree of dealumination is well below the total aluminium content and implies that approximately one-third of the acidic protons are retained in the limit of infinite steaming time at both dealumination temperatures. It seems that theta-1 has a higher resistance to dealumination than most other zeolites. Single-pulse ^{29}Si MASNMR studies of samples dealuminated at 873 K suggest that no extraneous silicon species are produced on dealumination in addition to the apparent retention of structural integrity, thus eliminating the possibility that the broad peaks in the aluminium spectra result from the presence of an amorphous phase caused by structural collapse. Peak fitting suggests that the Q^4 region may be fitted to

3 peaks in a 1:1:1 ratio. The framework Si/Al ratio was calculated for one sample from the ^{29}Si MASNMR spectrum and the calculated ratio was smaller than that suggested by ^{27}Al/XRF analysis suggesting perhaps the contribution of a significant proportion of Si-OH moieties to the Si(1Al) region. Subtle changes in the Q^3 region were also observed as a function of dealumination time. Other samples for the dealumination at 973 K yielded similar results. An interesting feature is that the resolution in the Q^4 region is not perceptibly improved as a function of dealumination.

A further example of the stability of the framework aluminium is provided by calcination of NH_4^+-theta-1 at 1173 K. The sample was previously heated at 4 K/min to 473 K and held at this temperature for 15 hours to completely remove any physisorbed water before raising the temperature to 1173 K at 4 K/min and holding for 6½ hours. Approximately one-third of the framework aluminium is retained and XRD data confirm that crystallinity is largely retained - a minor loss of crystallinity is indicated by broadening of the peaks at larger values of 2θ. A decrease in the d-spacings corresponding to a decrease in the size of the unit cell is also observed on calcination at 1173 K.

ESCA analysis of theta-1 samples prepared by hydrothermal dealumination in a vertical tubular furnace at 873 K show an increased surface enrichment of aluminium with increased severity of steaming due to migration of dislodged aluminium species, in agreement with other results[13].

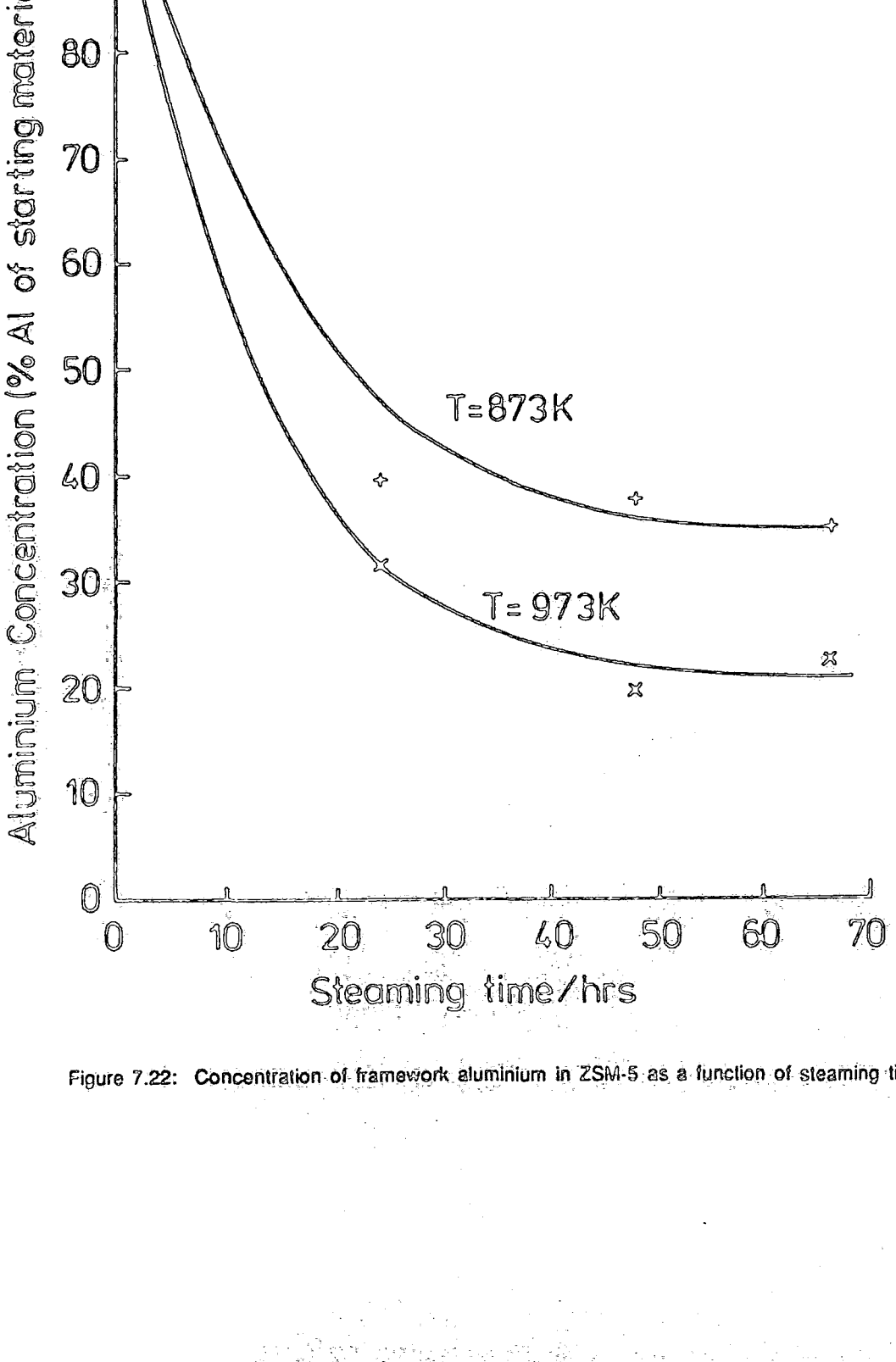

Figure 7.22: Concentration of framework aluminium in ZSM-5 as a function of steaming time.

7.12.2 Hydrothermal dealumination of ZSM-5

The dealumination studies were performed on the NH_4^+-form of ZSM-5. The ZSM-5 sample was prepared using the recipe outlined in Chapter Three. The organic template was removed by calcination at 823 K for 12 hours in air, and the sample was then converted to the ammonium form by ion exchange with ammonium nitrate as outlined in Section 3.3. The hydrothermal dealumination was performed in an identical manner to that outlined for theta-1, and the results obtained by ^{27}Al MASNMR and XRF are shown in Table 7.16.

The plot of framework aluminium as a function of steaming time is shown in Figure 7.22. It is clear that aluminium is removed from the framework at a faster rate at higher temperature as in the case of theta-1, and that the rate of dealumination is faster than that observed for theta-1 at both dealumination temperatures. Again, the final degree of dealumination is well below the total aluminium content, suggesting the retention of some acidic protons, although the degree of dealumination is greater than in the case of theta-1. Results in the literature have shown that an increase in the rate of dealumination occurs for samples with a greater initial concentration of aluminium[54]. However, in the present case, the initial framework Si/Al ratios for theta-1 and ZSM-5 are similar, which points to the importance of structural effects on the rate of dealumination. The larger channel size of ZSM-5, in addition to the two-dimensional channel network, would facilitate easier removal of aluminium than in theta-1 due to the greater water content during the dealumination process. Comparison of Figures 7.23(a) and (b) illustrates

TABLE 7.16 Hydrothermal dealumination of NH_4^+-ZSM-5 at 873 and 973 K

	Steaming time/hours						
		873 K			973 K		
	0	24	48	68	24	48	68
Four-coordinate Al, %wt. (NMR)	1.27	0.50	0.48	0.45	0.40	0.25	0.45
Six-coordinate Al, %wt. (NMR)	0.02	0.04	0.07	0.06	0.05	0.05	0.06
Asymmetric Al observed by NMR, %wt. (NMR)	0.86	1.62	1.68	1.70	1.77	1.89	o.70
Asymmetric Al invisible to NMR, %wt. (XRF, NMR)	0.00	0.00	0.00	0.00	0.00	0.09	0.00
Total Al %wt. (XRF)	2.15	2.15	2.23	2.21	2.22	2.29	2.27
Total Si %wt. (XRF)	40.0	40.4	41.2	41.0	41.5	42.2	42.3
Bulk Si/Al atomic ratio (XRF)	17.9	18.1	17.8	17.9	18.0	17.7	17.9
Framework Si/Al atomic ratio (XRF, NMR)	30.2	78.0	82.3	87.2	99.0	159.1	142.0

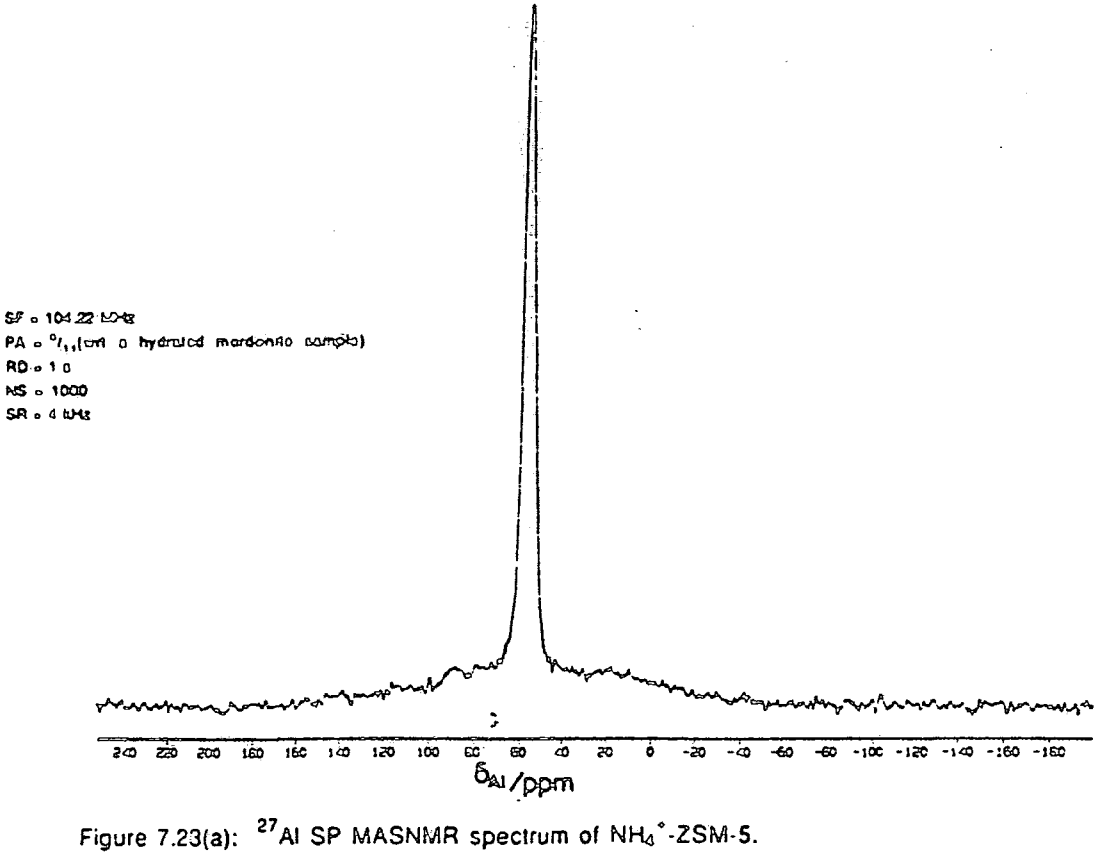

Figure 7.23(a): ^{27}Al SP MASNMR spectrum of NH_4^+-ZSM-5.

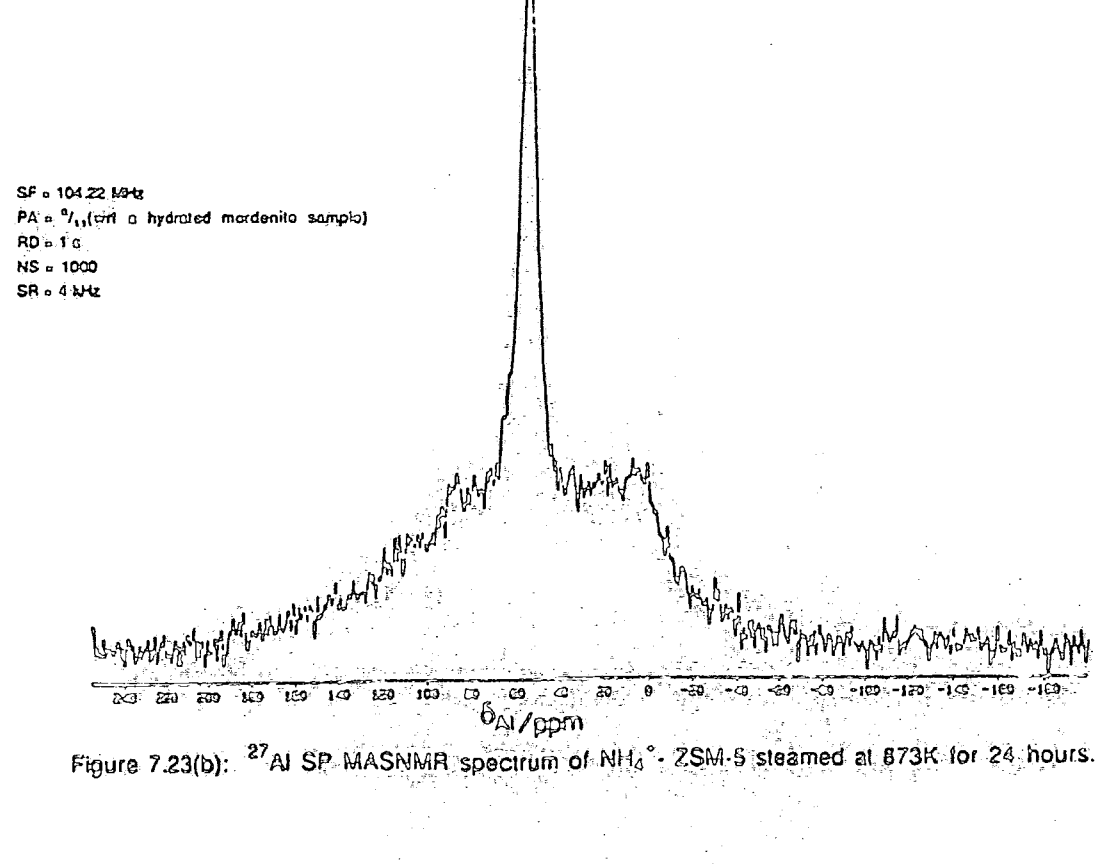

Figure 7.23(b): ^{27}Al SP MASNMR spectrum of NH_4^+- ZSM-5 steamed at 873K for 24 hours.

the nature of the species produced on dealumination at both 873 and 973 K. Signals associated with non-framework four- and six-coordinate aluminium are observed in all cases. There is no clear variation in intensity of the non-framework six-coordinate species as a function of either dealumination temperature or steaming time as was observed for theta-1. In addition, significant intensity is observed between the six- and four-coordinate aluminium positions in all cases. The linewidth of the broad species is typically of the order of 12 kHz for dealumination at 873 K and is increased on dealumination at 973 K for steaming times of 48 and 68 hours (∿13 kHz).

The results presented here for ZSM-5 suggest that all of the non-framework aluminium is NMR visible in agreement with very recent results by Freude *et al*[40], but in disagreement with earlier results by Freude *et al*[53]. Freude *et al* attribute the discrepancy due to hydration of the samples in the most recent paper. However, the results for theta-1 presented here and other results[55] suggest that invisible aluminium is a very real phenomenon, even in hydrated samples. It may be that the nature of the non-framework aluminium produced on dealumination is very sensitive to the dealumination procedure. Klinowski *et al*[56] have claimed that all of the aluminium in thermally treated zeolite Y is NMR visible.

7.12.3 Linebroadening mechanisms for non-framework aluminium species

Investigation of the linebroadening mechanism potentially provides further information on the non-framework aluminium species. Possible linebroadening mechanisms include:

(i) Second-order quadrupolar effects

As discussed earlier, second-order quadrupolar interactions significantly influence the width of the central transition resonance if the quadrupolar nucleus is in a distorted environment. If the broadening of the central line as caused by second-order quadrupolar effects is greater than the rotational frequency of the sample, then no narrowing would be observed[57].

(ii) Chemical-shift distribution

The range of four-coordinate Al-O species is 40-90 ppm and the six-coordinate Al-O range is 0-20 ppm[58]. Five-coordinate Al-O species have been claimed to exist between 30 and 40 ppm[59]. Of course, all of these ranges may be extended to even lower frequency by a significant second-order quadrupolar shift. It is clear that the observed broadening could result from a distribution of chemical species and the broadening mechanism is thus of the inhomogeneous type.

(iii) Relaxation broadening

Motional effects of water associated with non-framework aluminium could lead to fast relaxation caused by a specific fluctuation of the electric field gradient. In addition, the protons more directly associated with the aluminium could be mobile, thus contributing to relaxation effects. For isolated non-framework aluminium species and large channels, the non-framework species could have a fair degree of mobility associated with them. The linebroadening mechanism in this case is of the homogeneous type.

a)

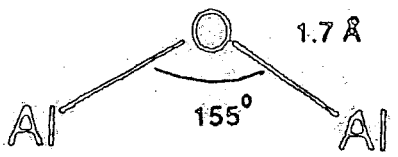

b)

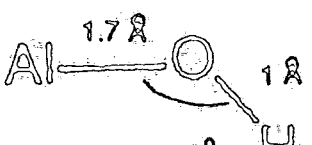

Figure 7.24: Bond angle and bond length data used for the calculation of the ^{27}Al-^{27}Al and ^{1}H-^{27}Al dipolar interactions.

(iv) Dipolar interactions

Both aluminium-aluminium and aluminium-hydrogen dipolar interactions would lead to a broadening of the non-framework aluminium signal. For the arrangements shown in Figures 7.24(a) and (b) calculations suggest that the most probable values of the dipolar interactions are 134 kHz and 2·5 kHz respectively. Both of these interactions should easily be removed by magic angle spinning. In fact an Al—O—H bond angle of ~25° would be required to give rise to a dipolar splitting of the order of the width of the observed broad component!

In an attempt to deduce the linebroadening mechanism, the non-framework component was observed as a function of magnetic field strength for identical states of dehydration. The results for a variety of zeolites are shown in Table 7.17.

TABLE 7.17 Linewidth of broad non-framework four-coordinate aluminium species as a function of magnetic field strength

^{27}Al frequency (MHz)	52.15	104.22	130.2
hydrothermally dealuminated theta-1	11.6 kHz, 222 ppm	11.7 kHz, 112 ppm	-
acid treated ultrastabilized zeolite Y[55]	-	14.7 kHz, 141 ppm	16.7 kHz, 128 ppm
NH_4^+-ZSM-5/Silica binder calcined 1073 K[55]	-	14.7 kHz, 141 ppm	15.4 kHz, 118 ppm

---

If the linewidth was determined solely by second-order quadrupolar effects, as would be expected for Freude's isolated non-framework aluminium model, then there should be an inverse relationship between the linewidth in Hz and the magnetic field strength which is clearly not observed. If we make the not unreasonable assumption that the linebroadening

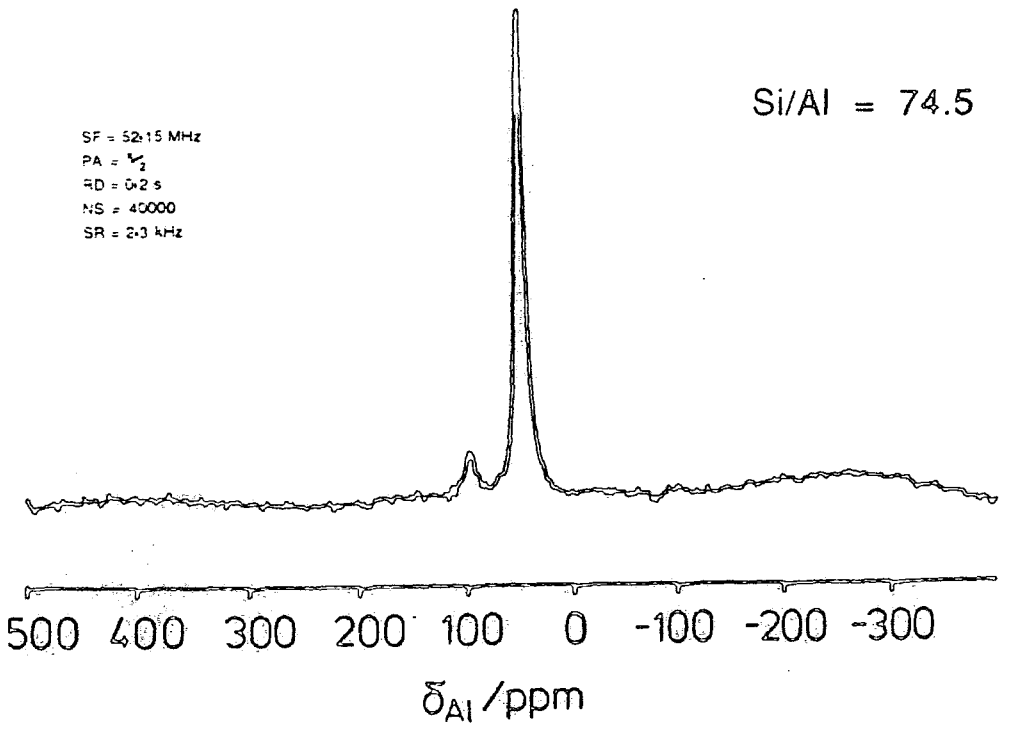

Figure 7.25: Selective observation of framework aluminium resonance on increasing the pulse duration for hydrothermally dealuminated theta-1.

mechanism is the same for all of the zeolite samples, then the decrease of the linewidth (in Hz) on going from 130.2 to 104.22 MHz suggests that second-order quadrupolar broadening does not govern the linewidth at 130.2 MHz. The decrease of the linewidth in Hz must be due to a distribution of chemical shifts. At lower fields, the second-order quadrupolar broadening becomes more important and for frequencies below 52.15 MHz, the linewidth of the broad component would be expected to increase for theta-1.

The second-order quadrupolar contribution to the non-framework aluminium resonance may be clearly demonstrated by increasing the duration of the radiofrequency excitation pulse from 0.5 to 4 μs when the intensity of the framework aluminium resonance is selectively increased with respect to the broad species (Figure 7.25). This would be expected on the basis of the discussion in Chapter Five where it was shown that half integer quadrupolar nuclei existing in a non-symmetrical environment nutate faster than in the more symmetrical case.

The effect of proton decoupling was investigated at an aluminium frequency of 78.15 MHz. Although there is no narrowing of the broad underlying aluminium species, the spectrum is broadened in the six-coordinate aluminium region in the absence of high-power proton decoupling suggesting that rotation at 2.8 kHz is not sufficient to completely average the ^{27}Al-^{1}H dipolar interaction (compare Figures 7.26(a) and (b)).

It seems that the linebroadening mechanism of the non-framework aluminium may be adequately explained in terms

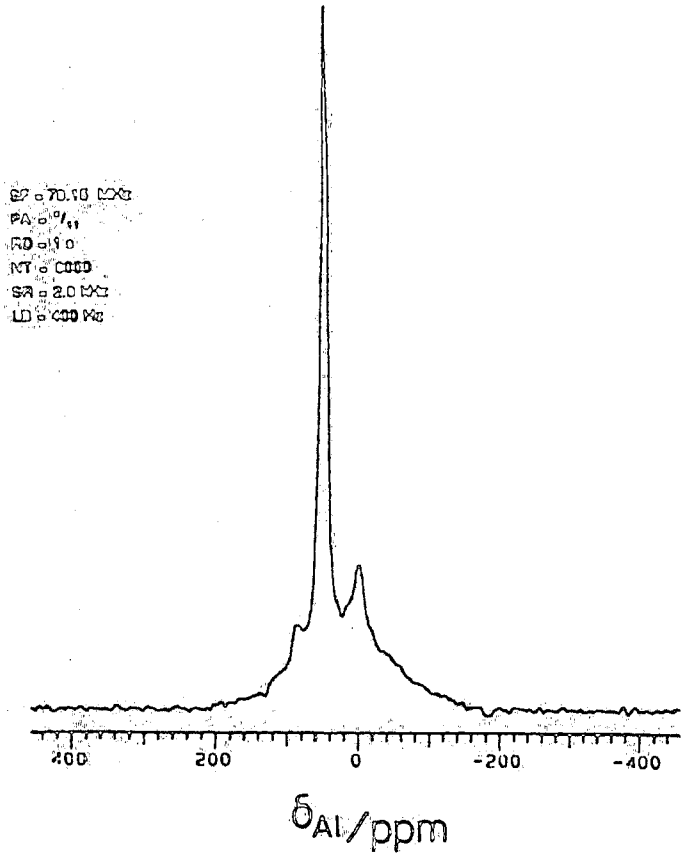

Figure 7.26(a): Proton-decoupled ^{27}Al SP MASNMR spectrum of a hydrothermally dealuminated sample of theta-1.

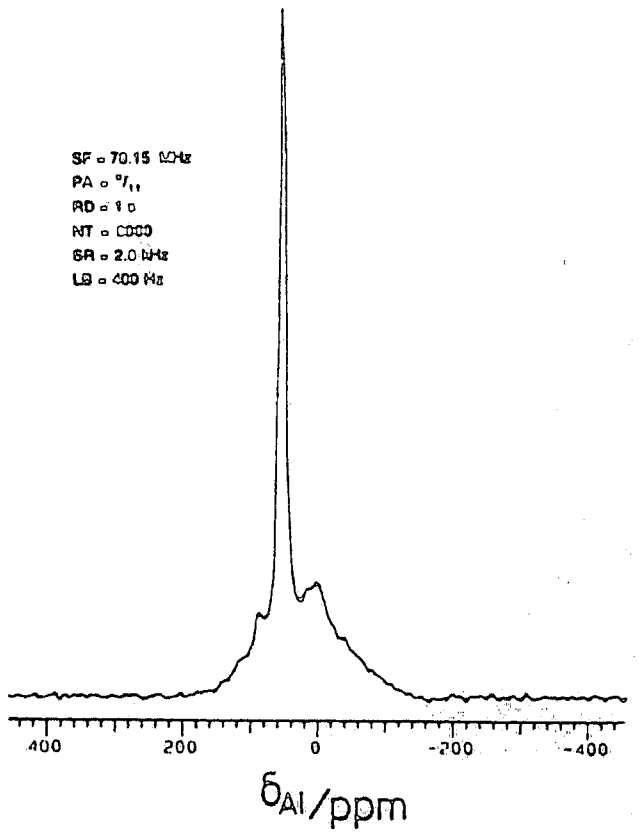

Figure 7.26(b): ^{27}Al SP MASNMR spectrum of a hydrothermally dealuminated sample of theta-1 obtained in the absence of proton decoupling.

of a combination of a range of chemical shifts (corresponding to a distribution of chemical environments) with a further contribution from second-order quadrupolar effects and a minor contribution from ^{27}Al-^{1}H heterodipolar coupling. There is no need to invoke relaxation effects to explain the observed broadening.

7.12.4 Hydrothermal dealumination mechanism

Given that the framework aluminium atoms are isolated from one another in highly siliceous zeolites such as theta-1 or ZSM-5, it would be expected that the rate of dealumination is first-order dependent on the concentration of framework aluminium. Dealumination data for ZSM-5 suggest that the dealumination reaction is second-order with respect to framework aluminium, which was explained by invoking the participation of H^+ in the catalysis reaction[54]. For the dealumination of theta-1 at 973 K and 873 K, both the first- and second-order rate equations used by Suzuki *et al* are inappropriate because no account was taken of the residual framework aluminium retained at infinite steaming time. It is found that the data may be fitted with reasonable accuracy to the first-order equation:

$$\frac{-dI}{dt} = k(I-Q) \qquad (7.1)$$

where Q is the concentration of residual framework aluminium. Integration yields $I = (I_o-Q)e^{-kt} + Q$ and the relevant plots for both 873 K and 973 K are shown in Figure 7.27. First-order rate constants of $3.40 \times 10^{-5} s^{-1}$ and $1.13 \times 10^{-5} s^{-1}$ are observed for dealumination at 973 K and 873 K respectively. Assuming an Arrhenius-type temperature dependence of the rate coefficient of the form $k=Aexp(-E_a/RT)$, with the further assumption of a temperature-independent pre-exponential factor

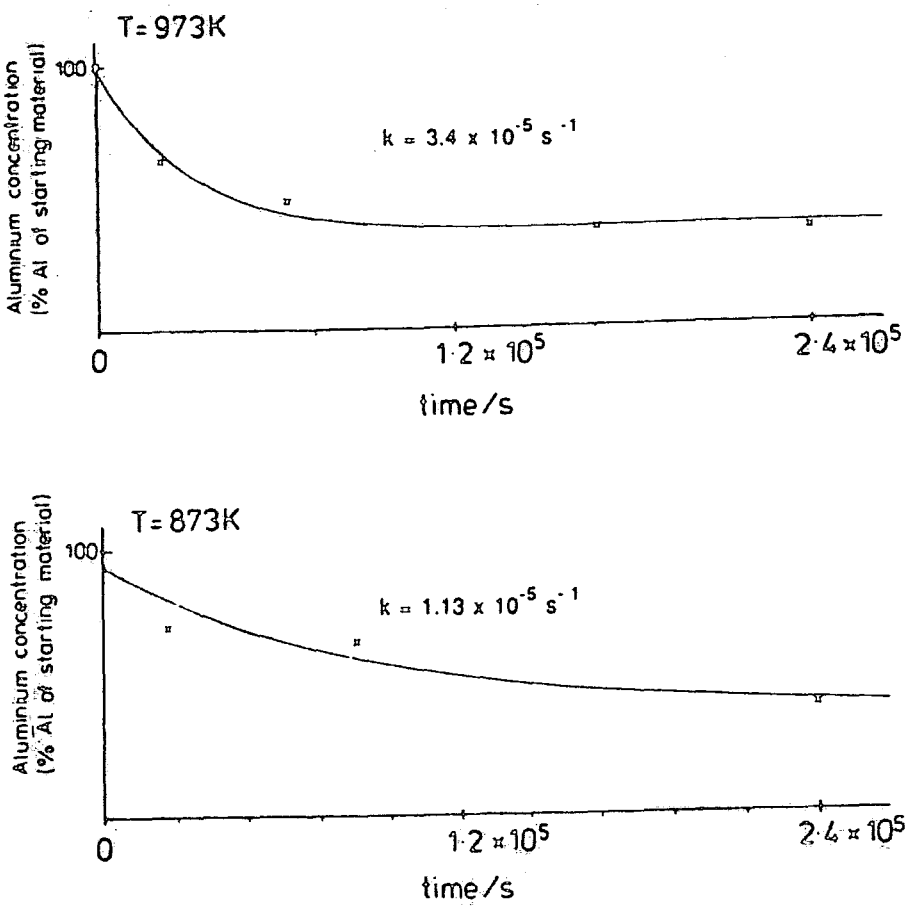

Figure 7.27: Plot of framework aluminium concentration as a function of steaming time for theta-1 fitted to the function: $I = (I_0-Q)\exp(-kt)+Q$.

leads to an activation energy for dealumination of approximately 80 $kJmol^{-1}$. The relevant point is that the dealumination process may be quite adequately described by first-order reaction kinetics although the data obtained at 873 K was of lower quality. No attempt was made to fit the data resulting from the dealumination of ZSM-5.

7.13 Application of multiple-pulse sequences to quadrupolar nuclei

As explained previously (Section 5.1), dehydration of ZSM-5 results in a cation dependent broadening. It has been suggested that the linewidth broadens due to a distortion of AlO_4 tetrahedra and a subsequent increase in the second-order quadrupolar broadening, but there have been no observations that would contradict the possibility of cation-promoted broadening - either static effects (the cation moving closer to the aluminium on dehydration) or motional effects (leading to a fast relaxation caused by specific fluctuations of the electric field gradient). A similar situation is observed on dehydration of NaY zeolite. The ^{23}Na resonance becomes broader and eventually disappears on dehydration. The possibility of the heterodipolar interaction between the sodium and aluminium accounting for the broadening may be eliminated on the basis of standard bond distances which do not allow a predicted broadening of more than 1 kHz for a static sample.

Clearly there is much to be gained from a pulse sequence that can distinguish between relaxation effects and second-order quadrupolar broadening. The empirical effect of MREV-8, π_z and CPMG pulse sequences was observed for a range of model systems. It should be noted that even if such pulse sequences do not lead to the removal of the second-order

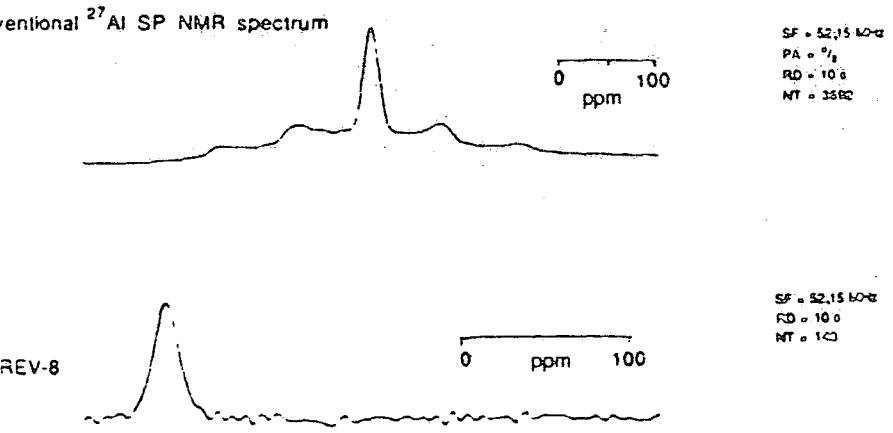

Figure 7.28(a): Application of the MREV-8 pulse sequence to aluminium bromide hexahydrate.

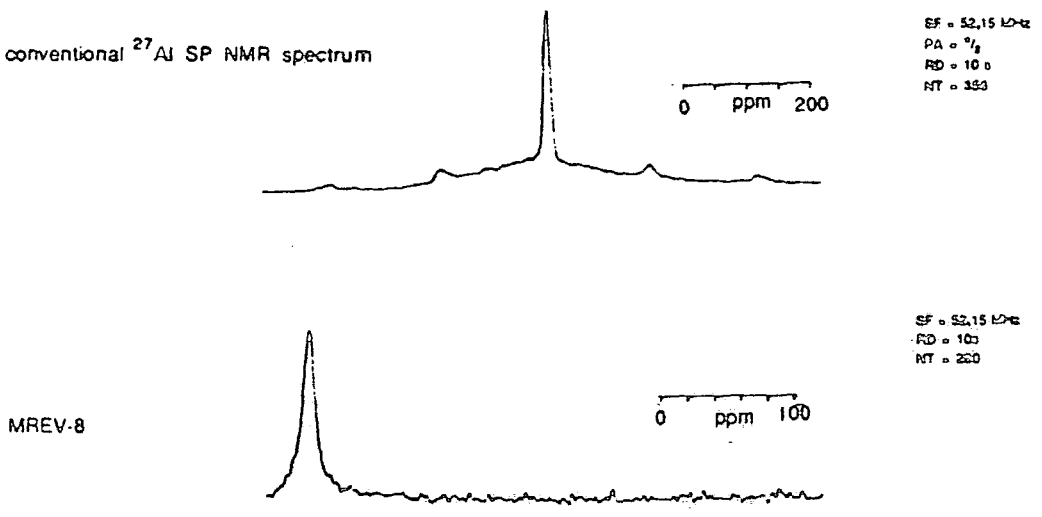

Figure 7.28(b): Application of the MREV-8 pulse sequence to aluminium chloride hexahydate.

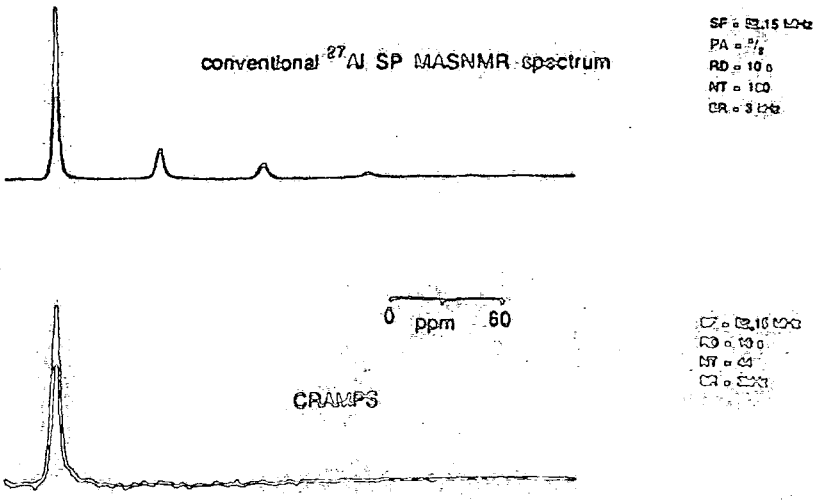

Figure 7.28(c): Application of CRAMPS (MREV-8) to aluminium bromide hexahydrate.

quadrupolar interaction, the pulse sequences may still scale down the second-order quadrupolar interaction. A combination of these sequences could lead to an unambiguous assignment of the linebroadening mechanisms in quadrupolar systems.

7.13.1 MREV-8

In addition to the above discussion, the interest in the MREV-8 sequence was also stimulated by the fact that quantification is often made very difficult in ^{27}Al MASNMR due to the overlap of spinning sidebands accompanying the four- and six-coordinate aluminium environments overlapping with the six- and four-coordinate resonances themselves. Clearly much time may be wasted finding an optimum spinning rate. However, the MREV-8 sequence scales the chemical shift but not the spin rate,and the apparent increase in spin rate could make the problem of quantification easier.

In this case, an aqueous solution of $AlCl_3.6H_2O$ was used as the tune-up sample for the CRAMPS experiment. 3μs $\pi/2$ pulses ($\omega_{rf}/2\pi=83\frac{1}{3}$ kHz) and a four-pulse cycle time of 36μs were used (spectral width = 13,889 Hz). The chemical shift scaling factor was determined by the co-addition of signals from an aqueous solution of $AlCl_3.6H_2O$, separated by 1 kHz offsets. The response of model solid state samples was observed in the presence of ^1H dipolar decoupling.

The effect of MREV-8 on static samples of aluminium bromide and chloride is shown in Figures 5.28(a) and (b). Clearly, the pulse sequence has removed the first-order quadrupolar powder pattern for the non-central transitions leaving only the central transition. The first-order quadrupolar spinning sideband pattern is also removed on application of

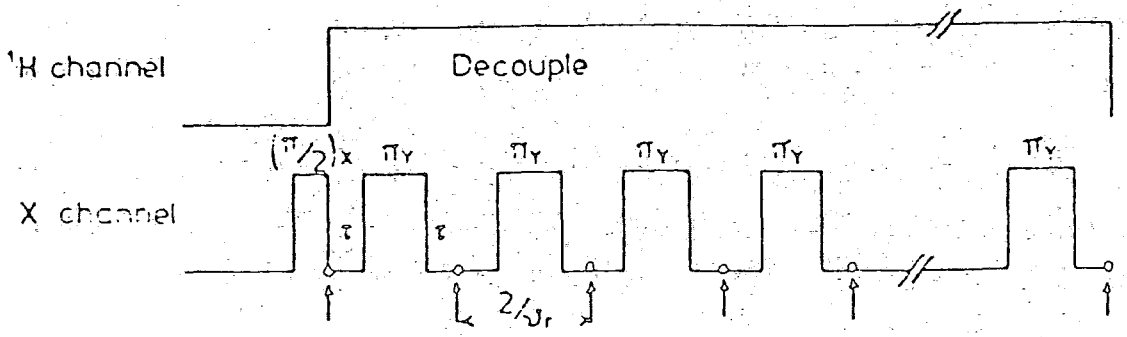

Figure 7.29(a): Rotation-synchronised CPMG pulse sequence (with proton decoupling).

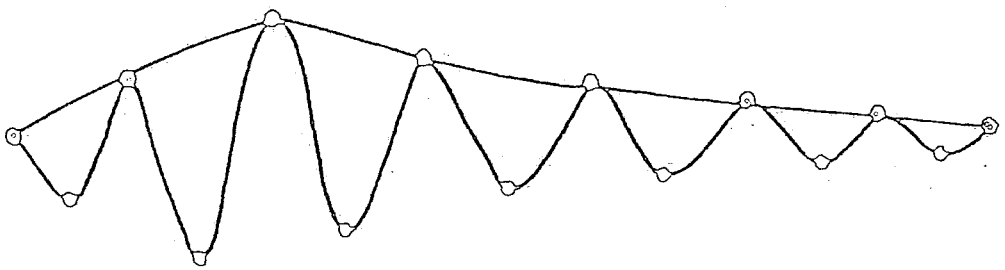

Figure 7.29(b): Echo intensity as a function of time.

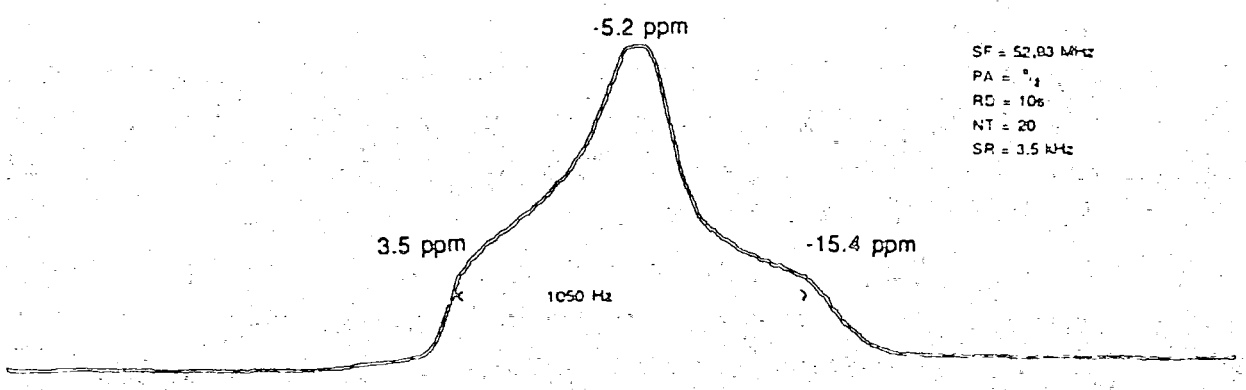

Figure 7.29(c): ^{23}Na SP MASNMR spectrum of sodium perborate.

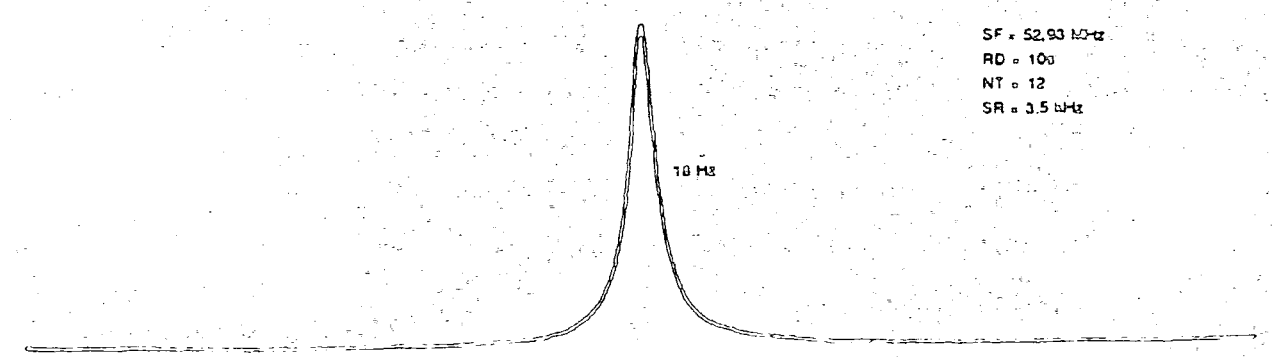

Figure 7.29(d): Fourier Transformation of echo intensity as a function of time for sodium perborate.

MREV-8 and MAS (Figure 5.28(c)). This effect would be expected because the first-order quadrupolar Hamiltonian has the same spin and space symmetry as the homodipolar Hamiltonian, so that whatever conclusions have been made about the latter will also be true of the former[60]. Unfortunately, no signal could be detected for samples with a larger quadrupole coupling and so it was not possible to assess the effect of the pulse sequence on the second-order quadrupolar broadening of the central transition. Variation in the pulse duration for the MREV-8 sequence did not result in the observaation of a signal and similar results were observed on repeating the experiment at a later date. This effect is difficult to explain although it could be related to the fact that the quadrupolar interaction has become too large to be averaged by the pulse sequence for the cycle time used. In fact, no signal could be observed for a sample of $KAl(SO_4)_2.12H_2O$ where $e^2qQ/h=395$ kHz.

7.13.2 CPMG

The rotation-synchronised pulse sequence shown in Figure 7.29(a) should refocus at time 2τ all the terms in the Hamiltonian describing the system that are linear in $\hat{I}_z$. Thus the effects of offset, field inhomogeneity and chemical shift will be refocused, unlike the case for homonuclear dipole-dipole coupling where the π pulse inverts both of the coupled spins so that the effects of either of these couplings continue unaltered by the pulse.

Papers by Solomon[61] and others [62,63] studying both the theoretical and experimental effects of two-pulse sequences $\{(\pi/2)_x-\tau-\phi_x-\tau$ and $(\pi/2)_x-\tau-\phi_y-\tau\}$ on half-integer spin

quadrupolar nuclei have suggested that the signal following such pulse sequences consists of both modulated and unmodulated terms. The decay of the unmodulated terms should be determined by spin-spin interactions. The effect of the CPMG pulse on $I=^3/2$ was calculated using a density matrix approach and the result is shown in Appendix B. Subject to the assumptions made, an unmodulated contribution resulting from the central transition term in the calculation is indeed predicted. The experimental conditions are such that the modulated contribution would not be detected.

The intention of the work described below was the stroboscopic observation of the signal resulting from the decay of the central transition term. Pseudo Fourier Transformation of data obtained by rotation-synchronised single-point acquisition should lead to a single peak, the linewidth of which is related to the spin-spin relaxation time. Initially, the effect of such a pulse sequence on model sodium compounds was investigated before the extension of the study to aluminium-containing compounds.

The spacing of the π_y pulses was two rotor periods, which made stable sample spinning crucial. Individual data points were acquired every other rotor period. The use of magic angle spinning helps to eliminate echoes resulting from any I-S dipolar interactions in addition to the removal of quadrupolar nucleus-proton dipolar interactions by high-power proton decoupling. The $\pi/2$ and π pulses were set using the usual definitions of maximum and minimum transverse magnetisations respectively. Ideally, it would have been preferable to use a soft $(\pi/2)_x$ pulse to effect selective excitation of the central transition, but this proved impossible

due to instrumental problems. Nutation experiments, described in Chapter Five, were used to examine whether or not the excitation was selective.

The pulse sequence was applied on resonance, with quadrature detection. The rotation synchronisation leads to the constraint that the time interval between the π_y pulses must typically be of the order of tenths of milliseconds. In addition, the time between the π_y pulses should be less than the T_2 of the signal.

Typically, when a train of echoes created by π_y pulses after the initial $(\pi/2)_2$ pulse was observed, the amplitude of the echoes traced out an oddly-shaped envelope in which the first few echoes increased in amplitude before a gradual decay in echo height occurred (Figure 7.29(b)). This was initially interpreted as resulting from terms in the relevant Hamiltonian that are not refocused and the eventual formation of a new state which then decays. However, in the case of a simple I=1/2 system, this type of behaviour may be caused by inaccuracies in the π pulse durations. The first point recorded results from pulse breakthrough and was removed from the decay by "left shifting". In fact, the first two points had to be removed so that the resulting decay could be correctly phased on Fourier Transformation.

Initial inspection suggests that modulation between consecutive points is occurring - however, in quadrature detection mode, consecutive points are real and imaginary.

The phase-shift between the real and imaginary points is determined by the phase difference between the detectors. The change in observed amplitude with time is thus more accurately described by the black lines joining the points in the Figure 7.29(b). The imaginary points could, of course, be removed by using single phase detection, although this would make the measurement of linewidth after the Fourier Transformation very difficult given that the CPMG pulse sequence is applied on-resonance. Given that the imaginary points are unlikely to effect the linewidth, the decision was taken to use quadrature detection to record the data. The results obtained are shown in Table 7.18, and the line-narrowing effect of the pulse sequence is illustrated in the frequency domain by comparison of Figures 7.29 (c) and (d).

TABLE 7.18 The effect of the rotation-synchronised CPMG sequence on the MAS linewidth (^{23}Na and ^{27}Al frequencies are 52.93 and 52.15MHz respectively)

sample	Nucleus observed	$\Delta\nu_{\frac{1}{2}}$ (MAS)/Hz	$\Delta\nu_{\frac{1}{2}}$ (CPMG)/Hz	T_2/s (1)	ω_Q/ω_{rf} (4)
sodium chloride	^{23}Na	60	1.7	0.19	∿0
Borax (2)	^{23}Na	∿450,∿200	13	2.4×10^{-2}	0.57,0.36 (5)
sodium perborate (3)	^{23}Na	∿715	18	1.8×10^{-2}	∿0.3
sodium aluminium sulphate	^{23}Na	∿1200	11	3.0×10^{-2}	∿0.8
aluminium bromide	^{27}Al	146	100	3.2×10^{-3}	∿0
albite	^{27}Al	1260	160	2×10^{-3}	0.64 (5)

(1) Calculated assuming a Lorentzian lineshape

(2) Two distinct resonances observed in single-pulse spectrum.

(3) Two crystallographically distinct sites present, but indistinguishable by single-pulse or nutation.

(4) Calculated from nutation excitation projection unless otherwise stated.

(5) Calculated from published quadrupole coupling data.[64,65]

Selective excitation of the central transition occurred in the case of sodium aluminium sulphate (the majority of the signal occurred at $2\omega_{rf}$ in the excitation projection of the nutation experiment) and there was essentially no difference in the general form of the signal produced by the CPMG pulse sequence in this case relative to the cases of non-selective and intermediate excitation. As expected, the pulse sequence refocused chemical shift effects in the case of borax and sodium perborate. The absence of modulation in the time domain does not prove that the second-order quadrupole interaction is refocused by the CPMG pulse sequence - it may be that the modulation frequency is large compared to the sampling frequency when it would not be detected.

The experimental evidence suggests that similar results to those predicted in Appendix B are observed when some of the assumptions are relaxed. The important point is that the application of such a pulse sequence to half-integer quadrupolar spin systems allows one to obtain a piece of datum related to the spin-spin relaxation time. The precise meaning of the datum obtained would be expected to depend on the extent to which the non-central transitions are excited by such a pulse sequence and a more sophisticated theoretical is required. It is envisaged that such a pulse sequence will prove valuable in distinguishing between relaxation broadening and second-order quadrupolar broadening of the central transition.

7.13.3 π_z-pulses

During the course of research the author's attention was drawn to a paper by Walker and Gerstein[66] which

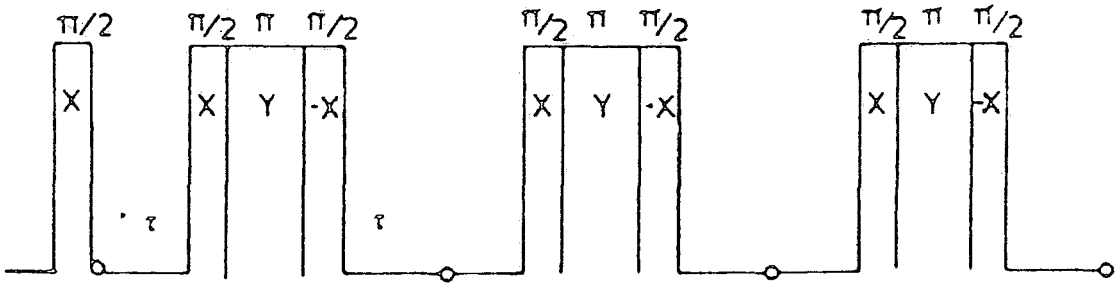

Figure 7.30(a): Pulse train of composite π_z pulses (after a preparation pulse) used in an attempt to selectively average the second-order quadrupolar interaction.

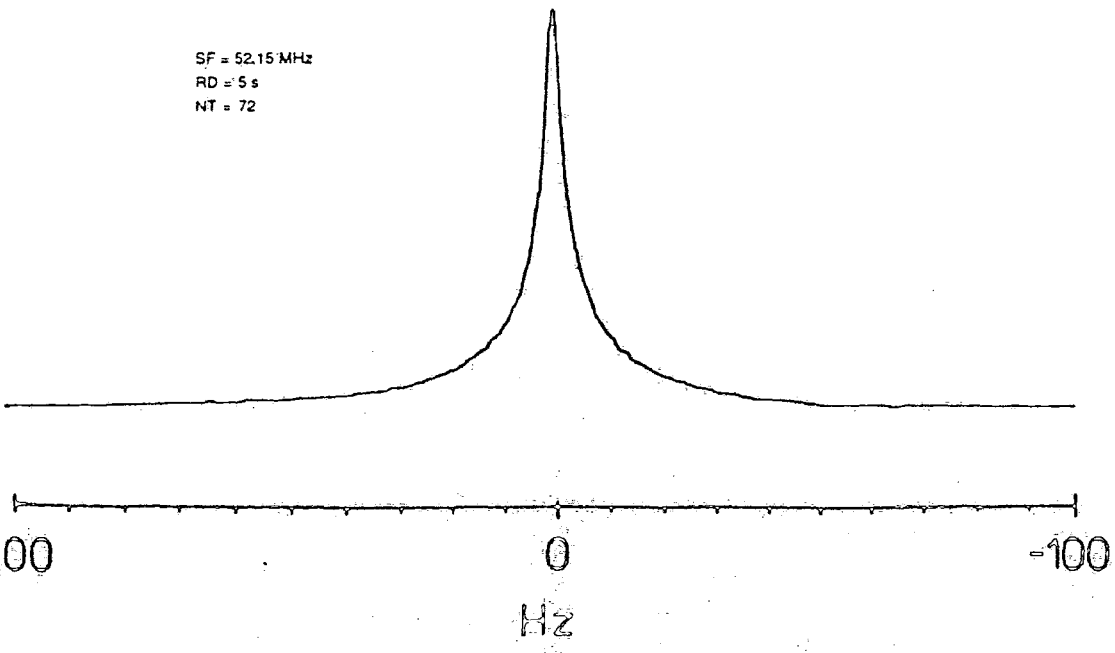

Figure 7.30(b): Application of the pulse sequence shown in Figure 7.30(a) to the aluminium containing background.

suggested that the pulse sequence $\tau-\pi_z-\tau$ selectively refocuses the second-order interaction at time 2τ to zeroth order in the Magnus expansion (following the application of a preparation pulse). The π_z pulse sequence is thus relevant to the problem, π_z being a selective π pulse (applied to the central transition) about Z in the rotating frame. Stroboscopic observation of the magnetisation at the peak of the echo amplitudes, accompanied by magic angle spinning should remove second-order broadening and yet retain chemical shift information.

A composite pulse sequence was used which has the overall effect of a π_z pulse:

$$\pi_z = (\pi/2)_x \pi_y (\pi/2)_{-x}$$

The composite pulse makes use of a similarity transformation, the pulses $(\pi/2)_y$ and $(\pi/2)_{-x}$ have the effect of rotating the rotation axes through $+\pi/2$ (from -Y to +Z) without altering the pulse duration about Y (Figure 7.30(a)). For most samples, great difficulties were experienced in trying to obtain a signal that could be confidentially distinguished from artefact. No improvement was observed on reducing the time between the π_z pulses and repeating the experiment on a static sample. The above sequence did however work very well on the aluminium containing background (Figure 7.30(b)). The observed signal was not sensitive to offset from resonance as was also observed in the CPMG sequence.

Unfortunately, recent communcations have suggested[67] that an error was made in the theoretical treatment. It seems that the echo does not necessarily represent refocusing of the second-order quadrupolar interaction, but may originate in the

refocusing of interactions that have an $\hat{I}_Z$ spin operator dependence.

7.14 General conclusion

In conclusion, the multinuclear approach provides a powerful tool for the investigation of zeolites. A combination of XRD and ^{29}Si NMR data shows that the diethanolamine template causes some distortion of theta-1 with respect to the calcined form. Such structural changes may have an important influence on catalytic reactions although the structural change is not observed with all organic molecules. In addition, the ^{13}C data allow the tentative suggestion of surface acid sites, although their nature is far from clear and further experiments involving other probe molecules are required. It is however clear that water has a stronger affinity for these sites than the diethanolamine template molecule.

The presence of Brönsted acid sites has been demonstrated in H-theta-1 and H,Na-Ga-ZSM-5 by ^{1}H NMR. The acid sites present in these samples have also been characterised by temperature-programmed desorption of ammonia. The TPD studies show that the peak associated with Brönsted acidity in the TPD derivative plot depends critically on the concentration of non-framework aluminium in the case of theta-1. The TPD studies also show that the peak associated with Brönsted acidity in H,Na-Ga-ZSM-5 occurs in a similar position to that observed in the aluminium analogue in agreement with the similarity of the relevant shifts in ^{1}H NMR.

^{27}Al NMR studies have shown that the hydrothermal dealumination of framework aluminium is first-order with respect

to the removable aluminium under strong dealumination conditions. A combination of variable magnetic field studies, various pulse duration experiments and high-power proton decoupling experiments have shown that the linebroadening mechanism for the non-framework aluminium is dominated by a distribution of chemical environments, second-order quadrupolar broadening and a minor contribution from ^{27}Al-^{1}H heterodipolar coupling.

The application of multiple-pulse sequences to half-integer spin quadrupolar nuclei has also been investigated as a potential means of deducing linebroadening mechanisms. Although the analysis of the effect of the CPMG pulse sequence could benefit from a more sophisticated theoretical treatment than has been given, it is felt that the pulse sequence will prove useful in distinguishing between relaxation and second-order quadrupolar broadening of the central transition in half-integer spin quadrupolar nuclei.

REFERENCES - CHAPTER SEVEN

1. T.L. Barr and M.A. Lishka, J.Am.Chem.Soc., 108,3178 (1986).

2. J.B. Nagy, Z. Gabelica and E.G. Derouane, Zeolites, 3, 43 (1983).

3. G.W. West, Aust.J.Chem., 37, 455 (1984).

4. C.A. Fyfe, G.J. Kennedy, C.T. de Schutter and G.T. Kokotailo, J.Chem.Soc., Chem.Commun., 541 (1984).

5. C.A. Fyfe, H. Strobl, G.T. Kokotailo and G. Barlow, J.Am.Chem.Soc., 110, 3373 (1988).

6. G. Debras, A. Gourgue, J.B. Nagy and G. de Clippeleir, Zeolites, 6, 241 (1986).

7. R.D. Farlee, D.R. Corbin and A.J. Vega, in Proceedings of the 25th Rocky Mountain Conference, Denver (1983).

8. K.R. Franklin and B.M. Lowe, Zeolites, 8, 508 (1988).

9. I.D. Gay and S. Liang, J. Catal., 44, 306 (1976).

10. W.H. Dawson, S.W. Kaiser, P.D. Ellis and R.R. Innera, J.Am.Chem.Soc., 103, 6780 (1981).

11. D.L. Van der Hart, W.L. Earl and A.N. Garroway, J.Magn. Reson., 44, 361 (1981).

12. A.J. Vega, J.Am.Chem.Soc., 110, 1049 (1988).

13. J.N. Ness, D.J. Joyner and A.P. Chapple, Zeolites, 9, 250 (1989).

14. S.A.I. Barri, G.W. Smith, D. White and D. Young, Nature, 316, 533 (1984).

15. D. Freude, J. Haase, J. Klinowski, T. Adrian Carpenter and G. Ronikier, Chem.Phys.Lett., 119, 365 (1985).

16. E. Lippmaa, A. Samoson and N. Mägi, J.Am.Chem.Soc., 108, 1730 (1986).

17. C.A. Fyfe, G.C. Gobbi, J.S. Hartmann, J. Klinowski and J.M. Thomas, J.Phys.Chem., 86, 1247 (1982).

18. A.P.M. Kentgens, K.F.M.G.J. Scholle and W.S. Veeman, J.Phys.Chem., 87, 4357 (1983).

19. A. Samoson and E. Lippmaa, 100, 205 (1983).

20. G. Debras, A. Gourge, B. Nagy and G. De Clippeleir, Zeolites, 6, 161 (1986).

21. J.B. Uyterrhoeven, L.G. Christner and W.K. Hall, J.Chem.Phys., 69, 2177 (1978).

22. J.F. Knifton, J.Chem.Soc., Chem.Commun., p.41 (1981).

23. C.E. Bronnimann, I.S. Chuang, B.L. Hawkins and E. Maciel, J.Am.Chem.Soc., 109, 1567 (1987).

24. J.M. Thomas and J. Klinowski, Advances in Catalysis, 33, 199 (1986).

25. D. Freude, M. Hunger and H. Pfeifer, Chem.Phys.Lett., 91, 307 (1982).

26. D. Freude, T. Fröhlich, M. Hunger, H. Pfeifer and G. Scheler, Chem.Phys.Lett., 98, 263 (1983).

27. D. Freude, M. Hunger, H. Pfeifer, G. Scheler, J. Hoffmann and W. Schmitz, Chem.Phys.Lett., 105, 427 (1983).

28. D. Freude, M. Hunger, H. Pfeifer and W. Schweiger, Chem. Phys.Lett., 128, 62 (1986).

29. G. Engelhardt, H.-G. Jerschkewitz, U. Lohse, P. Sarv, A. Samoson and E. Lippmaa, Zeolites, 7, 291 (1987).

30. K.F.M.G.J. Scholle, W.S. Veeman, J.G. Post and J.H.C. van Hoaf, Zeolites, 3, 214 (1983).

31. Z. Luz and A.J. Vega, J.Phys.Chem., 91, 374 (1987).

32. K. Stahl, Ake Kuich and Subtra Ghose, Zeolites, 9, 303 (1989).

33. K.F.M.G.J. Scholle, A.P.M. Kentgens, W.S. Veeman, P.Frenken and G.P.M. van der Velden, J.Phys.Chem., 88, 5 (1984).

34. P.H. Kasai and P.M. Jones, J.Mol.Catal., 27, 81 (1984).

35. V.V. Mank, N.G. Vasilyev, F.D. Outcharenko and J.F.Zubenko, Dokl.Akad.Nauk,SSSR, 207, 133 (1972).

36. M. Hunger, D. Freude and H. Pfeifer, Catalysis Today, 3, 507 (1988).

37. N.Y. Topsøe, K. Pendensen, and E.G. Derouane, J.Catal., 70, 41 (1981).

38. N.R. Meshram, S.G. Hegde and S.B. Kulkarni, Zeolites, 6, 434 (1986).

39. C.V. Hidalgo, H. Itoh, T. Hattari, M. Niwa and Y. Murakami, J.Catal., 85, 362 (1982).

40. E. Brunner, H. Ernst, D. Freude, M. Hunger, C.B. Krause, D. Prager, W. Reschetilowski, W. Schweiger and K.-H Bergk, Zeolites, 9, 282 (1989).

41. A. Auroux, P.C. Gravelle, J.C. Vedrine and M. Rekas, in Proceedings of the 56th International Zeolite Conference (Naples, 1980), p.433, Heydon, London (1980).

42. E. Brunner, D. Freude, M. Hunger, H. Pfeifer, W. Reschetilowski and B. Unger, Chem.Phys.Lett., 148,276 (1988).

43. L. Pauling, "The Nature of the Chemical Bond", Cornell University Press, New York (1980).

44. W.H. Jolly, "The Principles of Inorganic Chemistry", McGraw-Hill Inc. (1976).

45. J. Dwyer, F.R. Fitch and E.E. Nkang, J.Phys.Chem., 87, 5402 (1983).

46. E. Kassab, K. Seiti and M. Allavena, J.Phys.Chem., 92, 6705 (1988).

47. K.G. Ione, L.A. Vostrikova, E.A. Paukshtis, E.N. Yurchenko and V.G. Stepanov, Akad.Nauk.SSSR, 261, 1160 (1981).

48. C.T. Chu and C.D. Chang, J.Phys.Chem., 89, 1569 (1985).

49. J. Klinowski, J.M. Thomas, C.A. Fyfe and G.C. Gobbi, Nature (London), 296, 533 (1982).

50. V. Bosáček and V.M. Mastikhin, J.Phys.Chem., 91, 260 (1987).

51. R.D. Shannon, K.H. Gardner, R.H. Staley, G. Bergetet, P. Gallezot and A. Arovs, J.Phys.Chem., 89, 4778 (1985).

52. D. Freude, T. Fröhlich, H. Pfeifer and G. Scheler, Zeolites, 3, 171 (1983).

53. D. Freude, E. Brunner, H. Pfeifer, D. Prager, H.-G. Jerschkewitz, U. Lohse and G. Oehlmann, Chem.Phys.Lett., 139, 325 (1987).

54. T. Sano, K. Suzuki, H. Shoji, S. Ikai, K. Okabe, T. Murakami, S. Shin, H. Hagiwara and H. Takaya, Chem.Lett., 7, 1421 (1987).

55. D. Roberts, Private Communication.

56. P.P. Man, J. Klinowski, A. Trokiner, H. Zanni and P.Papon, Chem.Phys.Lett., 151, 143 (1988).

57. D. Freude and H.J. Behrens, Cryst.Res.Techn., 16 36 (1984).

58. H. Stade, D. Müller and G. Scheler, Z. Anorg.Allg.Chem., 510 16 (1984).

59. J.-P. Gilson, G.C. Edwards, A.W. Peters, K. Rajagopalan, R.F. Wormskecher, T.G. Roberie and M.P. Shatlock, J.Chem.Soc., Chem.Commun, p.91 (1987).

60. M. Mehring and H. Raber, Solid State Commun., 13. 1637 (1973).

61. I. Solomon, Phys.Rev., 110, 61 (1958).

62. I.D. Weisman and L.H. Bennet, Phys.Rev., 181, 1341 (1969).

63. P.A. Osment, Ph.D. Thesis, University of York (1987).

64. J.D. Cuthbert and H.E. Petch, J.Chem.Phys., 39, 1247 (1963).

65. J. Kirkpatrick, R.A. Kinsey, K.A. Smith, D.M. Henderson and E. Oldfield, Am.Mineral, 70, 106 (1985).

66. R.D. Walker and B.C. Gerstein, Phys.Rev.B, 31, 3167 (1985).

67. R.D. Walker, Ph.D. Thesis, Iowa State University (1984).

APPENDIX A

F_1 Projections for $I=3/2$ and $I=5/2$ quadrupolar nuclei as a function of ω_Q/ω_{rf}. ($\omega_Q = e^2qQ/\hbar 8I(2I-1)$ and ω_{rf} is the strength of the radio-frequency B_1 field). The projections were obtained from W.S. Veeman.

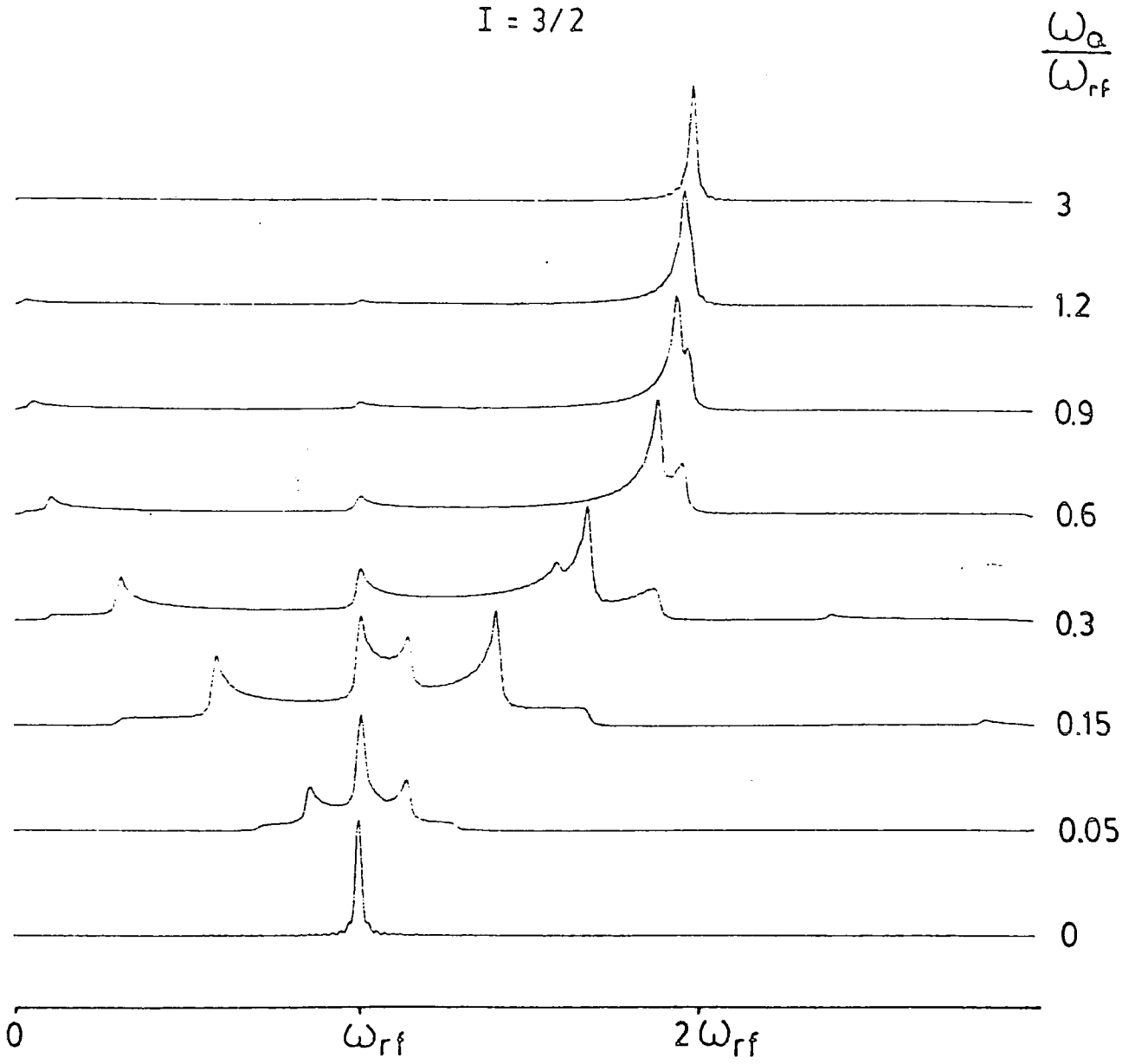
I = 3/2
ωa/ωrf
3
1.2
0.9
0.6
0.3
0.15
0.05
0
0
ωrf
2ωrf

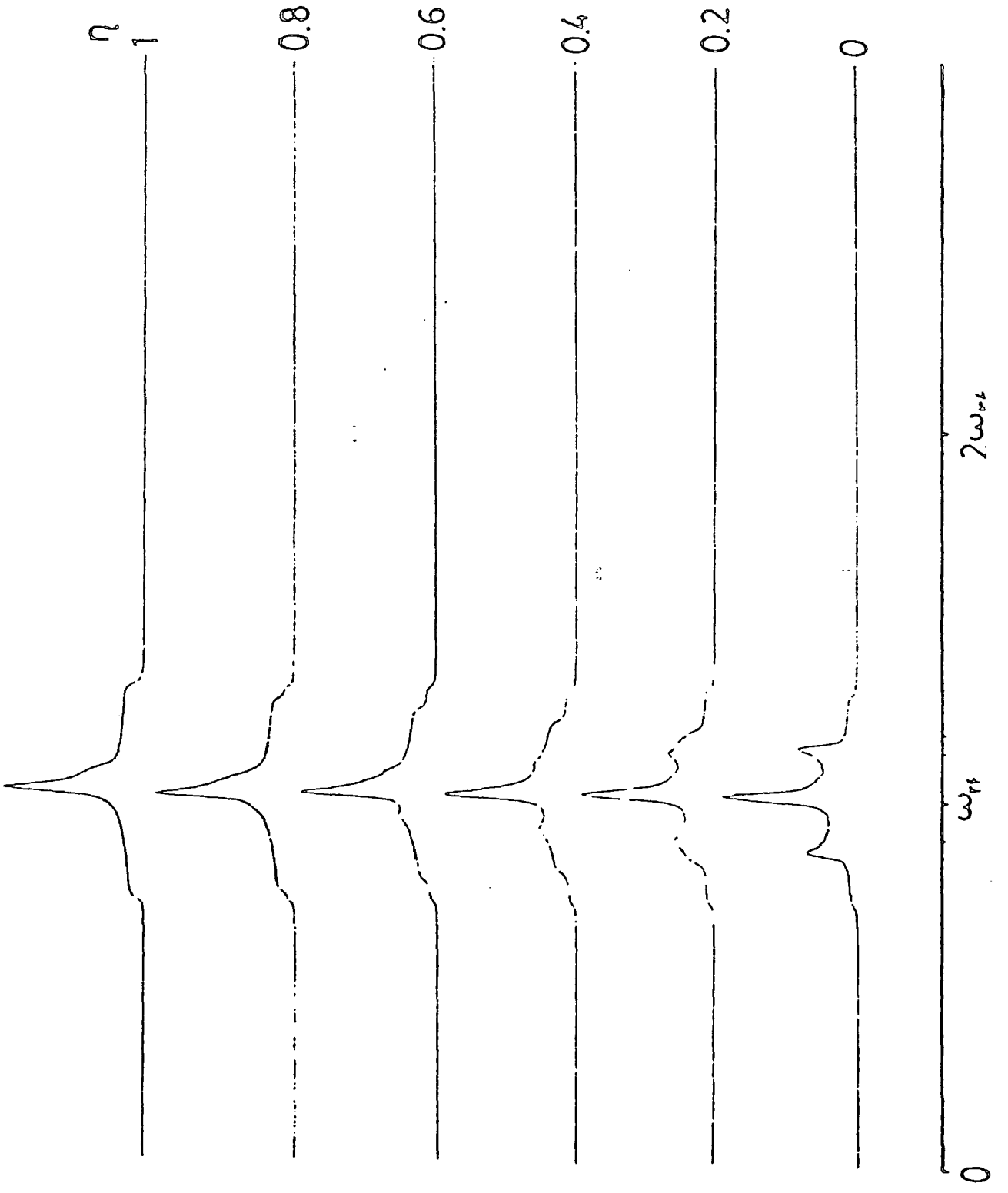
η
1
0.8
0.6
0.4
0.2
0
0
ω_{pe}
$2\omega_{pe}$

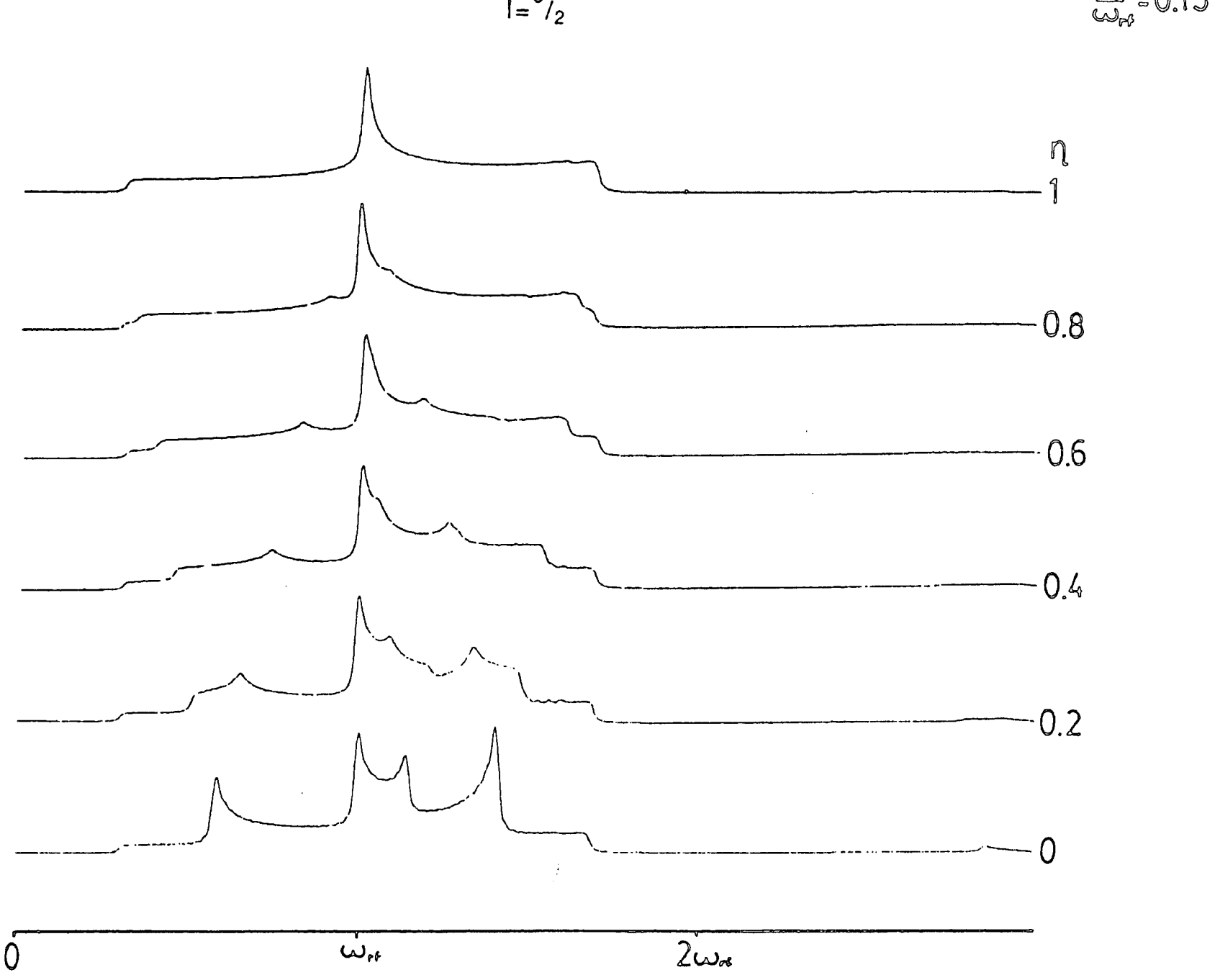
η
1
0.8
0.6
0.4
0.2
0
0
ω_{rf}
$2\omega_{rf}$

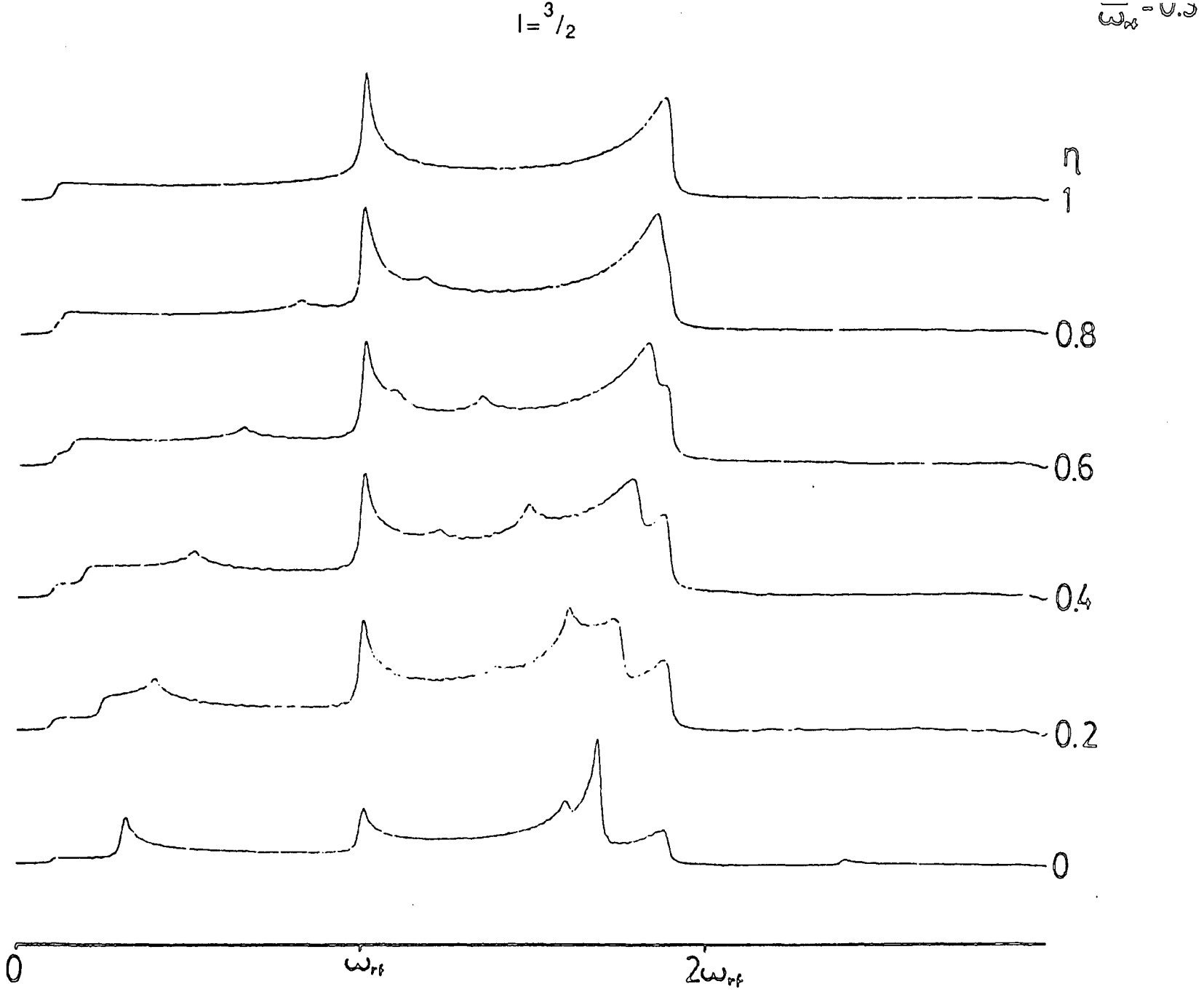
I = 3/2
η
1
0.8
0.6
0.4
0.2
0
0
ω_rf
2ω_rf

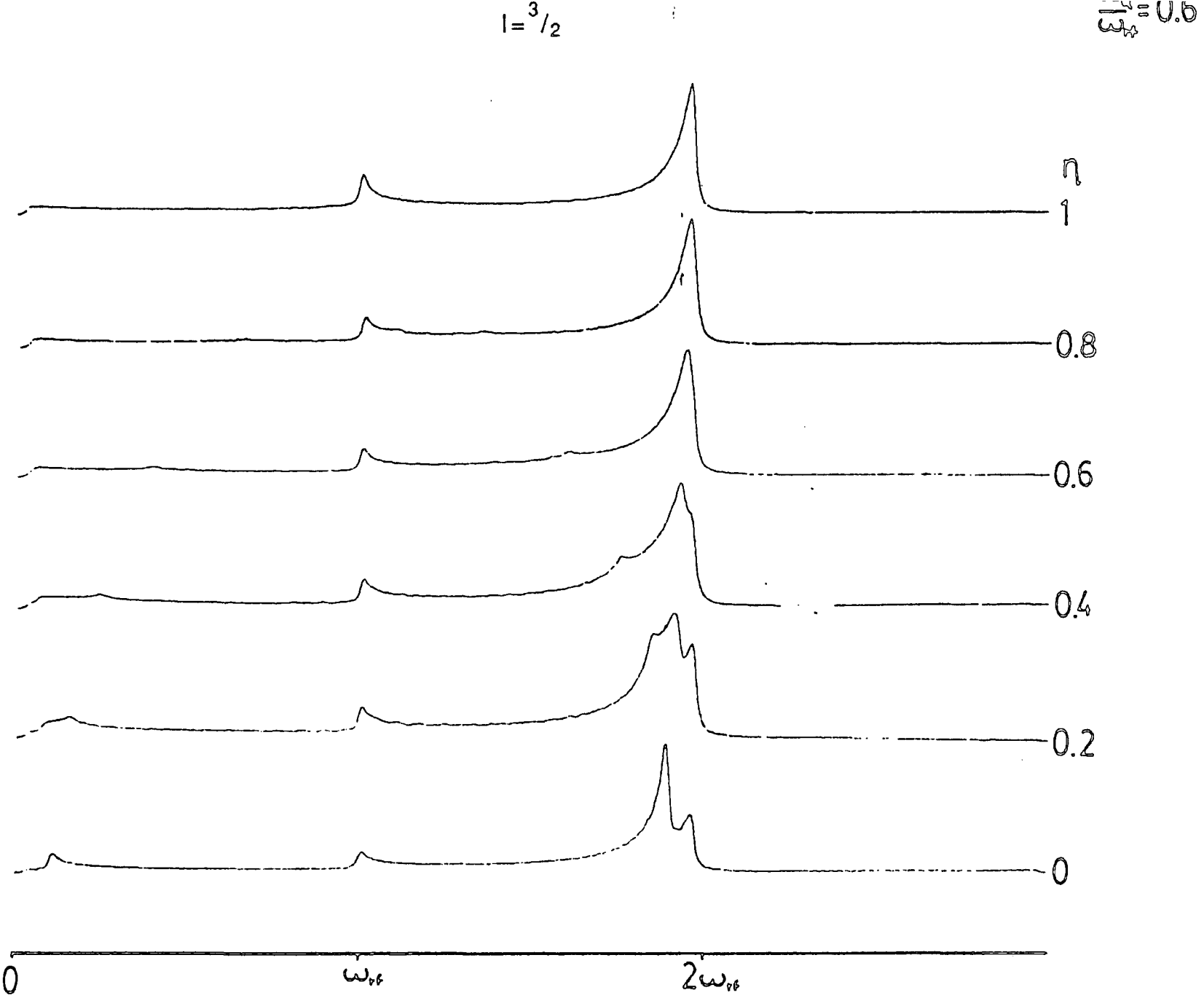
I = 3/2
η
1
0.8
0.6
0.4
0.2
0
0
ω
2ω

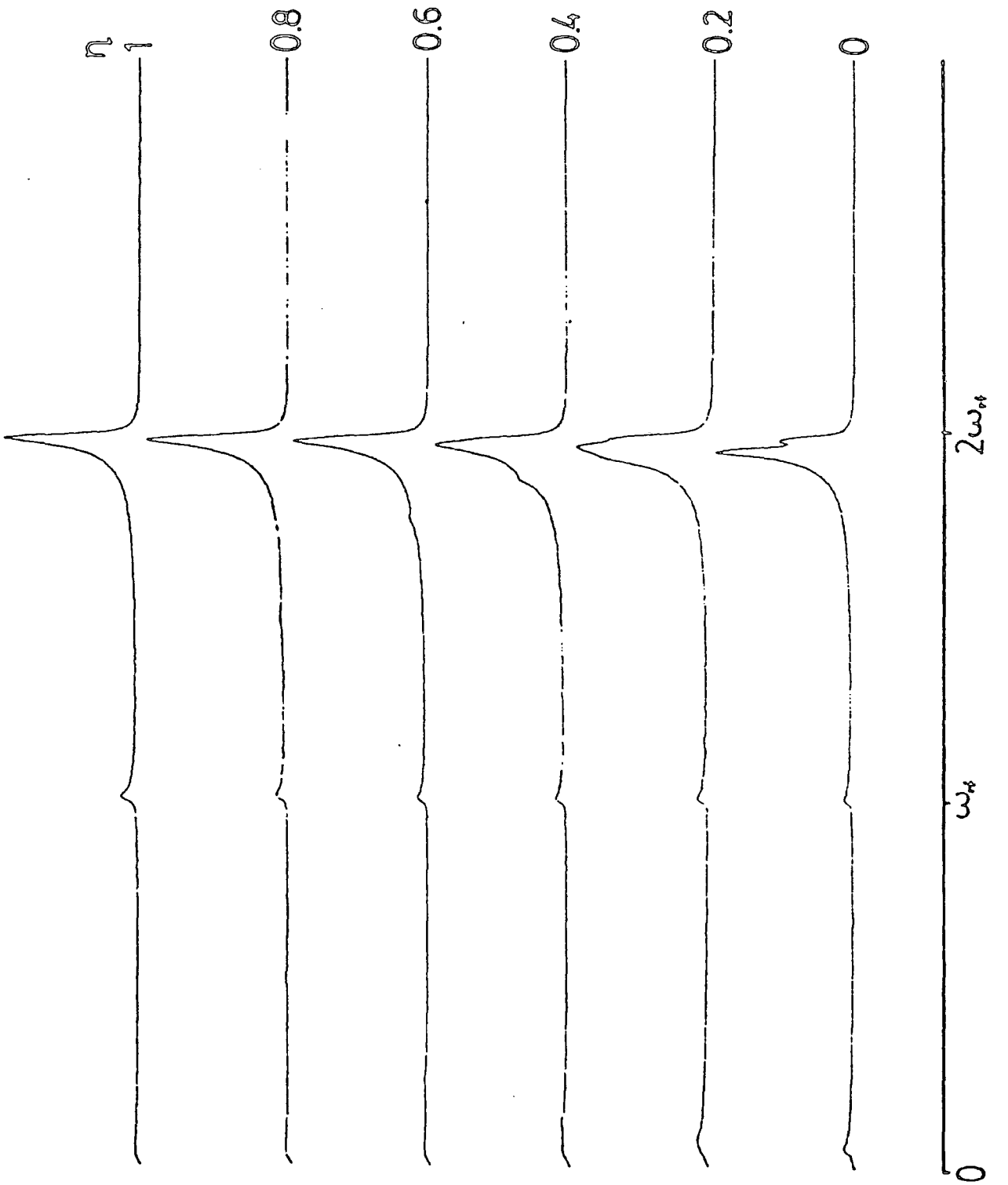
η
1
0.8
0.6
0.4
0.2
0
0
ω_{rf}
$2\omega_{rf}$

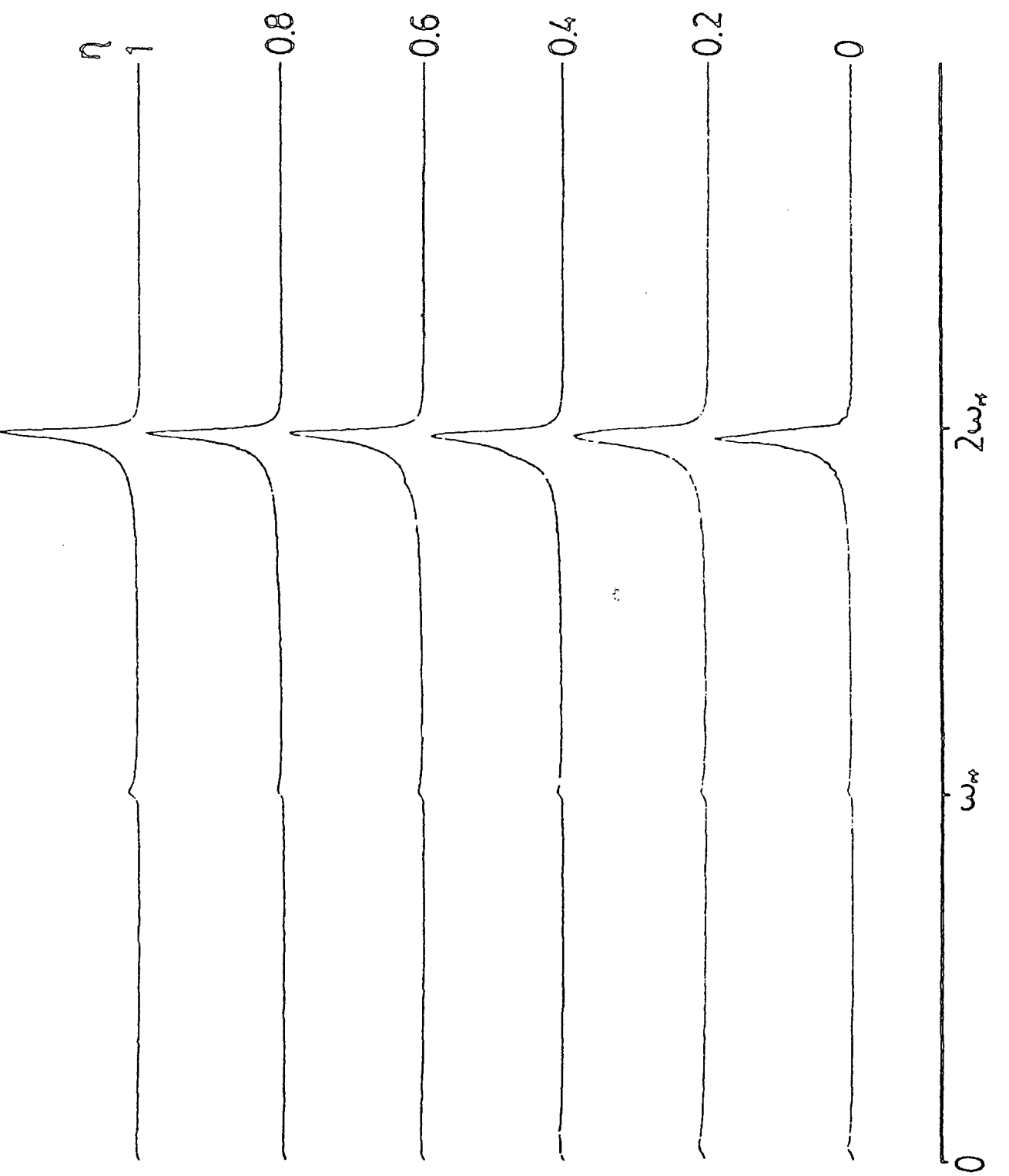
η
1
0.8
0.6
0.4
0.2
0
0
ω_s
$2\omega_s$

I = 1/2

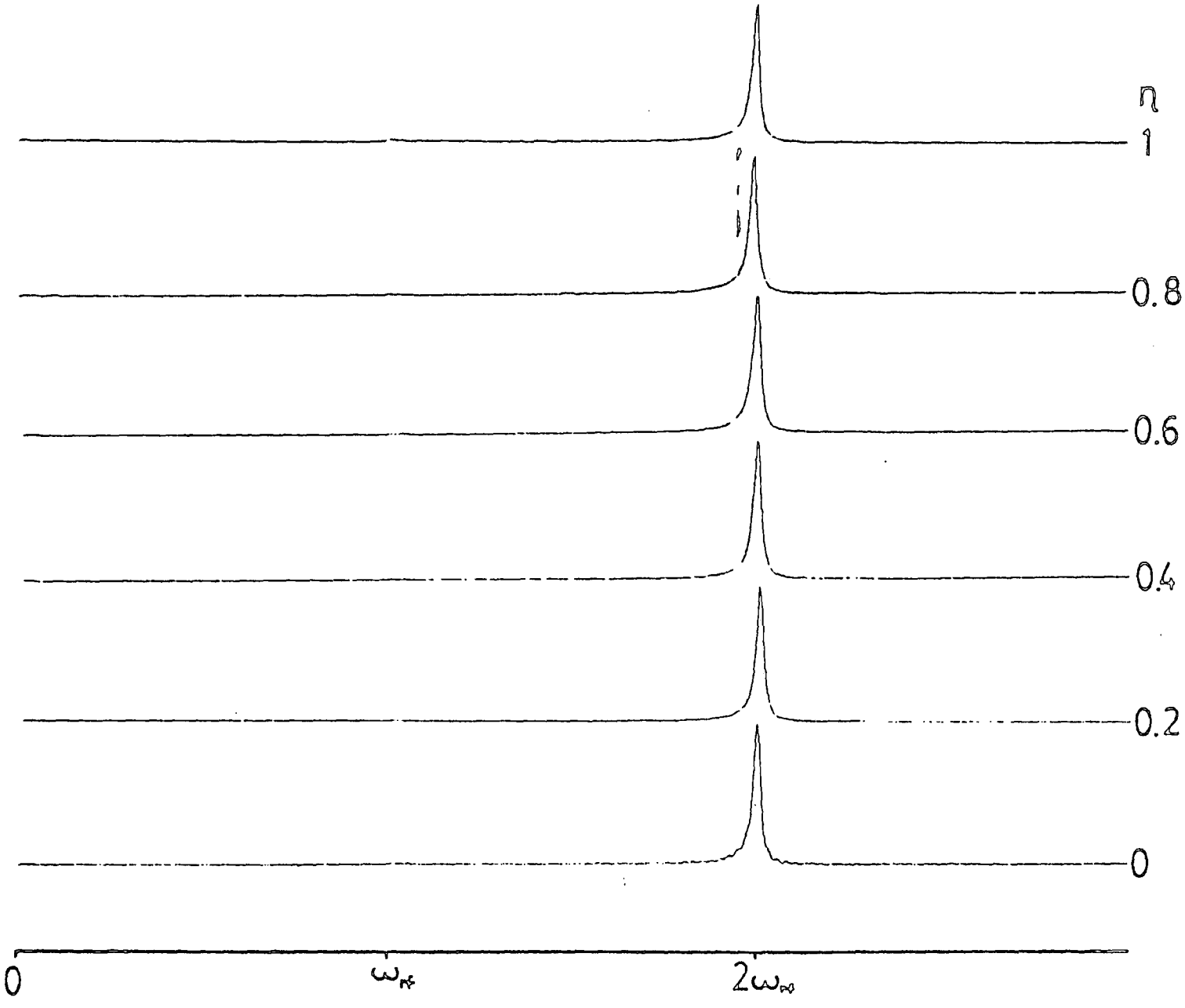

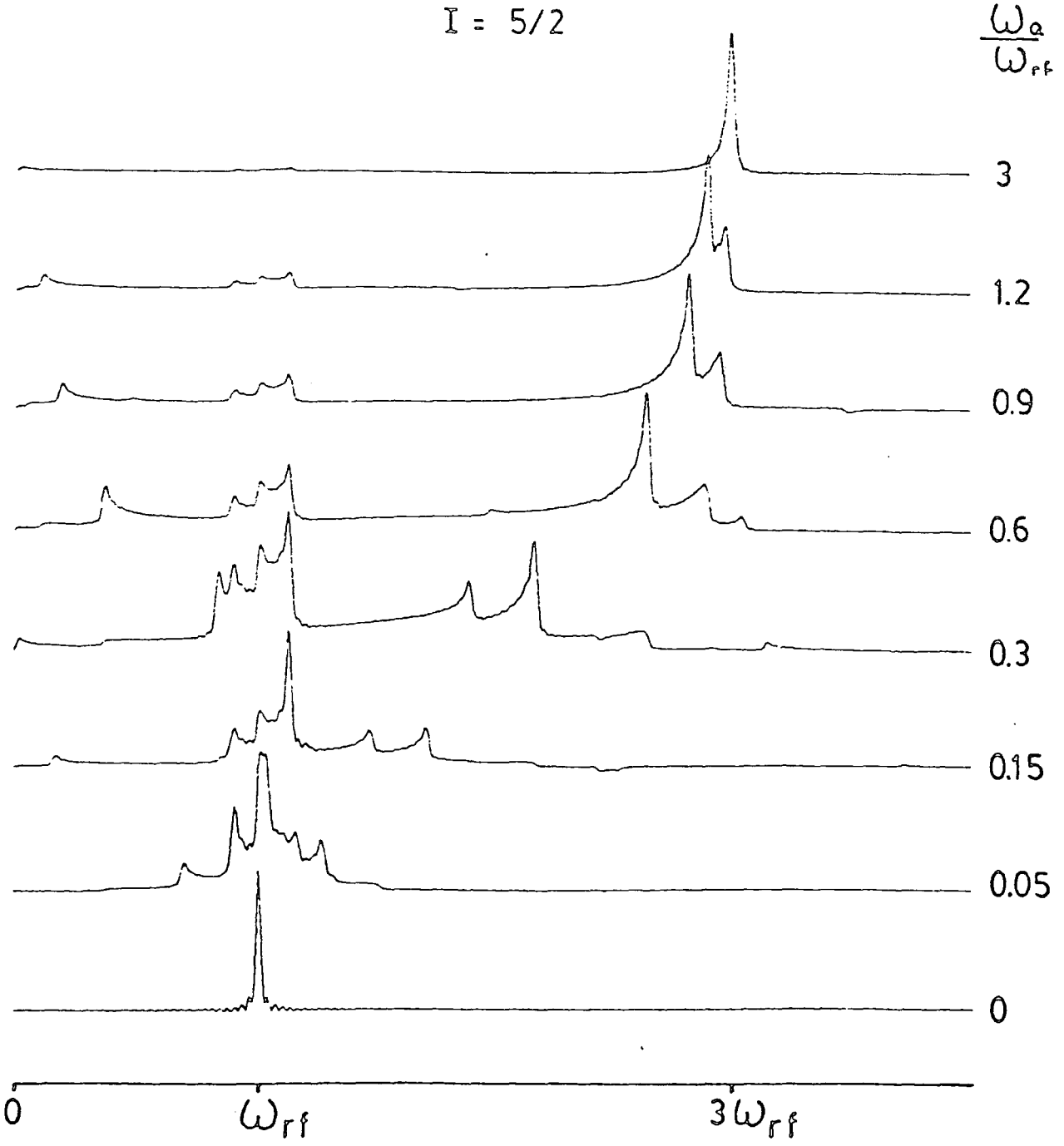
I = 5/2
ωa/ωrf
3
1.2
0.9
0.6
0.3
0.15
0.05
0
0
ωrf
3ωrf

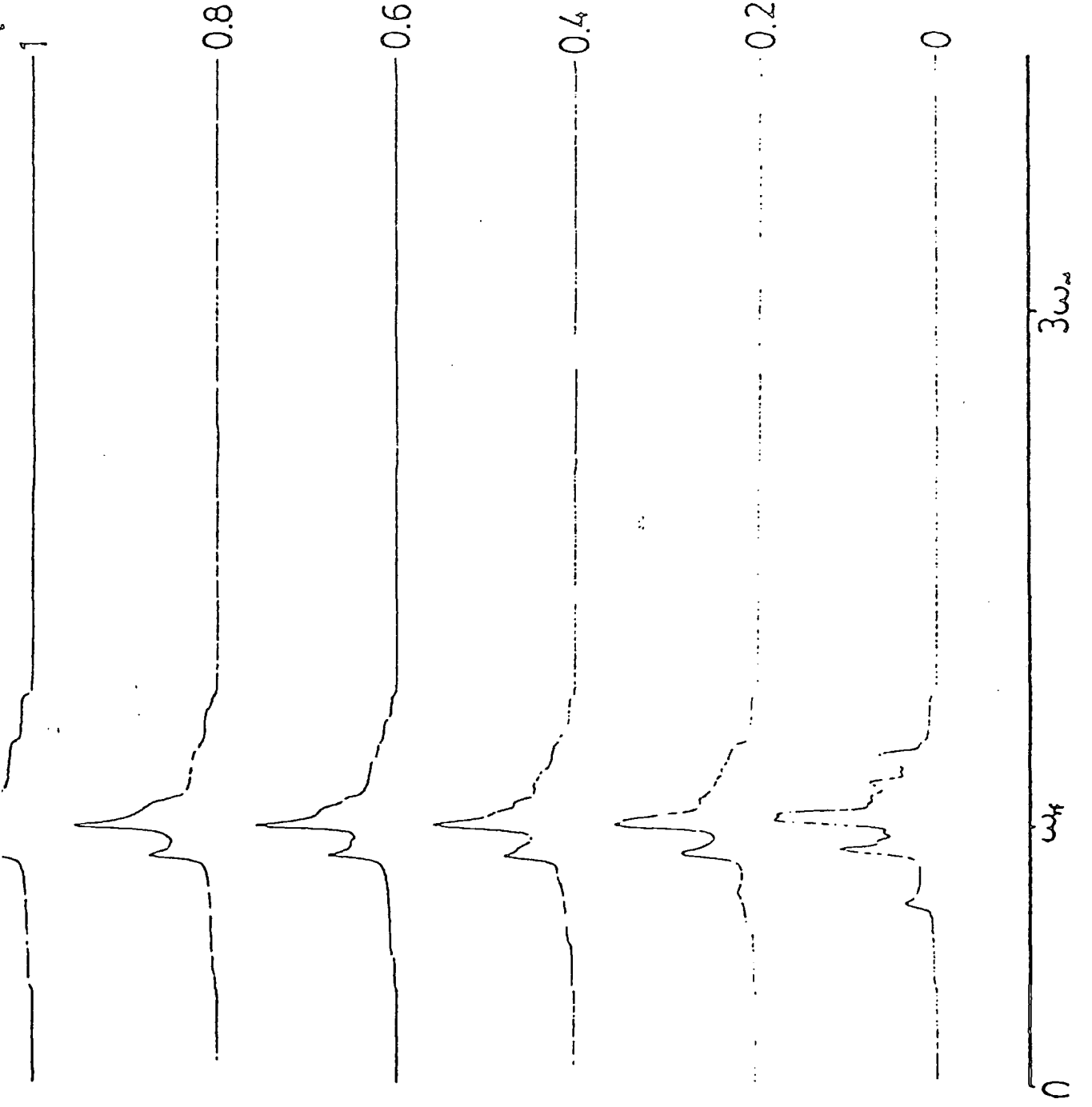
1
0.8
0.6
0.4
0.2
0
0
ω_4
$3\omega_4$

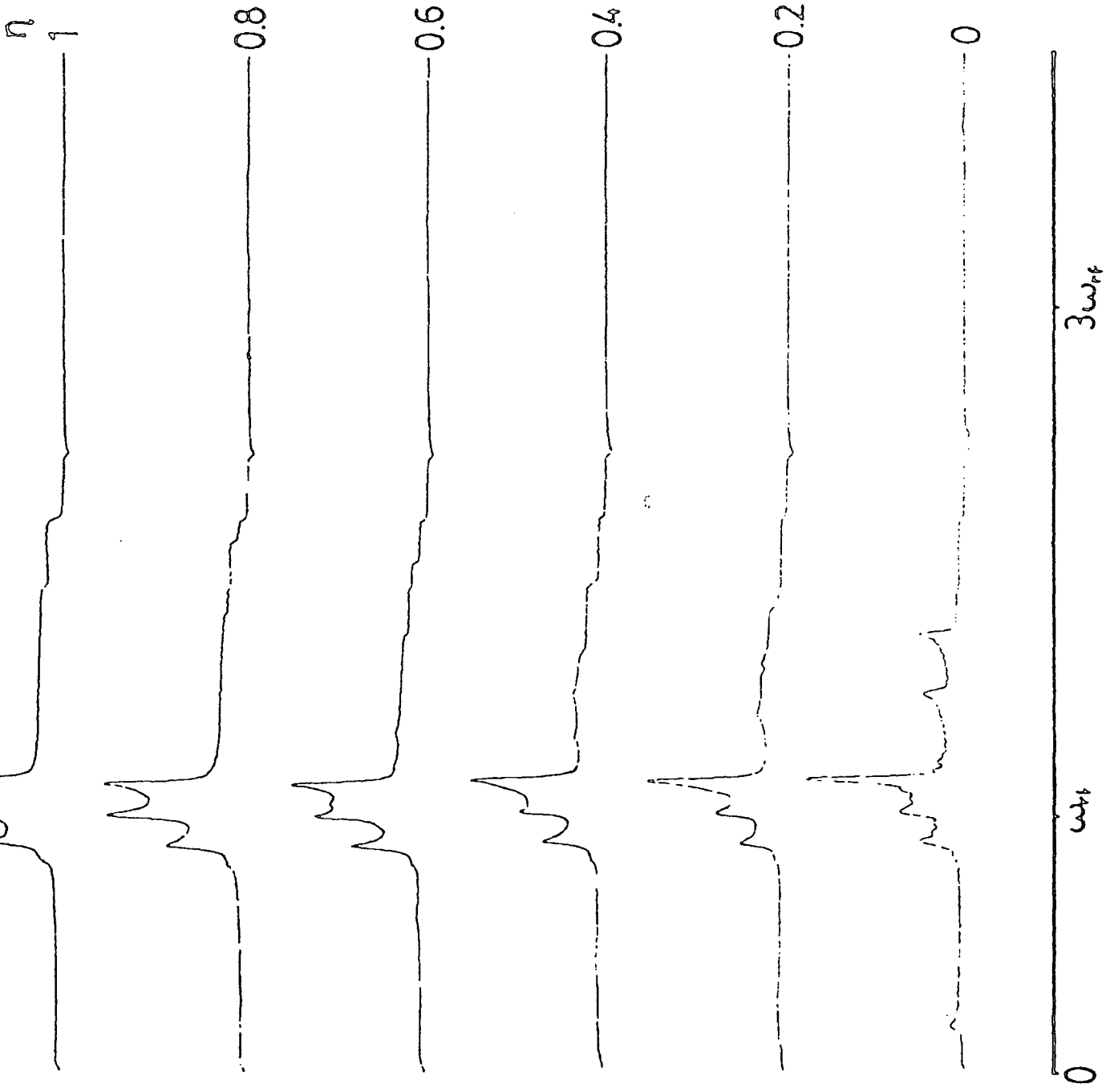
η
1
0.8
0.6
0.4
0.2
0
0
ω₄
3ω₄₄

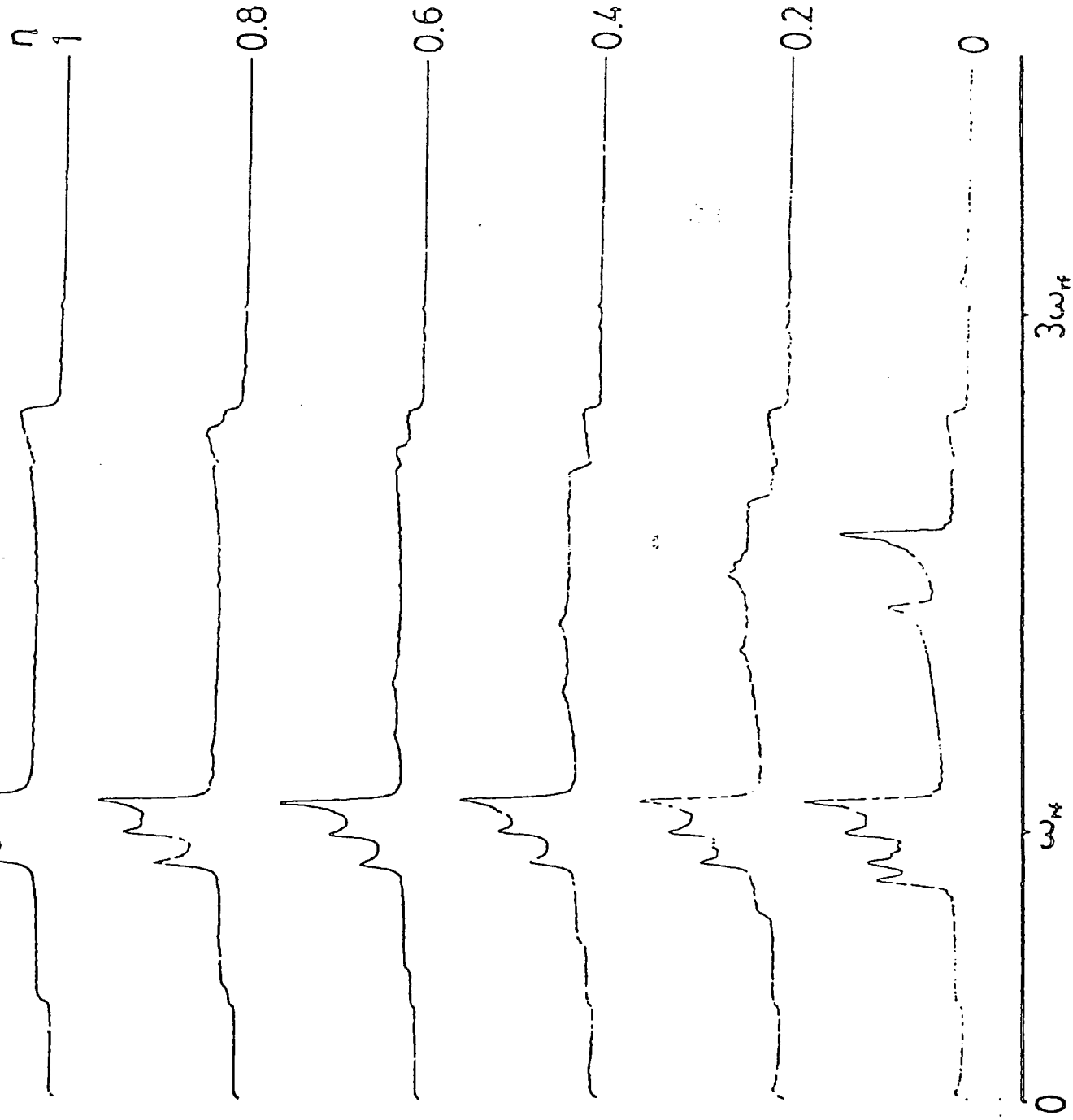
η
1
0.8
0.6
0.4
0.2
0
0
ω_{rf}
$3\omega_{rf}$

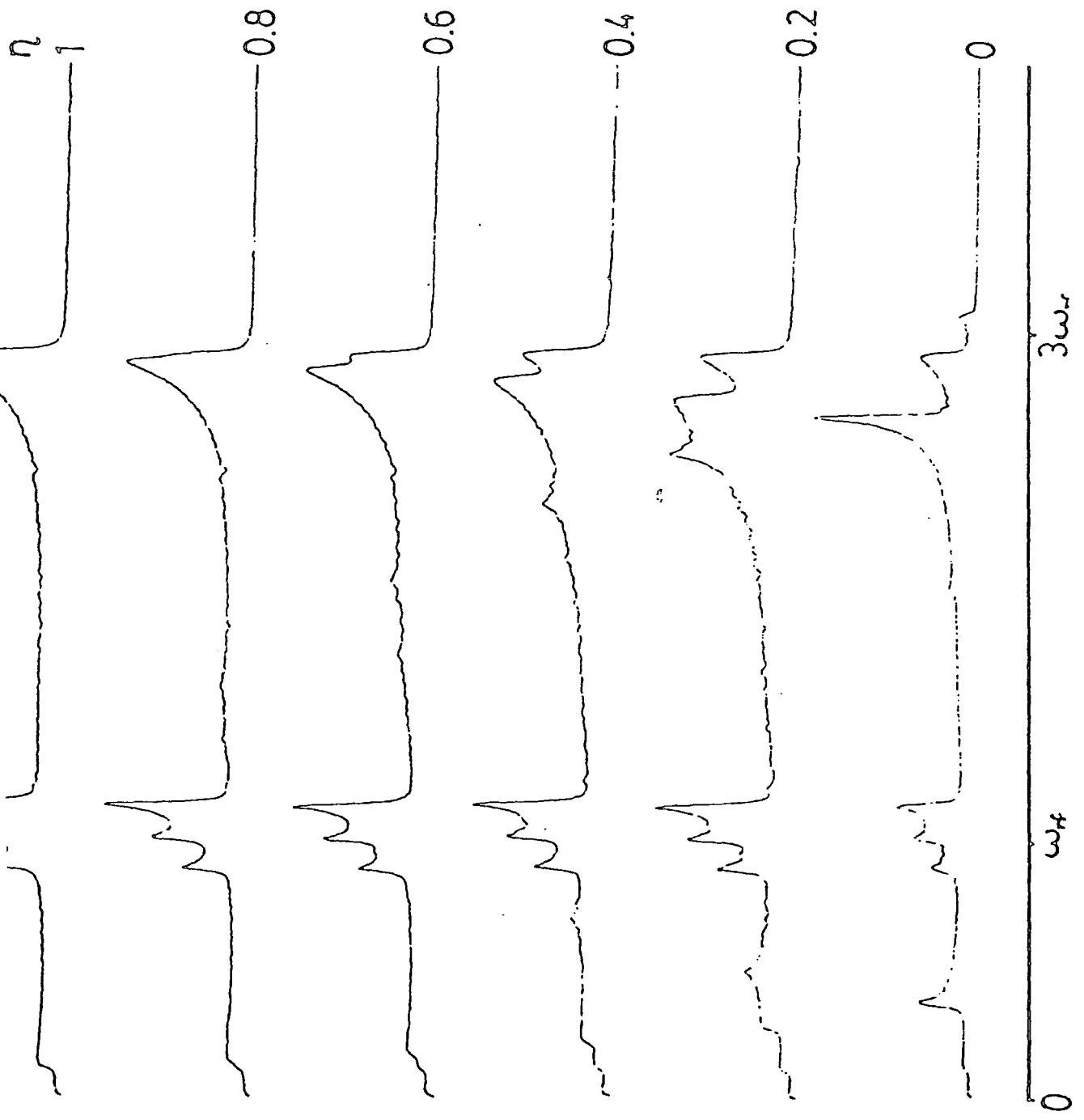
η
1
0.8
0.6
0.4
0.2
0
0
ω_r
3ω_r

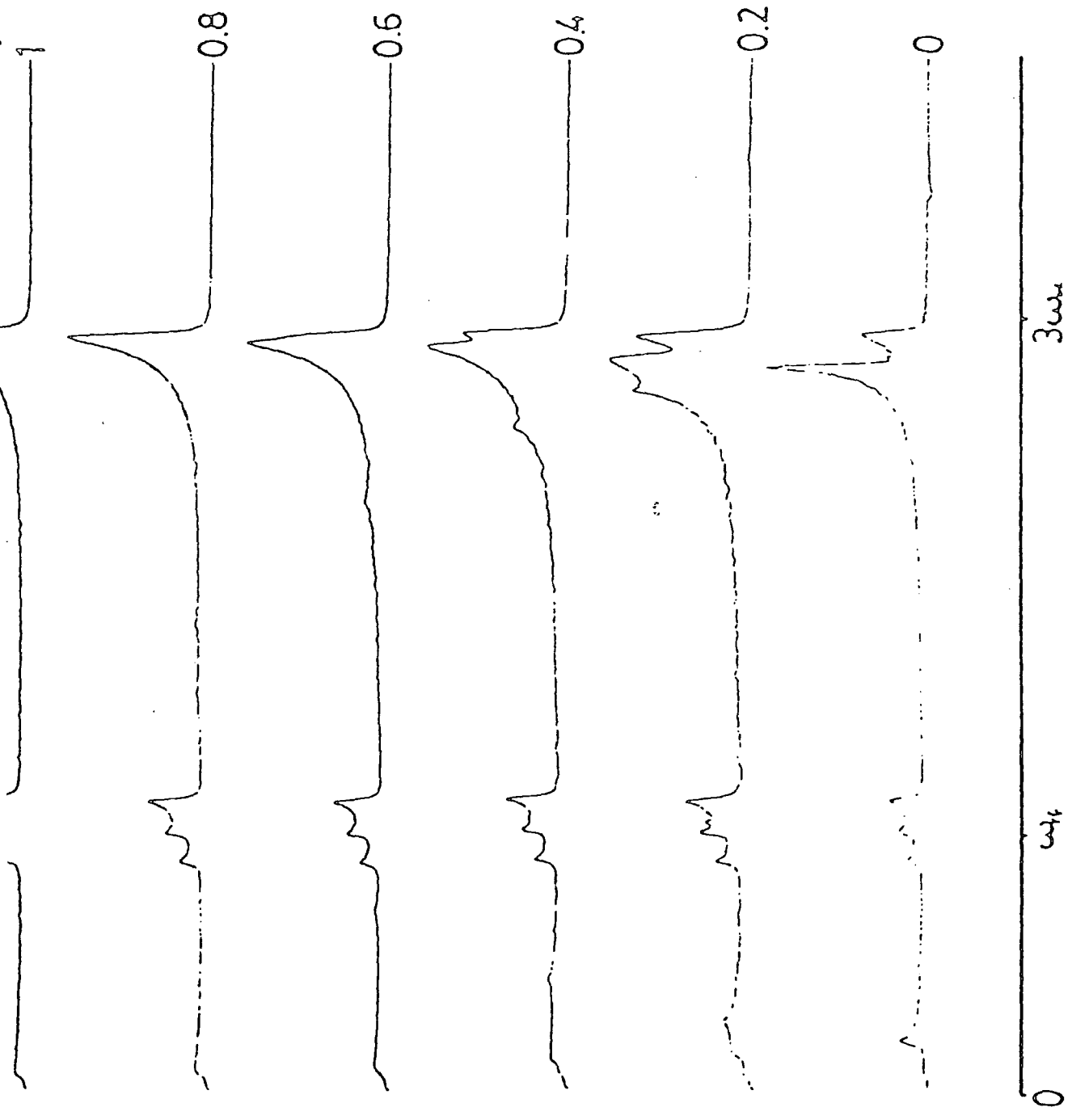
1
0.8
0.6
0.4
0.2
0
0
3ω₄
ω₄

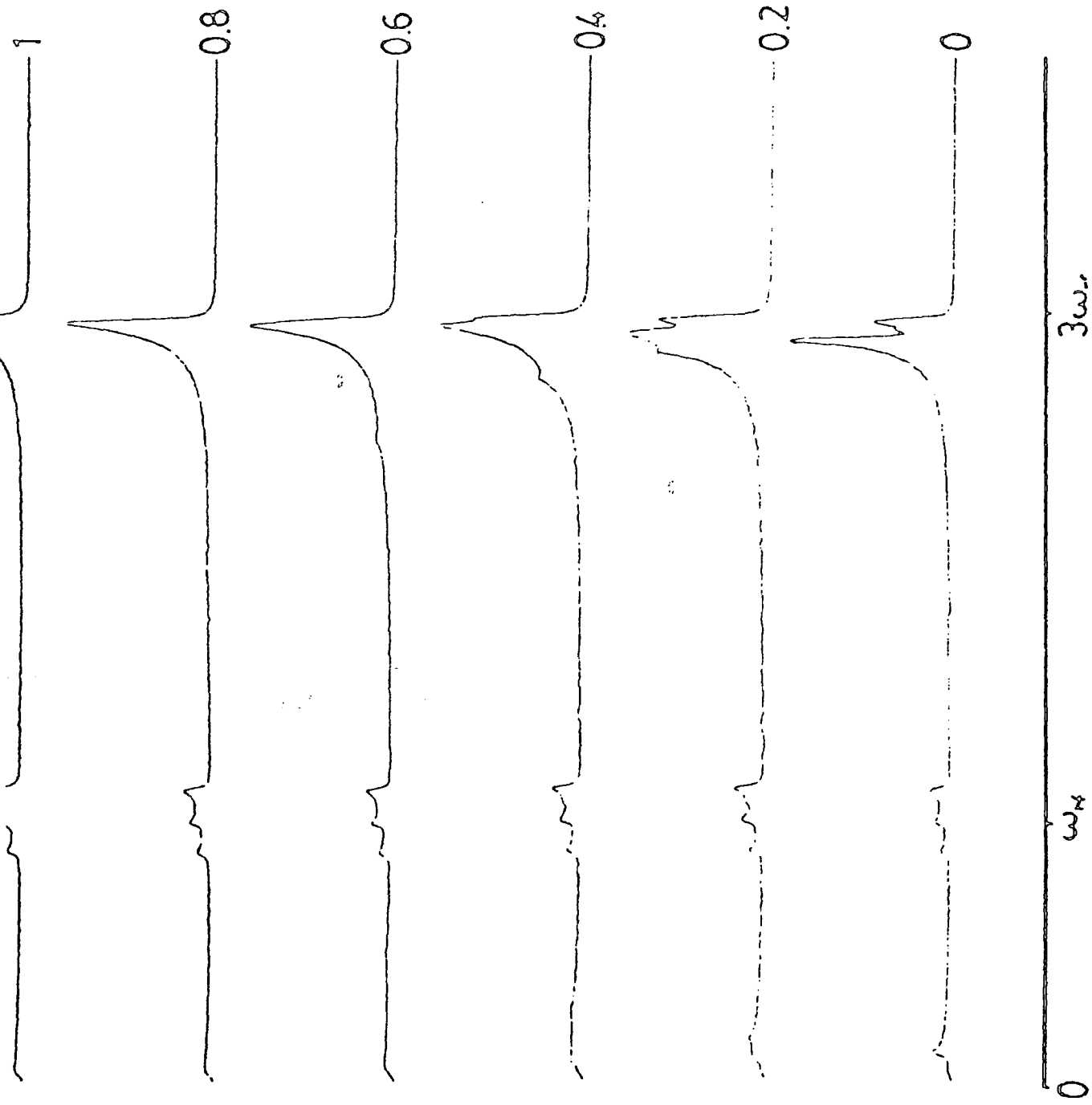
1
0.8
0.6
0.4
0.2
0
0
ω_x
$3\omega_x$

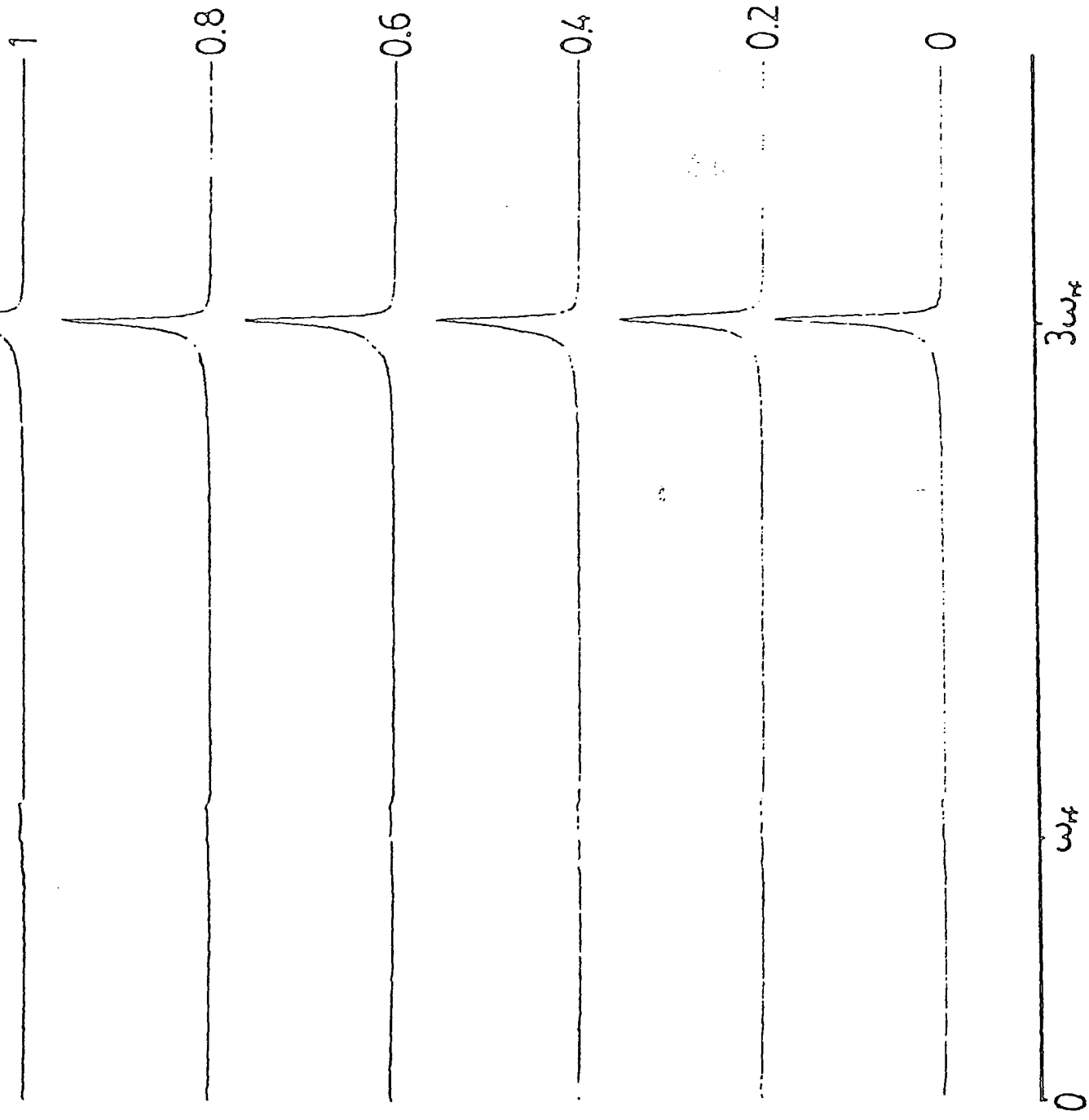
1
0.8
0.6
0.4
0.2
0
$3\omega_H$
ω_H
0

APPENDIX B

Investigation of the effect of the CPMG pulse sequence on a spin $I=^{3}/_{2}$ system using the density matrix formalism.

The following simplifying assumptions are made:

(1) The only interaction that the system is subjected to in the rotating frame is the r.f. field, $\hat{H}_{rf}$. Since the total Hamiltonian is of the form: $\hat{H}_T = \hat{H}_Z + \hat{H}_Q + \hat{H}_\Delta + \hat{H}_{rf}$ this assumption implies that evolution under the influence of the Zeeman, Quadrupole and Chemical Shift Hamiltonians must be negligible for the duration of the pulse. Thus, Wigner rotation matrices may be used to predict the effect of r.f. pulses. In this application, the Euler angles correspond to the characteristic flip angle, β, and the phase of the pulse with respect to the y-axis in the rotating reference frame, α. Thus, the density matrix following a β^o_α pulse, $\hat{\rho}^+$, is given in terms of the density matrix existing before the pulse, $\hat{\rho}^-$, such that[1,2,3]:

$$\hat{\rho}^+ = \mathcal{D}_{m'm}(\alpha,\beta,-\alpha)\hat{\rho}^- \mathcal{D}^\dagger_{m'm}(\alpha,\beta,-\alpha) \qquad (B.1)$$

where $\dagger$ denotes the complex adjoint matrix.

(2) The magnetic field is so large that the quadrupole interaction may be treated as a first-order perturbation.

(3) Dipolar and chemical shift interactions may be neglected with respect to the quadrupolar interaction. Thus the crucial point is that $\omega_{rf} >> \omega_Q$.

(4) The pulse sequence is applied to a static sample.

Initially, however, it is necessary to ascertain the mode of time-evolution for each element in the density matrix after perturbation by a r.f. pulse.

In the laboratory frame, the equation of motion of a particular element $\hat{\rho}_{ij}$ is given by[2]:

$$\frac{d\hat{\rho}_{ij}}{dt} = \frac{-i}{\hbar}[\hat{H},\hat{\rho}]_{ij} \qquad (B.2)$$

The Hamiltonian, $\hat{H}$, may be considered to consist of two types of term. The first, $\hat{H}_o$, is a large time-independent component representing the interaction of the spin angular momentum with the static field, B_o. The second, $\hat{H}_{int}$, is a much smaller component containing all the perturbing Hamiltonians. B_o is large in the sense that $||\hat{H}_o|| >> ||\hat{H}_{int}||$

Thus, $$\frac{d\hat{\rho}_{ij}}{dt} = \frac{-i}{\hbar} [\hat{H}_o + \hat{H}_{int}, \hat{\rho}]_{ij} \qquad (B.3)$$

Since $||\hat{H}_o|| >> ||\hat{H}_{int}||$, it is convenient to transform to the interaction representation which is the quantum mechanical equivalent of the rotating reference frame. Exponential operators are used to define this representation where the effects of $\hat{H}_o$ vanish. The time evolution of the density matrix is caused only by $\hat{H}_{int}$ and is thus comparatively slow[4].

$$\hat{\rho}_{ij} = \exp(-i\hat{H}_o t/\hbar)\hat{\rho}^* \exp(i\hat{H}_o t/\hbar) \qquad (B.4)$$

$$\hat{H}_{int} = \exp(-i\hat{H}_o t/\hbar)\hat{H}^*_{int} \exp(i\hat{H}_o t/\hbar) \qquad (B.5)$$

The equation of motion of the spin density matrix in the interaction representation is given by:

$$\frac{d\hat{\rho}^*_{ij}}{dt} = \frac{-i}{\hbar} [\hat{H}^*_{int}, \hat{\rho}^*_{ij}]_{ij} \qquad (B.6)$$

The commutation relationship may be expanded in the interaction representation using the eigenstates of $\hat{H}_o$ as a basic set of states[3]:

$$\frac{-i}{\hbar} [\hat{H}^*_{int}, \hat{\rho}^*]_{ij} = \frac{-i}{\hbar} \sum_k \langle i|\hat{H}^*_{int}|k\rangle\langle k|\hat{\rho}^*|j\rangle - \langle i|\hat{\rho}^*|k\rangle\langle k|\hat{H}^*_{int}|j\rangle \qquad (B.7)$$

Now, $\langle n|\hat{H}^*_{int}|m\rangle = \exp(i(E_n - E_m)t/\hbar)\langle n|\hat{H}_{int}|m\rangle$ where $|n\rangle$ and $|m\rangle$ are eigenstates of $\hat{H}_o$.

Thus,

$$\frac{-i}{\hbar}[\hat{H}^{*}_{int},\hat{\rho}^{*}]_{ij} = \frac{-i}{\hbar}\sum_{k}\exp\{it(E_i-E_k)/\hbar\}\langle i|\hat{H}_{int}|k\rangle\langle k|\hat{\rho}^{*}|j\rangle$$

$$- \exp\{it(E_k-E_j)/\hbar\}\langle i|\hat{\rho}^{*}|k\rangle\langle k|\hat{H}_{int}|j\rangle \qquad (B.8)$$

Since the variation of $\hat{\rho}^{*}$ with time is slow, it is reasonable to assume that the contributions of terms with rapidly varying exponentials average approximately to zero[4], and to neglect them in comparison with the secular terms for which $E_n=E_m$. This is precisely equivalent to retaining in the perturbation Hamiltonian, $\hat{H}_{int}$, the part that commutes with $\hat{H}_o$ and corresponds to a first-order approximation. In this case, the eigenstates $|n\rangle$ and $|m\rangle$ are simultaneously eigenstates of $\hat{H}_o$ and $\hat{H}_{int}$. When the full quadrupole Hamiltonian is used, there are terms present which do not commute with the Zeeman Hamiltonian, and in the interaction representation, the non-secular parts of $\hat{H}_Q$ are time dependent.

The Spin-$^3/_2$ Thermal Equilibrium Density Matrix[3]

The density matrix operator for the spin system at thermal equilibrium, at a temperature, T, using the high temperature approximation is given by

$$\hat{\rho}_{eq} = \frac{(\underset{\sim}{1}-\hat{H}/kT)}{Tr(\underset{\sim}{1})} \qquad (B.9)$$

The Hamiltonian has the form (including only secular terms):

$$\hat{H} = \gamma\hbar B_o\hat{I}_z + \frac{e^2qQ\hbar}{8I(2I-1)}\ (3\cos^2\beta-1)(3\hat{I}_z^2-\hat{I}^2) \qquad (B.10)$$

$$= -\gamma\hbar B_o\hat{I}_z + \frac{\Omega_Q\hbar}{3}\ (3\cos^2\beta-1)(3\hat{I}_z^2-\hat{I}^2) \qquad (B.10a)$$

where $\Omega_Q = 3e^2qQ/8I(2I-1)$ and β is the appropriate Euler angle, equal to the polar angle θ of the principal axis system in the laboratory frame.

When the relationships $\varepsilon = \frac{\gamma\hbar B_o}{kT}$ and $\tau = \frac{\Omega_Q\hbar(3\cos^2\theta-1)}{3kT}$

are defined, the thermal equilibrium density matrix, in the Zeeman basis set

($|1\rangle = |\hat{I}_z = +^3/2\rangle$, $|2\rangle = |\hat{I}_z = +^1/2\rangle$, $|3\rangle = |\hat{I}_z = -^1/2\rangle$, $|4\rangle = |\hat{I}_z = -^3/2\rangle$) is given by:

$$\hat{\rho}_{eq} = \frac{1}{4}\begin{pmatrix} 1+\frac{3\varepsilon}{2}-3\tau & 0 & 0 & 0 \\ 0 & 1+\frac{\varepsilon}{2}+3\tau & 0 & 0 \\ 0 & 0 & 1+\frac{\varepsilon}{2}+3\tau & 0 \\ 0 & 0 & 0 & 1-\frac{3\varepsilon}{2}-3\tau \end{pmatrix} \quad \text{(B.11)}$$

However $\varepsilon >> \tau$ is valid for the high-field case, and the terms of order τ may be neglected from the calculation.

Evolution under the first-order quadrupolar Hamiltonian

In this case, non-secular terms may be neglected and the equation of motion of element $\hat{\rho}_{ij}$ is given by:

$$\frac{d\hat{\rho}_{ij}}{dt} = \frac{i}{\hbar}[\hat{\rho},\hat{H}]_{ij} = \frac{i}{\hbar}\sum_k \langle i|\hat{\rho}|k\rangle\langle k|\hat{H}_{int}|j\rangle - \langle i|\hat{H}_{int}|k\rangle\langle k|\hat{\rho}|j\rangle \quad \text{(B.12)}$$

where the * denoting the interaction representation has been dropped. $\hat{H}_{int}$ in this case is $\frac{\Omega_Q\hbar}{3}(3\cos^2\theta-1)$, the chemical shift, dipolar and offset Hamiltonians being neglected.

$$\begin{aligned}
\dot{\hat{\rho}}_{12} &= -2i\Omega_Q(3\cos^2\theta-1)\hat{\rho}_{12} & \dot{\hat{\rho}}_{21} &= 2i\Omega_Q(3\cos^2\theta-1)\hat{\rho}_{21} \\
\dot{\hat{\rho}}_{34} &= 2i\Omega_Q(3\cos^2\theta-1)\hat{\rho}_{34} & \dot{\hat{\rho}}_{43} &= -2i\Omega_Q(3\cos^2\theta-1)\hat{\rho}_{43} \\
\dot{\hat{\rho}}_{13} &= -2i\Omega_Q(3\cos^2\theta-1)\hat{\rho}_{13} & \dot{\hat{\rho}}_{31} &= 2i\Omega_Q(3\cos^2\theta-1)\hat{\rho}_{31} \\
\dot{\hat{\rho}}_{24} &= 2i\Omega_Q(3\cos^2\theta-1)\hat{\rho}_{24} & \dot{\hat{\rho}}_{42} &= -2i\Omega_Q(3\cos^2\theta-1)\hat{\rho}_{42}
\end{aligned} \quad \text{(B.13)}$$

$$\dot{\hat{\rho}}_{11} = \dot{\hat{\rho}}_{22} = \dot{\hat{\rho}}_{33} = \dot{\hat{\rho}}_{44} = \dot{\hat{\rho}}_{41} = \dot{\hat{\rho}}_{14} = 0$$

Straightforward integration gives ($\Omega = 2\Omega_Q(3\cos^2\theta-1)$

$$\hat{\rho}_{12}(t) = \hat{\rho}_{12}(0)\exp(-i\Omega t) = \hat{\rho}^*_{21}(t) \qquad \text{(where * denotes complex conjugate in this instance)}$$

$$\hat{\rho}_{34}(t) = \hat{\rho}_{34}(0)\exp(i\Omega t) = \hat{\rho}^*_{43}(t) \qquad \text{(B.14)}$$

$$\hat{\rho}_{13}(t) = \hat{\rho}_{13}(0)\exp(-i\Omega t) = \hat{\rho}^*_{31}(t)$$

$$\hat{\rho}_{24}(t) = \hat{\rho}_{24}(0)\exp(i\Omega t) = \hat{\rho}^*_{42}(t)$$

The other elements do not evolve with time.

Wigner Rotation Matrices

The general rotation matrix for $I=^3/_2$ has the form[3]:

$$D(\alpha,\beta,-\alpha) = \begin{pmatrix} a & -b & c & -d \\ b^* & f & -e & c \\ c^* & e^* & f & -b \\ d^* & c^* & b^* & a \end{pmatrix}, \quad D^\dagger(\alpha,\beta,-\alpha) = \begin{pmatrix} a & b & c & d \\ -b^* & f & e & c \\ c^* & -e^* & f & b \\ -d^* & c^* & -b^* & a \end{pmatrix} \qquad \text{(B.15)}$$

where $a = \cos^3(\beta/2)$

$b = \sqrt{3}\cos^3(\beta/2)\sin(\beta/2)e^{-i\alpha}$

$c = \sqrt{3}\cos(\beta/2)\sin^2(\beta/2)e^{-2i\alpha}$

$d = \sin^3(\beta/2)e^{-3i\alpha}$

$e = [2\cos^2(\beta/2)\sin(\beta/2)-\sin^3(\beta/2)]e^{-i\alpha}$

$f = [\cos^3(\beta/2)-2\cos(\beta/2)\sin^2(\beta/2)]$

where β is the flip angle and α is the phase of the pulse relative to the y-axis.

When a $(\pi/2)_x$ pulse is applied to the thermal equilibrium matrix, $\hat{\rho}_{eq}$, the matrix defined as $\hat{\rho}(o)$ is produced having the elements[3]:

$$
\begin{aligned}
4\hat{\rho}_{11} &= 4\hat{\rho}_{22} = 4\hat{\rho}_{33} = 4\hat{\rho}_{44} = 1 \\
4\hat{\rho}_{12} &= 4\hat{\rho}^{*}_{21} = -4\hat{\rho}_{43} = -4\hat{\rho}^{*}_{34} = -(\sqrt{3}i\varepsilon/2) \\
4\hat{\rho}_{23} &= 4\hat{\rho}^{*}_{32} = -i\varepsilon \\
4\hat{\rho}_{13} &= 4\hat{\rho}^{*}_{31} = 4\hat{\rho}_{24} = 4\hat{\rho}^{*}_{42} = 4\hat{\rho}_{14} = 4\hat{\rho}^{*}_{41} = 0
\end{aligned}
\qquad \text{(B.16)}
$$

which then evolve as shown above. The effect of a π_y pulse on the general density matrix at time t after the $(\pi/2)_x$ pulse is given by:

$$
\frac{1}{4}\begin{pmatrix} 0 & 0 & 0 & -1 \\ 0 & 0 & 1 & 0 \\ 0 & -1 & 0 & 0 \\ 1 & 0 & 0 & 0 \end{pmatrix}\begin{pmatrix} 1 & \frac{-\sqrt{3}i\varepsilon e^{-i\Omega t}}{2} & 0 & 0 \\ \frac{\sqrt{3}i\varepsilon e^{i\Omega t}}{2} & 1 & -i\varepsilon & 0 \\ 0 & i\varepsilon & 1 & \frac{-\sqrt{3}i\varepsilon e^{i\Omega t}}{2} \\ 0 & 0 & \frac{\sqrt{3}i\varepsilon e^{-i\Omega t}}{2} & 1 \end{pmatrix}\begin{pmatrix} 0 & 0 & 0 & 1 \\ 0 & 0 & -1 & 0 \\ 0 & 1 & 0 & 0 \\ -1 & 0 & 0 & 0 \end{pmatrix}
\qquad \text{(B.17)}
$$

$$
= \frac{1}{4}\begin{pmatrix} 1 & \frac{-\sqrt{3}i\varepsilon e^{-i\Omega t}}{2} & 0 & 0 \\ \frac{\sqrt{3}i\varepsilon e^{i\Omega t}}{2} & 1 & -i\varepsilon & 0 \\ 0 & i\varepsilon & 1 & \frac{-\sqrt{3}i\varepsilon e^{i\Omega t}}{2} \\ 0 & 0 & \frac{\sqrt{3}i\varepsilon e^{-i\Omega t}}{2} & 1 \end{pmatrix}
\qquad \text{(B.18)}
$$

It can be seen that the π_y pulse interconverts elements whose time-dependence under the first-order quadrupolar Hamiltonian is in the same sense and thus time evolution under this second-rank tensor interaction is unaffected by the π_y pulse. At a time t after the π_y pulse, the resulting density matrix is

$$
\frac{1}{4}\begin{pmatrix} 1 & \frac{-\sqrt{3}i\varepsilon e^{-2i\Omega t}}{2} & 0 & 0 \\ \frac{\sqrt{3}i\varepsilon e^{2i\Omega t}}{2} & 1 & -i\varepsilon & 0 \\ 0 & i\varepsilon & 1 & \frac{-\sqrt{3}i\varepsilon e^{2i\Omega t}}{2} \\ 0 & 0 & \frac{\sqrt{3}i\varepsilon e^{-2i\Omega t}}{2} & 1 \end{pmatrix}
\qquad \text{(B.19)}
$$

The observable signal $S(t) = \gamma\hbar Tr\ (\hat{\rho}(t)\hat{I}_+)$. Thus at time t following the π_y pulse the signal is given by:

$$\frac{\gamma\hbar}{4}\ Tr\left[\begin{pmatrix} 1 & \frac{-\sqrt{3}i\varepsilon e^{-2i\Omega t}}{2} & 0 & 0 \\ \frac{\sqrt{3}i\varepsilon e^{2i\Omega t}}{2} & 1 & -i\varepsilon & 0 \\ 0 & i\varepsilon & 1 & \frac{-\sqrt{3}i\varepsilon e^{2i\Omega t}}{2} \\ 0 & 0 & \frac{\sqrt{3}i\varepsilon e^{-2i\Omega t}}{2} & 1 \end{pmatrix}\begin{pmatrix} 0 & \sqrt{3} & 0 & 0 \\ 0 & 0 & 2 & 0 \\ 0 & 0 & 0 & \sqrt{3} \\ 0 & 0 & 0 & 0 \end{pmatrix}\right] \qquad \text{(B.20)}$$

$$\text{Thus, } S(2t) = \frac{\gamma\hbar i\varepsilon}{4}(2+3\cos 2\Omega t) \qquad \text{(B.21)}$$

$$\text{and} \qquad S_y(2t) = \frac{\gamma\hbar\varepsilon}{4}(2+3\cos 2\Omega t) \qquad \text{(B.22)}$$

The presence of a time-independent contribution and the absence of an echo are consistent with previous work[5,6,7] concerning the application of two-pulse sequences $\{(\pi/2)_x - t_1 - \phi_x - t_2$ and $(\pi/2)_x - t_1 - \phi_y - t_2\}$ to half-integer spin quadrupolar nuclei.

Generalisation of the above expression to that expected for the n^{th} echo and the inclusion of Lorentzian relaxation terms for both the central and non-central transition leads to:

$$S_y(2nt) = \frac{\gamma\hbar\varepsilon}{4}\ [2\exp(^{-2nt}/_{T_2}) + 3\exp(^{-2nt}/_{T_2'})\cos 2n\Omega t] \qquad \text{(B.23)}$$

where T_2 and T_2' are relaxation times associated with the central and non-central transitions respectively. The above equation indicates an unmodulated contribution and one modulated at a frequency $^{\Omega}/_{2\pi}$. The time is only defined at discrete points of t and so the modulation will only be observed

if the frequency of the modulation is small with respect to the sampling frequency. However, given the typical sampling frequency of 1.75 kHz, it was not surprising to observe an absence of modulation even for modest values of the quadrupole coupling constant. Absence of modulation would also result if T_2' were much shorter than T_2 such that the intensity of the non-central transition contribution was negligible before the application of the first π pulse.

Fourier Transformation of the signal indicated in equation B.23 in the absence of modulation would be expected to yield a peak at zero frequency characterised by a line-width at half height of $^1/_{\pi T_2}$. Simplistically, the T_2 value may be considered as the spin-spin relaxation time constant of the central transition, although it is to be expected that the precise meaning will be a function of the extent to which the non-central transitions are excited. Further consideration reveals that an unmodulated term will result in the expression for the signal generated by a CPMG pulse sequence o any half-integer quadrupolar nucleus, although not in the case of an integer quadrupolar nucleus.

However, for most of the compounds studied, the ratio ν_Q^2/ν_L is non-trivial and second-order effects should be taken into consideration. An identical treatment to that given above using the full quadrupole Hamiltonian, albeit with some dubious assumptions, reveals that the application of the above sequence should still result in the presence of both modulated and unmodulated terms. The relevant modulation frequency in this case is of the order of the Larmor frequency for the compounds studied and so no modulation would be expected under the experimental conditions used.

REFERENCES - APPENDIX B

1. E.P. Wigner, "Group Theory and its Applications.

2. C.P. Slichter, "Principles of Magnetic Resonance", Ed.2, Springer series on Solid State Science, Volume 1, Springer-Verlag (1978).

3. G. Hoatson, Ph.D. Thesis, UEA (1980).

4. A. Abragam, "The Principles of Nuclear Magnetism", Oxford University Press, London and New York (1961).

5. I. Soloman, Phys.Rev., 110, 61 (1958).

6. I.D. Weisman and L.H. Bennet, Phys.Rev., 181, 1341 (1969).

7. P.A. Osment, Ph.D. Thesis, University of York (1987).

APPENDIX C

The Board of Studies in Chemistry requires that each postgraduate research thesis contains an appendix which lists:

(a) all research colloquia and research seminars and lectures arranged by the Department of Chemistry and Durham University Chemical Society during the author's residence as a postgraduate student;

(b) all research conferences attended and papers presented by the author during the same period;

(c) details of the postgraduate induction course.

UNIVERSITY OF DURHAM

Board of Studies in Chemistry

COLLOQUIA, LECTURES AND SEMINARS GIVEN BY INVITED SPEAKERS 1ST AUGUST 1986 TO 31ST JULY 1987

ALLEN, Prof. Sir G. (Unilever Research) Biotechnology and the Future of the Chemical Industry	13th November 1986
BARTSCH, Dr. R. (University of Sussex) Low Co-ordinated Phosphorus Compounds	6th May 1987
BLACKBURN, Dr. M. (University of Sheffield) Phosphonates as Analogues of Biological Phosphate Esters	27th May 1987
BORDWELL, Prof. F.G. (Northeastern University, U.S.A.) Carbon Anions, Radicals, Radical Anions and Radical Cations	9th March 1987
CANNING, Dr. N.D.S. (University of Durham) Surface Adsorption Studies of Relevance to Heterogeneous Ammonia Synthesis	26th November 1986
CANNON, Dr. R.D. (University of East Anglia) Electron Transfer in Polynuclear Complexes	11th March 1987
CLEGG, Dr. W. (University of Newcastle-upon-Tyne) Carboxylate Complexes of Zinc; Charting a Structural Jungle	28th January 1987
DOPP, Prof. D. (University of Duisburg) Cyclo-additions and Cyclo-reversions Involving Captodative Alkenes	5th November 1986
DORFMULLER, Prof. T. (University of Bielefeld) Rotational Dynamics in Liquids and Polymers	8th December 1986
DODGER, Dr. E.M. (Cranfield Institute of Technology) Alternative Fuels for Transport	12th March 1987
GREENWOOD, Prof. N.N. (University of Leeds) Glorious Gaffes in Chemistry	16th October 1986
HAMER, Dr. M. (I.C.I. Chemicals & Polymer Group) The Role of Organometallics in Advanced Materials	7th May 1987
HEBERSTEY, Dr. P. (University of Nottingham) Demonstration Lecture on Various Aspects of Alkali Metal Chemistry	5th February 1987
HUDSON, Prof. R.F. (University of Kent) Aspects of Organophosphorus Chemistry	17th March 1987
HUDSON, Prof. R.F. (University of Kent) Homolytic Rearrangements of Free Radical Stability	18th March 1987

JARMAN, Dr. M. (Institute of Cancer Research) The Design of Anti Cancer Drugs	19th February 1987
KRESPAN, Dr. C. (E.I. Dupont de Nemours) Nickel(0) and Iron(0) as Reagents in Organofluorine Chemistry	26th June 1987
KROTO, Prof. H.W. (University of Sussex) Chemistry in Stars, between Stars and in the Laboratory	23rd October 1986
LEY, Prof. S.V. (Imperial College) Fact and Fantasy in Organic Synthesis	5th March 1987
MILLER, Dr. J. (Dupont Central Research, U.S.A.) Molecular Ferromagnets; Chemistry and Physical Properties	3rd December 1986
MILNE/CHRISTIE, Dr. A./Mr. S. (International Paints) Chemical Serendipity - A Real Life Case Study	20th November 1986
* NEWMAN, Dr. R. (University of Oxford) Change and Decay: A Carbon-13 CP/MAS NMR Study of Humification and Coalification Processes	4th March 1987
OTTEWILL, Prof. R.H. (University of Bristol) Colloid Science a Challenging Subject	22nd January 1987
PASYNKIEWICZ, Prof. S. (Technical University, Warsaw) Thermal Decomposition of Methyl Copper and its Reactions with Trialkylaluminium	11th May 1987
ROBERTS, Prof. S.M. (University of Exeter) Synthesis of Novel Antiviral Agents	24th June 1987
RODGERS, Dr. P.J. (I.C.I. Billingham) Industrial Polymers from Bacteria	12th February 1987
SCROWSTON, Dr. R.M. (University of Hull) From Myth and Magic to Modern Medicine	6th November 1986
SHEPHERD, Dr. T. (University of Durham) Pteridine Natural Products; Synthesis and Use in Chemotherapy	11th February 1987
THOMSON, Prof. A. (University of East Anglia) Metalloproteins and Magnetooptics	4th February 1987
* WILLIAMS, Prof. R.L. (Metropolitan Police Forensic Science) Science and Crime	27th November 1987
* WONG, Prof. E.H. (University of New Hampshire, U.S.A.) Coordination Chemistry of P-O-P Ligands	29th October 1986
* WONG, Prof. E.H. (University of New Hampshire, U.S.A.) Symmetrical Shapes from Molecules to Art and Nature	17th February 1987

UNIVERSITY OF DURHAM

Board of Studies in Chemistry

COLLOQUIA, LECTURES AND SEMINARS GIVEN BY INVITED SPEAKERS
1ST AUGUST 1987 to 31st JULY 1988

BIRCHALL, Prof. D. (I.C.I. Advanced Materials) Environmental Chemistry of Aluminium	25th April 1988
BORER, Dr. K. (University of Durham Industrial Research Labs.) The Brighton Bomb - A Forensic Science View	18th February 1988
BOSSONS, L. (Durham Chemistry Teachers' Centre) GCSE Practical Assessment	16th March 1988
BUTLER, Dr. A.R. (University of St. Andrews) Chinese Alchemy	5th November 1987
CAIRNS-SMITH, Dr. A. (Glasgow University) Clay Minerals and the Origin of Life	28th January 1988
DAVIDSON, Dr. J. (Herriot-Watt University) Metal Promoted Oligomerisation Reactions of Alkynes	November 1987
GRADUATE CHEMISTS (Northeast Polytechnics and Universities) R.S.C. Graduate Symposium	19th April 1988
GRAHAM, Prof. W.A.G. (University of Alberta, Canada) Rhodium and Iridium Complexes in the Activation of Carbon-Hydrogen Bonds	3rd March 1988
GRAY, Prof. G.W. (University of Hull) Liquid Crystals and their Applications	22nd October 1987
HARTSHORN, Prof. M.P. (University of Canterbury, New Zealand) Aspects of Ipso-Nitration	7th April 1988
HOWARD, Dr. J. (I.C.I. Wilton) Chemistry of Non-Equilibrium Processes	3rd December 1987
LUDMAN, Dr. C.J. (Durham University) Explosives	10th December 1987
McDONALD, Dr. W.A. (I.C.I. Wilton) Liquid Crystal Polymers	11th May 1988
MAJORAL, Prof. J.-P. (Université Paul Sabatier) Stabilisation by Complexation of Short-Lived Phosphorus Species	8th June 1988
MAPLETOFT, Mrs. M. (Durham Chemistry Teachers' Centre) Salters' Chemistry	4th November 1987
NIETO DE CASTRO, Prof. C.A. (University of Lisbon and Imperial College) Transport Properties of Non-Polar Fluids	18th April 1988

OLAH, Prof. G.A. (University of Southern California) New Aspects of Hydrocarbon Chemistry)	29th June, 1988
PALMER, Dr. F. (University of Nottingham) Luminescence (Demonstration Lecture)	21st January 1988
PINES, Prof. A. (University of California, Berkeley, U.S.A.) Some Magnetic Moments	28th April 1988
RICHARDSON, Dr. R. (University of Bristol) X-Ray Diffraction from Spread Monolayers	27th April 1988
ROBERTS, Mrs. E. (SATRO Officer for Sunderland) Talk - Durham Chemistry Teachers' Centre - "Links Between Industry and Schools"	13th April 1988
ROBINSON, Dr. J.A. (University of Southampton) Aspects of Antibiotic Biosynthesis	27th April 1988
ROSE van Mrs. S. (Geological Museum) Chemistry of Volcanoes	29th October 1987
SAMMES, Prof. P.G. (Smith, Kline and French) Chemical Aspects of Drug Development	19th December 1987
SEEBACH, Prof. D. (E.T.H. Zurich) From Synthetic Methods to Mechanistic Insight	12th November 1987
SODEAU, Dr. J. (University of East Anglia) Durham Chemistry Teachers' Centre Lecture: "Spray Cans, Smog and Society"	11th May 1988
SWART, Mr. R.M. (I.C.I.) The Interaction of Chemicals with Lipid Bilayers	16th December 1987
TURNER, Prof. J.J. (University of Nottingham) Catching Organometallic Intermediates	11th February 1988
UNDERHILL, Prof. A. (University of Bangor) Molecular Electronics	25th February 1988
WILLIAMS, Dr. D.H. (University of Cambridge) Molecular Recognition	26th November 1987
WINTER, Dr. M.J. (University of Sheffield) Pyrotechnics (Demonstration Lecture)	15th October 1987

UNIVERSITY OF DURHAM

Board of Studies in Chemistry

COLLOQUIA, LECTURES AND SEMINARS GIVEN BY INVITED SPEAKERS
1ST AUGUST 1988 to 31st JULY 1989

SHMAN, Mr. A. (Durham Chemistry Teachers' Centre) The Chemical Aspects of the National Curriculum	3rd May, 1989
VEYARD, Dr. R. (University of Hull) Surfactants at your Surface	15th March, 1989
YLETT, Prof. B.J. (Queen Mary College, London) Silicon-Based Chips:- The Chemist's Contribution	16th February, 1989
ALDWIN, Prof. J.E. (Oxford University) Recent Advances in the Bioorganic Chemistry of Penicillin Biosynthesis	9th February, 1989
ALDWIN & WALKER, Drs. R.R. & R.W. (Hull University) Combustion: Some Burning Problems	24th November, 1988
OLLEN, Mr. F. (Durham Chemistry Teachers' Centre) Lecture about the use of SATIS in the classroom	18th October, 1988
UTLER, Dr. A.R. (St. Andrews University) Cancer in Linxiam: The Chemical Dimension	15th February, 1989
ADOGAN, Prof. J.I.G. (British Petroleum) From Pure Science to Profit	10th November, 1988
ASEY, Dr. M. (University of Salford) Sulphoxides in Stereoselective Synthesis	20th April, 1989
ATERS & CRESSEY, Mr. D. & T. (Durham Chemistry Teachers' Centre) GCSE Chemistry 1988: "A Coroner's Report"	1st February, 1989
RICH, Dr. D. (University College London) Some Novel Uses of Free Radicals in Organic Synthesis	27th April, 1989
NGWALL, Dr. J. (Ciba Geigy) Phosphorus-containing Amino Acids: Biologically Active Natural and Unnatural Products	18th October, 1988
RINGTON, Dr. R.J. (University of Newcastle-upon-Tyne) Polymetalate Assembly in Organic Solvents	1st March, 1989
EY, Dr. J. (Southampton University) Spectroscopy of the Reaction Path: Photodissociation Raman Spectra of NOCl	11th May, 1989

HALL, Prof. L.D. (Addenbrooke's Hospital, Cambridge) — 2nd February, 1989
NMR - A Window to the Human Body

HARDGROVE, Dr. G. (St. Olaf College, U.S.A.) — December, 1988
Polymers in the Physical Chemistry Laboratory

HARWOOD, Dr. L. (Oxford University) — 25th January, 1988
Synthetic Approaches to Phorbols Via Intramolecular Furan Diels-Alder Reactions: Chemistry under Pressure

JÄGER, Dr. C. (Friedrich-Schiller University GDR) — 9th December, 1988
NMR Investigations of Fast Ion Conductors of the NASICON Type

JENNINGS, Prof. R.R. (Warwick University) — 26th January, 1989
Chemistry of the Masses

JOHNSON, Dr. B.F.G. (Cambridge University) — 23rd February, 1989
The Binary Carbonyls

JONES, Dr. M.E. (Durham Chemistry Teachers' Centre) — 14th June, 1989
Discussion Session on the National Curriculum

JONES, Dr. M.E. (Durham Chemistry Teachers' Centre) — 28th June, 1989
GCSE and A Level Chemistry 1989

LUDMAN, Dr. C.J. (Durham University) — 18th October, 1988
The Energetics of Explosives

MACDOUGALL, Dr. G. (Edinburgh University) — 22nd February, 1989
Vibrational Spectroscopy of Model Catalytic Systems

MARKO, Dr. I. (Sheffield University) — 9th March, 1989
Catalytic Asymmetric Osmylation of Olefins

McLAUCHLAN, Dr. K.A. (University of Oxford) — 16th November, 1988
The Effect of Magnetic Fields on Chemical Reactions

MOODY, Dr. C.J. (Imperial College) — 17th May, 1989
Reactive Intermediates in Heterocyclic Synthesis

MORTIMER, Dr. C. (Durham Chemistry Teachers' Centre) — 14th December, 1988
The Hindenberg Disaster - an Excuse for Some Experiments

NICHOLLS, Dr. D. (Durham Chemistry Teachers' Centre) — 11th July, 1989
Demo. "Liquid Air"

PAETZOLD, Prof. P. (Aachen) — 23rd May, 1989
Iminoboranes XB≡NR: Inorganic Acetylenes?

PAGE, Dr. P.C.B. (University of Liverpool) — 3rd May, 1989
Stereocontrol of Organic Reactions Using 1,3-dithiane-1-oxides

POLA, Prof. J. (Czechoslovak Academy of Sciences) 15th June, 1989
Carbon Dioxide Laser Induced Chemical Reactions - New Pathways in Gas-Phase Chemistry

REES, Prof. C.W. (Imperial College London) 27th October, 1988
Some Very Heterocyclic Compounds

REVELL, Mr. P. (Durham Chemistry Teachers' Centre) 14th March, 1989
Implementing Broad and Balanced Science 11-16

SCHMUTZLER, Prof. R. (Technische Universitat Braunschweig) 6th October, 1988
Fluorophosphines Revisited - New Contributions to an Old Theme

SCHROCK, Prof. R.R. (M.I.T.) 13th February, 1989
Recent Advances in Living Metathesis

SINGH, Dr. G. (Teesside Polytechnic) 9th November, 1988
Towards Third Generation Anti-Leukaemics

SNAITH, Dr. R. (Cambridge University) 1st December, 1988
Egyptian Mummies: What, Where, Why and How?

STIBR, Dr. R. (Czechoslovak Academy of Sciences) 16th May, 1989
Recent Developments in the Chemistry of Intermediate-Sited Carboranes

VON RAGUE SCHLEYER, Prof. P. (Universitat Erlangen Nurnberg) 21st October, 1988
The Fruitful Interplay Between Calculational and Experimental Chemistry

WELLS, Prof. P.B. (Hull University) 10th May, 1989
Catalyst Characterisation and Activity

CONFERENCES ATTENDED

(1) BZA Annual Meeting, Chislehurst, July 1987.

(2) NMR Discussion Group, University of Manchester, March 1988.

(3) BRSG and the CISG, NMR in Colloid and Interface Science, University of Bristol, April 1988. Poster Presentation: "Multinuclear magnetic resonance characterisation of high-silica theta-1".

(4) Ninth International N.M.R. Meeting, University of Warwick, July 1989. Poster Presentation: "NMR studies of the zeolite theta-1".

PAPERS PRESENTED:

"Multinuclear magnetic resonance characterisation of the zeolite theta-1". Graduate Symposium, University of Durham, April 1989.

POSTGRADUATE INDUCTION COURSE, October 1986

1. Departmental Organisation.
2. Safety matters.
3. Electrical appliances and infrared spectroscopy.
4. Chromatography and microanalysis.
5. Atomic absorptiometry and inorganic analysis.
6. Library facilities.
7. Mass Spectroscopy.
8. Nuclear magnetic resonance spectroscopy.
9. Glassblowing techniques.